



Universitat Autònoma de Barcelona

ADVERTIMENT. L'accés als continguts d'aquesta tesi queda condicionat a l'acceptació de les condicions d'ús establertes per la següent llicència Creative Commons:  http://cat.creativecommons.org/?page_id=184

ADVERTENCIA. El acceso a los contenidos de esta tesis queda condicionado a la aceptación de las condiciones de uso establecidas por la siguiente licencia Creative Commons:  <http://es.creativecommons.org/blog/licencias/>

WARNING. The access to the contents of this doctoral thesis it is limited to the acceptance of the use conditions set by the following Creative Commons license:  <https://creativecommons.org/licenses/?lang=en>



**Universitat Autònoma
de Barcelona**

PhD Thesis

***In vivo* modulation of neuromelanin levels: therapeutic approaches via VMAT2-overexpression and application of transcranial focused ultrasound in a neuromelanin-producing Parkinson's disease model**

Joan Compte Barrón

**Director: Dr. Miquel Vila Bover
Tutor: Dr. Joan Xavier Comella Carnicé**

**PhD in Neurosciences
Institut de Neurociències
Universitat Autònoma de Barcelona**

Barcelona, 2022



"la Caixa" Foundation

The project that gave rise to these results received the support of a fellowship from "la Caixa" Foundation (ID 100010434). The fellowship code is LCF/BQ/DI18/11660063



MARIE SKŁODOWSKA-CURIE ACTIONS

Research Fellowship Programme



European
Commission

Horizon 2020
European Union funding
for Research & Innovation

This project has received funding from the European Union's Horizon 2020 research and innovation programme under the Marie Skłodowska-Curie grant agreement No. 713673

CONTENTS

LIST OF CONTENTS

I. Introduction.....	1
1. Parkinson's disease pathogenesis.....	1
1.1 Motor circuit impairment.....	1
1.2 Neuronal death.....	3
1.3. Symptomatology.....	5
2. Etiology of Parkinson's disease.....	10
2.1 Parkinson's disease genetics.....	10
2.1.1 Autosomal-dominant forms of Parkinson's disease.....	11
2.1.1.1 <i>SNCA</i>	11
2.1.1.2 <i>LRRK2</i>	13
2.1.1.3 <i>VPS35</i>	15
2.1.2 Autosomal-recessive forms of Parkinson's disease.....	16
2.1.2.1 <i>PRKN</i>	16
2.1.2.2 <i>PINK1</i>	16
2.1.2.3 <i>PARK7</i>	17
2.1.2.4 <i>ATP13A2</i>	17
2.2 Risk factors.....	18
3. Epidemiology of Parkinson's disease.....	19
4. Treatment of Parkinson's disease.....	23
4.1 Management of motor symptoms.....	23
4.2 Management of non-motor symptoms.....	26
4.3 Traditional advanced therapies.....	28
4.3.1 Deep brain stimulation.....	29
4.3.2 Infusion therapies.....	30
4.4 Emerging advanced therapies.....	30
4.4.1 Transcranial focused ultrasound.....	31
4.4.1.1 Applications.....	33
4.4.1.2 Mechanisms of biological effects.....	34
4.4.2 Cell transplantation.....	37
4.4.3 Gene therapy.....	38
5. Parkinson's disease animal models.....	39
5.1 Neurotoxin-induced animal models.....	40
5.1.1 1-Methyl-4-phenyl-1,2,3,6-tetrahydropyridine.....	41
5.1.2 6-Hydroxydopamine.....	42
5.1.3 Paraquat.....	43
5.1.4 Rotenone.....	44
5.1.5 Other neurotoxicity-based animal models.....	45
5.2 Genetic animal models.....	46
5.2.1 <i>SNCA</i> modelling.....	47

5.2.1.1 <i>SNCA</i> transgenic modelling.....	47
5.2.1.2 <i>SNCA</i> viral vector-mediated modelling.....	48
5.2.2 <i>LRRK2</i> modelling.....	49
5.2.3 Other genetic animal models.....	49
6. Neuromelanin.....	50
6.1 Origin and classification.....	50
6.2 Presence of neuromelanin in human brain.....	53
6.3 Presence of neuromelanin in brains of other species.....	55
6.4 Synthesis of neuromelanin	56
6.4.1 Dopamine.....	56
6.4.2 Dopamine metabolism.....	59
6.4.2.1 Oxidative deamination.....	59
6.4.2.2 Ortho-methylation.....	59
6.4.2.3 Oxidation to aminochrome.....	61
6.4.2.3.1 Aminochrome metabolism.....	63
6.4.3 VMAT2.....	67
6.4.3.1 Implication of VMAT2 in Parkinson’s disease.....	68
6.4.4 Altered dopamine metabolism in Parkinson’s disease.....	69
6.4.5 Mechanism of neuromelanogenesis.....	72
6.5 Physiological roles of neuromelanin.....	76
6.5.1 Protective roles.....	77
6.5.2 Deleterious roles.....	78
6.6 Selective vulnerability of neuromelanin-containing neurons in Parkinson’s disease.....	81
6.7 Neuromelanin in Parkinson’s disease.....	86
6.8 Novel neuromelanin-accumulating Parkinson’s disease animal model.....	91
II. Hypothesis and objectives.....	99
III. Materials and Methods.....	103
1. Materials.....	103
1.1 Compounds and reagents.....	103
1.2 Kits.....	104
1.3 Buffers and solutions.....	104
1.4 Primary antibodies.....	105
1.5 Secondary antibodies.....	106
1.6 Stains.....	106
1.7 Equipment.....	106
1.8 Software.....	108
2. Methods.....	109
2.1 Animal handling.....	109
2.2 Viral vector production.....	109
2.3 Stereotaxic injection.....	110
2.4 tFUS experimental setup.....	111
2.5 MRI sequences.....	112

2.6 Ultrasound system.....	113
2.7 Anatomical sequences analysis.....	114
2.8 Cylinder behavioral test.....	114
2.9 Intracardiac perfusion.....	115
2.10 Microtomy.....	116
2.11 Immunohistochemistry on paraffin-embedded brain slices.....	117
2.12 Immunofluorescence on paraffin-embedded brain slices.....	119
2.13 Chromatographic determination of dopaminergic metabolites...121	
2.13.1 Calibration curves and quality control sample preparation.....	121
2.13.2 Sample preparation.....	122
2.13.3 UPLC-MS/MS Analysis.....	122
2.14 TH stereology counting.....	123
2.15 Densitometry.....	125
2.16 Neuromelanin quantification.....	126
2.17 Development and validation of artificial intelligence-based algorithms for automated quantification of neuroinflammation.....	126
2.17.1 CNN algorithms are a reliable method to detect and quantify GFAP-positive astrocytes, CD68-positive macrophages, and Iba-1-positive microglia in rat substantia nigra.....	128
2.17.2 CNN algorithms are a reliable method to assess changes in inflammation.....	134
2.17.3 CNN algorithms are also able to detect inflammation in human brain tissue.....	136
2.18 General statistical analysis.....	139
2.19 Statistical analysis of CNN algorithms.....	139
IV. Results.....	142
CHAPTER I: <i>In vivo</i> reduction of age-dependent neuromelanin accumulation mitigates features of Parkinson's disease.....	142
1. VMAT2 overexpression reduces catechol oxidation, NM accumulation and LB-like inclusion formation in NM-producing rats.....	142
2. VMAT2 overexpression prevents NM-linked neurodegeneration....	147
3. Attenuated neurodegeneration by VMAT2 overexpression is associated with a reduction in extracellular NM debris and inflammation.....	149
4. Preservation of striatal DA levels and metabolism by VMAT2 overexpression prevents motor deficits in NM-producing rats.....	150
CHAPTER II: MRI-guided transcranial focused ultrasound attenuates Parkinson's disease-like features in neuromelanin-producing rats.....	153
1. Early-stage MRI-guided tFUS application in NM-producing parkinsonian rats.....	153
2. tFUS reduces intracellular NM levels and extracellular NM debris in NM-producing parkinsonian rats.....	154
3. Reduction of extracellular NM debris by tFUS is linked to an	

attenuation of PD-like neuroinflammation.....	155
4. tFUS attenuates NM-linked nigral neurodegeneration.....	157
5. Preservation of motor function by tFUS in NM-producing parkinsonian rats.....	159
V. Discussion.....	163
VI. Conclusions.....	180
VII. Bibliography.....	184
VIII. Annex.....	239

LIST OF TABLES

Table 1. Most studied brain regions presenting cell loss in PD.....	5
Table 2. Neurotransmitters and pharmacologic agents related to PD symptoms.....	27
Table 3. Summary of the principal neurotoxins involved in PD modelling and their principal features.....	46
Table 4. Summarized role duality of NM in SNpc neurons.....	77
Table 5. Multiple reaction monitoring (MRM) acquisition settings.....	123
Table 6. Results for counting recall, precision and F1-score of the CNN algorithm compared to human observers.....	133
Table 7. Formulas for calculating recall, precision and F1-score for the CNN algorithm.....	139

LIST OF FIGURES

Figure 1. DA pathways affected in PD.....	1
Figure 2. Motor cortex circuitry changes in PD.....	3
Figure 3. Clinical symptoms associated with PD.....	6
Figure 4. Staging of neurodegeneration in clinical PD.....	7
Figure 5. Hypothetical models for neuronal degeneration in PD.....	9
Figure 6. Summary of genetic variants in PD grouped according to allele frequency and associated risk.....	11
Figure 7. α -synuclein aggregation in higher-ordered structures.....	12
Figure 8. Subcellular organelles and intracellular pathways potentially affected by α -synuclein and LRRK2 synergistic interaction.....	14
Figure 9. Overview scheme of genes associated with PD directly or as risk factors.....	19
Figure 10. Sex differences in PD.....	21
Figure 11. Dopaminergic targets in PD.....	24
Figure 12. Emerging future therapeutic strategies for PD.....	31
Figure 13. Biological effects of tFUS.....	33
Figure 14. Overview of the tFUS setup and parameters.....	37
Figure 15. Percentages of animal models used in PD research from January 1990 to June 2018.....	40
Figure 16. Structures of neurotoxic molecules known to induce nigrostriatal damage in common PD animal models.....	40
Figure 17. Core structures of eumelanin and pheomelanin.....	51
Figure 18. NM-containing regions in the human brain.....	51
Figure 19. Transmission electron microscopy of NM-containing organelles.....	52
Figure 20. NM progressive accumulation in the human brain.....	54

Figure 21. Schematic representation of NM accumulation in human DA neurons.....	55
Figure 22. NM presence in the human (control vs PD) brain and in other species DA neurons.....	56
Figure 23. Cycle of DA in the neuronal terminal.....	58
Figure 24. DA degradation catalyzed by MAO and COMT.....	61
Figure 25. DA oxidation to aminochrome.....	63
Figure 26. One-electron reduction of aminochrome.....	64
Figure 27. Two-electron reduction of aminochrome.....	65
Figure 28. Glutathione conjugation of aminochrome and DA <i>o</i> -quinone.....	66
Figure 29. Possible mechanism for the synthesis of NM pigment.....	67
Figure 30. Summary of DA oxidation to <i>o</i> -quinones multiple fates.....	71
Figure 31. Hypothesized scheme summarizing NM-containing organelle formation in human SN.....	74
Figure 32. Neuronal vulnerability in PD.....	85
Figure 33. Human-like NM production in tyrosinase-overexpressing rats.....	92
Figure 34. Physiologic and therapeutic implications of a potential pathological threshold of intracellular NM accumulation in DA neurons.....	94
Figure 35. Molecular mechanisms of NM-linked neurotoxicity.....	95
Figure 36. tFUS apparatus and Thermoguide software used for experimentations...	114
Figure 37. Anatomical levels of rat SN used for quantifications.....	125
Figure 38. Workflow of the automatized counting method using the Aiforia platform.....	127
Figure 39. Deep-learning algorithms detection of GFAP ⁺ -astrocytes and CD68 ⁺ -macrophages in an inflammatory milieu in rat.....	129
Figure 40. Validation of the Aiforia platform.....	130
Figure 41. Deep-learning algorithms detection of different reactivity states of Iba-1 ⁺ cells in an inflammatory milieu in rat.....	132

Figure 42. Representation of a typical inflammation milieu upon eNM stimulation...	134
Figure 43. Deep-learning algorithms detection of GFAP ⁺ -astrocytes and CD68 ⁺ -macrophages in a human inflammatory milieu.....	137
Figure 44. Deep-learning algorithms detection of different reactivity states of Iba-1 ⁺ cells in a human inflammatory milieu.....	138
Figure 45. Overexpression of functional VMAT2 in the nigrostriatal pathway of rats.....	142
Figure 46. Reduced catechol oxidation, NM accumulation and LB-like pathology by VMAT2 overexpression in NM-producing rats.....	143
Figure 47. hTYR and hVMAT2 transduction efficiency in AAV-hTYR- and AAV-hVMAT2-injected animals, alone or in combination.....	145
Figure 48. Schematic representation of DA metabolism and oxidation pathways.....	147
Figure 49. VMAT2 overexpression prevents SNpc neurodegeneration in NM-producing rats.....	148
Figure 50. VMAT2 overexpression reduces extracellular NM debris and inflammation in the SNpc of NM-producing rats.....	150
Figure 51. VMAT2 overexpression preserves striatal DA levels and motor function in NM-producing rats.....	151
Figure 52. Summary of VMAT2 overexpression-mediated therapeutic effect in NM-accumulating PD rats.....	152
Figure 53. Schematic representation of the experimental design for the tFUS treatments in parkinsonian NM-producing rats.....	153
Figure 54. tFUS reduces intracellular and extracellular NM accumulations by tFUS in NM-producing parkinsonian rats.....	155
Figure 55. tFUS diminishes PD-like inflammatory changes in NM-producing parkinsonian rats.....	156
Figure 56. tFUS attenuates SN neurodegeneration in NM-producing parkinsonian rats.....	158
Figure 57. tFUS preserves [dorso]striatal TH-positive fibers and long-term motor function.....	160

LIST OF ABBREVIATIONS

3-MT	3-methocytyramine
5SCD	5-S-cysteinyl dopa
5SCDA	5-S-cysteinyl dopamine
6-OHDA	6-hydroxydopamine
AADC	aromatic amino acid decarboxylase
ABC	avidin biotin complex
AD	Alzheimer's disease
AAV	Adeno-associated virus
BBB	blood-brain barrier
CNN	convolutional neural network
COMT	catechol-o-methyltransferase
CSF	cerebrospinal fluid
DA	dopamine, dopaminergic*
DA4d	dopamine -1,1,2,2-d4 hydrochloride
DAB	diaminobenzidine tetrachloride
DAPI	4',6-diamidino-2-phenylindole
DAT	dopamine transporter
DBS	deep brain stimulation
DLB	dementia with Lewy Bodies
DMNV	dorsal motor nucleus of the vagus nerve
DOPAC	3,4-dihydroxyphenylacetate
DOPAL	3,4-dihydroxyphenylacetaldehyde
DOPE	3,4-dihydroxyphenylethanol
e.g.	<i>exempli gratia</i> (example given)
eNM	extracellular NM
EV	empty vector
Fig	figure
g	gram
GDNF	glial cell line-derived neurotrophic factor
h	hour
hTyr	human tyrosinase
HVA	homovanillic acid
i.e.	<i>id est</i> (that is)
IF	immunofluorescence
IHC	immunohistochemistry
iLBD	incidental Lewy Body disease
I_{spta}	spatial peak temporal average intensity
I_{sppa}	spatial peak pulse average intensity
L-DOPA	levodopa
LB	Lewy body
LC	locus coeruleus
LN	Lewy Neurite
LP	Lewy Pathology
m	month

MAO	monoamine oxidase
MI	mechanical index
MPP	phenylpyridium ion
MPTP	1-methyl-4-phenyl-1,2,3,6-tetrahydropyridine
NM	neuromelanin
PBS	phosphate-buffered Saline
PD	Parkinson's disease
ROS	reactive oxygen species
RT	room temperature
SAM	S-adenosyl-L-methionine
SN	substantia nigra
SNpc	substantia nigra pars compacta
SNpr	substantia nigra pars reticulata
STN	subthalamic nucleus
STR	striatum
TBS	tris-buffered Saline
tFUS	transcranial focused ultrasound
TH	tyrosine hydroxylase
TI	thermal index
Tyr/TYR	tyrosinase
US	ultrasound
UV-Vis	ultraviolet-visible
VMAT2	vesicular monoaminergic transporter-2
VTA	ventral tegmental area
w	week
w/v	percent of weight of solution in the total volume of solution

*Only when referred to neurons

SUMMARY

Parkinson's disease (PD) is the second most common neurodegenerative disorder after Alzheimer's disease. Global estimates suggest that there are currently over 8.5 million individuals living with this disorder, whose prevalence is expected to reach 12 million affected individuals by 2050. The principal neuropathological hallmarks of PD are the selective loss of neuromelanin-containing neurons in the substantia nigra and the presence of intracellular inclusions called Lewy bodies. Despite being considered a movement disorder characterized by progressing worsening, PD is also associated with many non-motor symptoms which accentuate overall disability. Presently, there is no permanent cure for the disorder, with available treatments aimed at restoring striatal dopamine and addressing non-motor symptoms. However, none of these is curative and PD remains a progressive disorder that ultimately causes severe affliction. Traditionally, Parkinson's disease research has focused on α -synuclein (the principal component of Lewy bodies), although until recently no animal model that reproduces the progressive nature of the disease has been developed. We generated a new rodent model based on human tyrosinase overexpression that accumulates neuromelanin over time and shows progressive neuronal dysfunction followed by eventual death. Using this model, we present herein two innovative neuromelanin-modulating strategies for reducing neuronal demise and PD-like features in these animals.

In Chapter I, the therapeutic effect of VMAT2 overexpression in neuromelanin-accumulating animals is described. We demonstrate that VMAT2 overexpression reduces cytosolic dopamine, thereby decreasing neuromelanin precursors. In turn, intracellular levels of neuromelanin are kept below a pathological threshold. This translates to a preservation of nigral neuron integrity and reduced neuronal death. Neuronal survival preserves striatal fiber integrity and restores striatal dopamine, ensuring a significant improvement in motor function.

In Chapter II, the therapeutic effect of the application of transcranial focused ultrasound is described. We demonstrate that the application, by itself, reduces neuromelanin levels and inflammation in the substantia nigra, and preserves the nigrostriatal pathway. In turn, PD-like phenotype is rescued and motor performance is improved.

I. INTRODUCTION

PREFACE

Two hundred years ago James Parkinson first described a clinical condition characterized by a uncontrolled trembling coining it as *shaking palsy*¹; nowadays the scientific community refers to it, in his honor, as Parkinson's Disease (PD). This malady remains not only without a cure, but with the global prevalence of PD expected to double from 6.2 million cases in 2015 to 12.9 million cases by 2040, PD now sits as the most common movement disorder and the second most common neurodegenerative disease, after Alzheimer's Disease (AD)². PD was initially classified merely as a movement disorder, but patients are known to also display a myriad of non-motor features, including cognitive deterioration, autonomic impairment, sleep alterations, depression and, incipient hyposmia³. Despite significant advances that have been made in assessing the neuropathology of PD and its progression throughout the nervous system, as well as the neurophysiological and molecular mechanisms and alterations inherent to the disease, PD currently has no cure. However, prolonged and thorough research efforts have given rise to highly efficacious therapeutic approaches, focused mainly on pharmacological treatment with levodopa (L-DOPA) and dopamine (DA) agonists, but also with considerable technological developments, such as the application of deep brain stimulation. These advances have elevated PD to the paradigm of a neurodegenerative disease that can be effectively managed, potentially enabling symptom control and quality of life to be maintained for decades after disease onset. PD remains nevertheless a progressive disorder that potentially causes significant disability, particularly due to the increasing severity of therapy-resistant motor and non-motor symptoms. Therefore, mitigating disease progression and preventing disability worsening are crucial issues that current and future research need efforts must address. Also, of utmost relevance is the need to discover reliable biomarkers enabling the identification both of preclinical (patients with no clinical signs or symptoms) and prodromal (patients with early non-motor and with or without early, but subtle motor symptoms) phases of the disease and for therapeutic strategies to be developed that delay disease progression and minimize its impact on affected patients. The present dissertation presents two novel strategies aimed at reverting PD-like motor symptomatology in a humanized rat model of PD.

1. PARKINSON'S DISEASE PATHOGENESIS

1.1 MOTOR CIRCUIT IMPAIRMENT

While PD is primarily characterized by movement deficits, it also encompasses many non-motor symptoms. The term “parkinsonism” recapitulates a characteristic constellation of motor impairments that are associated with PD, including decreased and slow movement (akinesia and bradykinesia), muscular rigidity, gait instability and tremor at rest⁴. Parkinsonism results, in large part, from the degeneration of neuromelanin (NM)-containing DA neurons in the substantia nigra *pars compacta* (SNpc)⁵, and the resulting reduction in DA levels in the striatum (STR), the main synaptic target of SNpc axons, forming the nigrostriatal pathway⁶ (Fig. 1).

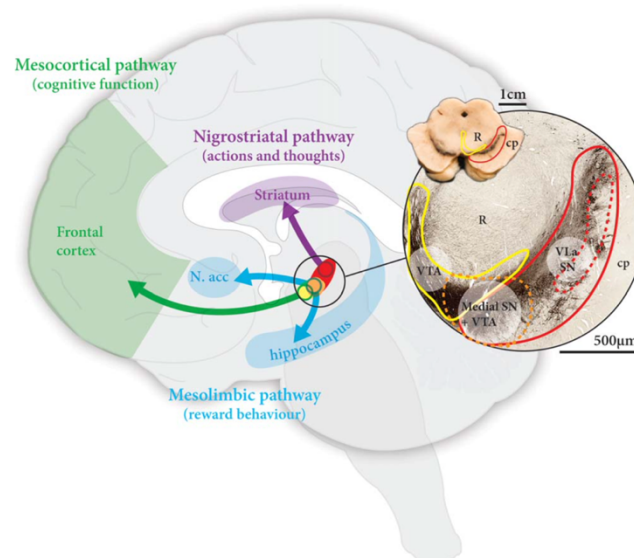


Figure 1. DA pathways affected in PD. Red outline: SN, which contains both DA neurons in the *pars compacta* that give rise to nigrostriatal projections, and GABA neurons in the *pars reticulata*, which innervate the thalamus. Dotted red line: ventrolateral (VLa) SN, which is selectively damaged in patients with PD. Yellow outline: ventral tegmental area (VTA), which contains both DA and non-DA neurons that project to limbic and cortical regions. Dotted orange outline: medial SN and VTA, which give rise to mesolimbic projections that are specially affected in patients with PD with dementia. cp, cerebral peduncle; N. acc, nucleus accumbens; R, red nucleus. From Halliday et al., 2014⁷.

Nigral DA neuron degeneration is the neuropathological hallmark of PD, with loss of the physiological dopaminergic modulation altering cortico-striatal plasticity and transforming the basal ganglia into a disruptive filter that impairs the ability to acquire and express habitual-automatic movements as will be described below⁸. Specifically, DA loss in PD correlates with profound changes in the activity of neurons in the basal ganglia-thalamocortical circuits. The basal ganglia consist of the SNpc, the SN *pars*

reticulata (SNpr), the (neo)STR (containing the caudate nucleus and putamen), the external and internal segments of the globus pallidus and the subthalamic nucleus (STN). These structures form part of larger functional and anatomical parallel circuits that include areas of the frontal cortex and the ventral thalamus as well. Depending on the frontal cortical area of origin, the functions of associated basal ganglia-thalamo-cortical circuits are designated as “motor”, “associative/cognitive” and “limbic”^{9,10}. The general anatomical arrangement of the basal ganglia is similar across these circuits. Glutamatergic excitatory cortical inputs reach the basal ganglia via the STR and STN, and, to a lesser extent, via the thalamus. The information is then transmitted to the output nuclei of the basal ganglia, the globus pallidus internus and SNpr. Projections from the STR to the output nuclei are divided into “direct” and “indirect” pathways. Whereas the former pathway is a monosynaptic connection between medium spiny neurons that express DA D1 receptors and GABAergic neurons in the globus pallidus internus and the SNpr, the latter pathway originates from medium spiny neurons that express DA D2 receptors, which project to the globus pallidus externus, and reaches the internus via the STN as a glutamatergic relay. Importantly, the loss of striatal DA is associated with morphological (non-dopaminergic) changes throughout the basal ganglia, including a decrease in the density of dendritic spines on spiny neurons in the STR and alterations to intrastriatal and pallido-subthalamic connectivity.

The STN is another major entry pathway for extrinsic cortical information into the basal ganglia. The cortico-subthalamic route, together with its continuation to the globus pallidus internus/SNpr has been termed the “hyperdirect” pathway because information flowing along this projection reaches the basal ganglia output structures with a shorter delay than information transmitted along the direct and indirect corticostriatofugal systems¹¹. Due to the defined scope of the present dissertation, only the motor circuitry will be addressed. Figure 2 reflects the consequences of the loss of DA in the described motor circuitry, which give rise to classic parkinsonian motor symptomatology in PD.

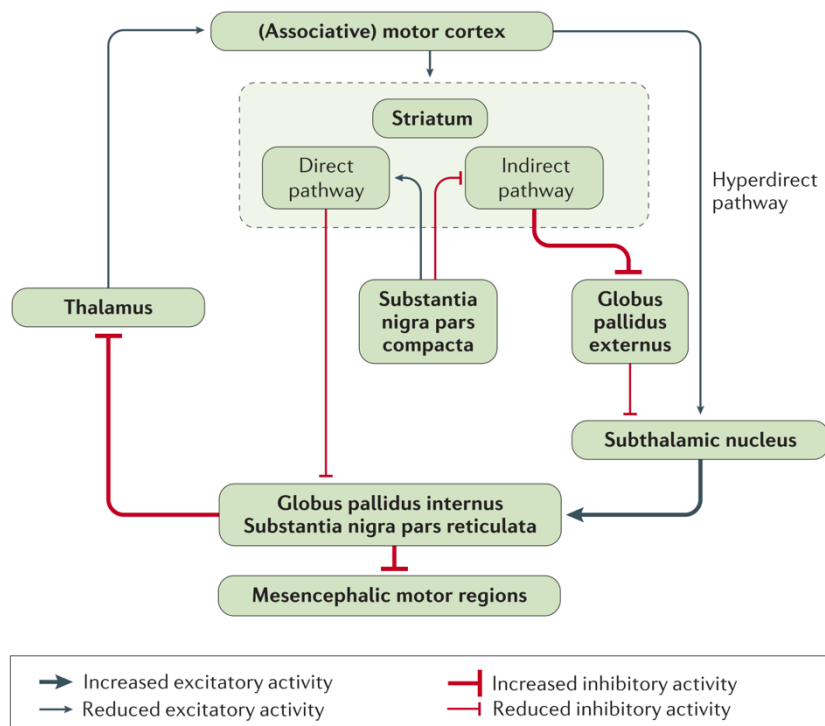


Figure 2. Motor cortex circuitry changes in PD. The motor circuit consists of corticostriatal projections from the primary motor cortex, supplementary motor area, cingulate motor cortex and premotor cortex, terminating on the dendrites of striatal medium spiny neurons. The hyperdirect pathway has direct connectivity from the motor cortex to the subthalamic nucleus. The globus pallidus internus and substantia nigra pars reticulata are the two main output nuclei of the basal ganglia and project to the mesencephalic motor regions and ventrolateral thalamus. Striatal projections to these output nuclei are divided into direct and indirect pathways via which striatal dopaminergic tone regulates the GABAergic output activity of the basal ganglia. As shown, parkinsonism is associated with severe changes in these relays. In fact, nigrostriatal DA deficiency has opposing effects on the direct (its excitatory activity becomes reduced) and indirect (its inhibitory activity becomes reduced) pathways. Ultimately, DA loss results in over-inhibition of the mesencephalic motor regions, causing classical PD movement symptomatology. From Poewe et al., 2017¹².

1.2 NEURONAL DEATH

As mentioned above, the loss of SNpc DA neurons in PD, which has been postulated to be preceded by alterations in synaptic transmission and axonal transport¹³, is responsible for the core motor symptoms of this disease¹⁴. Apart from nigral cell loss, a further pathological hallmark is the presence of cytoplasmic Lewy bodies (LB) in these neurons. These structures, together with Lewy neurites (LN), are predominantly formed from aggregated α -synuclein, but also include a large number of different molecules, proteins and organelles, such as ubiquitin, p62, tubulin, neurofilaments, lipids and mitochondria¹⁵. It has been estimated that Lewy pathology (LP, i.e., the presence of both

LB and LN) is present in the SNpc in roughly 70% of clinically “typical” PD cases^{16–18}. However, LP and neuronal loss in PD are not only restricted to the SNpc but are also found in different regions of the central, peripheral and enteric nervous systems¹⁹. It is important to note that, although *postmortem* LP has been used as marker of PD progression state^{20,21}, the relationship between LP and neuronal dysfunction and death is uncertain. In fact, the presence of LP in a particular cell type has been suggested to indicate a successful response to proteostatic stress and not a loss of function^{22,23}. Furthermore, LP is found in other synucleinopathies that have an undefined connection to PD, particularly patients diagnosed with dementia with LB (DLB) and incidental LB disease (iLBD), the latter of which is widely suspected to be an earlier stage of PD or DLB²⁴. Also, patients with multiple system atrophy show an abnormal α -synuclein signature²⁵.

Considering the broad localization of LP and the co-existence and progressive nature of PD symptoms, it is important to highlight that many other cell types, apart from SNpc DA neurons, potentially degenerate in this disease. Table 1, which is based on literature reports from 1953 to 2015 compiled by Giguère et al. (2018), lists values of neuronal loss in PD in the most studied brain regions²⁶. Other regions that have been assessed but to a lesser extent include the amygdala, the hippocampus, the laterodorsal tegmental nucleus and the oral pontine reticular nucleus²⁶. Since major neuronal demise in PD takes place in NM-containing cells, and given that NM is a central player in the present dissertation, it is appropriate for me to place additional emphasis on them here. As will be further discussed, NM-producing neurons are catecholaminergic cells found primarily in the brainstem, namely in the midbrain and pons²⁷. However, some NM-containing neurons have also been reported to be present in other brain regions²⁸ and appear to be intact in PD²⁹, suggesting that NM *per se* is not sufficient to propagate cell demise. Therefore, the fact that four regions with the highest reported neuronal loss contain NM-producing neurons, indicates the vulnerability – which will be later addressed – of these cells in an NM-specific context in PD (Table 1). Intriguingly, despite displaying NM accumulation, each region synthesizes a different monoamine transmitter. Moreover, high levels of cytosolic monoamines are reactive and hypothesized to underlie selective neuronal death under different conditions³⁰. In this

sense, nigral neuronal loss is indisputable with an average decline of almost 70%, followed by the raphe nuclei (obscurus and median; not dorsal), dorsal motor nucleus of the vagus nerve (DMNV), and locus coeruleus (LC) with similar percentage losses (around 57%). The LC displays the highest reported decrease (94%) for a brain region in PD.

Table 1. Most studied brain regions presenting cell loss in PD. Cell loss quantifications derive from different techniques: stereological counting, computer-assisted, manual and observational. Results for brain regions with no or only 1 stereological study are shown in italics. Average losses based on stereological counting studies are shown in parentheses. *In the dorsal raphe nucleus, no neuronal death was detected. Generated from original articles spanning the period from 1953 to 2015. Based on Giguère et al., 2018²⁶.

Region	Loss of neurons range (%)	Average of neuronal death (%)
Substantia nigra pars compacta	37% - 90%	69% (68%)
Raphe nuclei	<i>37% - 90%*</i>	<i>59% (0%)</i>
Dorsal motor nucleus of the vagus nerve	<i>30% - 77%</i>	<i>58% (55%)</i>
Locus coeruleus	<i>21% - 94%</i>	<i>55% (-)</i>
Nucleus basalis of Meynert	<i>17% - 90%</i>	<i>54% (-)</i>
Ventral tegmental area	<i>31% - 77%</i>	<i>49% (31%)</i>
Pedunculopontine nucleus	<i>31% - 50%</i>	<i>44% (41%)</i>
Thalamus	<i>0% - 70%</i>	<i>36% (30%)</i>
Hypothalamus	<i>0% - 50%</i>	<i>34% (50%)</i>
Sympathic/parasympathic ganglia	<i>0% - 43%</i>	<i>19% (-)</i>
Cortex	<i>0%</i>	<i>0% (0%)</i>
Olfactory bulb	57% loss - 100% increase	57% (-)

1.3 SYMPTOMATOLOGY

PD is mostly known as being a movement disorder, since the specific degeneration of DA neurons in the SNpc disrupts the nigrostriatal pathway, which oversees controlled motor activity. In this regard, classical PD motor symptoms involve movement and physical tasks including tremor, bradykinesia, stiffness, and imbalance. Non-motor symptoms, derived from the death of multiple neuron types as mentioned above, affect many organ systems, such as the gastrointestinal and genitourinary systems, and are heterogeneous in nature³¹. Individuals recently diagnosed with PD typically exhibit a gradual development of non-motor symptomatology before the onset of motor

symptoms. These so-called prodromal non-motor features include loss of smell, rapid eye movement behavior disorder, constipation, orthostatic hypotension, urinary dysfunction, excessive daytime sleepiness, and depression³². It is noteworthy that two of the regions postulated to degenerate first in PD, namely LC and DMNV, were reported to be linked to early symptoms. In this regard, LC is involved in the initiation of activity states (such as the sleep-wake cycle) and modulation of the collection and processing of sensory information during the attentive state²⁸, whereas DMNV plays an important role in the autonomic control of the gastrointestinal tract, the cardiac and respiratory systems, as well as in the regulation of hypothalamic hormones^{29,30}.

Whereas these symptoms are not PD-specific, when they occur concomitantly, there is greater risk for developing PD³². For example, more than 90% of individuals with idiopathic rapid eye movement sleep behavior disorder eventually develop an α -synucleinopathy, usually PD or a related condition like DLB or multiple system atrophy³³. Moreover, an estimated 30%–50% of PD patients exhibit sleep dysregulation³⁴. The non-motor symptom burden increases as PD progresses, usually entailing mild neuropsychiatric disorders and incipient cognitive impairment. Advanced PD is characterized mainly by dyskinesias (involuntary muscle movements), hallucination, excessive daytime sleepiness, and severe forms of motor symptomatology, autonomic dysfunction, and cognitive deterioration³¹. A summary of all known symptoms related to PD that have been described to date, is presented in figure 3.

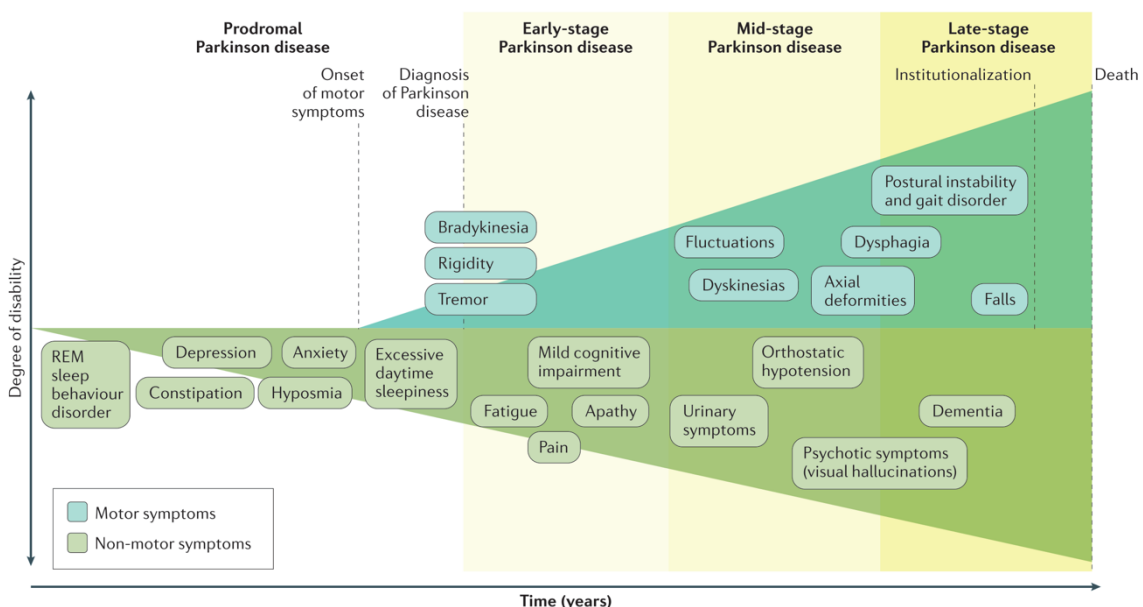


Figure 3. Clinical symptoms associated with PD. Diagnosis of PD occurs with the onset of motor symptoms (early-stage PD) usually in the patient’s late fifties, but can be preceded by a prodromal phase of years or even decades^{35,36}, which is characterized by specific non-motor symptoms, that increase both in intensity and number along the course of the disorder. Progressive disability from PD is driven by the combination of these non-motor problems with intensifying severity of cardinal motor features, the development of L-DOPA-induced motor complications (mid-stage PD) and the evolution of poorly L-DOPA-responsive motor impairments (late-stage PD). REM, rapid eye movement. From Poewe et al., 2017¹².

While prodromal symptoms are associated with early PD brainstem pathology (stage 1/2, Figure 4), motor symptoms are thought to appear once neuropathological progression results in loss of approximately half of DA neurons in the SN (stage 3/4)³⁷. The level of cell demise required for motor symptomatology onset is somewhat controversial; some studies have set the threshold as low as 40%³⁸, while others have it at 50%^{39,40} or even 60% to 70% in some cases^{41,42}.

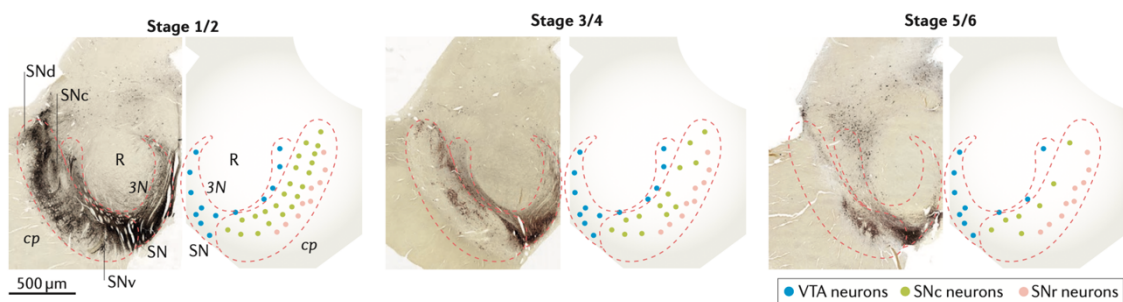


Figure 4. Staging of neurodegeneration in clinical PD. Transverse sections of PD midbrains at different stages of disease progression are shown. The typical distribution of DA neurons is shown in the left panels and schematized in the right panels. Heavily pigmented neurons of the *substantia nigra pars compacta* (SNc) are depicted in green; less pigmented neurons of the ventral tegmental area (VTA) are depicted in blue; neurons of the SN *reticulata* (SNr) are depicted in pink. The initial loss of ventral-tier SNc observed in stage 4 PD patients is depicted in the middle panels, with greater cell loss observed over time at later stages, as indicated in the rightmost panels. SNd, dorsal tier of the SNc; SNv, ventral tier of the SNc; 3N, third nerve; R, red nucleus; cp, cerebral peduncle. Modified from Surmeier et al., 2017⁴³.

It is indisputable that neuronal loss in the SNpc is consequently the cardinal pathological hallmark in PD. Up to 2018, the average cell loss reported for studies involving stereological methods was around 68%²⁶. But, at the same time, neuronal loss in the SNpc specifically –not in the reticulata–, as well as more pathological changes than any other region, was reported to occur in the context of normal aging^{44–46}. This age-related cell demise rate was estimated to take place at a *slow* rate of 4.7%³⁷ and at a *moderate* rate of 9.8%⁴⁷. Regardless of the rate, many studies have measured aging-related cell loss in other brain regions, though none have shown any degree of neuronal loss similar

to that seen in the SN⁴⁶. In fact, neuronal numbers have been shown to remain relatively stable throughout old age in the majority of analyzed brain regions⁴⁸, whereas in other non-SNpc DA populations, like the ventral tegmental area (VTA) or the retrorubral area, neuronal loss might reach 50%⁴⁹, emphasizing the preferential vulnerability of DA neuronal populations, not only in neurodegenerative disorders like PD, but also with normal aging. As will be thoroughly described in upcoming sections, DA neurons in the SNpc present a unique environment, which favors their specific susceptibility, and not only in PD. A combination of differentiating factors such as a distinctive cellular architecture (characterized by their large, complex axonal arborization) and consequent tight energy budget⁵⁰, a constant basal oxidative stress due to their autonomous pacemaking activity⁵¹, a potentially neurotoxic metabolism such as that entailed by DA⁵², a double edge sword component such as NM⁵³, elevated levels of a highly-reactive element such as iron^{54,55}, and a particularly high bioenergetic demand^{56,57} contribute to this susceptibility. Furthermore, they are especially prone to suffer impairment of protein degradation processes and mitochondrial dysfunction, which affect many of the cited mechanisms that are so intimately linked to PD.

Of all the other nuclei affected in PD which have neurons exhibiting similarities with the DA neurons in the SN, are the noradrenergic neurons in the LC, which also undergo significant loss (estimated at around 70%)⁵⁸. LC neurons were reported to show alterations in the ultrastructure of their synaptic mitochondria in PD, suggesting that mitochondrial dysfunction is a deleterious process which might also occur within noradrenergic neurons⁵⁹. In any case, independently of the required amount of neuronal death for the motor symptoms to appear, PD progression seems to be an accelerated process of normal aging in terms of neuronal decline (Fig. 5).

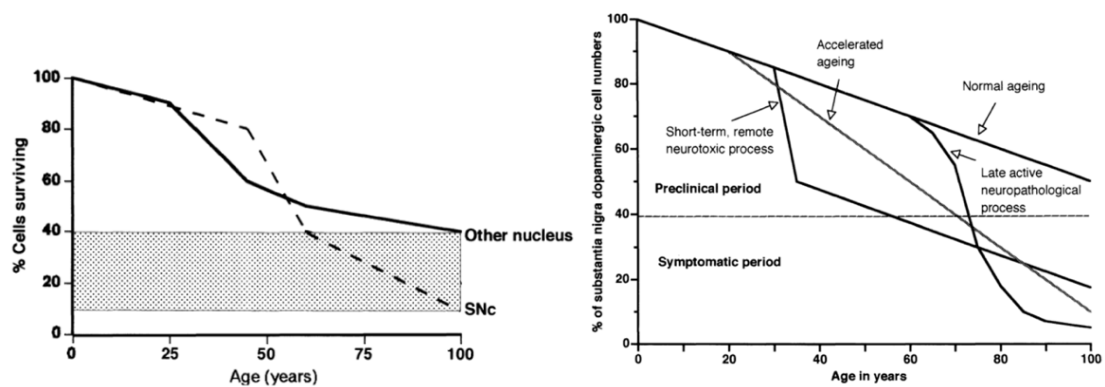


Figure 5. Hypothetical models of neuronal degeneration in PD. *Left*, Model illustrating differential rates of neurodegeneration in different PD brain nuclei. The shaded region depicts the period in which SNpc cell loss is sufficient to produce classical motor symptomatology, but where sufficient neurons remain to make neuroprotection a viable strategy. The degree of neuronal loss in other nuclei resulting in clinically detectable symptoms is different in each case, as is the therapeutic window. *Right*, Different models of the rate of progression of SNpc neurodegeneration in normal aging and PD, both in the early and late onset forms of the disease, are represented. From Przuntek et Müller, 1999³⁸.

For the clinical establishment of PD, individuals need to meet at least 2 out of 4 supportive criteria, namely resting tremor, a strong improvement with DA therapy, the presence of L-DOPA-induced dyskinesias, or the presence of either olfactory loss or cardiac sympathetic denervation. In this regard, 3 different PD subtypes, defined by motor and non-motor symptomatology, have been proposed: (1) mild motor predominant: younger age of onset, mild motor and non-motor symptoms, slow progression, good medication response; (2) intermediate: intermediate age at onset and symptomatology, moderate-to-good response to medication, moderate progression; (3) diffuse malignant: baseline motor symptoms accompanied by rapid eye movement sleep behavior disorder, mild cognitive impairment, poorer response to medication, rapid progression^{60,61}. In this categorization, the mild motor predominant form is the most common (49%–53%), followed by the intermediate form (35%–39%), with the diffuse malignant form being the least frequent (9%–16%)^{60,61}. Another widely used scale and universal staging system for overall functional disability in PD is the Hoehn and Yahr scale, which describes five stages of PD progression: from 1 one being the earliest stage with very mild symptoms (unilateral involvement only), towards stage 5 that reflects the most advanced stage of the disease characterized by confinement of the patient to bed or a wheelchair⁶². Another recent scaling for PD proposed by the Movement Disorder Society is the Unified PD Rating Scale⁶³. This staging system consists of 4 different

categories ranging from 1, where patients display minimal symptoms, to 4, which corresponds to the most severe symptoms.

2. ETIOLOGY OF PARKINSON'S DISEASE

2.1 PARKINSON'S DISEASE GENETICS

The identification of rare genetically-driven forms of PD and subsequent functional studies related to disease-causing mutations have substantially advanced our understanding of the cellular dysfunction(s) driving neurodegeneration⁶⁴. Indeed, studying individual mutations has contributed enormously to defining cellular phenotypes linked to molecular signaling pathways related to a specific gene, since these phenotypes may subsequently serve as cellular archetypes for habitual sporadic forms of the disease⁶⁵. Genetics provides one way by which PD phenotypes can be classified. Current stratification factors for PD include age of onset (early- vs late-onset PD, typically with a cut-off of 50 years of age), the presence or absence of familial history (familial vs sporadic) and the presence or absence of known pathological variants (monogenic vs idiopathic)⁶⁶. Different subgroups may have separate etiologies, treatments and prognosis⁶⁷. Strikingly, the majority of PD cases are sporadic, whereas only 10% of patients report an hereditary component⁶⁸. In the late 1990s, Polymeropoulos et al. identified, for the first time, mutations responsible for PD, thereby clearly showing that PD may be an hereditary disorder^{69,70}. Since then, new chromosomal regions have been reported and, currently, PD genetics' nomenclature encompasses 18 specific chromosomal loci termed *PARK* (to denote their potential link to PD), which are numbered in chronological order of identification (*PARK1*, *PARK2*, etc.). Only 7 of these chromosomal regions contain genes with mutations that unequivocally cause monogenic PD, where a mutation in a single gene is enough to cause the phenotype.

From these, mutations in *SNCA* (*PARK1*, 4), *LRRK2* (*PARK8*) and *VPS35* (*PARK17*) are responsible for autosomal-dominant forms of the disease, while mutations in *PRKN* (*PARK2*), *PINK1* (*PARK6*), *DJ-1* (*PARK7*) and *ATP13A2* (*PARK9*) are responsible for PD displaying an autosomal recessive mode of inheritance (Fig. 6). Evidence for *EIF4G1*

(*PARK18*) has been reported, but remains inconclusive⁷¹. In autosomal-dominant disorders, one mutated allele of the gene is sufficient to cause the disease, while in contrast, autosomal-recessive disorders, two mutations (the same (homozygous), or different (compound heterozygous)), one on each allele, are necessary to provoke the disease. Strikingly, mutations in mitochondrial DNA of the SN of PD patients have been also described⁷². Therefore, despite a marked genetically heterogeneous background, PD is a complex and multifactorial disorder, which presumably results from an intricate interplay of factors including several genes, environmental exposure, gene-environment interactions (e.g., influence of environmental agents on gene expression), modifying effects by susceptibility alleles, and their impact on the developing and aging brain. Next, current knowledge and understanding of PD molecular genetics will be addressed.

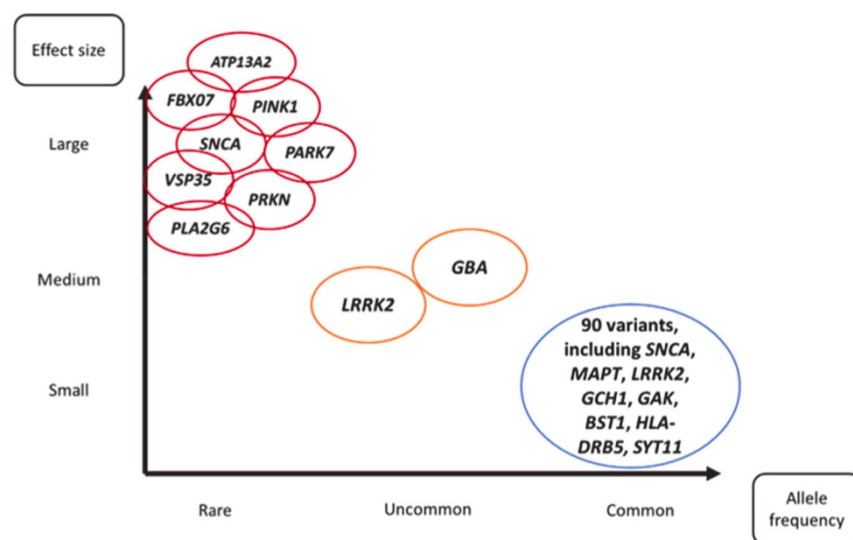


Figure 6. Summary of genetic variants in PD grouped according to allele frequency and associated risk. From these, only 7 have been confirmed to cause monogenic PD: *SNCA*, *LRRK2*, *VSP35*, *PRKN* (*parkin*), *PARK7* (*DJ-1*), *PINK1* and *ATP13A2*. From Jacob & Mullin, 2021⁶⁶.

2.1.1 AUTOSOMAL-DOMINANT FORMS OF PARKINSON'S DISEASE

2.1.1.1 *SNCA*

The gene encoding the 140-amino acid-long cytosolic α -synuclein protein was the first gene with mutations reported to cause autosomal-dominant PD⁶⁹. Affected patients usually have early-onset PD (i.e., before 50 years of age) and initially have a good response to L-DOPA treatment. Nonetheless, the disease progresses rapidly and often

entails dementia and cognitive decline, and, sometimes, atypical features such as central hypoventilation and myoclonus⁷³. LB are present and spread through the SN, LC, hypothalamus and cerebral cortex⁶⁹. However, mutations in *SNCA* are infrequent and, so far, only six different missense mutations⁷⁴ as well as increased copy number (duplications^{75,76} -also found in sporadic cases⁷⁷- or triplications^{76,78}) have been reported. Missense mutations appear to have a high degree of penetration, suggested to reach 85% for the A53T mutation⁶⁹ (the most frequent mutation). On the other hand, gene amplification is reduced and estimated to be 33%⁷⁹. It is noteworthy that gene dosage has been related with clinical symptoms, with an increased number of *SNCA* genes associated with an earlier onset, more severe phenotype, and faster disease progression^{80–82}. *SNCA* connection with PD derives from the fact that its missense mutations tend to confer α -synuclein with stable β -sheets, thereby exacerbating the formation of toxic oligomers, protofibrils and fibrils⁸³ (Fig. 7). In this sense, point mutations in *SNCA* have been postulated to cause PD through a neurotoxic gain of function, where LB may constitute the neuron's attempt to purge mutated α -synuclein⁸⁴.

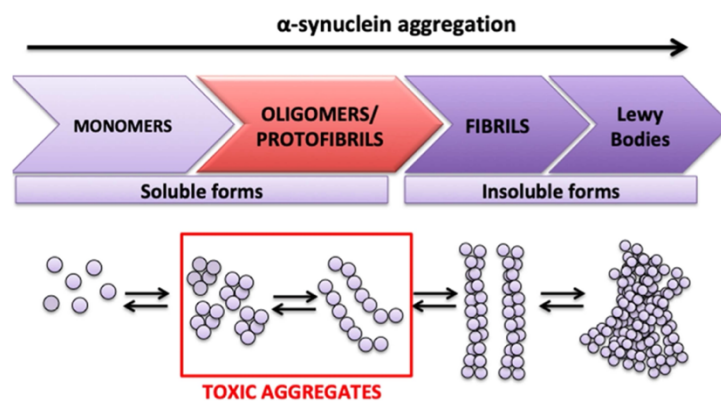


Figure 7. α -synuclein aggregation in higher-ordered structures. Under certain conditions, α -synuclein starts aggregating in oligomers and/or protofibrils, which become cytotoxic. Subsequently, these aggregates are further structured into insoluble fibrils, which end up constituting an important moiety of LB. Modified from Eleuteri et al, 2019⁸⁵.

Increased levels of α -synuclein protein, regardless of the cause, can promote self-aggregation and interfere with proteasomal and lysosomal functions, leading to further accumulation of the protein^{86,87}. Thus, enhanced production or impaired clearance of α -synuclein could initiate a vicious cycle with continued accumulation and misfolding of

the protein and the subsequent formation of noxious oligomers and amyloid fibrils⁸⁸. In this sense, despite having a highly conserved structure and a large number of interacting proteins (particularly mitochondrial components), science has failed so far to elucidate the exact roles of α -synuclein in physiological functions and the concrete pathomechanisms underlying its involvement in neurodegenerative diseases such as PD or DLB⁸⁹. The best-studied deleterious properties of α -synuclein include its capacity to induce stress in the endoplasmic reticulum, Golgi apparatus malfunction, and endolysosomal system impairment, alongside the widespread damage caused by the imbalance associated with its toxic aggregation⁸⁹. Therefore, it is yet not clear if α -synuclein accumulation is the first step of cytotoxicity or if it is a consequence of impairments in the aforementioned organelles that take place beforehand.

2.1.1.2 LRRK2

Mutations in the *LRRK2* gene are the most frequent cause of both late-onset autosomal-dominant and sporadic PD, with a mutation frequency ranging from 2% to 40% in different populations⁹⁰⁻⁹². Interestingly, patients with mutations in this gene present core clinical features that are indistinguishable from sporadic PD^{93,94}. Clinically, *LRRK2*-linked PD frequently shows mid-to-late onset and progresses slowly, where patients respond favorably to L-DOPA therapy and rarely develop dementia⁷³. Neuropathological findings are mostly inconsistent, since both LB pathology and pure nigral degeneration without the presence of LB have been described⁹⁵. Over 100 *LRRK2* mutations, both missense and nonsense, have been described, but only seven have been shown to be pathological⁹⁶. The G2019S mutation is the most common and has been found in both familial and sporadic PD cases. In contrast to all other pathological mutations⁹³, the G2019S variant displays reduced penetrance, which increases with age⁹⁷. These paradoxical features reflect the concept presented above, by which PD develops in response to a combination of genetic, environmental and age-related factors. The G2019S mutation of *LRRK2* may therefore serve as an ideal model system to investigate mechanisms underlying sporadic PD pathogenesis⁹⁴. The *LRRK2* gene encodes the 2527-amino acid-long, multi-domain leucine-rich repeat kinase 2 protein, which has been

associated with multiple signaling pathways, but whose exact physiological function is yet to be fully elucidated⁹⁸.

PD-associated mutants have been shown to alter various intracellular vesicular trafficking pathways, especially those related to endolysosomal protein degradation events⁹⁹. Furthermore, mutant (G2019S) LRRK2 activates the MKK4-JNK-c-Jun pathway, resulting in nigral DA neuron death¹⁰⁰. It has also been reported to cause progressive dysfunctions in DA transporters¹⁰¹. Regarding its association with α -synuclein, despite it being revealed that LRRK2 co-localizes with early stages of aggregating α -synuclein in the lower brainstem of PD patients¹⁰², contradictory conclusions have been obtained based on different animal models: some claim that LRRK2 potentiates α -synuclein-mediated cytotoxicity and propose that inhibition of the former may be used as a potential therapeutic approach to attenuating neurodegeneration caused by the latter¹⁰³; others conclude that high LRRK2 levels are well tolerated and not sufficient to drive or exacerbate neuronal α -synucleinopathy¹⁰⁴. Pathways, potentially impaired by the interaction between both proteins are schematized in figure 8.

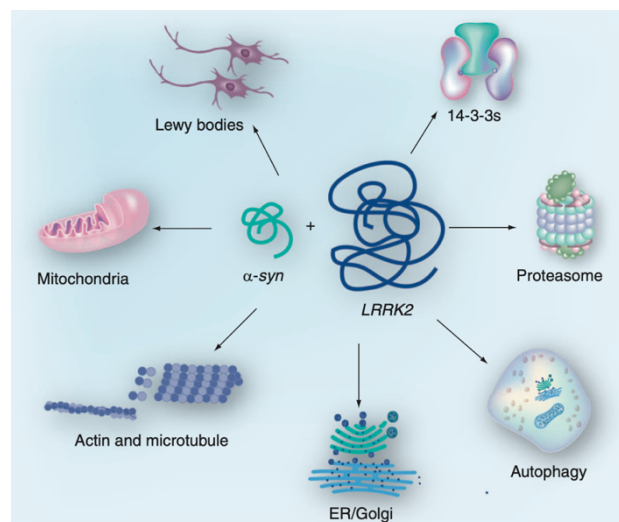


Figure 8. Subcellular organelles and intracellular pathways potentially affected by synergistic interactions between α -synuclein and LRRK2. These include mitochondrial dysfunction, Lewy body formation, interactions between the same complex through association with 14-3-3 proteins, proteasome impairment, malfunctioning autophagy, ER/Golgi apparatus fragmentation, and cytoskeleton destabilization. ER, endoplasmic reticulum. From Liu et al., 2012¹⁰⁵.

2.1.1.3 VPS35

The recently discovered missense mutation D620N in the *vacuolar protein sorting 35* (*VPS35*) gene was identified as a novel cause of autosomal-dominant PD^{106,107}. This mutation, which is the only pathological mutation identified so far, has a reduced penetrance, causing disease in 1.3% of familial cases and 0.3% in sporadic PD^{108,109}. The phenotype associated with this mutation recapitulates typical late-onset PD (except for an earlier mean age¹¹⁰) features like asymmetric onset, good L-DOPA response, and motor complications⁷¹. Severe cognitive or psychiatric disturbances are rare and brain pathology (e.g., LB presence) in carriers of this mutation remains unknown. *VPS35* encodes the 796-amino acid-long vacuolar protein sorting ortholog 35 protein, which acts as the central hub of the retromer cargo recognition complex, a key player in autophagy and, to a lesser extent, in signal transduction. Specifically, *VPS35* is localized at the level of the early endosome and is well characterized as a controller of the retrograde trafficking of cargo protein from the early endosome to the trans-Golgi network^{111,112}. *VPS35* protein levels were reported to be decreased in SN DA neurons in sporadic PD patients. Different animal and cellular models focusing the aforementioned mutation have implicated *VPS35* in impaired autophagy¹¹³ and DA release¹¹⁴, widespread tau-positive pathology¹¹⁵, control of DA transporter (DAT) recycling¹¹⁶, and altered LRRK2-mediated Rab protein phosphorylation¹¹⁷. Since a direct link between *VPS35* and α -synuclein was established (*VPS35* deficiency causes α -synuclein accumulation), particular focus has been placed on unraveling *VPS35*'s key role in controlling lysosomal function, macroautophagy, and chaperone-mediated autophagy, which are the main degradation pathways of α -synuclein^{113,118,119}. These connections with other PD-related proteins support the notion that endosomal trafficking and recycling of synaptic vesicles are involved in the pathogenesis of PD.

2.1.2 AUTOSOMAL-RECESSIVE FORMS OF PARKINSON'S DISEASE

2.1.2.1 *PRKN*

PRKN was the second gene identified to be associated with PD and the first one causing an autosomal-recessive form of the disorder. *PRKN* mutations – mostly deletions – are the most commonly known cause of early-onset PD, accounting for up to 77% of familial cases with an onset <30 years¹²⁰, and for 10%-20% of early-onset PD patients in general¹²¹. In the latter scenario, the disease usually starts in the third to fourth decade of the patient's life, progresses slowly, and responds very well to L-DOPA treatment⁷³. *PRKN* codes for the 465-amino acid-long Parkin protein, which is an E3 ubiquitin ligase that conjugates ubiquitin protein(s) to lysine residue(s) of target proteins determining their cellular fate¹²². Apart from its involvement in the proteasomal degradation system, Parkin also plays a role in the maintenance of mitochondrial structure and DNA integrity¹²³. Intriguingly, although functional Parkin has been postulated to be required for LB formation¹²⁴, autopsy studies have generated conflicting results with respect to the existence of LB in this genetic form of PD, reporting both the lack¹²⁵ and the presence¹²⁶ of these cytoplasmic inclusions.

2.1.2.2 *PINK1*

Mutations in *PINK1* are the second most common cause of autosomal-recessive early-onset PD. The frequency of *PINK1* mutations varies between 1% and 9%⁷³. Interestingly, in contrast to *PRKN*, the majority of *PINK1* mutations are either missense or nonsense⁷³. Some studies have confirmed LB-pathology in *PINK1*-mutated PD patients¹²⁷⁻¹²⁹, while others have reported its absence¹³⁰. *PINK1* encodes the 581-amino acid-long PINK1 protein, which is a ubiquitously expressed kinase harboring a mitochondrial targeting motif that concentrates the most of the gene's loss-of-function mutations⁷³. Interestingly, *PINK1* has been reported to share a common mechanism with Parkin for sensing and selectively eliminating damaged mitochondria^{131,132}. In this pathway, *PINK1* is stabilized on impaired mitochondria, thereby recruiting Parkin from the cytosol,

which, in turn, becomes enzymatically active and initiates the autophagic clearance of mitochondria (i.e., mitophagy).

2.1.2.3 *PARK7*

PARK7 is the third gene associated with autosomal-recessive PD, being mutated in about 1% – 2% of the early-onset form of the disorder¹³³. Literature reports assessing LB-pathology in *PARK7*-mutated patients are scarce¹³⁴. *PARK7* codes for the 189-amino acid-long DJ-1 protein, which is a ubiquitously expressed deglycase that functions as a cellular sensor of oxidative stress^{135,136}. However, although DJ-1's specific functions remain unclear, both Parkin and PINK1 are two of the many proteins with which it has been shown to interact. Together, they form a ubiquitin ligase complex that promotes unfolded protein degradation, which plays an important role in the maintenance of mitochondrial structure and recycling¹³⁷. Disease-causing mutated versions of DJ-1 protein, which are improperly folded and unstable¹³⁸, have been described to heterodimerize with wild-type DJ-1¹³⁹, thereby reducing its neuroprotective function and antioxidant activity¹⁴⁰.

2.1.2.4 *ATP13A2*

Mutations in *ATP13A2* have been found to cause an atypical early-onset form of PD called Kufor-Rakeb syndrome¹⁴¹. This condition is characterized by a juvenile onset with rapid, but L-DOPA-responsive, disease progression, accompanied by dementia, supranuclear gaze palsy and pyramidal signs. *ATP13A2* codes for the 1180-amino acid-long ATP13A2 protein, which is normally located in the lysosomal membrane and acts as a late endolysosomal transporter, has been postulated to offer protection against genetic and environmental risk factors for PD¹⁴². Most mutations give rise to truncated proteins that are retained in the endoplasmic reticulum and subsequently degraded by the proteasome⁷³.

2.2 RISK FACTORS

PD shows an age-dependent prevalence in which about 1% of the global population at 65 years of age and over, and about 4% – 5% of individuals aged 85 years and over, are affected¹⁴³. In this regard, apart from age, which is the principal risk factor for the development of PD, other genetic and non-genetic risk factors have been associated with disease onset. Non-genetic factors include smoking, coffee and dairy product consumption, physical activity, dyspepsia, general anesthesia and exposure to pesticides, oils and metals^{144,145}. Genetic factors include variants in several *PARK*-designated (*SNCA*, *LRRK2*, *UCHL1* and *PARK 16*, for example) and non-*PARK* genes (*APOE*, *HLA-DRA*, *MAPT*, *GAK* and *GBA*, for example)⁷³. In addition to *SNCA* and *LRRK2*, both of which can be involved in monogenic forms of the disease and act as risk factors, β -glucocerebrosidase (*GBA*'s encoded protein) stands out as a well-validated PD-associated risk factor.

Loss-of-function mutations in this lysosomal enzyme lead to its inability to cleave its native lipid substrates (glucosylceramide and glucosylsphingosine) into recyclable moieties¹⁴⁶. This results in their toxic accumulation in the lysosome, causing a multi-organ-wide range of symptoms gathered under the disorder known as Gaucher's disease. Interestingly, it was first observed that relatives of patients affected with Gaucher's disease manifested an increased incidence of PD¹⁴⁷. Later, a multicenter study concluded that *GBA* mutations are the largest genetic risk factor for developing PD, enhancing one's risk approximately 5-fold and highlighting the importance of the lysosomal pathway in the pathogenesis of the disease¹⁴⁸. Furthermore, it was also concluded that the age at onset was lower among subjects with *GBA* mutations than in those without. Mutations in *GBA* have been also associated with the presence of LB¹⁴⁹.

Taken together, the different mutations in PD-associated genes may act in series and/or in parallel pathways¹⁵⁰. However, all genetic causes of PD ultimately lead to a loss of DA neurons in the nigrostriatal pathway, and as such, it is plausible that there are some common final molecular mechanisms¹⁵⁰. As discussed, many genes appear to be involved in PD onset, either in a direct manner or as potential risk factors for developing

the disease. A schematic illustration of the different physiological pathways that are impaired in PD is given in figure 9. It should be kept in mind that the strong genetic influence on PD reviewed in this section is only one of the described factors influencing the development of the disease. In the following chapters, other key elements such as NM and environmental components will also be addressed.

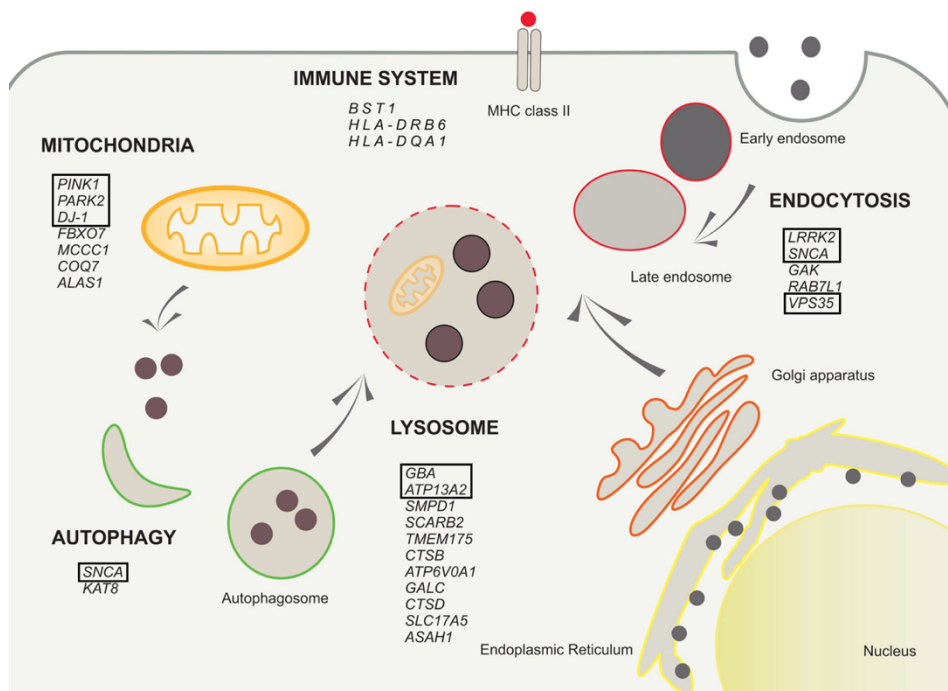


Figure 9. Schematic overview of genes associated with PD, either directly or as risk factors. Genes encode for proteins that participate primarily in mitochondrial turnover, lysosomal function, autophagy, endocytosis and/or in the immune system. Black squares indicate genes discussed in this section. Adapted from Billingsley et al., 2018¹⁵¹.

3. EPIDEMIOLOGY OF PARKINSON'S DISEASE

Worldwide incidence calculations of PD range from 5 to >35 new cases per 100,000 individuals per year¹⁵². Prevalence estimations range from 1 to 2 per 1000 in unselected populations¹⁵³ while, globally, the disease has been estimated to affect 1% of the population above 60 years¹⁴³. Noticeably, PD is a rare condition before the age of 50 years and reaches a prevalence of 4% in the highest age groups, demonstrating the critical influence of age on disease progression^{152,154,155}. To this end, the age of onset for just one quarter of affected individuals is younger than 65 years, and less than 50 years

for 5%–10%¹⁵⁶. However, this range suggests differences in the demographics of the populations used for each study and in the methodology employed, particularly with respect to case ascertainment and the diagnostic criteria used¹⁵⁷. Mortality in PD cases is not increased in the first decade after disease onset, but rises thereafter, doubling that of the general population¹⁵⁸. On the other hand, advances in health care are leading to prolonged survival rates, thus doubling the anticipated number of patients with PD between 2015 and 2040². Therefore, as the global population ages, a gradual increase in the personal, economic and societal burden is expected^{159–162}. To understand the magnitude of the current and upcoming implications of PD on society, the fact that 6.1 million individuals had PD globally in 2016, compared with 2.5 million in 1990, becomes self-explanatory¹⁶². To date, different survival rates after diagnosis have been reported for PD patients, ranging from 6.9¹⁶³ to 20¹⁶⁴ years. Intriguingly, causes of death of individuals with PD are similar to causes in non-PD cohorts, with death often occurring before advanced stages of the disease are reached¹⁶⁵. The most common cause of death in PD patients dying of PD-related symptoms is aspiration pneumonia¹⁶⁶.

It is also of utmost importance in epidemiological studies to assess the impact of sex on disease prevalence. In fact, with minor deviations¹⁶⁷, it is widely accepted that PD is twice as common in men than in women^{168–171}. Specifically, the lower incidence in women is represented with age-standardized male:female incidence ratios, which range from 1.3 to 2.0 depending on the origin of the analyzed populations^{158,171–173}. Consistent with these studies, a worldwide systematic analysis revealed a male:female prevalence ratio of 1.40¹⁷⁴ and a general higher relative risk in men compared to women of 1.5¹⁷⁵. Lower reported incidence ratios or even exceptions to figures reported above, correspond to studies in Asia^{170,176–178}, suggesting that methodological differences, environmental factors, genetics, ethnicity and/or sex differences could serve as decisive factors in the assessment of PD epidemiology¹⁷⁹.

As a general rule, both male:female incidence and prevalence ratios for PD markedly increase with age. Nevertheless, this trend appears to be more evident for incidence than for prevalence, presumably because the mortality risk is higher for men with PD, but not for women, than in the healthy population¹⁸⁰. Also, given the fact that the onset

of PD usually occurs earlier in men than in women¹⁸¹, and the mortality of PD patients rises with disease duration, the death rate from the disease could also explain the increased incidence in men without a concomitant rise in prevalence¹⁵². Globally, the male sex is associated both with higher incidence and prevalence ratios, earlier disease onset, more severe motor symptoms and progression, and usually more cognitive decline compared with females. As shown in figure 10, apart from incidence, prevalence and disease onset, men tend to also be more affected by the most important clinical features of PD.

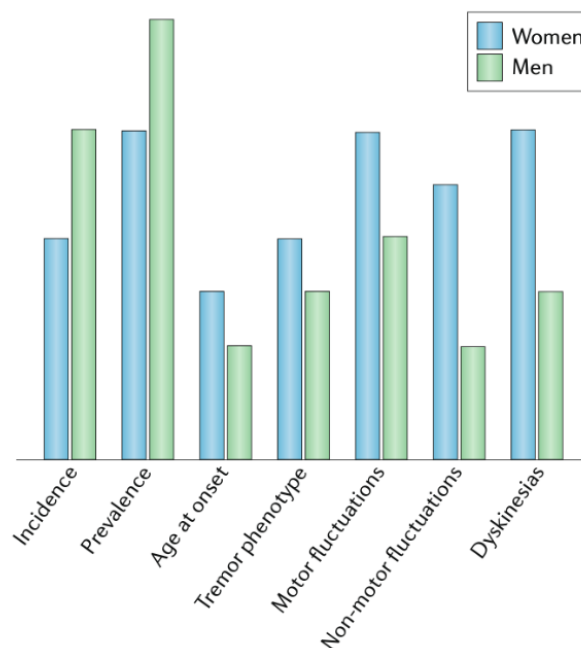


Figure 10. Sex differences in PD. Women with PD (blue bars) tend to have later age at disease onset, lower PD prevalence and incidence; higher rates of tremor phenotype, and a greater likelihood of dyskinesia and motor and non-motor symptoms compared with men (green bars). From Meoni et al. 2020¹⁷⁹.

It is also relevant to highlight several aspects arising from innate divergences in PD between men and women. First is the fact that sexual dimorphisms in dopaminergic pathways have been found in the basal ganglia both in PD patients^{182,183} and unaffected individuals^{184,185}. Secondly, it has been postulated that sex steroid hormones adjust the dopaminergic system in both normal and pathological states^{185–187}, where a potential neuroprotective effect of estrogens against dopaminergic damage through anti-inflammatory, anti-oxidative, and anti-apoptotic mechanisms^{188,189}, in addition to potential inhibitory effects on the formation and stabilization of α -synuclein, has been

suggested in women with PD¹⁷⁹. Sex hormones are the most important factor for driving structural and functional sexual differentiation in the brain, but also act as critical drivers of sex differences in disease susceptibility. In this regard, several studies postulate that a longer lifetime exposure to estrogens is associated with a reduced risk of PD and less severe symptoms at disease onset in woman^{189–191}. Consequently, the decrease in estrogen levels after menopause has been associated with an increased risk of PD^{181,192,193}. Intriguingly, another remarkable fact is that female rats and monkeys have a higher number of DA neurons in the SN than males¹⁹⁴.

In spite of a lack of studies specifically analyzing the effects of sex on PD symptoms, some sex-based differences in the clinical features of PD have been reported, which are summarized in figure 10. In this regard, women are more prone to show a tremor-dominant phenotype at disease onset compared to men, and to present a slower disease progression¹⁸¹. Focusing on motor symptoms, women also show an older average age and milder symptoms at disease onset compared to men¹⁹⁰. This suggests, as described above, a more favorable PD phenotype in women than in men due to higher dopaminergic activity and the potentially protective effect of estrogens^{181,195}. Furthermore, a large-scale study reinforced the idea of a sex effect on motor progression in recently diagnosed patients, with women showing a more delayed progression than men¹⁹⁶. Nevertheless, over the disease course, the female sex appears to be independently associated with the advancement of motor symptoms¹⁹⁷, with women tending to present a higher risk of developing L-DOPA-induced dyskinesias^{198,199}, as well as a shorter time to dyskinesia occurrence²⁰⁰, and an earlier onset of wearing-off (re-emergence of motor and non-motor fluctuations before the next L-DOPA dose) intervals²⁰¹. Conversely, the male sex has been associated with more severe motor symptoms throughout the PD course²⁰². Supporting this finding, another study demonstrated that the diffuse malignant phenotype, characterized by severe motor features, autonomic and cognitive deficits at diagnosis, and the presence of REM sleep behavior disorder, was present at a higher frequency in men compared to woman²⁰³.

In contrast to motor symptoms, several studies indicate sex differences in the prevalence and severity of non-motor symptoms in PD patients²⁰⁴. Notwithstanding

methodological differences in the assessment, some of non-motor PD symptoms seem to be robustly associated with sex. For instance, restless legs syndrome, constipation, mood symptoms such as anxiety, nervousness, sadness and lack of motivation, and pain are more common in women^{205–207}. On the other hand, urinary complications, sexual dysfunction, drooling and excessive sleepiness during day are more prevalent in men^{205,206,208–211}. Overall, women are more prone to present a higher amount of non-motor symptoms than men²⁰⁵. It is important to highlight the emerging role of sex in several non-motor symptoms occurring in the PD premotor phase, such as gustatory and olfactory impairments, and sexual dysfunction, which are more prevalent in men than in women²¹². Furthermore, in another study in which several non-motor symptoms were stratified for their capacity to discriminate patients with early PD from controls, REM sleep behavior disorder was associated with PD only in women, whereas dysautonomia was a predictor of PD only in men, indicating that sex-specific differences are present even in the preclinical phase of the disease²¹³.

4. TREATMENT OF PARKINSON'S DISEASE

4.1 MANAGEMENT OF MOTOR SYMPTOMS

Currently, there is no cure for PD and no standard treatment since every patient requires a personalized form of care. As discussed above, loss of DA neurons in the SNpc leading to striatal DA depletion is the core mechanism underlying PD motor symptoms. In this regard, routine pharmacologic treatments for such symptoms are based primarily on DA replacement therapy: DA's precursor L-DOPA, DA agonists, monoamine oxidase B (MAO-B) and catechol-*o*-methyltransferase (COMT) inhibitors are commonly used. COMT and MAO-B inhibitors block enzymes that degrade DA, as will be further reviewed below, prolonging the benefits of L-DOPA. Of the four treatment options, L-DOPA remains the most effective treatment at all stages of PD thanks to its ability to cross the blood-brain barrier (BBB) and to act as a direct precursor of DA²¹⁴. Treatment decision-making does not respond to a 'one size fits all' criterion and must take into consideration benefits and potential complications consequent to the acuteness and recurrence of symptoms displayed by the patient. L-DOPA use, for instance, results in more functional improvements but has increased dyskinesia risks, particularly at higher doses³¹. MAO-B-

inhibitors, of which selegiline and rasagiline are irreversible inhibitors and the newer safinamide is a reversible inhibitor, and DA agonists are associated with less robust symptom relief but a lower manifestation of dyskinesias²¹⁵. While initially used DA agonists were ergoline derivatives, which were directly associated with pleuropulmonary and cardiac valvular fibrosis, currently used agents (apomorphine and pramipexole being the main examples) are non-ergoline drugs and devoid of major safety concerns¹². Figure 11 illustrates the different dopaminergic targets in PD and their mechanisms of action.

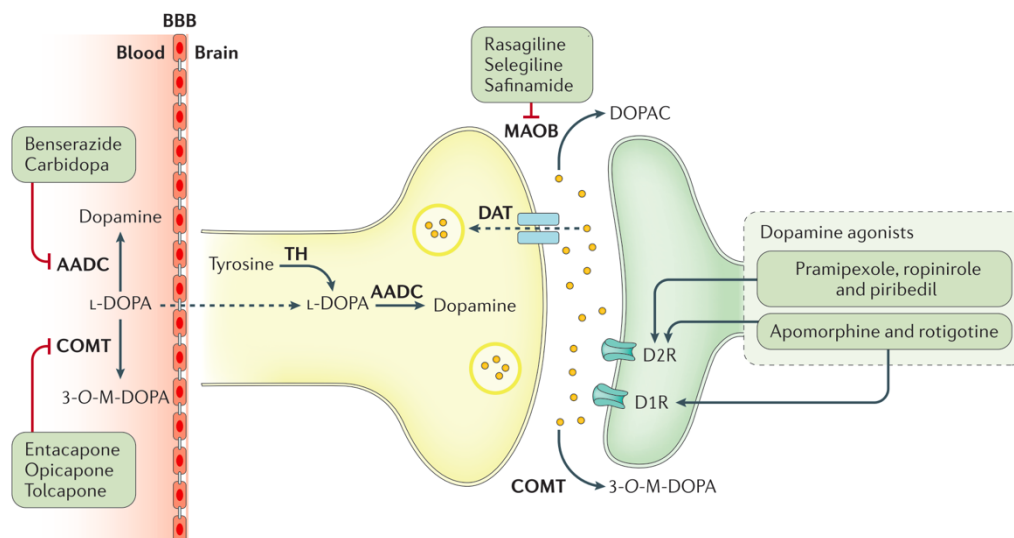


Figure 11. Dopaminergic targets in PD. Presynaptic targets include L-DOPA replacement combined with peripherally active inhibitors of aromatic amino acid decarboxylase (AADC) or COMT. MAO-B inhibitors enhance the synaptic availability of DA (both endogenous and exogenous), whereas DA agonists act postsynaptically. Dashed arrow from blood to brain indicates the ability of L-DOPA to cross the blood-brain barrier (BBB) compared to peripheral DA. Dashed arrow through the DA transporter (DAT) denotes DA reuptake from the synaptic cleft to the presynaptic neuron. 3-O-M-DOPA, 3-O-methyl-DOPA; D1R, DA D1 receptor; D2R, DA D2 receptor DOPAC, 3,4-dioxyphenylacetic acid; TH, tyrosine hydroxylase. From Poewe et al., 2017¹².

Ultimately, most PD patients use medications from multiple classes, usually L-DOPA as baseline treatment which is complemented with other drugs mentioned above as adjuncts; this is done to attain complementary benefits while limiting high doses in order to minimize adverse effects³¹. For example, the DA agonist apomorphine is used in individuals with advanced PD displaying severe *off* episodes (i.e., periods of difficulty moving, walking or speaking that may occur as medication wears off or at random). Also, current L-DOPA preparations include inhibitors (carbidopa or benserazide) of enzyme aromatic amino acid decarboxylase (AADC) to prevent peripheral metabolism of DA, thereby

enhancing L-DOPA bioavailability (Fig. 11). Consequently, the peripheral metabolism of L-DOPA is shifted toward the activity of a secondary metabolic pathway involving the ortho-methylation of L-DOPA via COMT. Therefore, patients who have developed motor fluctuations of the wearing-off type typically complement their treatment with a COMT inhibitor, which, by acting peripherally, will further enhance the bioavailability and half-life of L-DOPA.

Extending the duration of effect of individual L-DOPA doses via COMT inhibitors has become a first-line treatment approach^{216,217}. An additional non-DA targeting family of compounds that can be used to act synergistically with L-DOPA treatment, or even as monotherapy in early PD cases, to help relieve tremor symptoms, is comprised of anticholinergic drugs. Since DA neuron loss in the SNpc causes DA striatal depletion, this may give rise to an imbalance between the DA and cholinergic neurological pathway activity. Consequently, anticholinergics are believed to reverse this asymmetry by reducing the degree of neurotransmission mediated by striatal acetylcholine²¹⁸. Other non-DA targeting drugs given as L-DOPA adjuncts include the antiviral drug amantadine, which is the most effective pharmacological treatment for L-DOPA induced dyskinesias^{216,219}, and cholinesterase inhibitors, although they are infrequently used due to the lack of a demonstrated robust and reproducible benefit (Table 2). In this sense, and from a clinical point of view, while long-term DA replacement therapy has been reported to restore physiological synaptic plasticity in the DA-denervated STR²²⁰, concomitantly, it also seems to cause functional short- and long-term alterations to neural transmission²²¹. Furthermore, DA replacement therapy is known to cause well-known complications (starting after 4-5 years of L-DOPA treatment), among which are dyskinesias^{222,223}, motor fluctuations (wearing-off episodes derived from the mentioned *on-off* effect)²²⁴ and, very rarely, DA dysregulation syndrome (a pattern of addictive drug use)²²⁵ that could negatively impact the rehabilitative outcome.

At this point is important to highlight that response to DA-based treatments differs between men and women. Several studies have postulated that men should receive a higher DA dosage than women^{202,226,227}. Moreover, robust research suggests that this sex difference is directly related to differences in L-DOPA pharmacodynamics and

pharmacokinetics between sexes^{228–232}, where body weight is thought to play a prominent role. On the other hand, women show higher L-DOPA plasma concentrations compared to men, which is related to lower body weight and reduced rates of L-DOPA clearance, resulting in greater L-DOPA bioavailability. Apart from body weight, other factors such as anomalous responses to L-DOPA and differences in energetic metabolism²³³ may interact and contribute to the variations in L-DOPA dyskinesias that have been observed between both sexes. Furthermore, some examples exist of sex-specific genetic variants modulating the risk of L-DOPA-induced complications. First, sexual dimorphism in genes implicated in DA metabolism such as monoamine oxidase type B could explain why men carrying certain alleles require higher doses of L-DOPA²³⁴. And, second, specific polymorphisms have been linked to a protective effect against dyskinesia development in men but not in women^{198,235}.

Independent of sex-associated factors, L-DOPA's limitations at treating the full spectrum of parkinsonian signs and symptoms (followed by declining effectiveness), have been demonstrated in PD populations for 10 years and longer²³⁶. However, advanced symptoms generally exhibit minor to no benefit from PD therapies because impairments causing the dysfunctions are located beyond the dopaminergic pathways²³⁷. Therefore, once the benefits of neurotransmitter-related pharmacologic agents have been exhausted there is frequently a deterioration of patients' quality of life quality and overall health status in line with the type and severity of symptoms. In such cases advanced therapies may be necessary.

4.2 MANAGEMENT OF NON-MOTOR SYMPTOMS

In some patients, selected non-motor symptoms including anxiety, pain, depression, panic attacks, and restlessness, can fluctuate in response to DA therapy and become equally or even more disabling than motor symptoms^{238,239}. Many of these non-motor complaints do not respond to DA replacement therapy, with some in fact worsened or precipitated by this treatment²³⁸. Anatomical targets for these ailments include efferent, afferent and intrinsic basal ganglia connections, various brainstem-originating projections, as well as intrinsic cortical connections and, finally, abundant targets

outside the central nervous system²⁴⁰. Apart from non-DA neurotransmitter and neuromodulatory systems in these different regions that have been implicated in the symptoms of PD, noradrenergic, adenosinergic, glutamatergic, serotonergic, GABAergic, histaminergic, cholinergic and opioidergic pathways may also be involved²⁴¹. Table 2 summarizes the range of possible drugs, in addition to DA-modifying drugs, targeting specific neurotransmitters with a view to alleviate PD non-motor symptomatology.

Table 2. Neurotransmitters and pharmacologic agents related to PD symptoms. Dopaminergic and non-dopaminergic treatments for motor and non-motor symptoms of PD. From Armstrong and Okun, 2020³¹.

Symptom or Sign	Neurotransmitters and Drugs Influencing the Neurotransmitter				
	Dopamine	Serotonin	Norepinephrine	Acetylcholine	Other
Motor impairment (eg, bradykinesia, rigidity, tremor, gait disturbance)	Levodopa preparations, dopamine agonists (eg, pramipexole, ropinirole), monoamine oxidase-B inhibitors (eg, rasagiline, selegiline), catechol-O-methyl transferase inhibitors (eg, entacapone)			Anticholinergic agents for tremor (eg, trihexyphenidyl) ^a ; cholinesterase inhibitors for gait (eg, rivastigmine) ^{a,b}	Amantadine ^c
Cognitive impairment	Monoamine oxidase-B inhibitors ^{a,b}			Cholinesterase inhibitors	
Psychosis	Quetiapine, clozapine ^a	Pimavanserin		Cholinesterase inhibitors ^{a,b}	
Depression, anxiety	Dopamine agonists ^a	Selective serotonin reuptake inhibitors, selective serotonin and norepinephrine reuptake inhibitors, tricyclic antidepressants	Selective serotonin and norepinephrine reuptake inhibitors, tricyclic antidepressants	Tricyclic antidepressants	

^a Indicates US Food and Drug Administration approved for another use but off-label use for the sign or symptom in this row.

^c Amantadine may affect multiple neurotransmitter systems including dopamine and glutamate.

^b Studied for this use with insufficient evidence to date to support routine use.

Cognitive dysfunction, depression and autonomic failure are among the most prevailing and troublesome non-motor complaints in PD. In this regard, cholinesterase inhibitors can have remarkable beneficial effects on cognitive disturbances in PD patients who also display dementia, an effect possibly related to the loss of cholinergic projections from the nucleus basalis of Meynert^{242,243}. On the other hand, the most effective treatment for psychotic symptoms in PD is clozapine^{242,243}. All other available typical neuroleptics worsen parkinsonism, probably by blocking striatal DA D2 receptors¹². It is not known whether depression in PD has the same anatomical and pathogenetic bases as depression in the general population²⁴⁴; however, limited evidence suggests that tricyclic antidepressants may be more effective than selective serotonin reuptake inhibitors at combating depression in PD²⁴². Finally, since autonomic dysfunction is very common in PD, especially in late stages of the disease, pharmacological therapies are largely directed at autonomic nervous system targets. These therapies consist of the

noradrenaline precursor droxidopa, the mineralocorticoid fludrocortisone and adrenergic agents to treat orthostatic hypotension, in addition to anti-muscarinics for urinary incontinence, and pro-kinetic drugs to ameliorate constipation^{219,242,245}.

As a drug-free alternative, rehabilitation therapy has been proposed in recent years as an effective and complementary treatment for the management of all PD symptoms and across all disease stages. In this sense, effective exercise interventions for PD include gait, balance, strength²⁴⁶ and progressive resistance²⁴⁷ training, aerobic²⁴⁶ and treadmill²⁴⁸ exercise, music- and dance-based approaches^{249,250}, and tai chi²⁵¹. From these, diverse exercise approaches may alleviate, or even improve, different motor aspects (i.e., symptoms, function, balance, and gait) of the disease. Additionally, physiotherapy, occupational therapy and speech therapy have also been reported to be useful for this purpose and for addressing dysphagia and hypophonia^{31,246,252}. In this sense, the great value of rehabilitation is the possibility to treat many of the disabling PD disturbances that do not respond to DA replacement therapy since they derive from the participation of systems outside of the dopaminergic structures cited above²⁵³.

4.3 TRADITIONAL ADVANCED THERAPIES

Since its advent in 1969²⁵⁴, L-DOPA has been the gold standard and prevailing drug administered to PD patients. Its beneficial effects signified the confirmation that parkinsonian motor symptoms are reversible consequences of striatal DA deficiency and constituted the zenith of the translation of basic neuroscience to clinical research started a decade beforehand and was led by, among others, Carlsson, Hornykiewicz, Birkmayer, Sano, Yahr, McGeer and Cotzias. However, despite its unquestionable benefits, with disease progression and years of treatment, L-DOPA reaches a threshold usage above which motor improvement requires higher doses to combat severe wearing-off episodes and other complications as discussed before. In this regard, advanced therapies are useful for PD patients who have medication-responsive motor symptoms, but who have reached a stage where their symptoms are unresponsive to dosage increase, and who present the mentioned complications³¹.

4.3.1 DEEP BRAIN STIMULATION

Surgical approaches to PD include deep brain stimulation (DBS) and direct lesions in the nuclei of the basal ganglia^{255–257}. These procedures have been postulated to produce clinical benefit by modulating pathologic oscillatory signals²⁵⁸. DBS is based on the finding that high-frequency electrical stimulation of specific brain targets can mimic the effect of a lesion without the need for damaging brain tissue²⁵⁹. The technique involves a craniotomy with implantation of stimulating electrodes connected to a pulse generator, usually implanted in the chest, that requires replacement every 2 to 25 years, depending on the device^{260,261}. Since its invention, numerous clinical trials have confirmed the initial observation of the dramatic antiparkinsonian efficacy of DBS of the STN, which is nowadays a robust, evidence-based therapy for motor fluctuations and dyskinesias in patients with advanced PD²¹⁶. The stimulation-induced improvement is linked to the L-DOPA treatment response; that is, patients with motor symptoms who do not clinically improve upon dopaminergic treatment are unlikely to respond to DBS, with drug-resistant tremor being the only exception to this rule¹². Ideal candidates for DBS treatment have young-onset, idiopathic PD with excellent L-DOPA response but motor complications due to long-term medical therapy²⁶². It has been demonstrated that bilateral DBS of the STN strongly improves motor symptomatology (with a 40% to 60% reduction in the severity of motor signs) and the overall performance of activities of daily living by inhibiting hyperactivation derived from marked damage of the nigrostriatal pathway^{256,263}. Furthermore, total daily DA drug dosage is markedly reduced (up to 50%) following the DBS procedure²⁶⁰. As a direct consequence, both dyskinesias and hypokinetic fluctuations are substantially reduced.

The globus pallidus internus constitutes an alternative surgical target for the treatment of motor complications, but does normally not result in a reduction of medication²⁶⁴. Randomized trials comparing the two structures have produced conflicting results of either a similar²⁶⁵ or inferior²⁶⁶ long-term efficacy of this approach on motor symptoms. Despite its beneficial performance, DBS entails an important burden in terms of expensive equipment and labor, and requires a high level of interdisciplinary expertise in the correct surgical placement of the electrode, postoperative programming and the

adjustment of neurostimulation and drug therapy^{262,267}. A more versatile and affordable alternative to targeting both structures is to perform lesion surgery (i.e. ablation) on them^{268–271}. However, lesion surgery entails significantly more adverse sequelae than DBS²⁷² and is usually not applied bilaterally due to risks of speech, swallowing, or cognitive deficits¹⁵⁶ and the development of sporadic and uncontrollable dyskinesias encompassed by the term hemiballismus^{273,274}.

4.3.2 INFUSION THERAPIES

Continuous infusions of L-DOPA or apomorphine provide constant DA stimulation and are good alternatives to DBS for controlling motor fluctuations in patients with advanced PD presenting severe wearing-off episodes. Apart from its aforementioned short half-life, oral L-DOPA has unpredictable absorption characteristics, compromising even more its bioavailability. Therefore, aiming to reach long-term efficacy for the control of motor fluctuations, L-DOPA treatment – coupled with carbidopa – is also available as an intestinal gel^{275,276}. This therapeutic delivery requires a percutaneous endoscopic gastrojejunostomy. Another approach to address complex response fluctuations is again with the use of a pump therapy, where apomorphine is delivered either intravenously²⁷⁷ or subcutaneously²⁷⁸.

4.4 EMERGING ADVANCED THERAPIES

Emerging therapies for PD patients at an advanced stage of the disease aim at refining existing lesion techniques like transcranial focused ultrasound (tFUS) or by achieving structural or neurochemical brain repair via cell transplantation or gene therapy. Figure 12 shows emerging therapies under intense investigation in the field of PD research. However, since these therapies are outside the scope of the present dissertation, they will not be further discussed. Other approaches that will not be presented here include glucagon-like peptide 1 receptor agonists and other antidiabetic agents (like exenatide), iron targeting therapies, A2A receptor antagonists, brain connectomic studies and

improved precision of neuromodulation targets, as well as repetitive transcranial magnetic stimulation²⁷⁹.









Target	Therapy	
	Preclinical studies	Clinical studies
 SNCA	Beta-2 adrenergic receptor, siRNA, non-steroidal anti-inflammatory drugs, antistreptolysin O	Thiazolidinedione (glitazones)
 Misfolded α -synuclein fibrils	Anti-LAG3 antibody, small molecule inhibitors, CLR01, KYP	Active or passive immunotherapy (eg, BIIB065), nilotinib, deferiprone
 Autophagy lysosomal pathway	LTI-291, AT3375	Ambroxol, glucosylceramide synthase inhibitors
 Calcium ion homeostasis	Calcium ion channel blockers	Calcium ion channel blockers (eg, isradipine)
 Mitochondria dysfunction Parkin pathway	Ursolic acid, mitochondrial division inhibitor 1, Miro reduction, sirolimus	11-dehydrosinulariolide, MitoQ, exenatide, LRRK2 small molecule kinase inhibitors
 Neurotrophic factors	Brain-derived neurotrophic factors, vascular endothelial growth factor	Cerebral dopamine neurotrophic factor, glial cell line-derived neurotrophic factor, neurturin
 Inflammation	Anti-inflammatory (eg, non-steroidal anti-inflammatory drugs)	Sargramostim, exenatide, liraglutide, lixisenatide, AZD3241
 Oxidative stress	DJ-1 chaperones	Deferiprone, inosine, coenzyme Q10, caffeine, nicotine, creatine
Therapies under investigation		

Figure 12. Emerging therapeutic strategies for PD. These therapies are aimed at slowing down disease progression or postponing the onset of disease manifestations in people in the prodromal phase of PD. The pipeline of planned or ongoing trials aiming at disease modification is broad, including many targets and, in many cases, multiple drugs for each target. For each target, both preclinical and clinical examples are represented. From Bloem et al., 2021¹⁵⁶.

4.4.1 TRANSCRANIAL FOCUSED ULTRASOUND

Ultrasound (US) therapy is one of the most versatile and safest diagnostic tools in medicine. tFUS refers to US that is focused via a curved transducer, lens or phased array, whereby the pressure is highest at a small target and minimal elsewhere²⁸⁰. tFUS is an emerging technique for non-invasive neurostimulation, that, compared to magnetic or electric non-invasive brain stimulation^{281–283}, has a higher spatial resolution, which is useful for mapping small brain areas²⁸⁴, and can reach deep structures^{285–287}. Moreover, recent studies suggest that different structures of the central^{285,288} and peripheral

nervous^{289,290} system can be conceivably targeted by this technique. Depending on stimulation conditions and frequency ranges, tFUS is able to achieve a wide gamut of effects, ranging from suppression or facilitation of neuronal activity to tissue ablation. The technique has been employed successfully to achieve neuromodulation under safe conditions in common laboratory animal models^{291,292} and primates, both human²⁹³ and non-human^{287,294}.

One application that has gained momentum in the last decade is unilateral tFUS guided by magnetic resonance imaging. This technology focuses beams of ultrasonic energy precisely and accurately on millimeter-sized structures deep in the brain, without damaging surrounding non-targeted tissue^{295–297}. It has already been successfully applied in PD patients to lesion the thalamus^{298,299}, STN^{300,301} and globus pallidus interna³⁰² in the search of motor symptom alleviation. A particular advantage of tFUS compared to other fixed-brain-ablation techniques, namely DBS or radiofrequency, is that it does not require craniotomy, thereby avoiding serious potential risks like hemorrhage or stroke³⁰³. Once approved by the Food and Drug Administration (FDA), non-invasive tFUS therapy is likely to be most effective against tremor but is not indicated for bradykinesia or rigidity.

In PD, as for other neurodegenerative diseases, despite many encouraging preclinical studies suggesting neuroprotective effects of candidate agents, they lack success when translated into clinical trials³⁰⁴. One of the main reasons for this major drawback is the limited permeability of the BBB that hampers completely, or to a great extent, the sufficient delivery of candidate drugs to the target brain region³⁰⁵. Therefore, any therapy or precise technique with the capacity of mitigating the barrier's highly restrictive physiology would revolutionize the field of brain drug delivery. In fact, during the last decade, a large number of studies have leveraged a very interesting facet of tFUS's versatility, namely its therapeutically relevant ability to transiently open the BBB. It has been demonstrated that therapeutic tFUS-mediated approaches targeting the opening of the BBB may prolong the conventional therapeutic time window for delivering drugs to target brain regions^{306–308}. In this way, when combined with the systemic injection of biologically inert lipid-shelled microbubbles (alternatively, cationic

microbubbles and liposomal-plasmid DNA complexes have been also applied³⁰⁵), which expand and contract when activated with ultrasound, tFUS is able to temporarily increase the barrier's permeability, thereby opening a myriad of potential neuroprotective approaches, including the delivery of genes, antibodies, growth factors and neuroprotective/neurorestorative drugs.

4.4.1.1 APPLICATIONS

tFUS has already been demonstrated to provide a direct neuroprotective parenchymal effect³⁰⁹ and to increase gene delivery^{310,311}, thereby increasing DA neuron survival. Furthermore, this strategy has been successfully applied to remove extracellular β -amyloid plaques in mouse models of AD disease by stimulating the microglia-mediated clearance of plaques^{312,313}. Interestingly, tFUS has also been shown to decrease ultraviolet light-induced hyperpigmentation in experimental animal models by mechanically eliminating melanin and pigmented debris from the epidermis and upper dermis³¹⁴. These findings have laid the foundations for prospective therapies that leverage tFUS's non-invasiveness and both direct (i.e., mechanical/thermal lesion) and indirect (BBB permeability increase) mechanisms. Figure 13 summarizes the three principal features of tFUS that are being exploited with therapeutic aims. Other emerging tFUS effects that are at a more preliminary stage of development include hyperthermia to increase the radiosensitivity and immunogenicity of tumor cells, US-responsive drug carriers for targeted delivery, histotripsy for non-invasive mechanical fractionation of blood clots or large volumes of tissue²⁸⁰.

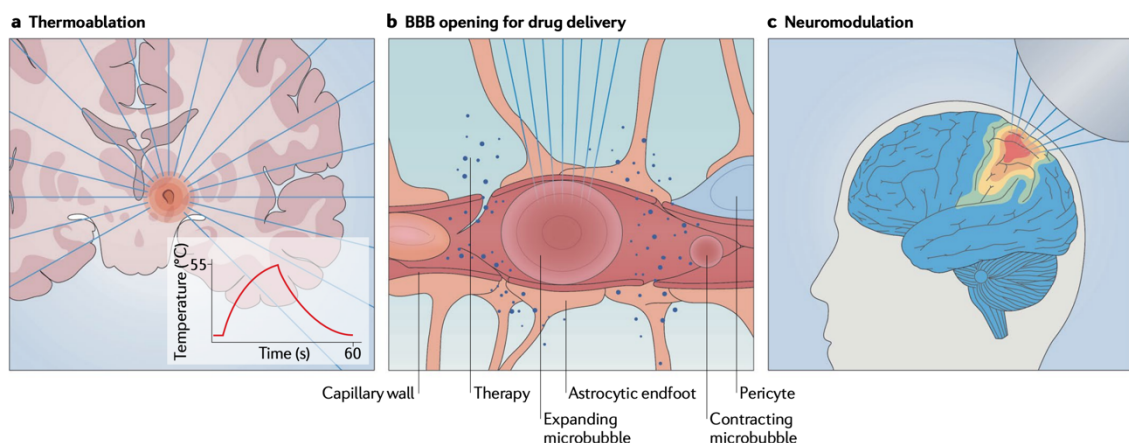


Figure 13. Biological effects of tFUS. The diverse biological effects of tFUS on brain tissue can be categorized as predominantly thermal or mechanical. The panels illustrate tFUS techniques that have been demonstrated in humans. High-intensity tFUS delivered through the intact skull creates a coagulative necrotic lesion with millimetric precision for incisionless neurosurgery (a). Stable cavitation of intravascular microbubbles under tFUS induces mechanical forces on the BBB that transiently increase its permeability thereby allowing drug delivery strategies (b). tFUS neuromodulation potentially offers higher spatial and temporal resolution than existing techniques, with the ability to non-invasively target deep brain regions (c). From Meng et al., 2021²⁸⁰.

4.4.1.2 MECHANISMS OF BIOLOGICAL EFFECTS

The effect of US as a neuromodulator and potential neurotherapeutic agent depends on the frequency ranges applied^{315–317}. Accordingly, tFUS techniques can be broadly divided into “high” and “low” power therapies, where high power applications include high intensity FUS (primarily used for tissue ablation) and low power strategies encompassing techniques for neuromodulation and ultrasonic enhancement of drug uptake (especially, when microbubbles are introduced into the system)³¹⁸. Two factors, namely temperature elevation and cavitation, are essential to explain the biological effects of US.

With high-intensity tFUS, ultrasound absorption in the target structure causes localized necrosis within seconds³¹⁹. To achieve this thermoablative effect of tFUS, temperatures need to reach $> 56\text{ }^{\circ}\text{C}$ ³²⁰. The other principal dictating effect of tFUS is cavitation, which refers to the change of a liquid to a gas state when subjected to reduced pressures and/or interactions of US with gas bubbles²⁸⁰. Depending on the intensity and center frequency, cavitation can result in stable oscillation (stable or non-inertial cavitation) or can result in violent bubble collapses (inertial cavitation) that create large forces in their vicinity. The air bubbles can have an endogenous origin (for instance, in the lungs or intestine), they can be formed by the mechanical wave itself (if the peak rarefaction pressure is small enough to enable the liquid to reach vaporization) or, alternatively, be exogenously injected for clinical aims³²¹ or involve gene/drug delivery strategies³²². In inertia cavitation, bubbles expand during the low-pressure phase of the US wave and begin to contract during the high-pressure phase, eventually resulting in unmanageable collapsing, which produces significant local heating and damaging shockwaves. In this

regard, histotripsy is an emerging method that has been designed to control this type of cavitation, allowing rapid mechanical tissue ablation with high-energy ultra-shot US pulses³²³.

Regarding the exact mechanisms underlying low-intensity tFUS-induced neuromodulation, many hypotheses have been proposed but are yet to be completely deciphered³²⁴. As for high-intensity tFUS, the initial theories for low-intensity tFUS-induced neuromodulation rely on thermal effects and cavitation. Regarding temperature, since its increase is often less than 0.1 °C, thermal effects in low-intensity tFUS are virtually negligible³²⁵. In relation to cavitation, one hypothesis suggests that the US generates nanobubbles in the lipophilic zone of the plasma membrane, which then vibrate according to the pressure variations, thereby altering the local curvature of the bilayer and, overall, changing neuronal excitability³²⁶. Nevertheless, since it has been reported that nanobubbles are formed at an US intensity larger than 0.1 W/cm², generation of micro or nanobubbles at the intensity used in standard animal models neuromodulation protocols is yet to be demonstrated in humans³²⁵. tFUS-mediated BBB opening *per se* has been demonstrated to generate considerable reductions in brain pathology and result in memory improvement in the amyloid AD disease mouse model^{313,327} as well as after delivery of antibodies against beta-amyloid³¹² and tau³²⁸. In PD animal models, tFUS application by itself has been reported to entail protective effects at the neuronal level³²⁹ and beneficial outcomes on locomotor behavior³³⁰ in rodents.

Exogenously administered microbubbles have been reported to ease stable cavitation at a reduced power, thereby allowing a transient opening of the BBB without causing mechanical or thermal injury to the vessel or parenchyma (Fig. 13)³³¹. In PD animal models, tFUS coupled with microbubbles has been reported to facilitate the delivery of viral vectors targeting α -synuclein³³² and neurotrophic proteins³³³. In humans, the feasibility of microbubble-mediated tFUS-induced BBB opening has been safely and successfully applied in AD³³⁴ and amyotrophic lateral sclerosis patients³³⁵. In the context of PD, one study still in progress is assessing the safety, efficacy and reversibility of microbubbles-coupled tFUS application to the BBB³³⁶.

In stable cavitation, bubbles oscillate without collapsing but can exert sufficient mechanical stress on the vessel walls that comprise the BBB. Recent theories concentrate on the effects of acoustic radiation forces on the permeability of ion channels such as mechanosensitive channels³³⁷ and voltage-gated sodium, potassium and calcium channels³³⁸. Another hypothesis involving plasma membrane deformation has been postulated, suggesting that vibration of the surrounding intra- and extracellular environment uncouples mechanical changes in either the plasma membrane tension or the lipid bilayer, thereby modulating neuronal activity³³⁸. Recently, and contrary to these theories on the mechanisms involved with the direct modulation of ion channels and membranes, an indirect US neuromodulation through auditory or cochlear pathways *in vivo* was proposed^{339,340}.

The different mechanisms of action exerted by tFUS depend on the physical parameters under which the US waves are applied. These are: the spatial peak temporal average intensity (I_{spta} , the temporal average intensity, calculated at the position of the spatial maximum), the spatial peak pulse average intensity (I_{sppe} , is the pulse average intensity, calculated at the position of the spatial maximum), mechanical index (MI, gives an estimation of the likelihood of inertial cavitation), thermal index (TI, is the steady-state temperature increase in soft tissue during ultrasound sonication), thermal index for cranial bone (TIC, is a modification of TI, when the skull is close to the transducer face). I_{spta} , TI and TIC are related to the risk of thermal bio-effects, whereas I_{sppe} and MI are related to the risk of cavitation. A sketch of a typical experimental setup for tFUS application in rats featuring the aforementioned indices is shown in figure 14.

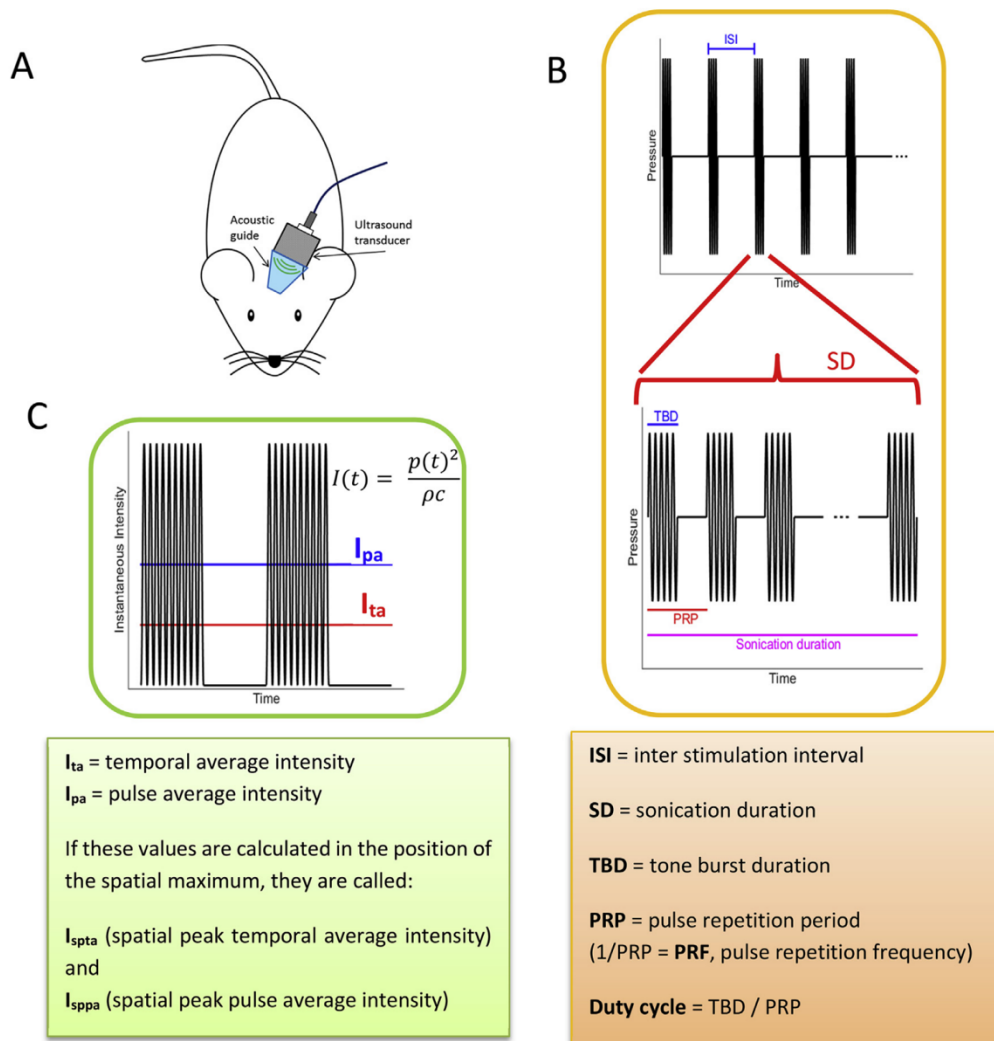


Figure 14. Overview of the tFUS setup and parameters. A) The ultrasound pressure wave is generated by a transducer and delivered to the target via a guide filled with acoustic gel. B) The *pressure* stimulus over time is shown to indicate the main parameters. C) The main *intensity* values are shown for a fixed space position, together with their relationship with the pressure signal.

4.4.2 CELL TRANSPLANTATION

Two approaches for cell transplantation in the PD therapeutic field have been applied with the global objective of reducing PD motor symptoms by restoring striatal DA transmission and connectivity. First, fetal cell transplantation envisaged that immature DA neurons obtained from aborted embryos or fetuses could not only restore striatal DA transmission and connectivity, but also alleviate motor symptomatology^{341,342}. Nevertheless, subsequent trials evidenced a lack of clinical benefit, except for patients under 60 years of age, and the not uncommon appearance of uncontrollable graft-

induced dyskinesias^{343–345}. The current consensus is that there are progressive signs of degeneration (loss of DA transporters and TH, as well as the appearance of LP) in grafted neurons, but that it takes over a decade before these pathological changes might impair the function of the transplants³⁴⁶. At the same time, however, quantitative evidence of beneficial graft effects up to 18 years after surgery has also been demonstrated³⁴⁷. A European-wide completed trial in 2021 but whose results are yet to be published, aims to clarify whether graft induced dyskinesias can be avoided; this study will also contribute to laying the foundations for future trials using stem cell-derived neurons as a source of transplantable DA neurons³⁴⁸.

The second approach to cell transplantation involves using stem cells as donor tissue. Over the past two decades, experimental stem cell therapy in PD animal models has dramatically increased and produced robust, valuable data for the field³⁴⁹. Nowadays, it is possible to generate DA neurons from both human embryonic stem cells and human induced pluripotent stem cells; these are capable of surviving grafting into animals, grow axons and achieve functional recovery from lesion-induced deficiencies³⁴⁹. Clinical trials involving both sources have already begun³⁵⁰.

4.4.3 GENE THERAPY

The two main strategies for gene therapy in PD make use of the viral vector-mediated expression of neurotransmitter-synthesizing enzymes or growth factors. In this sense, it has been suggested that members of the glial cell line-derived neurotrophic factor (GDNF) family protect nigral DA neurons from death and promote regeneration of their axons following damage³⁵¹. From the two different trials with GDNF injections into the STR, one concluded potentially favorable effects on motor symptomatology³⁵², whereas the second failed to show clinical benefit³⁵³. Neurturin, a less potent member of the GDNF family that had demonstrated promising results in MPTP-treated monkeys³⁵⁴, has also been tested in humans, but has not yet entered into clinical trials^{355,356}. A trial studying the potential beneficial effect of another neurotrophic factor, namely cerebral DA neurotrophic factor, is ongoing²⁷⁹. Clinical trials using the viral vector-mediated expression of key enzymes in the DA synthesis pathway like TH³⁵⁷ and AADC^{358–360} have

also commenced with encouraging outcomes. Furthermore, two clinical trials targeting the STN with the viral vector-mediated delivery of glutamate decarboxylase to inhibit GABAergic-induced firing showed promising results^{361,362}.

5. PARKINSON'S DISEASE ANIMAL MODELS

Modeling neurodegenerative diseases has been fruitful and yielded new insights into the pathogenesis of these disorders. In particular, these models have been instructive for modeling different stages of the corresponding illness, providing insights into early to late manifestations. These models have also successfully served as platforms to test novel therapeutics¹⁵⁰. In the case of PD, an ideal model should display pathological and clinical features of the disease, involving both dopaminergic and non-dopaminergic systems, the central and peripheral nervous systems, and exhibit both motor and non-motor symptoms, where the former should be responsive to DA replacement therapy. Furthermore, age-dependence and the progressive nature of PD should be also reflected^{150,363}. Another key determinant that ought to be evident in an animal model is the presence of LB and LN, both containing α -synuclein and ubiquitin-proteasomal proteins among others¹⁵⁰. This vast array of necessary factors to recapitulate the human disease as reproducibly as possible renders PD animal modelling a highly complex task. Being this multifactorial yet remaining open to new discoveries that elucidate the mechanism(s) conforming to the disease, none of the current models display all of the mentioned features of PD. In this sense, animal models of PD have been classically divided into two categories: genetic and neurotoxic models. Each group has its own strengths and weaknesses, but neurotoxic models are preferentially selected by researchers due to their overt neurodegeneration and subsequent motor symptomatology. Figure 15 summarizes the most frequently used species for modelling PD.

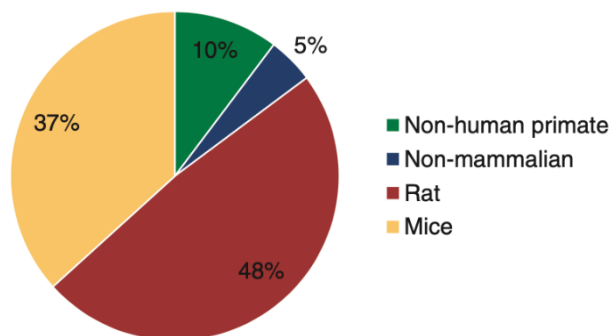


Figure 15. Percentages of animal models used in PD research from January 1990 to June 2018. Numbers are derived from 23000 original article publications and were obtained from following searches on Web of Science: “Parkinson AND (mice OR mouse)”; “Parkinson AND rat”; “Parkinson AND (primate OR monkey)”; “Parkinson AND (non-mammalian OR drosophila OR elegans)”. From Stoker and Greenland, 2018³⁶⁴.

5.1 NEUROTOXIN-INDUCED ANIMAL MODELS

In this section, PD animal models generated with classical molecules used to induce PD-like nigrostriatal pathway degeneration will be covered (Fig. 16). Importantly, no neuroregenerative or neuroprotective agent identified from studies on PD neurotoxicity-based models has been reported to be efficacious in PD patients. A lack of predictive value of these models may be due to their acuteness and their failure to replicate the majority of PD features¹⁵⁰.

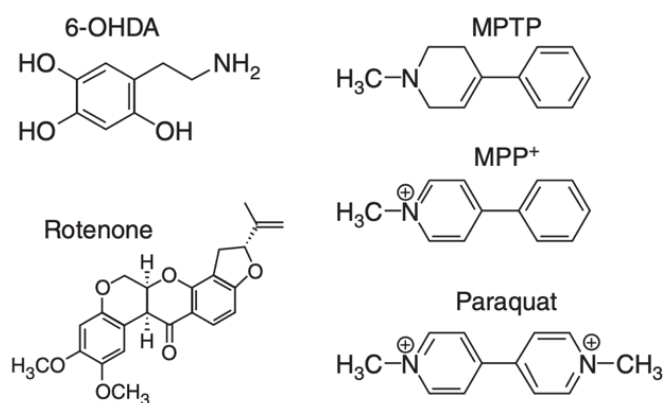


Fig 16. Structures of neurotoxic molecules known to induce nigrostriatal damage in common PD animal models. These include MPTP, which is readily converted into MPP⁺, 6-OHDA, rotenone and paraquat. MPTP; 1-methyl-4-phenyl-1,2,3,6-tetrahydropyridine; MPP⁺, 1-methyl-4-phenylpyridinium ion; 6-OHDA, 6-hydroxydopamine. From Tieu, 2011³⁶³.

5.1.1 1-METHYL-4-PHENYL-1,2,3,6-TETRAHYDROPYRIDINE

Since its discovery, 1-methyl-4-phenyl-1,2,3,6-tetrahydropyridine (MPTP) has contributed markedly to providing insights into the potential pathogenesis and mechanisms of cell death in PD³⁶⁵. Studies using this model have led to concepts such as environmental toxicity as a potential cause of sporadic PD and mitochondrial dysfunction as a potential pathological mechanism. MPTP is a lipophilic protoxin that crosses the BBB and is converted to the active toxic cation 1-methyl-4-phenylpyridium ion (MPP⁺), predominantly in serotonergic neurons and glial cells (mainly nigral and striatal astrocytes) via MAO-B³⁶⁶. MPP⁺ is then released via the organic cation transporter 3 into the extracellular space³⁶⁷, where it is taken up by neighboring DA neurons through DAT³⁶⁸. Upon accumulation in the cytosol, MPP⁺ is internalized by mitochondria, causing the inhibition of complex I of the electron transport chain; this results in ATP depletion and increased oxidative stress, ultimately leading to cell death^{369–371}.

Other noxious factors include superoxide radicals and nitric oxide that are produced secondarily to MPP⁺ intoxication; these combine to generate peroxynitrite that causes tyrosine residue nitration in intracellular proteins, including tyrosine hydroxylase, with a resultant loss of DA neurons³⁷². Neuronal destruction in the SNpc and VTA has an active phase of degeneration beginning 12 h post-injection and continues for up to 4 days³⁷³. Furthermore, microglial activation occurs in the SN following MPTP administration, with glial cells also producing free radicals and nitric oxide synthase³⁷⁴. Many animal species have been PD-modelled with MPTP, with the monkey being the gold standard for preclinical testing of therapeutic strategies for PD³⁶³. However, rodents are more popular due to the reduced demand on resources and the need for trained personnel to manage the monkey model.

The strength of the MPTP animal model is the specific and reproducible neurotoxic effect on the nigrostriatal dopaminergic pathway³⁷⁵ and the ease of administration of this agent via intraperitoneal injection. LB-like cytoplasmic inclusions have been described in MPTP-injected monkeys³⁷⁶, but not in mice. Nonetheless, it has been

reported that mice infused with a chronic low dose of MPTP over one month using osmotic minipumps present inclusions that are immunoreactive for both ubiquitin and α -synuclein³⁷⁷. In addition to the nigrostriatal damage, MPTP has also been demonstrated to induce loss of DA neurons in the enteric nervous system and alter colon motility³⁷⁸, with gastrointestinal dysfunction being a commonly observed symptom in PD patients.

5.1.2 6-HYDROXYDOPAMINE

6-hydroxydopamine (6-OHDA) is a naturally-occurring analog of DA that is widely used to lesion the nigrostriatal dopaminergic (or LC, alternatively) system; it is capable of inducing degeneration of both DA and noradrenergic neurons, and is thus used as a model of PD^{379–381}. These neurons are particularly vulnerable to 6-OHDA because their plasma membrane DA and noradrenergic transporters have high affinity for this molecule³⁸². Once taken up, 6-OHDA accumulates in the cytosol where it is readily oxidized, leading to the generation of ROS and ultimately, oxidative stress-related cytotoxicity³⁸³. When injected into the SN, DA neuron degeneration takes place within 12 h, this process preceding a significant loss of striatal terminals 2-3 d later³⁸⁴. When delivered to the STR, 6-OHDA induces a slow, progressive, partial damage to the nigrostriatal structure in a retrograde fashion over a period of up to 3 weeks^{385,386}.

This latter route of administration offers a more PD-relevant model since nigrostriatal lesioning is less extensive and progressive; this approach has been shown to produce non-motor symptoms, including cognitive, psychiatric and gastrointestinal dysfunction^{386,387}. Due to the difficulty to target small brain structures such as the SN or medial forebrain bundle, 6-OHDA is used more frequently in rats than in mice to model PD³⁸⁸. Furthermore, although unusual, this molecule has also been used in other animal models such as cats, guinea pigs, dogs and monkeys^{389,390}. 6-OHDA is commonly injected unilaterally into the SN, medial forebrain bundle, or STR. The major advantage of using the 6-OHDA model is its unique effect on animals' quantifiable circling motor abnormality³⁹¹. Typically, unilateral stereotaxic injection into one hemisphere (i.e., the

hemiparkinsonian model) is performed, leaving the contralateral side as an internal control. No LB-like inclusions are detected in 6-OHDA treated animals.

5.1.3 PARAQUAT

Since its identification³⁹², the widely used herbicide paraquat (N,N'-dimethyl-4,4'-bipyridinium), which has a similar molecular structure to MPP⁺, has also been used to model PD in mice. Despite their structural similarities, paraquat displays different transport and neurotoxic mechanisms compared to MPP⁺. For example, in spite of both compounds being cations, paraquat has the ability to penetrate the BBB through the neutral amino acid transporter³⁹³. Interestingly, the extent to which paraquat accumulates in the brain is age-dependent, with the highest levels being detected in 2-week-old or over 12-month-old rats³⁹⁴. This finding speaks for a role of the BBB since young and old animals exhibit a higher BBB permeability. Furthermore, in contrast to MPP⁺, paraquat is not a good substrate for DAT³⁹⁵, for which reason its mechanism of entry into DA neurons remains unknown. The toxicity of paraquat is exerted inside the mitochondria³⁹⁶ and is primarily mediated by redox cycling with cellular diaphorases such as NADPH oxidase and nitric oxide synthase, which lead to the generation of superoxide³⁹⁷. When injected into mice, paraquat has been reported to induce motor deficits and the loss of nigral DA neurons in a dose³⁹⁸- and age-dependent manner^{399,400}.

However, despite being seemingly selective for DA neurons, paraquat-induced damage in cell bodies and terminals has not been consistently observed^{401,402}. Strikingly, even in those studies in which a loss of nigral DA neurons was detected, paraquat damage was not sufficient to perturb striatal DA levels^{399,401}. When combined with the fungicide manganese ethylenebisdithiocarbamate (Maneb), a more significant loss of DA neurons and a trend towards a reduction (i.e., not statistically significant) of striatal DA are produced⁴⁰¹. Therefore, even with Maneb complementation or long-term periodic doses⁴⁰³, it remains unclear how reported paraquat-induced motor deficits can be attributed to such a reduced loss of striatal DA. In any case, since epidemiological studies have suggested an increased risk for PD after exposure to paraquat, the strength of the paraquat model is its potential relevance as an environmental toxicant since it

constitutes a risk factor for developing PD^{404,405}. In conclusion, despite also causing LB-like inclusion formation⁴⁰⁶ and LC neurodegeneration⁴⁰⁷, the lack of a significant effect of paraquat on striatal DA depletion in the commonly used regimens appears to limit the use of this model to the exploration of new neuroprotective PD therapies.

5.1.4 ROTENONE

Rotenone is a pesticide that has also been used in PD modelling. Due to its high lipophilicity, rotenone readily crosses the BBB and enters all cells without being dependent on a specific transporter. Similarly to MPP⁺, the mechanism of cytotoxicity of rotenone is primarily mediated by its strong mitochondrial complex I inhibition³⁶³. After initial studies using high rotenone doses, where widespread lesions beyond the nigrostriatal system were reported^{408,409}, Greenamyre and colleagues devised a chronic low-dose regimen that produced selective nigrostriatal neurodegeneration and α -synuclein-positive cytoplasmic inclusions. Their study demonstrated that despite brain-wide complex I inhibition, specific neurodegeneration occurs in the nigrostriatal pathway, thus confirming the inherent vulnerability of DA neurons to mitochondrial failure and the direct connection between complex I inhibition and PD. Regardless of its experimental advantages, the rotenone infusion model has not been widely adopted in PD research, mainly due to the high variability in animal sensitivity and reproducibility, and the lack of parkinsonian neuropathology and phenotype^{410–412}. Nevertheless, with the aim of addressing these inconsistencies, Cannon et al. developed a revised model in which rotenone was delivered via a medium chain fatty acid vehicle⁴¹³. With this protocol, daily rotenone injections (up to 3 weeks) were reported to produce a consistent lesion load in the nigrostriatal system, LB-like inclusions that were positive for α -synuclein and ubiquitin, and motor deficits. In a complementary study by the same researchers, gastrointestinal lesion upon rotenone treatment was also found⁴¹³. As with the paraquat model, the main strength of the rotenone model resides in its direct association with PD etiology, reinforcing the idea that environmental factors may play a role in the pathogenesis of the disease's sporadic phenotype^{414,415}.

5.1.5 OTHER NEUROTOXICITY-BASED ANIMAL MODELS

At this point it is important to highlight that motor deficits induced by the four presented neurotoxin-based models have been reported to be alleviated by the administration of L-DOPA, thereby confirming the nigrostriatal damage and its direct link to motor symptomatology^{391,416–418}. Other compounds have also been used as neurotoxins to deplete striatal DA and damage the nigrostriatal pathway, but, due to different compound-specific factors, they are not commonly in use. These compounds include reserpine^{419,420}, whose administration resulted in the first pharmacological PD model to be published and served to initially confirm the role of striatal DA in motor function and for L-DOPA to be proposed as a potential PD treatment. Other compounds are lipopolysaccharide⁴²¹; α -methyl-*p*-tyrosine⁴²²; isoquinoline derivatives^{423,424}; and amphetamines, particularly methamphetamine⁴²⁵.

Finally, to design a fine-tuned PD model it is relevant to emphasize that despite reported DA neuronal damage, some neurotoxins primarily destroy cell bodies, which is the case of paraquat, while others such as methamphetamine for example, harm the nerve terminals. Some compounds are toxic both to cell bodies and terminal; these include MPTP, 6-OHDA and rotenone. Differences in the neurodegenerative damage between models based on different compounds reinforce the theory that neuronal damage to the terminals and cell bodies can be controlled by distinct mechanisms, thus highlighting the value of different disease models not only for developing therapeutic approaches but also for unraveling new pathways and to more fully elucidate partially-described ones. Furthermore, depending on the acuteness of the provoked lesion, different compounds and diverse doses of each of them can be applied to model different stages of the modelled disease. Table 3 summarizes the principal features of each neurotoxic rodent PD model.

Table 3. Summary of the principal neurotoxins involved in PD modelling and their principal features. Features correspond only to rodent data obtained by standard protocols.

Features Toxins	Type of neurodegeneration	Damage in SN cell body	Damage in striatal terminals	Motor symptoms	Non-motor symptoms	Time to cause degeneration in SN	Progressive effects	LB
MPTP	Acute or subacute	Yes	Yes	Yes	Yes	12 h - 4 d	No	No
6-OHDA	Acute	Yes	Yes	Yes	Yes	12 h - 3 d	No	No
Rotenone	Acute	Yes	Yes	Yes	Yes	Not determined	No	Yes
Paraquat	Acute or sub-acute	Yes	Conflicting	Yes	Not determined	Not determined	Yes	Yes

5.2 GENETIC ANIMAL MODELS

Genetic models are robust experimental tools since they are based primarily on the use of genes associated with potential mechanisms known to cause PD in humans^{390,426}. Using genetic manipulation to model PD, either in animals or cellular systems, researchers have traditionally performed both transgenic overexpression or knock-in of autosomal dominant genes implicated in PD such as A53T mutant α -synuclein⁴²⁷, *LRRK2*⁴²⁸, *VPS35*¹¹⁵ and *EIF4G1*⁴²⁹ and knockout or knockdown models for autosomal recessive genes such as *PRKN*⁴³⁰, *DJ-1*⁴³¹ and *PINK1*⁴³². Other models generated with gene mutations that are causal or constitute strong risk factors for PD include *GBA*⁴³³, *ATP13A2*⁴³⁴ and *SYT11*⁴³⁵.

Cellular models offer the advantage to investigate the molecular functions of genes and proteins implicated in PD. By harnessing molecular, biochemical, and pharmacologic approaches, cellular studies can be carried out relatively quickly and robustly, and have provided insights into the function of specific proteins and molecular pathways involved in PD. One of the principal cellular models employed in PD research is the SH-5YSY neuroblastoma cell line. Induced pluripotent stem cells that are reprogrammed from patients' own fibroblasts⁴³⁶ or peripheral blood mononuclear cells are another frequently used cell model in PD research⁴³⁷. Nevertheless, the results of cell-based studies need to be interpreted cautiously since they lack the 3D cytoarchitecture of organs as well as components of cell-to-cell communication, organ-to-organ circuits, and physiological compensatory mechanisms. Although still with limitations, organoids serve as more accurate models that have been used in PD research⁴³⁸. Their major drawback is that they are often prone to artifacts and/or misinterpretation of data and

must be validated against animal model data¹⁵⁰. Since *Drosophila* and *C. elegans* lack the complexity of vertebrates, and they do not express many of the key proteins implicated in PD¹⁵⁰, they will not be reviewed here.

While in the remainder of this section will specifically focus on genetic modelling of PD in rodents, it should be noted that other models beyond the scope of this dissertation also encompass such areas as the modelling of α -synuclein pathology in the peripheral nervous system, including the enteric nervous system^{439,440}. Also of note is the fact that the validation of findings in transgenic models has relied on human *postmortem* tissue, although the latter only reflects end-stage illness¹⁵⁰. However, footprints of early disease pathology often remain and serve as the gold standard by which the scientific community measures the ability of animal models to mimic human pathological processes¹⁵⁰. The two principal and widely studied autosomal-dominantly inherited causes of PD are mutations in *SNCA* and *LRRK2*. With respect to the former, both transgenic and viral vector-mediated models have been developed. Evidence of α -synuclein toxicity, seeding and anatomical spread⁴⁴¹ has led to the development of yet more models in which α -synuclein pre-formed fibrils^{442,443} or inclusions^{444–446} have been introduced. However, these will not be covered here as they are not within the scope of the present project. In relation to *LRRK2* modelling, only transgenic models are currently available.

5.2.1 SNCA MODELLING

5.2.1.1 SNCA TRANSGENIC MODELLING

Three autosomal dominant *SNCA* point mutations that are fully penetrant, but rare, have been identified in PD: A53T, A30P and E46K^{150,447}. Many efforts to replicate familial PD by generating transgenic mice carrying these mutations have been made, but none of the models mimics progressive DA neurodegeneration and parkinsonian motor deficits⁴⁴⁸. Importantly, the phenotypic outcome of α -synuclein overexpression in mice depends heavily on the promoter used to drive transgene expression⁴⁴⁹. Despite the lack of overt degenerative pathology in DA neurons, several mouse α -synuclein models show functional abnormalities in the nigrostriatal system as well as α -synuclein aggregation,

with some of these models being DA responsive^{449–453}. Also, some of the models exhibit marked behavioral dysfunction and motor impairments⁴⁵⁴. Interestingly, truncated forms of α -synuclein are believed to be more toxic than full length human α -synuclein, and transgenic mice expressing a truncated version of the protein show a reduced number of nigrostriatal DA neurons due to cell loss during early development⁴⁵⁵. As mentioned above, α -synuclein's toxicity seems to occur via mitochondrial dysfunction among other mechanisms. In this regard, since mitochondrial dysfunction causes α -synuclein aggregation, and α -synuclein is capable of directly damaging mitochondria, there is a feed-forward loop that has the potential to initiate degeneration in PD¹⁵⁰. Intriguingly, while DA neurons in α -synuclein knockout mice are resistant to MPTP and other mitochondrial toxins^{42,456}, α -synuclein overexpressing mice are more sensitive paraquat⁴²⁷, which also targets mitochondria, and exhibit mitochondrial abnormalities including mitochondrial DNA damage and degeneration⁴⁵⁷. Furthermore, DA neurons progressively degenerate and accumulate LB-like inclusions containing α -synuclein in DA-specific mitochondrial transcription factor A knockouts⁴⁵⁸.

5.2.1.2 SNCA VIRAL VECTOR-MEDIATED MODELLING

In addition to transgenic strains, α -synuclein overexpression can be induced by the targeted injection of viral vectors. Advantages of this method include a specific focus on the nigrostriatal system, the induction of pathology in adulthood, and the possibility to adjust transgene dosage⁴⁵⁹. Recombinant adeno-associated virus (AAV) and lentivirus are the most commonly used vectors for gene transfer. Of note, different AAV serotypes have been used for α -synuclein transgene overexpression in the SNpc of rodents⁴⁴³. In this regard, while AAV2 has been widely used⁴⁴³, AAV6 has been reported to yield the largest DA cell loss (80% after 8 weeks) with subsequent profound motor deficits⁴⁶⁰. On the other hand, lentiviral-mediated overexpression of α -synuclein has demonstrated to provide protein aggregation but no clear cell loss or behavioral changes with any of the α -synuclein genotypes⁴⁵⁹. In addition to the viral vector, the genetic variant of the α -synuclein transgene influences the PD phenotype. For instance, the AAV-mediated expression of wild-type (WT) or A53T mutated versions of the protein seem to elicit a

comparable pathology, while the expression of A30P results in a weaker and delayed pathology^{459,461,462}. Viral vector-mediated α -synuclein models demonstrating nigral DA cell loss with matching DA striatal depletion and motor deficits have also been reported in non-human primates^{463,464}.

5.2.2 *LRRK2* MODELLING

As mentioned above, *LRRK2* mutations linked to PD, of which G2019S is the most common one, display autosomal dominant inheritance, but with incomplete and varying penetrance, depending on the population⁴⁶⁵. Most *LRRK2* transgenic rodent models have been unsuccessful in replicating PD hallmarks^{150,466}. No *LRRK2* modelling has been reported in non-human primates, but inhibitors of *LRRK2* kinase have been proposed as a potential therapeutic option in PD⁴⁶⁷. Due to the large size of *LRRK2*, models have been generated by means of a bacterial artificial chromosome⁴⁶⁸, herpes simplex virus or adenoviral vector packaging⁴⁵⁹. In rodents, transfection of the *LRRK2*-G2019S version was demonstrated to be more toxic than WT *LRRK2*, causing more neurodegeneration and the formation of inclusions⁴⁶⁹. In fact, injection of *LRRK2*-G2019S in the mouse STR has been shown to induce the degeneration of about 50% of SNpc DA neurons⁴⁷⁰. A combination of transgenic models can enhance PD-like pathology, as in the case of overexpression of *LRRK2* in A53T α -synuclein transgenic mice where DA cell neurodegeneration and α -synuclein aggregation were accentuated¹⁰³. Despite not being robust at mimicking most of the features of PD, *LRRK2* models are useful to understand the interplay between different genetic mutations and environmental factors and to untangle the mechanisms behind their implication in PD⁴⁵².

5.2.3 OTHER GENETIC ANIMAL MODELS

As mentioned above, mutations in *PRKN*, *PINK1* and *DJ-1* have been linked to familial PD in an autosomal recessive way. Mutations in all three genes generate loss-of-function phenotypes, thus making knockout models ideal to study. However, none of them display DA neuron loss or motor deficits¹⁵⁰. Some *DJ-1* and *PRKN* models display,

nonetheless, changes in DA neurotransmission and mitochondrial dysfunction, and present nigrostriatal deficits^{430,471–473}. In a similar way, silencing PINK1 or Parkin gene expression in mice has not yielded better PD models compared to knockout models^{459,474}. Remarkably, both knockout- and viral vector-mediated knockdown of *PINK1* rendered DA neurons more sensitive to MPTP^{459,474}. Knockdown of *DJ-1* also enhanced toxicity in the MPTP mouse model, an effect that could be rescued by reintroducing the gene with the aid of viral vectors⁴⁷⁵. These examples of combinations of genetic and neurotoxic models have been of the utmost importance to highlight and confirm the complex interaction between multiple factors in PD pathology. Interestingly, overexpression of a specific mutated version of *PRKN*, namely Q311X, led to age-dependent DA neurodegeneration, α -synuclein aggregation, and some motor deficits, suggesting a potential gain of pathological function⁴⁷⁶. Overexpression of WT *PRKN* in non-human primates had protective effects when injected into the STR of α -synuclein-overexpressing animals⁴⁷⁷. This PD modelling opened the door for the overexpression of autosomal recessive genes to be considered as a potential treatment approach.

6. NEUROMELANIN

6.1 ORIGIN AND CLASSIFICATION

The origin of the name melanin derives from the Greek word *melanos* (which means dark) and is traditionally attributed to the Swedish chemist Berzelius⁴⁷⁸. Compared to peripheral forms of melanin, brain melanin has a similar structure and has therefore been termed 'neuromelanin'^{479,480}. Based on their precursor molecules, melanins have been classified as pheomelanin, eumelanin (Fig. 17), NM, whose formation will be addressed extensively below, and allomelanin, which is widespread in fungi and in some plants such as black oat, and which is formed by the oxidation of polyphenols⁴⁸¹.

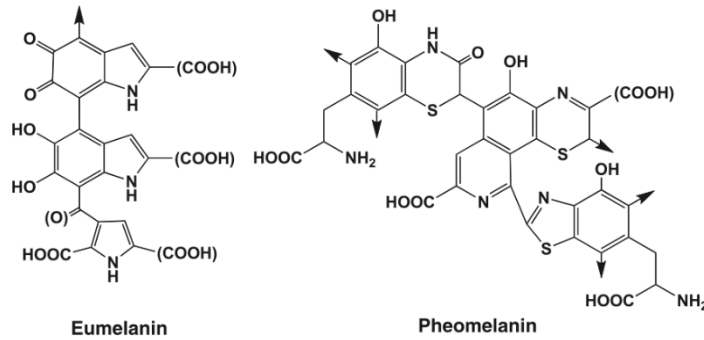


Figure 17. Core structures of eumelanin and pheomelanin. Note that the structures of eumelanin and pheomelanin are only representative models based on biosynthetic and degradative studies. The arrows indicate sites for attachment to other units. From Ito and Wakamatsu, 2008⁴⁸².

A century ago, Tretiakoff described for the first time the marked loss of pigmented neurons in the SN of *postmortem* brains of PD patients as seen with the naked eye. This finding is today the foremost diagnostic criterion for PD and constitutes the only strong clinicopathological correlation associated with the disease⁴⁸³. Several decades after Tretiakoff's observations, it was confirmed that NM is present in two of the three types of catecholamine-synthesizing cells, namely those synthesizing noradrenaline and DA, but not adrenaline^{484–486}. In this sense, apart from the SN (located in the midbrain), NM is also markedly present in the LC (located in the pons) and in the DMNV (located in the medulla oblongata) (Fig. 18).

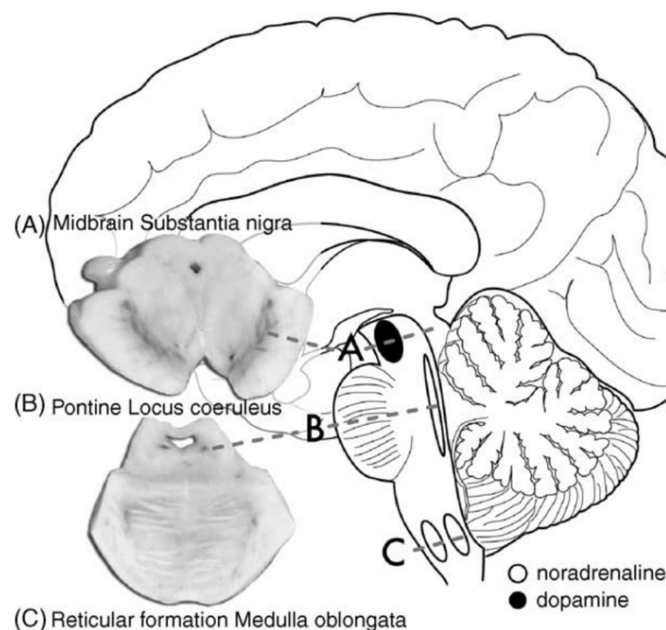


Figure 18. NM-containing regions in the human brain. Three main regions contain NM-producing neurons: the SNpc of the midbrain (A), the LC within the pons (B) and the DMNV within the medulla oblongata (C). From these, only SN and LC contain large clusters of pigmented neurons that can be seen macroscopically as darkened areas of tissue. From Fedorow et al., 2005²⁸.

NM is also present in other non-brainstem regions including in neurons of the cerebellum⁴⁸⁷, the hypothalamus²⁷, in spinal and sympathetic ganglia⁴⁸⁸ and in the dorsal raphe nucleus⁴⁸⁹. Of all the NM-producing brain centers, only the SN and LC harbor adequate pigmented cells to be visible macroscopically. In this regard, the SNpc exhibits the largest number of pigmented cells⁴⁹⁰. Interestingly, Gaspar et al. demonstrated that there is no correlation between the amount of NM and TH immunoreactivity, illustrating that, although being necessary for its production, the synthesis and use of DA/noradrenaline do not guarantee NM generation^{28,491}.

There is controversy in the literature regarding the formation of NM, as well as its actual structure and functionality, for which decades of intense research have not yielded conclusive data. Probably, the most accurate description of NM biochemistry and hypothesis of the most plausible mechanisms for NM generation have been provided by the Zecca-Zucca-Sulzer collaboration in recent decades as will be discussed next. In this sense, they came up with the most well founded, up-to-date theory regarding the process of NM formation and context, considering its highly-complex network of different constituents and biophysical properties⁴⁹². This knowledge has contributed to a thorough understanding of the NM pigment, which can nowadays be visualized by high-resolution transmission electron microscopy images and efficiently isolated from *postmortem* tissue (Fig. 19).

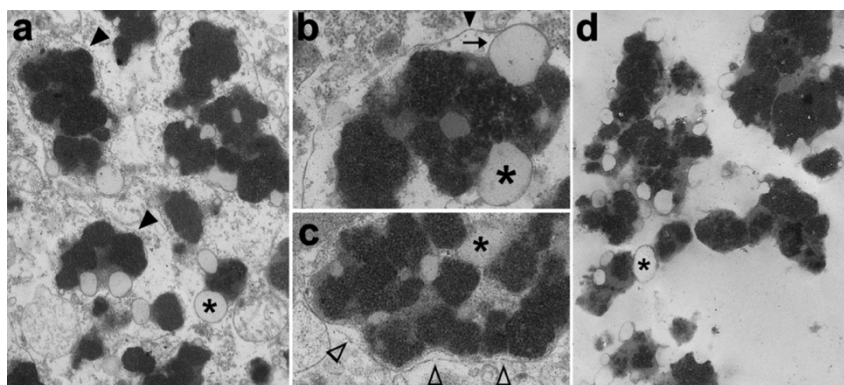


Figure 19. Transmission electron microscopy of NM-containing organelles. a-c, SN tissue of 89-year-old healthy subject. Intraneuronal NM-containing organelles of the SN are membrane bound (black arrowheads in a and b) and contain large amounts of NM pigment (black and electron dense), protein matrix and lipid bodies (asterisks). In c, empty arrowheads point to double membrane delimitating NM-containing organelles. d, NM-containing organelles isolated from the SN of the same subject. Note the purity and integrity of isolated NM-containing organelles as demonstrated by the absence of cellular and subcellular debris. Zucca et al., 2018⁴⁹².

6.2 PRESENCE OF NEUROMELANIN IN HUMAN BRAIN

As was pointed out recently, while the vast majority of adult DA cells in the human SN contain NM, a considerable number of DA-producing midbrain cells do not produce NM⁴⁹¹. This finding, apart from ruling out – at least partially – the traditionally accepted concept that NM production occurs via DA autooxidation, revealed the unique nature of NM-producing cells. NM deposition begins early in human life and the pigment abundance increases linearly with age (Fig. 20)⁴⁹³. Intriguingly, early descriptive studies showed that nigral neurons do not contain NM at birth⁵⁴⁵ and that the pigment is still undetectable 3 years later⁴⁹⁴. At a histological level, there is an extremely pale, very fine granular cytoplasmic material at around two years of age, while one year later NM first appears as light brown granules in the cytoplasm of DA neurons⁴⁹⁴. Again, this suggests either an improbable, excessively long incubation period for autooxidation, or a delayed development of regulatory mechanism. Supporting the latter notion, human fetal DA neurons exhibited a premature production of NM when implanted as a treatment into the STR of PD patients³⁴³. Interestingly, an abnormal development of NM in the SN occurs in Rett's syndrome (whose pathology, in some aspects, overlaps the PD motor phenotype⁴⁹⁵), a disabling neurodevelopmental disorder with onset in early childhood⁴⁹⁶. Hypopigmentation in this syndrome suggests that the production of NM is a key element for the physiological and functional maintenance of DA neurons during childhood⁴⁹⁷.

In this sense, once pigmentation has begun, the cellular volume occupied by NM steadily increases until 20 years of age, when nearly the entire cytoplasm contains pigment granules (Fig. 20)⁴⁹⁴. Strikingly, after the second decade of life, the cellular volume occupied by pigment stabilizes and there is no further increase with age⁴⁹⁴. In contrast, what does undergo important changes throughout life is the absolute concentration of NM, which increases linearly with age up to the ninth decade of life, starting at 0.3 to 0.8 $\mu\text{g}/\text{mg}$ tissue between 10 and 20 years of age and ending at up to 3.7 $\mu\text{g}/\text{mg}$ tissue between the fifth and ninth decades⁴⁹³. This rise in pigment quantity, probably due to the aggregation of NM granules, is accompanied by a constant increase of NM's optical

density and a modification of the pigment's coloration, which changes from yellow-brown to dark brown, consistent with DA oxidation⁴⁹⁴.

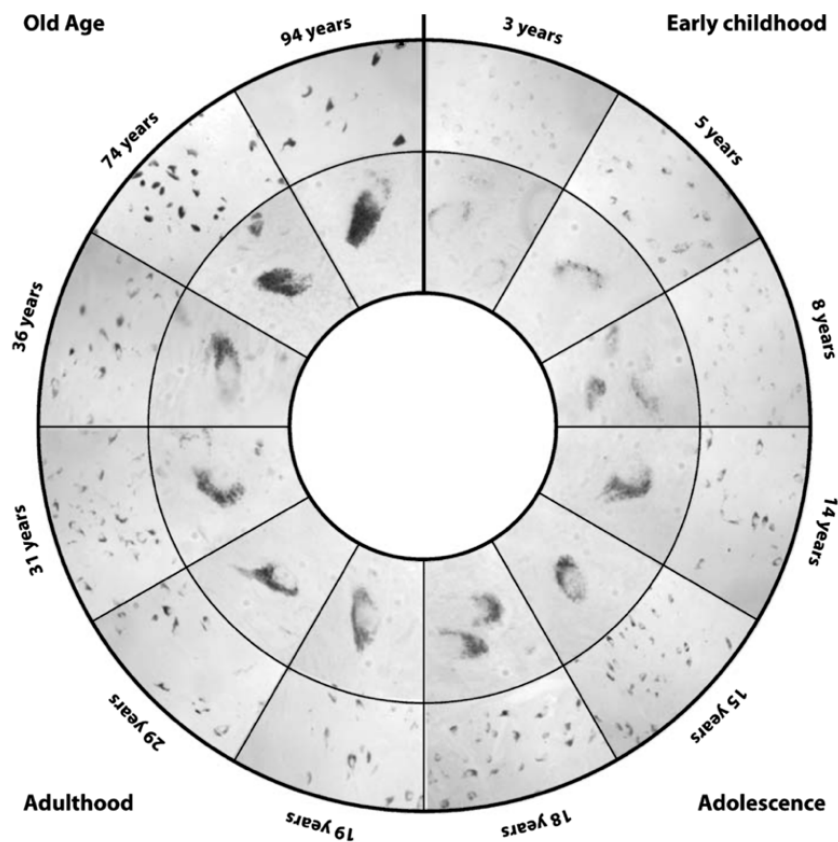


Figure 20. Progressive accumulation of NM in the human brain. Intermediate and high magnification photomicrographs of representative unstained NM-pigmented neurons from the ventral region of the human SN at different ages. The first appearance of NM pigment is at 3 years of age. The optical density of the NM pigment increases constantly throughout life, while the average volume occupied by it increases up to 20 years of age (3-18 years). After this vital stage, the average cellular volume occupied by NM does not increase significantly (19-94 years). From Halliday et al., 2006⁴⁹⁴.

Figure 21 recapitulates NM development in three different stages. The first phase involves the initiation of NM production, which becomes evident in the third year of life. The second stage features the increase in cellular volume occupied by NM and associated maturation. The last phase entails a slower, sustained maturation of NM without substantial volumetric growth. Overall, the identification of these stages and changes in the rate of NM production over time implies that NM is produced and maintained within DA neurons by regulated processes.

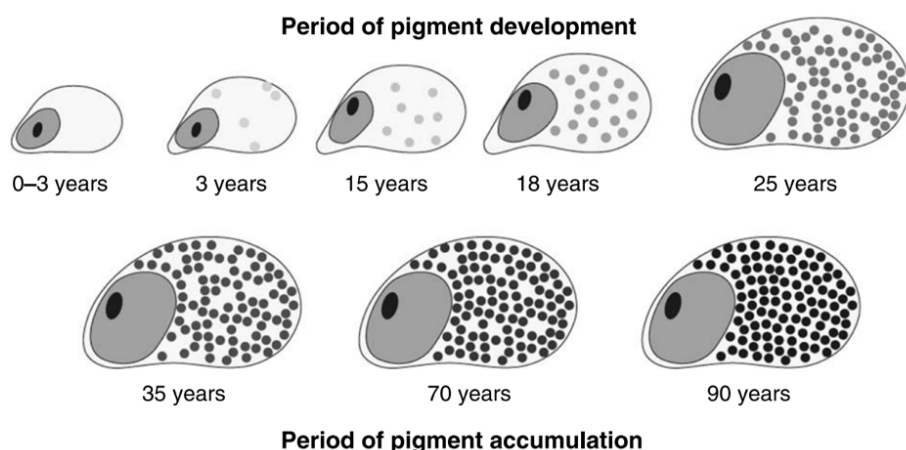


Figure 21. Schematic representation of NM accumulation in human DA neurons. Initiation of pigmentation occurs at around 3 years of age, followed by a rise in cell size and the cellular volume occupied by NM until 20 years of age. In adulthood, NM pigments aggregate and darken over time. From Halliday et al., 2006⁴⁹⁴.

6.3 PRESENCE OF NEUROMELANIN IN BRAINS OF OTHER SPECIES

Although NM is macroscopically visible in the adult human brainstem, few other species exhibit NM in the brain and, those that do, show significantly less than that in humans (Fig. 22). Importantly, NM is absent from all the commonly employed laboratory animals, including rodents⁴⁹⁸. As such, all of these species possess DA and noradrenaline neurons, but do not harbor NM-containing neurons²⁸. This fact highlights that NM production is not an inevitable consequence of catecholamine synthesis, with numerous additional factors likely to be in play. As in humans, catecholamine-containing neurons from other primates also contain a similar-in-ultrastructure NM, although, as commented, intracellular levels appear to be low^{499,500} (Fig. 22B). Pigmentation is most consistent in the SN of primates and within them, humans present the maximal intensity⁵⁰¹. In both, human and non-human primates, NM production is an age-dependent process^{494,502}. NM has also been reported to be present in other species as varied as dolphins⁵⁰³, dogs⁵⁰⁴, horses⁵⁰⁵, giraffes⁵⁰⁶ and frogs⁵⁰⁷. Interestingly, in spite of this vast array of different potential NM candidates, the melanin of cuttlefish has proven to be the most suitable model to study NM biochemistry⁵⁰⁸.

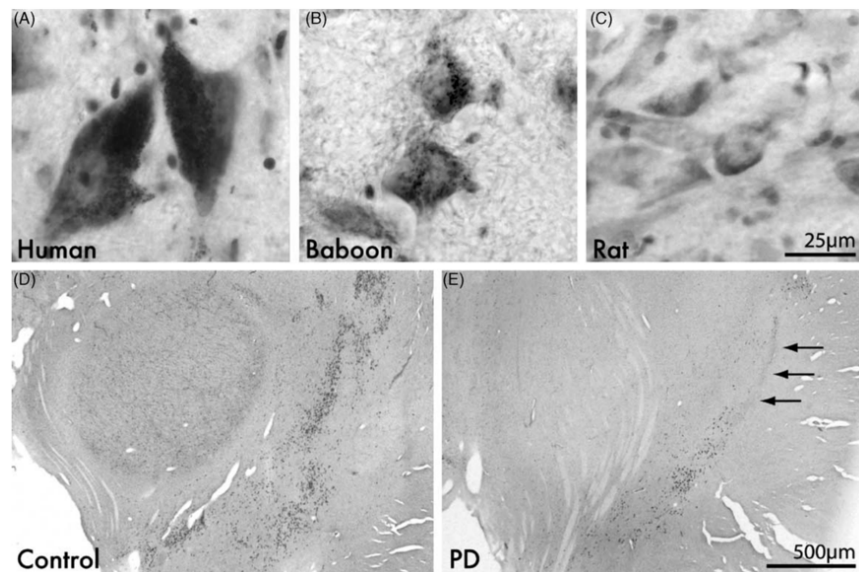


Figure 22. Presence of NM in DA neurons of the human brain (control vs PD) and in other species. Cresyl violet stained sections from the SN (A-E). Human DA neurons (A) accumulate greater quantity of NM compared with the pigmented DA neurons of the baboon (B). Rat DA neurons (C) do not contain NM. Pigmented DA neurons in PD SNpc have degenerated compared to control neurons, specifically in the lateral region (arrows). From Fedorow et al., 2005²⁸.

6.4 SYNTHESIS OF NEUROMELANIN

6.4.1 DOPAMINE

In mammals, DA is an essential neurotransmitter for behavior and behavioral states such as voluntary movement, arousal, motivation, reward and reinforcement of natural rewards such as food, water and reproductive activities⁵⁰⁹. These ascribed functions are attributed to four main pathways which utilize DA in the brain: the mesolimbic pathway (which projects from the VTA to an anterior structure called the nucleus accumbens); the mesocortical pathway (which also originates in the VTA and projects to the frontal cortices); the tuberoinfundibular pathway (which projects from the infundibular nucleus in the tuberal region of the hypothalamus to the median eminence); and the nigrostriatal pathway (which originates in the SNpc and projects to the STR, and constitutes the main focus of the present dissertation). Independently of the pathway involved, DA finds its origin in tyrosine, which is transported into the cell via a large neutral amino acid (LNAA) L-system transporter and is subsequently metabolized to DA via a multi-step process in the presynaptic neuron. First, the rate-limiting TH enzyme catalyzes the reaction of amino acid tyrosine to L-hydroxyphenylalanine (L-DOPA).

Subsequently, this molecule is decarboxylated by AADC to produce DA and CO₂. Being in the cytosol, which is at pH 7.4, DA has two hydroxyl groups that are dissociated, giving rise to its potential oxidation to neurotoxic *o*-quinones. Nevertheless, as TH and AADC are associated with the vesicular monoaminergic transporter-2 (VMAT2), newly synthesized DA is directly sequestered into synaptic vesicles. Specifically, VMAT2 is associated to the membranes of these vesicles and forms a stable complex with the other two enzymes⁵¹⁰. DA that is not immediately packaged is metabolized by MAO to 3,4-dihydroxyphenylacetaldehyde (DOPAL), and further oxidized by aldehyde dehydrogenase to 3,4-dihydroxyphenylacetate (DOPAC)⁵¹¹.

DA-loaded vesicles are then transported to the plasma membrane by motor proteins and interact with a series of protein complexes that first dock and then prime the vesicles for membrane fusion⁵¹². An action potential signals calcium influx, leading to a brief fusion of the vesicle with the plasma membrane and exocytosis of neurotransmitter^{513,514}. The number of neurotransmitter molecules released when a vesicle fuses with the plasma membrane is known as the quantal size⁵⁰⁹, which in DA neurons is regulated by vesicular monoamine transporter-2 (VMAT2) activity^{515,516}. DA then floods into the synaptic space, where it binds to specific receptors (DA receptors D1 and D2) and is degraded by COMT into 3-methoxytyramine (3-MT). Alternatively, it can be internalized back into the pre-synaptic neuron via the DA transporter (DAT), predominantly, and, to a lesser extent, via the D2 receptor^{517,518}. The combined action of MAO and COMT on DA yields homovanillic acid (HVA), one of DA's most commonly measured extracellular metabolites⁵¹⁹. Regardless of the neurotransmitter, neurons maintain a balance of neurotransmitter production, recycling and degradation that is reflected in the ratio of specific metabolites to their neurotransmitter of origin. Figure 23 summarizes the cycle of DA in a typical DA neuron terminal.

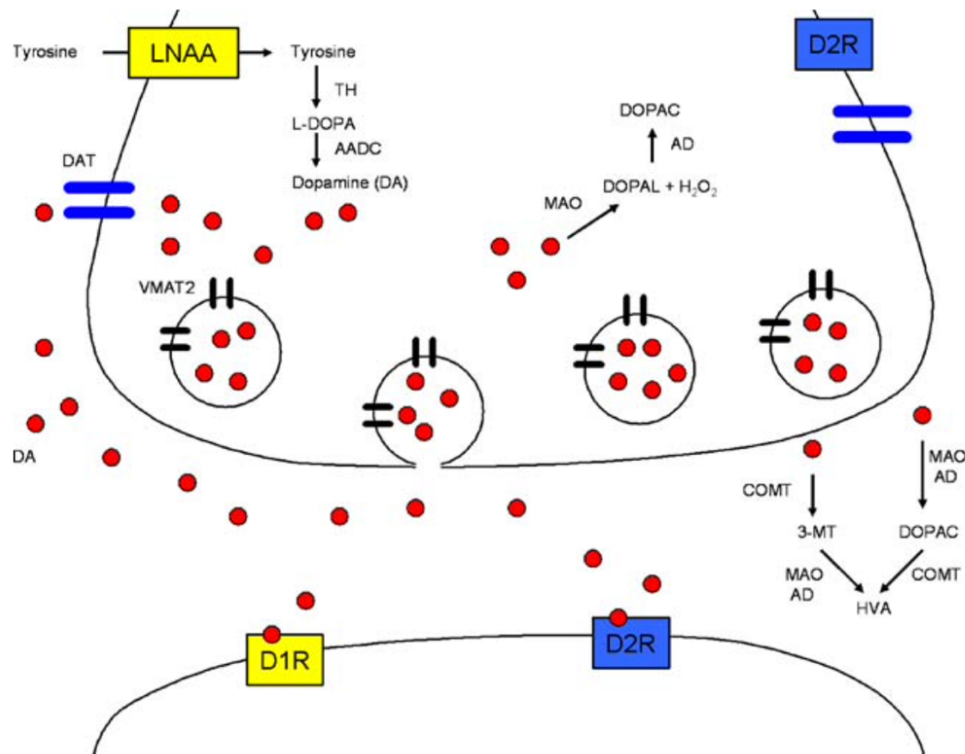


Figure 23. Cycle of DA in the neuronal terminal. Tyrosine is transported into the neuron by the large neutral amino acid (LNAA) transport system and then oxidized by TH to yield L-DOPA, which is readily decarboxylated by AADC to DA. Newly synthesized DA is then sequestered into synaptic vesicles by VMAT2. DA-loaded vesicles are taken to the axon terminal and made ready for release. An action potential leads to fusion of the vesicle with the plasma membrane and exocytosis of the neurotransmitter. DA is released into the synaptic space where it binds to receptors on pre- or postsynaptic neurons, is recycled into the presynaptic neuron via the DA transporter (DAT), or is degraded. Intracellular DA degradation by MAO yields DOPAL, which is further oxidized by aldehyde dehydrogenase (AD) to DOPAC. Extracellular DA is degraded by a two-step process: COMT activity yields 3-MT from DA and HVA from DOPAC, while extracellular MAO converts DA to DOPAC and 3-MT to HVA. From Guillot et Miller (2009)⁵⁰⁹.

From a biological point of view, it is important to note that the pH value inside the presynaptic vesicles ranges from 5 to 5.4. This acidic environment allows DA to be well protonated, thereby preventing its oxidation⁵⁰⁹. Thus, the multi-step conversion of tyrosine to DA in the vicinity of presynaptic vesicles prevents free DA from accumulating in the cytosol, thereby avoiding formation of the dangerous *o*-quinone. However, recently produced DA may leak and be released into the cytoplasm. In that case, free circulating DA spontaneously oxidizes to highly-reactive aminochrome even without the participation of a metal-ion catalyst⁵²⁰. As will be discussed in detail below, several mechanisms are available to avoid or minimize the potential toxicity of DA oxidation.

6.4.2 DOPAMINE METABOLISM

6.4.2.1 OXIDATIVE DEAMINATION

Leaked or excess DA can be deaminated in an oxidative process catalyzed by MAO enzymes, these being flavoenzymes with multiple isoforms located in the outer membranes of mitochondria, mainly in neurons and glial cells. Isoforms A and B are the principal types. The presence of MAO-A is restricted mostly to catecholaminergic neurons, whereas MAO-B is found in serotonergic and histaminergic neurons as well as in astrocytes^{521,522}. MAO-A catalyzes reactions involving monoaminergic neurotransmitters such as DA, serotonin, adrenaline, and noradrenaline, while MAO-B substrates include trace amines such as tyramine and phenylethylamine⁵²³. Interestingly, DA is mainly metabolized by MAO-B in the SN, where MAO-B is the main isoform present in glial cells; its enhanced activity is associated with loss of DA in the human brain⁵²⁴. To this end, an association between increased MAO-B levels (around 4-fold with aging) and PD has been described⁵²⁵.

Thus, in the SN, MAO-B catalyzes the reaction of DA to DOPAL, which is readily converted to DOPAC by aldehyde dehydrogenase (Fig. 24, reaction 1) or to 3,4-dihydroxyphenylethanol (DOPE) by aldehyde/aldose reductase (not shown). Remarkably, in rat brain, an enzyme called DOPAC reductase has been demonstrated to catalyze the conversion of DOPAC to DOPE⁵²⁶. Nevertheless, despite low DA cytosolic concentrations, MAO activity is associated with the generation of oxidative stress since during DOPAL and 3-methoxy-4-hydroxyphenylacetaldehyde—production, hydrogen peroxide, which is a precursor to the highly toxic hydroxyl radical, is formed as a byproduct. In PD models, rasagiline has been shown to have neuroprotective effects by inhibiting the formation of ROS derived from the deaminative oxidation of DA⁵²⁷.

6.4.2.2 ORTHO-METHYLATION

In a parallel to the above, DA can also be degraded by COMT, which is involved in the metabolism of various catecholamine neurotransmitters, including DA, noradrenaline,

adrenaline, catecholestrogens, and L-DOPA⁵²⁸⁻⁵³⁰. COMT has two different isoforms, the soluble S-COMT and the membrane-bound form MB-COMT, both of which are expressed in, but not restricted to, the brain⁵³¹. In this regard, while S-COMT is believed to be mainly responsible for the removal of biologically toxic, especially exogenous, catechols acting as a detoxifying shield between the blood and the other tissues⁵³², MB-COMT, on the other hand, is thought to be principally implicated in the termination of dopaminergic and noradrenergic synaptic neurotransmission when concentrations of catecholamines are physiologically low⁵³³. Thus, either isoform of this enzyme catalyzes the transfer of the methyl group of S-adenosyl-L-methionine (SAM) to hydroxyl groups of DA to produce 3-MT⁵³⁴ (Fig. 24, reaction 2). This is then metabolized by MAO to 3-methoxy-4-hydroxyphenylacetaldehyde. Finally, aldehyde dehydrogenase catalyzes the oxidation of the latter to HVA. This metabolite is the intersection point between both pathways as it is also formed by the COMT-mediated methylation of DOPAC's hydroxyl group (Figure 24, reaction 3). As discussed above, COMT inhibitors, such as entacapone or tolcapone, are commonly used as adjuncts to L-DOPA as a PD treatment strategy^{535,536}. From these two mechanisms, MAO appears to play a more dominant role in DA clearance⁵³⁷. Figure 24 depicts DA's oxidative deamination and ortho-methylation pathways.

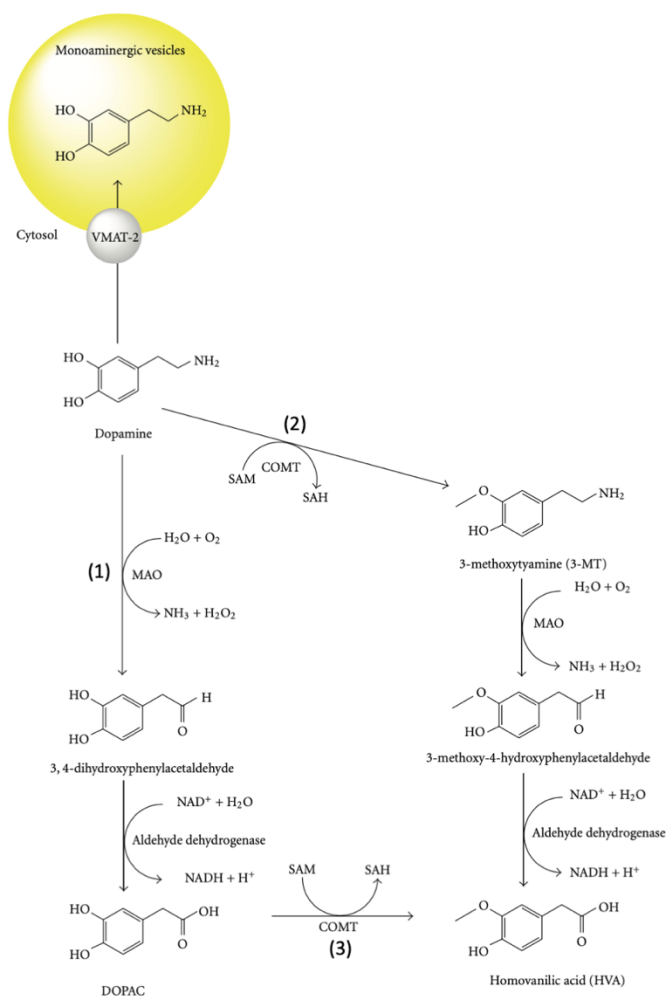


Figure 24. DA degradation catalyzed by MAO and COMT. DA oxidation to aminochrome is prevented by MAO- and COMT-mediated degradations. MAO catalyzes the oxidative deamination of DA to 3,4-dihydroxyphenylacetaldehyde (1), that is converted to DOPAC by aldehyde dehydrogenase. In a parallel way, COMT catalyzes the methylation of DA to 3-methoxytyramine (2) a substrate for MAO, which catalyzes the formation of 3-methoxy-4-hydroxyphenylacetaldehyde. As a common final product, homovanillic acid is formed from 3-methoxy-4-hydroxyphenylacetaldehyde via aldehyde dehydrogenase or from DOPAC via COMT (3). Modified from Muñoz et al., 2012⁵³⁸.

6.4.2.3 OXIDATION TO AMINOCHROME

DA's hydroxyl group protons are dissociated when DA is subjected to pH 7.4 in the cytosol. In turn, as stated above, in the presence of oxygen, DA spontaneously oxidizes without the involvement of a metal-ion catalyst. In this way, DA oxidation produces a DA *o*-semiquinone radical and a superoxide radical. The DA *o*-semiquinone radical can be one electron-oxidized by oxygen to produce DA *o*-quinone and a superoxide radical. Alternatively, two DA *o*-semiquinone radicals can react in a disproportionation reaction to produce one molecule of DA *o*-quinone and one molecule of DA. A third pathway

includes DA oxidation catalyzed by metals. For example, copper sulfate (II) and iron chloride (III) oxidize DA by forming a complex with it^{539,540}. Sodium metaperiodate also catalyzes the oxidation of DA, while manganese (III) oxidizes DA under aerobic and anaerobic conditions without forming superoxide radicals as it catalyzes the formation of both DA *o*-semiquinone and DA *o*-quinone⁵⁴¹. The last mechanism of DA oxidation includes enzymatic catalysis, either through peroxidase activity, such as the one harnessed by β -monooxygenase⁵⁴², lactoperoxidase⁵⁴³, prostaglandin H synthase⁵⁴⁴ or xanthine oxidase⁵⁴⁵, or via tyrosinase (Tyr), which catalyzes the two-electron oxidation of DA to DA *o*-quinone in the absence of oxygen consumption without generating DA *o*-semiquinone radicals⁵⁴⁶. All four reactions are schematized in the red square of figure 18. Of note, the animal model around which the present thesis is based, was generated by a single unilateral injection of human Tyr (hTyr) in the rat SN⁵⁴⁷.

Since DA *o*-quinone is only stable below pH 2.0, it is very unstable at physiological pH⁵⁴¹. In fact, DA's amino group spontaneously rearranges and undergoes cyclization to become aminochrome⁵⁴⁸. Paris et al. demonstrated that purified aminochrome is stable for around 3 h, which is a very long timeframe compared to its precursors, thereby proposing that aminochrome is the end product of DA oxidation in NM-containing DA neurons⁵⁴⁹. In this regard, despite active VMAT2 encapsulation and MAO metabolism, free cytosolic DA is oxidized to form aminochrome under certain conditions. Thus, the presence of NM in the SN of healthy controls indicates that DA oxidation occurs *in vivo* since aminochrome is the precursor of NM (as will be discussed below)⁵¹¹. Figure 25 summarizes the oxidation of DA to aminochrome and its subsequent metabolism.

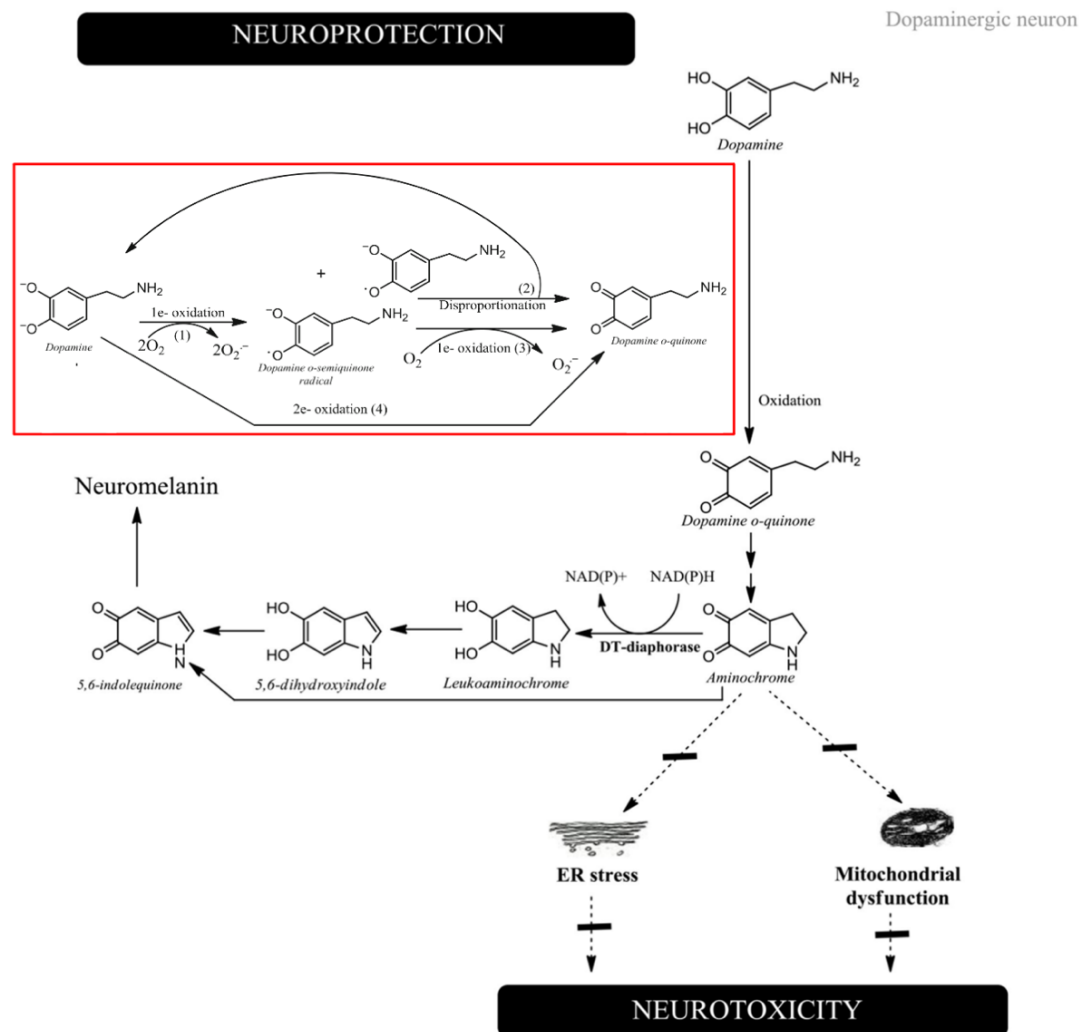


Figure 25. Oxidation of DA to aminochrome. Once formed, DA *o*-quinone undergoes oxidation and cyclization reactions to aminochrome. This molecule, widely known for its induced toxicity which causes ER stress and mitochondrial dysfunction among other effects, can be reduced by DT-diaphorase to leukoaminochrome, thereby preventing its neurotoxic effects. Leukoaminochrome rearranges into 5,6-dihydroxyindole, which oxidizes into 5,6-indolequinone and polymerizes into neuromelanin. Alternatively, aminochrome can directly tautomerize to 5,6-indolequinone. Red square from Segura-Aguilar and Paris, 2014⁵¹¹. Modified from Segura-Aguilar 2019⁵⁴⁸.

6.4.2.3.1 AMINOCHROME METABOLISM

Despite being much more stable than its precursors, aminochrome undergoes tautomerization to 5,6-dihydroxyindole, which is then oxidized to 5,6-indolequinone followed by further polymerization to form NM⁵⁵⁰. Nevertheless, under certain conditions, aminochrome can be reduced by different pathways. Aminochrome can undergo a one-electron reduction by flavoenzymes that use NADH or NADPH as electron

donors to generate a leukoaminochrome-*o*-semiquinone radical (Fig. 26). This radical, which is extremely reactive, autoxidizes back to aminochrome under aerobic conditions. In this process, molecular oxygen is reduced to a superoxide radical, which undergoes dismutation to hydrogen peroxide, the precursor of the highly-toxic hydroxyl radicals⁵⁵¹. This redox cycle induces NADH depletion required for the generation of ATP in the mitochondria or NADPH consumption required to catalyze the reduction of oxidized glutathione by glutathione reductase. It also induces oxidative stress, which has been extensively demonstrated to be neurotoxic to catecholaminergic cells^{539,552–554}.

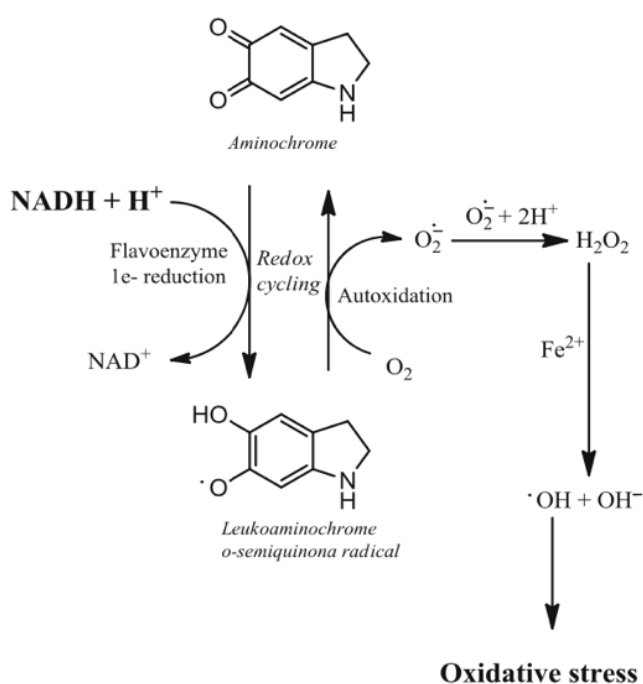


Figure 26. One-electron reduction of aminochrome. One-electron reduction of aminochrome by means of flavoenzymes using NAD(P)H initiates a neurotoxic cycle with deleterious consequences such as NADH depletion, indispensable for ATP production, and oxidative stress generation. From Segura-Aguilar and Paris, 2014⁵¹¹.

Aminochrome can also undergo a two-electron reduction catalyzed by DT-diaphorase, resulting in the formation of leukoaminochrome (Fig. 27). Under certain conditions in which the superoxide radical is available, cytosolic superoxide dismutase renders this reaction reversible, preventing leukoaminochrome autoxidation⁵⁵¹. *In vitro* results suggested a neuroprotective role of DT-diaphorase against aminochrome toxicity since its inhibition entails deleterious effects^{552,553}, which was extensively confirmed in later studies^{554–558}.

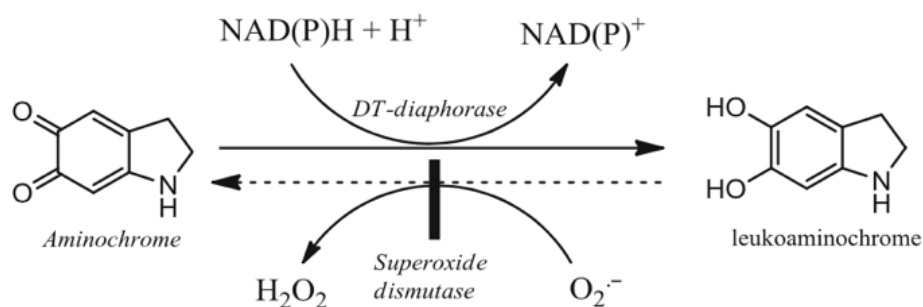


Figure 27. Two-electron reduction of aminochrome. Two e-electron reduction of aminochrome by means of DT-diaphorase entails a neuroprotective effect by avoiding the noxious effects of aminochrome's metabolism. Leukoaminochrome autoxidizes under conditions where superoxide radicals are available. However, the presence of superoxide dismutase in the cytosol prevents this process. From Segura-Aguilar and Paris, 2014⁵¹¹.

The last possible fate of aminochrome is its conjugation with glutathione by means of glutathione S-transferase M2-2, giving rise to 4-S-glutathionyl-5,6-dihydroxyindoline as a product. Similar to that seen with DT-diaphorase, glutathione S-transferase M2-2 prevents aminochrome-induced deleterious effects such as mitochondrial and lysosomal dysfunction^{559,560}, as well as the formation of neurotoxic α -synuclein oligomers⁵⁶¹. 4-S-glutathionyl-5,6-dihydroxyindoline is stable even in the presence of biological oxidizing agents such as oxygen, hydrogen peroxide, and superoxide radicals, suggesting that it is a final elimination product^{562,563}. Interestingly, this enzyme also catalyzes the conjugation of glutathione to DA *o*-quinone to 5-glutathionyl-DA, thus preventing the formation of aminochrome⁵⁶⁴. It is known from L-DOPA and DA biochemistry in melanocytes that all glutathione conjugates undergo degradation of the glutathione moiety (the tripeptide γ -L-Glu-L-Cys-Gly giving rise to a cysteinyl conjugate)⁵⁶⁵. This degradation can also take place in the form of oxidation in the presence of cysteine without glutathione involvement⁵⁶⁶. In the case of 5-glutathionyl-DA, it is converted to 5-S-cysteinyl DA (5SCDA, Fig. 28)⁵⁶⁴.

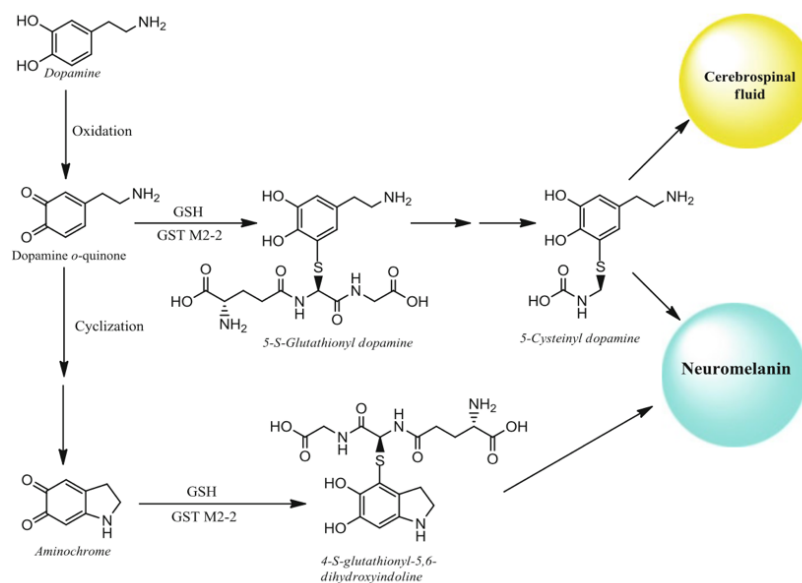


Figure 28. Glutathione conjugation of aminochrome and DA o-quinone. GST M2-2 conjugates aminochrome with GSH giving rise to 4-S-glutathionyl-5,6-dihydroxyindoline, a precursor of NM. This enzyme can also hinder aminochrome's neurotoxicity, preventing its formation by conjugating glutathione with DA o-quinone, ultimately generating 5-cysteiny DA, another precursor of NM. GSH, glutathione; GST M2-2, glutathione S-transferase. From Segura-Aguilar and Paris, 2014⁵¹¹.

Remarkably, 5SCDA has been detected in the cerebrospinal fluid of PD patients (establishing it as a potential biomarker in the early diagnosis of PD), in DA-rich regions of the brain such as the SN, caudate, putamen and globus pallidus, and in NM^{567–570}. Concomitantly, glutathione S-transferase M2-2 also catalyzes the conjugation of dopa o-quinone to 5-glutathionyl dopa, which undergoes the same degradation as its DA counterpart, ultimately leading to the production of 5-S-cysteiny DOPA (5SCD)⁵⁷¹. In addition, Mosca *et al.* hypothesized a possible last autooxidation step involving dihydrobenzothiazine as a product, before the polymerization of 5SCD?⁵⁷². 5SCD, apart from being one of the most widely used biomarkers for melanoma since the groundbreaking work of Ito *et al.*⁵⁷³, was also reported to be excreted in the urine of DOPA-treated PD-patients⁵⁷⁴. Therefore, glutathione conjugation appears to be an evolutionary mechanism to counteract aminochrome neurotoxicity. As will be discussed in the next section, 5SCDA (with 5SCD also likely to be implicated) is the core molecule around which pheomelanin pigment polymerizes⁵⁷⁵, while, in the absence of a cysteine/glutathione-context, 5,6-dihydroxyindole becomes the first building block of eumelanin upon sequential oxidation (Fig. 29)⁵⁷⁶. Thus, the primitive core of NM is a mixed melanogenesis of eumelanin, pheomelanin and different protein-DA adducts as will be discussed in detail in the next section.

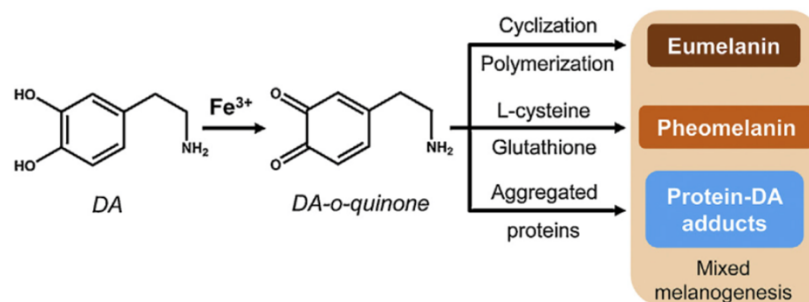


Figure 29. Possible mechanism for the synthesis of NM pigment. Excess DA present in the cytosol can be oxidized to DA *o*-quinone by ferric iron in a catalytic reaction. In the formation of NM pigment, DA *o*-quinone can undergo three different processes: (i) cyclization, further oxidation and polymerization to generate eumelanin; (ii) reaction with L-cysteine or glutathione to produce cysteinyl-DA compounds which are then oxidized to pheomelanin; and (iii) conjugation with protein residues to generate DA-protein adducts. The latter two reactions appear to be faster and lead to the formation of a protein-pheomelanin core, which is then coated by eumelanin. Iron(III) is incorporated into the melanic portion during NM's pigment formation. Modified from Zucca et al., 2017⁵⁷⁷

6.4.3 VMAT2

Monoamines such as DA, serotonin, adrenaline and noradrenaline are packaged by two different 12 transmembrane domain proteins known as vesicular monoamine transporters (VMATs), which are part of the larger solute carrier (SLC) protein family⁵⁷⁸. VMAT1 (SLC18A1) is located predominantly in the periphery and serves to sequester adrenaline, noradrenaline, and serotonin in melatonin synthesizing cells of the pineal gland. VMAT2 (SLC18A2), while being present in peripheral locations such as platelets⁵⁷⁹ and beta cells of the pancreatic islets⁵⁸⁰, is predominantly confined to the central nervous system^{578,581} where it packages several neurotransmitters including DA and noradrenaline⁵¹⁹. VMAT2, as an H⁺-ATPase antiporter, performs a pivotal action by using the vesicular electrochemical gradient to drive the packaging of cytosolic transmitter into presynaptic vesicles⁵⁸². As referred to above, VMAT2 not only packages DA into synaptic vesicles following its synthesis in the cytosol or presynaptic terminal reuptake, but it is also tightly associated with the cycle of production, packaging, storage, release, degradation and recycling of DA^{510,582,583}. Furthermore, as VMAT2's role in DA sequestration is indispensable for the isolation and stabilization of DA, disruptions to VMAT2's functionality implicate dysregulations of DA handling and are potentially linked to disorders such as PD^{584–586}.

6.4.3.1 IMPLICATION OF VMAT2 IN PARKINSON'S DISEASE

Disruption of neurotransmitter vesicle dynamics (transport, storage and release) has been implicated in a variety of neurodegenerative and neuropsychiatric conditions. In a PD-related context, VMAT2-mediated DA vesicular uptake is essential to prepare DA for subsequent release and to prevent its cytosolic accumulation and oxidation into potentially toxic *o*-quinones^{52,587–589}. Interestingly, an inverse relationship exists between NM content and VMAT2 immunoreactivity in human midbrain DA neurons⁵⁹⁰, with neurons exhibiting the highest VMAT2 levels being the ones with the lowest NM levels, and the least vulnerable to PD-linked neurodegeneration. Conversely, the most vulnerable ventral SNpc neurons accumulate the highest NM levels and exhibit the lowest VMAT2 levels⁵⁹⁰.

Solid evidence points to a potentially pathological perturbation of VMAT2 in PD. First, *postmortem* PD brains exhibit decreased VMAT2 expression, which suggests a deficiency in synaptic vesicle DA sequestration⁵⁸⁴. In addition, VMAT2 isolated from the nigrostriatal DA terminals of *postmortem* tissue from PD patients showed an impaired rate of DA uptake, suggesting that, in addition to a loss of VMAT2, the remaining VMAT2 is less efficient at sequestering DA⁵⁸⁶. Furthermore, VMAT2 mRNA is decreased in circulating platelets from PD patients, suggesting that a systemic VMAT2 deficiency is involved in the pathogenesis of PD⁵⁸⁵. Further to this, gain-of-function VMAT2 variants in humans have been associated with a decreased likelihood of developing PD^{591,592}. Accordingly, and in support of these findings, *postmortem* tissue from PD patients demonstrates an upregulated cytosolic DA metabolism as confirmed by an increase in the amount of DOPAC, DOPAL and HVA^{586,593}.

Extensive literature reports had used both *in vivo* and *in vitro* VMAT2 models to investigate the contribution of this transporter to PD development. Most robust VMAT2 modelling strategies include genetic mice used to assess the consequences of systemic VMAT2 deficiency (complete deletion of *VMAT2* is lethal⁵⁹⁴); these have successfully replicated motor and non-motor PD symptoms as well as age-dependent DA neurodegeneration^{595–598}. On the other hand, until recently, the potential benefits of

increased VMAT2 function were restricted to a *Drosophila* model^{599,600}. Over the past decade, several published VMAT2 overexpression studies in rodents have demonstrated neuroprotective effects (displaying concomitantly a lower toxicity of intracellular noxious wastes) including increased vesicular capacity for DA, DA vesicle volume, basal DA levels in STR, DA release, and better performances in both non-motor and locomotor activities^{601,602}. Furthermore, a VMAT2 hypomorphic mouse model displayed enhanced MPTP toxicity⁵⁹⁵, whereas VMAT2-overexpressing models exhibited significant protection from the toxin^{601,602}.

6.4.4 ALTERED DOPAMINE METABOLISM IN PARKINSON'S DISEASE

While a direct link between deleterious physiological events and the onset of motor symptoms is clear, the exact mechanism by which only NM-pigmented DA neurons undergo cell demise in PD remains a conundrum. Several mechanisms have been proposed to be involved in this neurodegeneration, with those dealing with mitochondrial dysfunction and endoplasmic reticulum stress being the stand-out examples. The brain is an organ that relies entirely on chemical energy (ATP) to achieve, among other critical tasks, the release of neurotransmitters such as DA. Therefore, the presence of functional mitochondria is indispensable for DA neurons to complete their main task, namely, trigger DA synapses to initiate movement. Evidence supporting mitochondrial impairment in PD includes deficits in complex I activity in postmortem brains⁶⁰³, complex I and IV deficiencies in the SN of PD patients⁶⁰⁴, the fact that several genes associated with familial forms of PD (i.e. *PRKN*, *DJ-1*, *PINK-1* and *HTRA2*) are linked to mitochondrial dysfunction⁶⁵, energy imbalances caused by *DJ-1* and *PINK1* mutations⁶⁰⁵, and impaired mitochondrial machinery^{606–608} and proper mitochondrial functioning⁶⁰⁹ by α -synuclein.

In a parallel way, PD is characterized, at the neuropathological level, by the aberrant accumulation of misfolded proteins^{610–612}. The presence of misfolded proteins can trigger a stress response in the endoplasmic reticulum called the Unfolded Protein Response (UPR) by which the cell seeks to restore proteostasis upon the toxic build-up of misfolded proteins^{613,614}. In this regard, Hoozemans *et al.* demonstrated that the UPR

activation markers pPERK and pelf2 α were detected in NM-containing DA neurons in the SN of PD patients. Remarkably, pERK did colocalized with α -synuclein⁶¹⁵. Furthermore, transcriptomic analyses of neurons derived from PD patient iPSCs revealed an α -synuclein-induced ER stress phenotype, marked by activation of the IRE1 α /XBP1 axis of the UPR⁶¹⁶. Also, key proteins in PD, such as α -synuclein itself and β -glucocerebrosidase, have been demonstrated to be directly associated with ER stress^{617,618}.

Despite these evident signs of mitochondrial and ER stress impairment, the molecular mechanism(s) by which they are triggered in NM-containing DA neurons is far from being fully understood. Involvement of exogenous neurotoxins such as MPTP⁶¹⁹ and the α -synuclein prion-like hypothesis⁶²⁰ have been postulated as plausible causes, but PD's extremely slow progression and the almost-exclusive death of NM-containing neurons render these hypotheses highly controversial. Therefore, the implication of NM appears to be preponderant in the selective demise of neurons containing this pigment, where an endogenous neurotoxin may be derived from it. In this regard, several highly reactive DA-derived NM precursors have been described that entail harmful consequences for the maintenance of neuronal integrity. For instance, the formation of DA *o*-quinone acts as a DA neuron-specific oxidative stress inducer⁶²¹. It has been described to form adducts with proteins critical for preserving cellular homeostasis, such as glutathione peroxidase-4⁶²², and UCHL-1, as well as with PD-related proteins such as DJ-1, parkin and α -synuclein^{22,623,624}. DA *o*-quinone also reacts with proteins responsible for ensuring mitochondrial function and integrity, such as complexes I, III and V of the electron transport chain, mortalin, mitofilin, and creatine kinase⁶²³. In fact, DA *o*-quinone has been directly associated with mitochondrial dysfunction⁶²⁵.

Further to the above, proteins whose expression is restricted to DA neurons such as TH and DAT, which are involved in the reuptake of DA from the synaptic cleft, are also potential targets of DA *o*-quinone^{626,627}. This quinone has also been reported to damage DNA itself⁶²⁸. Next on the downstream advance of the DA metabolic cascade is the chemically more stable aminochrome, which is the most studied *o*-quinone. It has been

postulated as the principal endogenous neurotoxin compromising neuronal viability due to its pleiotropic and deleterious effects on multiple cell components. In this sense, reactions in which aminochrome plays a potentially harmful role compromising neuronal viability include: α -synuclein aggregation to neurotoxic oligomers^{629,630}, proteasome dysfunction^{631,632}, lysosomal dysfunction^{558,560}, mitochondrial dysfunction^{552,554,633,634}, oxidative stress⁵⁵², inhibition of the fusion of autophagic vacuoles with lysosomes⁵⁶⁰, cytoskeleton architecture disruption^{549,635}, ER stress⁶³⁶ and neuroinflammation^{637,638}. Moreover, the unilateral injection of aminochrome into the rat STR caused generalized neuronal dysfunction⁶³⁹. Other products of DA metabolism that have also been demonstrated to cause neurotoxic effects include 5,6-indolequinone⁶⁴⁰, DOPAL^{593,641,642}, dopaminochrome^{643,644} (a 5,6-dihydroxyindole tautomer and different from aminochrome⁶⁴⁵) and, of course, NM, whose activity will be thoroughly covered in the next section. On the other hand, DOPE has been postulated as a cytoprotective compound in response to oxidative stress in DA neurons⁶⁴⁶. Figure 30 provides a comprehensive summary of the implications of DA metabolites covered in this section.

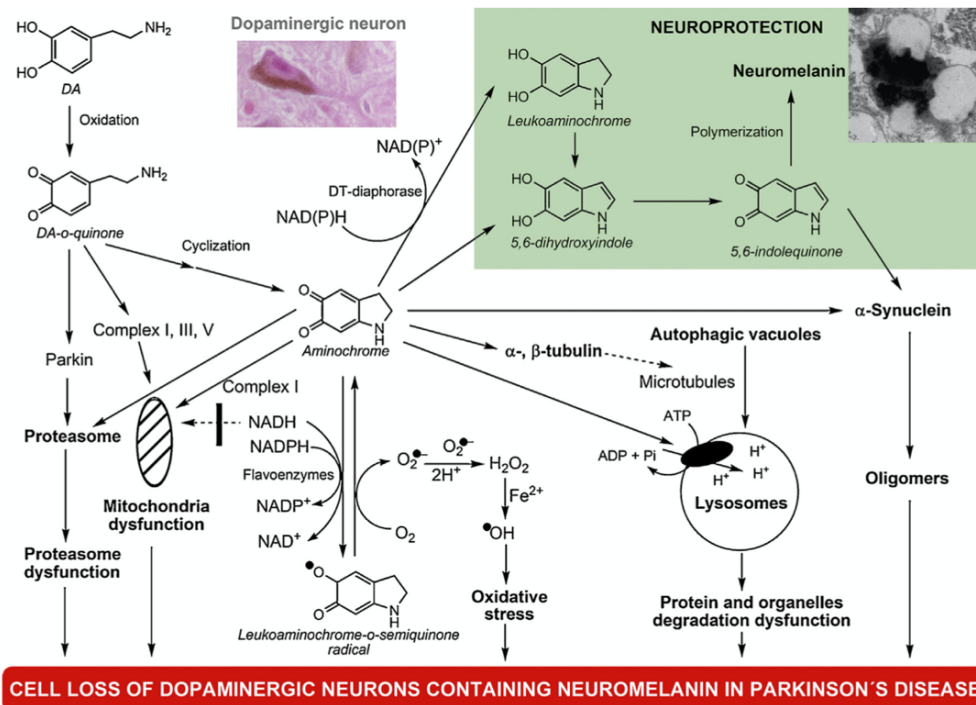


Figure 30. Summary of the multiple fates of DA oxidation to *o*-quinones. From left to right, DA oxidizes to DA *o*-quinone, which in turn can form adducts with parkin, resulting in the impairment of the proteasomal system. DA *o*-quinone can also form adducts with mitochondrial complexes I, III and V, thereby inducing mitochondrial dysfunction, or undergo intramolecular cyclization to aminochrome, which, in turn can: (i) inactivate the proteasome; (ii) inactivate

mitochondrial complex I; (iii) be reduced to the leucoaminochrome-*o*-semiquinone radical, which auto-oxidizes back to aminochrome, thereby generating oxidative stress; (iv) inactivate the vacuolar ATPase proton pump of lysosomes and thereby induce lysosomal dysfunction; (v) induce aggregation of α - and β -tubulin which prevents the formation of microtubules required for the fusion of autophagic vacuoles with lysosomes, thus inducing autophagic dysfunction; and (vi) induce α -synuclein aggregation to neurotoxic oligomers. These neurotoxic reactions of aminochrome can be avoided via aminochrome polymerization to NM or reduction of aminochrome to leucoaminochrome. From Zucca et al., 2017⁵⁷⁷.

6.4.5 MECHANISM OF NEUROMELANOGENESIS

Melanogenesis in mammals takes place within specialized organelles called melanosomes; these have been thoroughly characterized and involve the participation primarily of Tyr, Tyr-related protein 1 and Tyr-related protein 2⁶⁴⁷. Nevertheless, NM production as described above entails an intricate and entangled pathway that is still to be fully described. To arrive at what is currently known, groundbreaking works across the vast melanin research field have been conducted over the past century. In 1927, Raper published a pioneering study on the eumelanin formation pathway, proposing an enzymatic action of Tyr on the substrate tyrosine, resulting in an insoluble, dark-colored compound⁶⁴⁸. Almost 5 decades later, Prota et al. described the formation of pheomelanin after the incubation of tyrosine and Tyr in the presence of cysteine⁶⁴⁹. Interestingly, within the melanosome, melanin production and the ratios of eu- to pheomelanin are primarily regulated by the amount of Tyr present^{650,651}. Nevertheless, despite the reported evidence of Tyr at the mRNA⁶⁵², protein⁶⁵³ and enzymatic activity⁶⁵⁴ levels, as well as results from a microarray experiment (Entrez_id: 705792; NIH Blueprint NHP Atlas) that consistently detected transcripts at low levels, no Tyr protein expression has been detected in the human SN^{655,656}. The apparently conflicting results regarding the presence or absence of Tyr not only in the SN but in the human brain in general, may be attributed to the low levels at which Tyr is actually expressed, thus highlighting the need for adequate methodological approaches for its detection. Further studies are therefore required to confirm or rule out the potential contribution of Tyr or other enzymes to NM synthesis.

As part of intense research efforts, two complementary approaches have been employed to identify the chemical structure and composition of members of the

melanin family. These approaches consist of the mimicking melanogenesis *in vitro*^{657,658} and the analysis of liberated compounds after the degradation of synthetic and naturally occurring melanins^{659–662}. Consequently, groundbreaking findings helped to shape what is known about the actual conformation of NM, with particular focus placed on the melanin core. In this regard, it was revealed that NM exhibits properties of both eu- and pheomelanin^{569,663–665}. Wakamatsu et al. used chemical degradative methods to study the structure of NM in greater depth. They concluded that the melanin moiety in NM consists mainly of DA-derived units with 21-25% incorporation of Cys-DA-derived units, and that DOPA is not incorporated into NM to any significant extent (approximately 6% that of the level of DA)⁶⁶⁶.

Concomitantly, nuclear magnetic resonance (NMR)^{667–671}, matrix-assisted laser desorption/ionization mass spectrometry (MALDI)⁶⁷², X-ray scattering^{673–675}, pyrolysis-gas chromatography/mass spectrometry spectroscopy⁶⁷⁶ and electron paramagnetic (EPR) analysis^{677–679} on NM have been performed, adding valuable data to the body of knowledge concerning NM's specific architecture, such as the presence of peptide and lipid components. Furthermore, over the last two decades, via a combination of optimized proteomics, lipidomics, biochemical, and imaging techniques, robust research in the aging and neurodegeneration fields has progressively shed more light on the composition of NM^{680–685}. During that time, it was confirmed that NM pigment consists of a melanic core to which proteins (not only lysosomal proteins, but also cytosolic and ER proteins) and lipids are bound and which is confined within a cytoplasmic organelle that is surrounded by a double membrane^{686,687}. The first of two pioneering works by Sulzer et al., hypothesized an autophagic origin for NM-containing organelle formation⁶⁸⁶. NM has also been reported to interact with metals, showing a strong affinity for biologically relevant transition metals including iron (the most abundant transition metal), copper, and zinc^{688,689}, which are sequestered by the melanic portion of the molecule during the first steps of the organelle formation process, and maintained in a redox-inactive form⁶⁹⁰. Other metals likely to be sequestered into NM include aluminum, lead, mercury, cadmium, selenium, manganese, cobalt, chromium and molybdenum^{688,689,691,692}. Interestingly, NM binds iron at two sites that differ based on their binding potential, defined respectively as high and low affinity sites⁶⁹³. NM-

bound iron is in the ferric state most of which binds to high affinity sites, probably coordinated by catechol groups (specifically the dihydroxyindole groups) of the melanic component⁶⁹⁴. Previously, the presence of iron in the ferrous state was also reported⁶⁹⁵, where it was speculated that both reducing species were generated during DA autoxidation⁶⁹⁶.

Zucca et al. recently reported the most updated and exhaustive mechanism for neuromelanogenesis gleaned from the results of almost a century of research⁴⁹². This process, which is summarized in figure 31, commences with the oxidation of DA to DA-quinones (or semiquinones) via iron catalysis in the cytosol of an SN neuron. These highly unstable compounds can react with β -structured and aggregated proteins, thereby forming DA-protein adducts. Subsequently, these structures become progressively more complex by the oxidative polymerization of quinones, giving rise to the genesis of melanin-protein complexes, which can bind significant amounts of metals, mainly in the form of iron.

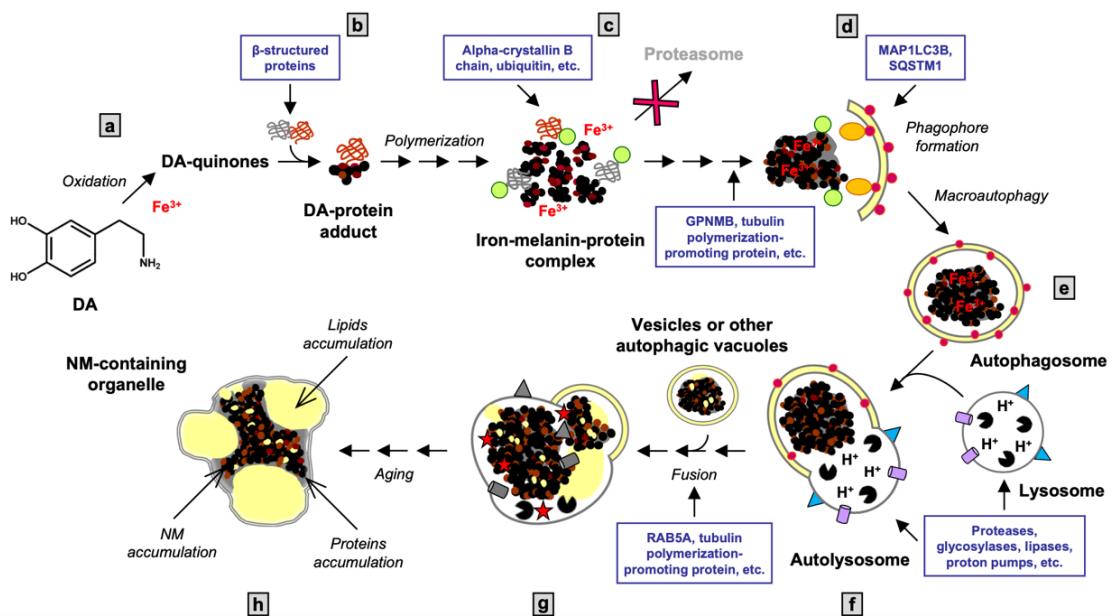


Figure 31. Scheme summarizing hypothesized NM-containing organelle formation in the human SN. Excess DA in the cytosol can be oxidized to quinones by ferric ion. These highly reactive compounds can bind to aggregated and β -structured proteins that accumulate in the cytosol. An oxidative polymerization reaction initiates formation of the melanin-protein component with eumelanin and pheomelanin moieties that can also bind large amounts of metals, particularly iron. Via macroautophagy, the resulting undegradable material is taken into autophagic vacuoles that fuse with lysosomes and other autophagic vacuoles containing lipid and protein components, thus forming the final NM-containing organelles. These contain NM pigment along with metals, abundant lipid bodies, and protein matrix. The process continues during the life of the neuron. Light green circles represent ubiquitin units; red circles represent

MAP1LC3B units; orange circles represent SQSTM1/p62 units; dented black circles represent enzymes; blue triangles represent different membrane proteins; violet cylinders represent proton pumps; red stars represent toxins. Zucca et al., 2018⁴⁹².

The amount of iron in NM isolated from the SN of healthy subjects can reach up to 10 $\mu\text{g}/\text{mg}$ of NM pigment⁶⁹¹. Nonetheless, NM in tissue is not completely saturated with iron and is able to chelate even greater quantities^{679,690}. Strikingly, NM pigment from the SN is able to accumulate up to 55-fold higher iron content compared to tissue concentration⁶⁹¹. During this accumulation process, toxic compounds and drugs may also bind. Furthermore, DA-adducts and proteins altered by misfolding can be recognized and bound by ubiquitin and alpha-crystallin B chain as part of the process to discard damaged and/or misfolded proteins by means of the proteasome system. Nevertheless, it is plausible that ubiquitinated-NM-derived products are too bulky to enter the proteasome and be properly degraded, causing them to accumulate in the cytoplasm. At this step, proteins such as tubulin polymerization-promoting protein and the glycoprotein Nmb may be engaged since they are implicated in the degradation of cellular debris and the formation of aggresome-like structures. Postulated by Gerlach et al. in *post mortem* tissue⁶⁹⁷, simultaneous studies by Double and Zecca confirmed the proteinaceous component of NM^{670,671}. Zecca's study revealed that the peptide component in NM constitutes around 15% of its weight. This already undegradable structure is subsequently isolated into autophagic vacuoles by the phagophore, a double membrane required for macroautophagy, which readily engulfs cumbersome material. This hypothesis is backed by the presence of classical macroautophagic markers such as MAP1LC3B and SQSTM1/p62, and by the visualization of a double membrane structure encompassing the NM-containing organelle. At this stage, autophagic vacuoles become autolysosomes by fusing with lysosomes, as well as different proteins and enzymes such as proteases, glycosylases, lipases, and proton pumps.

After fusing with lysosomes, the NM-derived, undegradable material contained in autophagic vacuoles can interact with other proteins and lipids carried by lysosomes. During this process, typical factors intimately related to PD such as age, degree of NM accumulation, and oxidative stress could markedly compromise lysosomal enzyme efficiency and fusion capacity. These organelles may then fuse with other autophagic

vacuoles containing NM precursors, other vesicles, or with other undegraded NM-containing organelles, etc. As a consequence of this fusion, lipids may accumulate with other undegraded lipids, leading to the generation of lipid bodies. Zecca et al. reported that lipid molecules represented around 20% of NM pigment mass (later adjusted by Engelen et al. to 18%⁶⁸²), while Fedorow et al. concluded that dolichol is the main component of it, representing about 14%^{28,671}. To a lesser extent cholesterol, α -tocopherol, ubiquinone-10, phospholipids, and lactones have been also found to form part of NM^{671,682,698}. Further fusion of these NM-containing organelles is thought to be mediated by tubulin polymerization-promoting protein, microtubule-associated protein tau, RAB5A, and other related proteins. The resulting NM structure comprises ~350 nm granules composed of small spherical substructures of diameter 30 nm⁶⁹¹.

Taken together, the most plausible mechanism for *neuromelaninogenesis* to date suggests that the NM-containing organelle is a macrostructure encompassing diverse components such as different types of melanin, metals, proteins and lipids, which forms as part of a steady process during aging. Eventually, this leads to the accumulation of a non-degradable mixture of constituents in highly-specialized, pigmented “autophagic lysosomes”⁶⁹⁹. Importantly, due to their multifaceted composition, together with oxidized and damaged proteins, these organelles may constitute a reservoir for toxins. In this regard, under cellular stress, these toxins together with NM pigment could be released, thereby promoting neuroinflammation and subsequent neurodegeneration as will be discussed below.

6.5 PHYSIOLOGICAL ROLES OF NEUROMELANIN

As discussed briefly above, the heterogeneous nature of NM has resulted in it has being reported to be involved in both protective and noxious mechanisms for cell fate, depending mostly on the cellular context (Table 4). While extensive literature reports cover this dual facet of NM, the exact circumstances under which it plays a neurotoxic role are still far from being fully elucidated.

Table 4. Summarized duality of roles played by NM in SNpc neurons. The scheme highlights the principal properties of NM described in the literature, underlying its double-edged protective and deleterious roles. *Left*, protective roles of NM achieved by buffering potentially neurotoxic compounds. *Right*, deleterious roles that NM can acquire under certain conditions, as in the context of PD.

Protective roles	Deleterious roles
Remove excess of catecholamines	Iron sequestration + oxidative stress generation
Chelate potentially toxic metals	Releasement of redox active metals and toxic compounds
Quench drugs and organic compounds	Neuroinflammation trigger
	Inducement of immune-based pathogenic mechanisms

6.5.1 PROTECTIVE ROLES

As seen with peripheral melanins, NM appears to have antioxidant and radical scavenging properties that contribute to its capacity to buffer cellular oxidative stress. These functions are of the utmost importance particularly for catecholaminergic neurons, which bear a high oxidative burden derived from reactive DA-derived metabolites^{700,701}, elevated iron levels both in the SN tissue and in NM pigment⁷⁰², and low levels of antioxidant molecules⁷⁰³. In fact, the synthesis of NM has been postulated as an evolutionary antioxidant mechanism to cope with excessive cytosolic quinones and semiquinones by trapping them in an inactive form, thereby evading their neurotoxic properties^{53,686}. Moreover, as discussed above, dihydroxyindole groups of NM are able to chelate a vast array of potentially toxic metals^{665,688,689,704}, in particular redox-active ferric ions, thereby reducing the formation of hydroxyl radicals^{705,706}. Furthermore, NM has been reported as an antioxidant agent that protects against the harmful consequences of lipid peroxidation⁷⁰⁷. NM may play a further chemoprotective role through its ability to sequester damaging molecules such as pesticides (e.g., paraquat⁷⁰⁸), toxic compounds (e.g., 1-methyl-4-phenylpyridinium ion (MPP+)⁷⁰⁹, beta-carbolines⁷¹⁰, and 1,2(N)-dimethyl-6-7-dihydroxyisoquinolinium⁷¹¹) and neuroleptic agents^{712–715}.

6.5.2 DELETERIOUS ROLES

Despite its diverse protective functions, the intrinsic biochemical properties of NM also entail a marked double-edged deleterious component, which has been studied for many decades. NM was postulated as a critical factor underlying neuronal vulnerability in PD^{716–718}. The direct relationship between NM and PD, which will be addressed thoroughly in the next section, was found in a study by Hirsch et al., where they concluded that melanized DA neurons in the SN seem to be differentially susceptible to degeneration in PD⁷¹⁷, with it also being reported that the mean NM content of surviving neurons of the SN in PD patients was less than that of control subjects⁷¹⁹. While this finding suggested a direct relationship between the vulnerability of DA neurons and NM content⁷²⁰, the specific connection and context in which it occurs have yet to be elucidated. In this regard, interesting data concerning the noxious effects of NM have been produced from cell culture experiments. It has been shown that NM impairs the ubiquitin proteasome system via direct inhibition of the 26S proteasome in SH-SY5Y neuroblastoma cells⁷²¹. This inhibition could result in the accumulation of ubiquitinated and denatured proteins in the cytoplasm, thereby severely compromising neuronal homeostasis. A study by the same group also postulated a direct oxidative effect of NM on mitochondria, which would lead to the production of reactive oxygen and nitrogen species⁷²². These studies nevertheless have an important limitation since the direct interaction of NM with cellular organelles or compartments is unlikely to occur due to NM's enveloped nature. Furthermore, cell culture experiments do not fully mimic the physiological conditions occurring in neurons, meaning that the drawing of conclusions should be made with these facts borne in mind.

While the potentially hazardous properties of isolated NM require further investigation in more complex environments such as organoids or 3D-cultures, NM-containing organelles demonstrate a marked neuroinflammatory effect when released into the extracellular space by dying or already dead neurons^{723–725}. This is a typical feature of the parkinsonian SN, where extracellular NM exacerbates neurodegenerative processes by engaging microglial activation. In fact, due to its insolubility, NM has been postulated to remain for long periods in the extracellular milieu, becoming an agent of chronic

inflammation by slowly releasing redox-active metals and toxic components efficiently immobilized within the organelle⁷²⁶. *In vitro* experiments confirmed that microglia are able to recognize human NM and actively phagocytose it, concomitantly releasing neurotoxic mediators such as nitric oxide, interleukin-6, tumor-necrosis factor- α (which is thought to play an important role in mediating neuronal loss⁷²⁷) and interferon- γ ^{728,729}, as well as ROS such as superoxide and hydrogen peroxide⁷³⁰. Interestingly, in the latter study by Zhang et al., it was shown that “young” microglia (10-20 days after plating) exhibited a more efficient phagocytic activity in terms of breaking down NM compared with “aged” microglia (4 weeks). This suggests that extracellular NM remains in tissue and induces a sustained microglial activation that is not fully capable of degrading it. Evidence from *postmortem* PD patient brains along with robust data obtained from different animal models of PD implies that neuroinflammation is a decisive contributor to the pathogenesis of the disease, leading to the massive loss of DA neurons in the SN^{547,730,731}. In this sense, while NM has been reported to activate proinflammatory microglia through a caspase-8-dependent non-apoptotic mechanism⁷³², the exact mechanism underlying neurodegeneration induced by activated microglia has not been completely elucidated, although macrophage antigen complex-1 and phagocytic oxidase seem to play important roles^{730,733}. Further cell culture experiments have shown that, in the absence of microglia, NM does not appear to be toxic per se for neurons^{730,733}.

It is of note that a maintained microglial engagement also takes place in healthy aged subjects presenting with extracellular NM deposits due to an age-related loss of SN pigmented neurons, indicating that NM neurotoxicity is not exclusive to PD⁷³⁴. This observation also suggests a pro-inflammatory action of NM upon release into the extracellular milieu, which is exacerbated in PD due to the massive neuronal demise and concomitant leakage of NM. In addition to activating microglia, NM has been associated with neuronal processes exhibiting swollen neurites, indicative of an ongoing neurotoxic effect⁷³⁰. These pathological processes could take place due to the potential exposure of neurites to the NM pheomelanin core, which has an oxidation potential that is thermodynamically favorable to generating oxidative stress (compared to the eumelanin core which does not)^{577,664}. They could also be due to inflammatory molecules induced by the presence of NM diffusing through brain tissue and acting as chemoattractant

agents for blood leukocytes, including macrophages, thus further exacerbating and spreading inflammation⁷²⁶.

NM has also been reported to cause other inflammation-associated mechanisms that affect other innate immune cells, such as astrocytes⁵⁴⁷ and dendritic cells⁷³⁵. An influence of NM on astrocytes was suggested in a previous study by the Vila group⁵⁴⁷, but has now been confirmed as it will be shown in the results section of the present thesis. Apparently, NM does not induce conformational changes to astrocytes in the same way it does with microglia, but a marked astrogliosis is present in the SN area replete with extracellular NM granules. However, cell culture experiments have suggested that astroglia, in comparison to microglia, do not contribute to the neurotoxic effects of NM⁷³³. Regarding NM-dendritic cell connections, it has been shown that NM is recognized by innate immune cells, thereby triggering their maturation⁷³⁵. Since dendritic cells are antigen-presenting cells known for inducing T- and B-cell responses⁷³⁶, this pioneering study introduced for the first time the hypothesis of a potential adaptive immune response against NM. In fact, in human DA neurons, major histocompatibility complex class I, which is induced by factors released from activated microglia, is highly concentrated in NM granules, suggesting a novel inflammatory T-cell mediated neurodegenerative process that could explain the selective death of NM-containing neurons observed in PD⁷²⁹.

Another deleterious role of NM derives from its iron occupancy levels. As discussed above, NM binds iron at two different locations defined as high and low affinity sites. Most of the iron is usually bound to the high affinity sites, but under certain clinical conditions, such as iron overload for example^{695,737-739}, the high affinity sites can be saturated and iron might also bind to the low affinity sites where it is sequestered in a reactive form and plays a toxic role by promoting redox reactions^{705,740}. In this way, NM plays a protective role under physiological conditions by scavenging potentially toxic iron, whereas a toxic gain of function may manifest for NM under iron overload conditions. This duality in binding iron can also be extrapolated to the other toxic compounds bound by NM since, despite an initial neuroprotective effect, NM may gradually release these into the cytosol under certain conditions^{708,715}. Moreover, if NM

is degraded by ROS^{705,741,742}, leakage of noxious compounds may also occur. In the cited cases, neuronal viability is compromised either directly by the noxious compounds or indirectly via promoting the formation of other ROS^{726,743}. As will be discussed in the next session, this double-edge sword property of NM seems to depend on the subject's age and/or the stage of disease progression, either for PD or any of the clinical conditions encompassed by the parkinsonian syndrome term⁷⁴⁴.

6.6 SELECTIVE VULNERABILITY OF NEUROMELANIN-CONTAINING NEURONS IN PARKINSON'S DISEASE

Although nigral NM-containing neurons and the presence of NM in the extracellular space are thoroughly described PD characteristics, the real agent(s) of change that triggers the conditions themselves, under which NM becomes neurotoxic and cell demise take place, remains elusive to date. At the beginning of the 1960s, Ehringer et al. reported the loss of DA in the STR as the biochemical landmark of PD, thereby explaining the classical motor symptoms and stressing the critical role of DA neurons in PD⁷⁴⁵. Furthermore, related parkinsonian syndromes such as dementia with LB⁷⁴⁶, progressive supranuclear palsy⁷⁴⁷, multiple system atrophy⁷⁴⁸ and corticobasal degeneration⁷⁴⁹ also present pigmented cell loss in the SN, although the pattern of such loss may differ³⁷. Nonetheless, the absence of NM in common animal models^{498,750} and the entangled, multi-origin nature of NM have rendered its research an intricate task, focused mainly on *postmortem* tissue or cell culture experiments. PD's hallmark protein, α -synuclein, is in contrast much easier to study given that it is a single unit forming the core component of LB and exhibits an age-related, ever-expanding presence in diseased patients. Indeed, Braak's fundamental work describing PD as a movement disorder characterized by a progressive neuronal deposition of α -synuclein in different brain regions²⁰, resulted in the scientific community awarding this protein a greater pathological importance over that of NM.

Strikingly, in the majority of regions, abnormal α -synuclein depositions cause only limited neuronal loss, the exception being the early destruction of nigral NM-containing DA neurons^{37,717,751,752}. The biological reason for the early selective vulnerability of DA

neurons remains fundamentally unclear, although valuable literature reports are available in this regard. First, as discussed above, DA metabolism results in the potential generation of toxic derivatives like aminochrome and, ultimately, NM⁵². Again, DA quinones have been shown to interact with and negatively impact the function of mitochondrial complexes I, III and V⁶²³ and other proteins such as tyrosine hydroxylase (TH), DAT and α -synuclein^{626,627}. These reactive by-products have been demonstrated to promote mitochondrial impairment, cause the pathological aggregation of proteins like α -synuclein, and to induce oxidative stress⁷⁵³. Interestingly, increasing the vesicular packaging of DA was shown to concomitantly reduce the susceptibility of DA neurons⁷⁵⁴, whereas down-regulating vesicular packaging entails the opposite effect⁵⁹⁷. Nonetheless, although highly relevant, DA toxicity alone does not fully explain the differential vulnerability of other DA neuron-containing nuclei like the VTA and does not contribute to the potential susceptibility of non-DA neurons in PD. Furthermore, and intriguingly, L-DOPA therapy, the function of which is to increase DA synthesis, does not appear to expedite neuronal loss^{755,756}. Therefore, even if DA toxicity contributes to SNpc DA neuron degeneration, it is certainly not the unique factor driving neurodegeneration in PD.

A second relevant point is that iron content was also postulated as an important contributor to the selective vulnerability of SNpc DA neurons. In normal physiological aging, however, iron is known to accumulate in the SNpc⁷⁵⁷⁻⁷⁵⁹. In this regard, since the mitochondrial electron transport chain relies on iron-sulfur clusters for proper functioning, and given the particularly high bioenergetic demands of DA neurons^{57,760}, increased iron content could, at least in part, underlie an elevated and sustained mitochondrial activity. Furthermore, considering the centrality of mitochondrial impairment in PD, iron might leak from the cell and surpass physiologically normal levels, thereby unchaining oxidative stress processes^{55,761,762}. In a parallel way, iron dyshomeostasis in PD could take place due to increasing amounts of NM chelating iron, thereby rendering it unavailable for proper mitochondrial functioning, despite NM having a much lower affinity for iron than other iron binding proteins such as ferritin²⁶.

Another of the proposed reasons behind nigral DA neuron vulnerability is related to the fact that these neurons demonstrate autonomous pacemaking. This distinctive physiology allows the action potential of these neurons to be slow and broad, thereby maximizing calcium entry and promoting a slow rhythmic activity⁷⁶³. In this sense, Ca²⁺ entry, through specialized Cav1.3 channels⁷⁶⁴, drives a sustained feed-forward stimulation of mitochondrial oxidative phosphorylation^{765,766}. Although these physiological properties help prevent bioenergetic failure when a certain activity threshold needs to be sustained, it may lead to chronic mitochondrial oxidative stress, which, over decades, could compromise mitochondrial function and increase mitophagy, thereby enhancing neuronal vulnerability to other proteostatic stressors like increased α -synuclein levels⁷⁶⁶. Along with a reduction in mitochondrial function with age, a constantly elevated level of oxidative stress has been proposed to be a causative factor in PD cell loss⁷⁶⁷. Remarkably, CaV currents and autonomous pacemaking are also a common feature of LC⁷⁶⁸ and DMNV⁷⁶⁹ neurons, and have also been postulated to be involved in their vulnerability.

Further to the above, the Achilles heel of SNpc DA neurons may rest not only on their unique molecular characteristics, but also their distinctive morphological features⁷⁶⁰. In this regard, cell susceptibility could be derived from the massive scale of their axonal arborization, leading to enormous numbers of axon terminals (it has been estimated that each human nigral DA neuron has over a million neurotransmitter release sites), elevated energetic requirements, and chronically high oxidative stress^{50,760}. The burden of coping with this tremendous bioenergetic load leaves little margin for additional bioenergetic stress for which minor mitochondrial disturbances could entail major consequences^{57,760}. The fact that the ATP requirement for propagation of one action potential grows exponentially with the degree of axonal branching reinforces the notion of axonal arborization as a key susceptibility factor in DA neurons⁷⁷⁰.

Another strong argument supporting this notion is that reducing SNpc DA neuron arborization to a level similar to that of VTA DA neurons (more resistant to PD^{717,771,772}), is enough to significantly reduce basal oxidative phosphorylation and reduce their vulnerability to neurotoxins like MPP⁺ and rotenone⁵⁷. One common aspect between

these hypotheses is that they all suggest that susceptible neurons are exposed to intense mitochondrial/bioenergetic demands. This could alter the oxidative stress response by depleting antioxidants like glutathione, as postulated to occur in PD⁷⁷³⁻⁷⁷⁵. This stress could potentially place neurons in a scenario in which the rate of oxidative phosphorylation required to maintain neurotransmitter release and cellular excitability (approximately half of the oxygen consumed by mitochondria in SNpc DA neurons in these two processes⁵⁷) reduce cellular resources, thereby compromising other key functions such as the degradation of damaged or misfolded proteins, like α -synuclein⁷⁶⁶.

In turn, this could cause preferential dysregulation of axon terminals, triggering a dying back cascade that culminates in cell death⁷⁷⁶⁻⁷⁷⁸. In this regard, axon terminal degeneration seen early in PD, prior to neuronal demise, could be in part an attempt by stressed cells to adapt to such excessively high metabolic needs²⁶. This retrograde process could also produce increased amounts of damaged axonal proteins to manage, conceivably promoting their accumulation in intracellular inclusions. Moreover, since α -synuclein is highly concentrated in axon terminals, it is plausible that retraction of axonal processes in a cell where protein degradation systems are saturated facilitates the creation of pathological aggregates, thereby enhancing cell death. Taken together, these mechanisms contributing to SNpc DA neuron vulnerability might explain why mutations in *GBA*^{779,780} and *PARK*⁷⁸¹⁻⁷⁸⁴ genes, leading to lysosomal and oxidative stress response, and mitophagy and vesicular trafficking defects respectively, are particularly present in different forms of PD. Figure 32 summarizes the main affected regions in PD and molecular features that may result in the specific susceptibility of DA neurons.

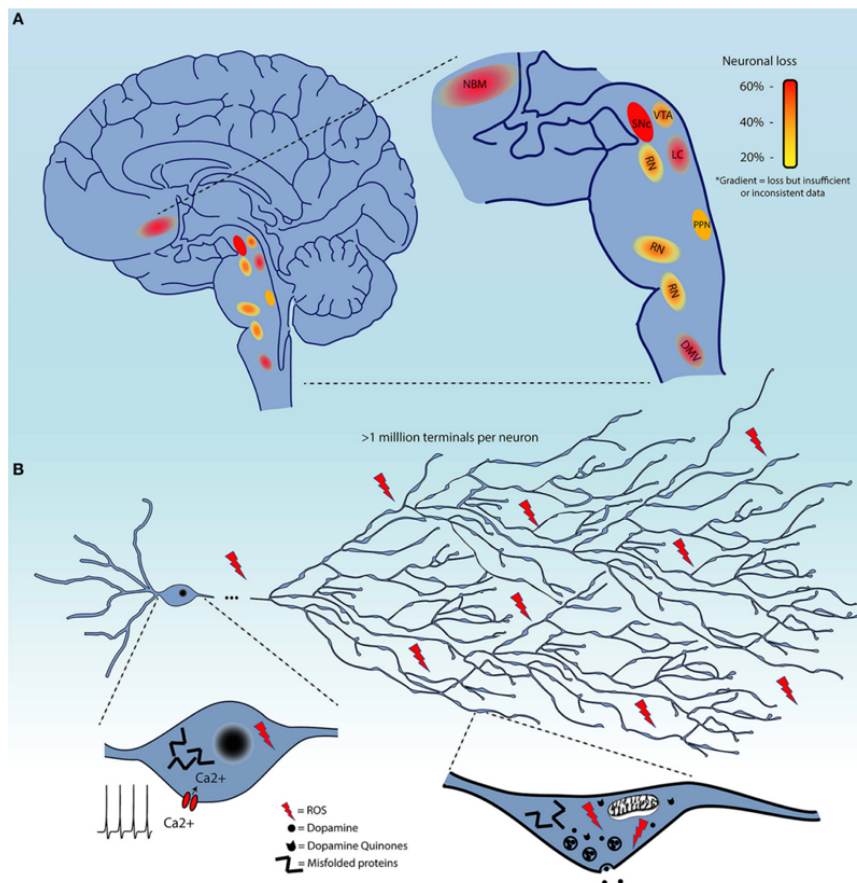


Figure 32. Neuronal vulnerability in PD. A, schematic representation of brain regions demonstrating cell loss in PD. These are color-coded based on the reported loss: red = 60%, orange = 40%, yellow = 20%. Color gradients indicate uncertainty in the extent of this cellular decline. B, summary of different factors implicated in PD's selective vulnerability of DA neurons, including exceptionally large axonal arborization, calcium-dependent pacemaking activity, and elevated levels of oxidative stress.

Despite their relevance to PD, DA neurons are present in numerous brain regions other than the SNpc. Interestingly, DA neurons were first described in the human brain by Dählstom and Fuxe who developed an alphanumeric categorization for the anatomical localization of the different catecholamine cell groups⁷⁸⁵. The most rostral group (i.e., olfactory) is numbered A16, while the most caudal (i.e., lower ventrolateral medulla) is termed the A1 group; as major nuclei involved in PD, DA neurons in the SNpc, which are divided into dorsal and ventral tiers, comprise the A9 group, while noradrenaline neurons in the LC and DMNV belong to the A6 and A2 groups, respectively. Interestingly, ventral tier-located A9 neurons show greater vulnerability to PD-associated degeneration^{37,752,786–788}. It is important to note that, with the exception of adrenaline neurons, catecholamine-containing neurons contain NM, and that those present in the SN show the highest densities of pigment⁷¹⁷. Several studies have tried to shed light on the causes underlying the vulnerability of NM-containing neurons, all of them dealing,

as reviewed extensively above, with the sustained bioenergetic demands and oxidative conditions to which they are subjected.

A noticeable finding is that α -synuclein does not form into LB early in A9 neurons²⁰, but instead are redistributed to the NM lipid moiety⁷⁸⁹. It has also been shown that DA production alone does not confer increased cellular vulnerability in PD as DA neurons in A8 and A10 which neighbor the SN accumulate α -synuclein abnormally *in situ*^{717,790}. Importantly, nigral A9 neurons can be distinguished from other DA and non-DA-containing neurons by their increased NM pigmentation^{53,717,719,720,791}. Furthermore, a study of rat midbrain DA neurons concluded that concerted categorical differences exist in gene expression profiling between DA subpopulations, which could explain their preferential susceptibility to degeneration⁷⁹². Recently, ten different DA neuron populations spatially localized within the SNpc were described; among them, a single subtype marked by expression of the *AGTR1* gene was specifically confined to the SNpc ventral tier and was highly susceptible to loss in PD⁷⁹³.

At this point, it becomes evident that NM plays a preponderant role – if not the principal one – in the enhanced and specific susceptibility of DA neurons to death in PD. Even so, interest in NM research was until recently surpassed by α -synuclein research, but this has changed thanks to robust studies in human PD confirming a direct implication of NM and to animal models focusing on NM that accurately mimic PD⁷⁹⁴.

6.7 NEUROMELANIN IN PARKINSON'S DISEASE

NM levels in PD patients were shown to decrease by up to 60% compared to age-matched controls, due to the loss of NM-containing neurons⁴⁹³. Moreover, the mean NM content in surviving neurons was significantly lower than that of control subjects⁷¹⁹. Paradoxically, other studies have reported that lightly pigmented neurons in PD patients are more vulnerable than heavily pigmented neurons to degeneration⁷⁹¹, thus highlighting an inverse relationship between the amount of NM and the relative vulnerability to PD⁷¹⁷. In this regard, in a recent paper from laboratory, we hypothesized

that PD appears earlier in those subjects that reach a certain pathological threshold of intracellular NM accumulation⁵⁴⁷. Supporting this concept, we found that intracellular NM levels are indeed above this threshold in the brains of PD patients and pre-symptomatic PD subjects (who are included in the incidental LB disease terminology for being autopsied individuals who present LB or LN without having clinical findings of parkinsonism or dementia), whereas age-matched healthy controls were below the threshold.

In this regard, since humans accumulate NM with age, our results in NM-producing animals imply that humans would potentially develop PD if they were to live long enough to reach the pathological threshold of intracellular NM accumulation. Robust literature is available supporting this concept, despite only some individuals actually develop PD (1-5% of the population over 60, increasing with age)¹⁴³: (i) 10-30% of apparently healthy people older than 60 years exhibit PD-type LB pathology in their melanized brainstem nuclei (i.e., ILBD)⁷⁹⁵; (ii) parkinsonian signs such as bradykinesia, stooped posture and gait disturbance are common in elderly individuals, in the absence of overt PD, reaching a prevalence of up to 50% in individuals over 80 years of age^{796,797}; (iii) multiple reports have documented an age-related loss of pigmented nigral neurons, estimated at about 5-10% per decade, in otherwise healthy individuals^{734,798}; (iv) compared to young adult brains, brains from aged individuals commonly exhibit a downregulation of dopaminergic phenotypic markers and α -synuclein accumulations within NM-laden SNpc neurons^{799,800} as well as abundant extracellular NM associated with sustained microglial activation⁷³⁴. Overall, NM-containing neurons from apparently healthy aged individuals exhibit early signs of neuronal dysfunction/degeneration. Whether these changes precede clinical PD or are part of normal brain aging remains to be determined. Based on our results, PD will likely appear in those subjects who have reached a pathological threshold of intracellular NM accumulation.

Another major connector between NM and neurodegeneration in PD is microglia-driven neuroinflammation. As briefly mentioned above, evidence from *postmortem* observations of brain tissue from PD patients and consistent findings obtained from several animal models of PD suggest that neuroinflammation is a leading contributor to

the pathogenesis of PD, causing the demise of DA neurons in the SN. Interestingly, once a direct link between age and PD was established, it was reported that the number of glial cells (including microglia and astrocytes) increases during normal aging of the human brain⁸⁰¹. *In vivo* experiments have shown that injecting NM^{706,730} and hTyr (which induces NM production⁵⁴⁷) into the rat SN induces microglial activation and degeneration of DA neurons. These results are supported by two facts: first, that the SN has been postulated to harbor the highest density of microglia in the brain⁸⁰² and second, that nigral DA neurons have the highest NM content in the brain⁷²⁰. Further to this, neurons containing high concentrations of DA may suffer its potential oxidation to generate reactive/toxic quinones under both low antioxidant⁷⁰³ and iron overload conditions (in tissue as well as loaded into NM)^{686,702}. At this point it is important to stress that during neurodegeneration in PD, released NM concomitantly discharges high amounts of metals and organic neurotoxins accumulated over time, which could further exacerbate microglial activation⁴⁹². Of the released agents, iron, which induces neurotoxicity due to its central role in generating hydroxy radicals (the most harmful reactive oxygen species (ROS))^{803,804}, has been widely implicated in brain aging and reported to play an important role in PD^{702,805}. Since age is the principal risk factor for developing PD, it is important to highlight elements contributing to an increase of total iron concentration with aging; these include altered BBB permeability, inflammatory state, redistribution of iron within the brain, and changes in iron homeostasis^{801,806}.

Interestingly, healthy subjects present a linear increase in SN total iron concentration throughout life, compared to levels in the LC, where it remains stable^{702,807}. In a parallel manner, total iron concentrations also increase in the SN of PD patients, with peak iron levels apparently correlating with disease severity^{695,738,739}. In this regard, the concentration of the NM-iron complex, which is the main iron compound in catecholaminergic neurons, also increases during aging in the SN and LC, being, as discussed above, much higher in the former. In turn, it is not surprising that increased levels of redox-active iron have been described in NM (and LB) from PD patients as well⁸⁰⁸⁻⁸¹¹, being markedly increased in patients displaying the most acute neurodegeneration⁸¹¹. In fact, NM granules from PD patient SN tissue accumulate more iron than is seen in healthy controls^{808,809}. As referred to above, NM can handle

significant amounts of iron under physiological conditions, but when iron overload is present NM starts binding it at the low affinity sites, unleashing the neurotoxic mechanism. In this regard, several factors have been proposed to explain the elevated accumulation of iron in the SN of PD patients and the related vulnerability of DA neurons.

First, two already cited mechanisms, including an increased permeability or dysfunction of the BBB during the disease^{812–814} and an exacerbated pro-inflammatory state^{801,815} (since neuroinflammation has been directly linked to the perturbation of iron homeostasis^{816,817}). And second, a vast array of alterations (including mutations, aberrant expressions and dysregulations) affecting key iron homeostasis maintenance proteins such as transferrin⁸¹⁸, ceruloplasmin^{819–821}, divalent metal ion transporter⁸²², homeostatic iron regulator protein⁸²³ and lactoferrin receptors⁸²⁴. It is worth noting that iron deposits were particularly increased in different cell types of the SN of PD patients (including macrophages, reactive microglia associated with extracellular NM, and astrocytes), demonstrating a marked iron content change in neighboring cells upon the DA neuron degeneration-related release of iron-rich sources such as iron itself, iron-containing-proteins and NM^{825,826}. These findings suggest that, during PD, there is a disturbance of iron homeostasis towards increased levels that exceed the buffering capacities of structures such as NM and ferritins. In turn, the overload of NM with redox-active iron leads to enhanced oxidative stress, which contributes significantly to the selective degeneration of NM-containing DA neurons of the SN.

Continuing with the deleterious consequences of neuronal degeneration in the SN in PD, it is worth considering that inflammatory molecules released from NM-activated microglia may diffuse through brain tissue and induce vascular reactions with the consequent efflux of blood leukocytes including macrophages into the brain parenchyma, further exacerbating the level of neuroinflammation. In this regard, evolution has provided a natural bridge between innate and adaptive immunity, consisting of antigen-presenting cells like macrophages themselves, B cells or dendritic cells that prepare T-cells to target a specific noxious agent. In this sense, it has been reported that NM is recognized by dendritic cells (DCs) *in vitro* and triggers their

maturation⁷³⁵. Moreover, these DCs phagocytize NM pigment and secrete interleukin-6 and tumor necrosis factor- α , in addition to inducing T cell proliferation⁷³⁵. If this process were to be operative *in vivo*, it could explain DC-mediated transport and presentation of antigens from NM, or any of its constituents, or specific combinations of these, to the adaptive immune system, leading to autoimmunity in susceptible individuals. This hypothesis could provide a rationale for an autoimmune-based pathological mechanism of PD, with NM as the initial root cause. However, compared to microglia, the density of DCs in the SN is lower and their response to NM activation is slower, suggesting only a minor role of DCs in PD-associated neuroinflammation and neurodegeneration⁵⁷⁷. In any case despite their potential critical role in the establishment of a long-lasting PD neuroinflammation milieu, scarce research in this field has been conducted. On the other hand, NM's influence on adaptive immunity has gained relevance in the past decade.

Remarkable advances have been made from studying adaptive immunity in PD and associations with NM. Cebrián and colleagues described MHC-I expression by SN DA and LC noradrenaline-containing neurons in human *postmortem* samples from adult control individuals and PD patients, indicating that they can be included in the category of antigen-presenting cells⁷²⁹. It is of note that protein oxidation has been suggested to provide an alert signal that induces MHC-I expression⁸²⁷ and, as mentioned above, DA-derived oxidative stress is associated with neurodegenerative diseases such as PD¹⁴. Interestingly, Cebrián's study reported MHC-I expression in NM-containing neurons (being clearly present in NM-containing organelles), both in control and in PD samples, while it was negligible in non-pigmented neurons, microglia and astrocytes. Notably, they also reported that MHC-I expression can be induced in cultured DA murine neurons by factors released from NM-activated microglia or by high cytosolic DA levels and related oxidative stress.

Further to the above, MHC-I components were detected both in NM-containing organelles and purified NM. In contrast, no MHC-II was ever observed in neurons or in any NM sample. In this regard, MHC-I could bind antigenic peptides derived by cleavage of foreign or native proteins and present them to the neuronal surface, potentially

triggering cytotoxic CD8⁺ lymphocyte responses and subsequent cell demise. Intriguingly, the presence of large numbers of both CD8⁺ and CD4⁺ infiltrating lymphocytes was detected in the human SN in close proximity to NM-containing neurons, this effect being particularly enhanced in PD^{828,829}. Moreover, CD4⁺ and CD8⁺ lymphocyte activation was detected in the cerebrospinal fluid of PD patients⁸³⁰, with these cells reported to recognize α -synuclein⁸³¹.

It seems plausible therefore that neurodegeneration in PD can be triggered by the excessive accumulation of NM and is propagated by an innate immunity-driven initial neuroinflammatory process induced by released NM. This process could be exacerbated by adaptive immunity-orchestrated events specifically targeting NM-containing neurons, and likely to be involved in self-perpetuating noxious yet undescribed mechanisms that accentuate progression to cell death.

6.8 NOVEL NEUROMELANIN-ACCUMULATING PARKINSON'S DISEASE ANIMAL MODEL

Despite the myriad of different PD models, all of them lack the unique characteristic of progressiveness displayed by PD patients. Furthermore, as it will be discussed later, of all the available PD animal models, only non-human primates present NM in an innate manner. In this regard, at the time of preparation of this thesis, only two animal models mimic human PD in the classical, progressive manner of disease development. The first of these demonstrates that disrupting mitochondrial complex I induces age-dependent parkinsonism⁸³² while the second one, developed in our laboratory, shows that overexpressing hTyr results in both NM production and an advancing PD-like disease development⁵⁴⁷. While several studies have injected human purified NM into animals in order to shed light on NM's functionality^{730,731}, our model is the only one using NM as a model agent. Remarkably, it recreates a humanized PD-reminiscent environment displaying ideal features to delve into molecular basis of PD and to study the feasibility of any NM-modulating therapeutic approach to fight the disease. Since it constitutes the main core of this thesis it is worthwhile to review its principal characteristics and advantages for modelling PD.

As stated before, the mechanism of synthesis of NM is poorly understood, but there is reported evidence of tyrosinase activity in human SNpc. Furthermore, apart from being the principal actor in the enzymatically-driven biosynthetic pathway of the synthesis of peripheral melanins, Tyr is able to oxidize the catechol ring of DA, which is an essential step required for NM synthesis⁸³³. Therefore, we hypothesized that, by overexpressing hTyr, NM could be in fact synthesized and gradually accumulated. However, prior to this PD model, it was not known whether brain Tyr could actually contribute to neuromelanogenesis. Strikingly, a single injection to the SNpc of rats with an AAV vector expressing hTyr resulted indeed in an age-dependent production and accumulation of NM-like pigment (henceforth referred to as NM) that was almost undistinguishable from human NM⁵⁴⁷ (Fig.33). *De novo* synthesized NM could be appreciated initially as a darkened area in the SNpc; this could be detected with different techniques as for the detection of human NM. The NM accumulates over time in SNpc DA neurons until occupying most of their cytoplasm, attaining levels consistent with those seen in elderly humans. Moreover, the NM was encapsulated within autophagic structures associated with lipid droplets as seen in human NM, and was also able to chelate metals⁵⁴⁷. Furthermore, this one-of-a-kind PD model managed to recapitulate the main pathological PD features, including hypokinesia, LB-like inclusion formation, and nigrostriatal degeneration⁵⁴⁷.

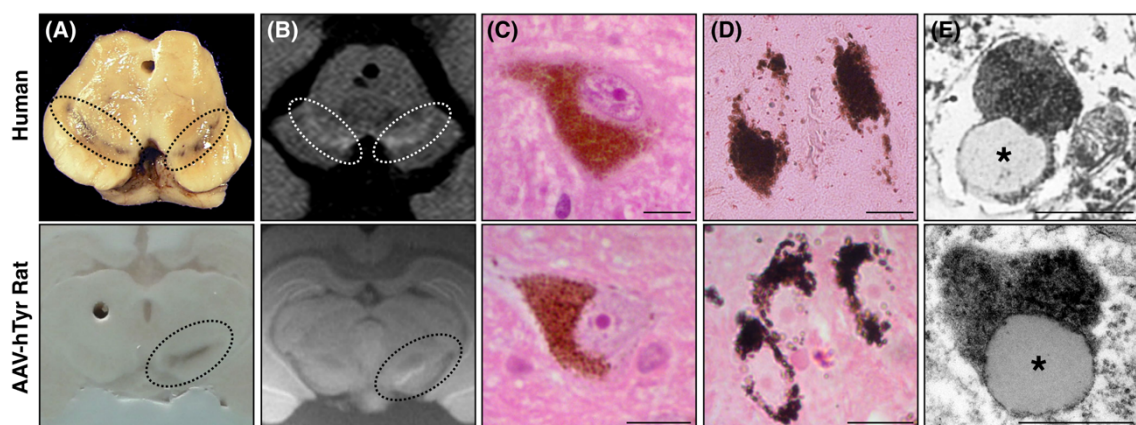


Figure 33. Human-like NM production in tyrosinase-overexpressing rats. Representative images from elderly human control brains (top) and brains from rats unilaterally injected with an adeno-associated viral (AAV) vector expressing hTyr above the right SNpc. Both species exhibit analogous NM production from a macroscopic (A, B), microscopic (C, D) and ultrastructural (E) point of view. (A), unstained midbrain (dashed outline, melanized SNpc); (B), NM-sensitive magnetic resonance imaging (dashed outline, melanized SNpc); (C) Hematoxylin-eosin staining; (D) Masson-Fontana staining; (E) electron microscopy (NM, electron dense matrix; asterisks, associated lipid droplets). From Vila, 2019⁸³⁴.

In parallel to DA cell death, the treated animals exhibited other neuropathological features typical of *postmortem* PD brains, comprising extracellular NM released from dying or already dead neurons, perivascular NM resulting from the migration of NM-filled microglia to blood vessels in an attempt to remove extracellular NM, and neuronophagic events (i.e., activated microglia surrounding NM or being in direct contact with it) indicative of an ongoing neuroinflammatory process⁵⁴⁷. Moreover, NM-filled neurons from these animals also mimic early signs of neuronal dysfunction similar to those occurring in PD patients, including a phenotypic loss of TH expression, impaired DA release, axonal swelling, and decreased striatal levels of DAT, all of which were accompanied by early motor deficits in these animals⁵⁴⁷.

Interestingly, advent of the AAV-hTyr-overexpressing animal model allows the build-up of NM to a specific threshold to be defined (as in the human situation described above), above which neuronal functionality is compromised and degeneration commences⁵⁴⁷. In fact, while intracellular NM levels appear above this particular pathological threshold in *postmortem* brains of both PD patients and pre-PD individuals (i.e., incidental LB disease, which describes a condition where clinically healthy individuals exhibit LB at autopsy and are thus considered to represent early, presymptomatic PD), NM levels remain below this threshold in brains from age-matched, healthy individuals⁵⁴⁷. This pathological limit is not only adaptable to human conditions, but the progression of NM accumulation can also be stratified in PD different stages. In this regard, nigrostriatal denervation at 4 months in our animal model is comparable to that seen in early PD patients (<10 years of disease evolution), while by 2 years the extent of denervation in rats reaches equivalent amounts to those observed in advanced PD patients (> 20 years of disease evolution)^{547,800}.

The occurrence of neuronal dysfunction before evident cell death may entail important therapeutic possibilities, as it provides a therapeutic window in which neuronal functionality could be potentially restored prior to neuronal demise (Fig.34). To this end, PD-like inclusion body formation in hTyr-overexpressing rodents, including both LB-like structures and their supposed precursors (pale body-like inclusions), are exclusively found within NM-containing neurons, peaking at the time of early dysfunction and being

substantially reduced once degeneration of the neurons has occurred⁵⁴⁷. This is another remarkable finding comparable to human development of the disease, where the number of neuronal inclusions in PD brains at advanced stages of the disorder is markedly lower than that observed in early PD brains²⁰. In this regard, it has been postulated that inclusion-containing neurons are those ultimately becoming dysfunctional and undergo preferential degeneration⁸³⁴. Consistent with this hypothesis, neuronal inclusion formation in both humans⁸³⁵ and hTyr-overexpressing animals⁵⁴⁷ is usually associated with TH downregulation, which is an indicator for DA neuronal dysfunction at early stages of neurodegeneration⁷¹⁷.

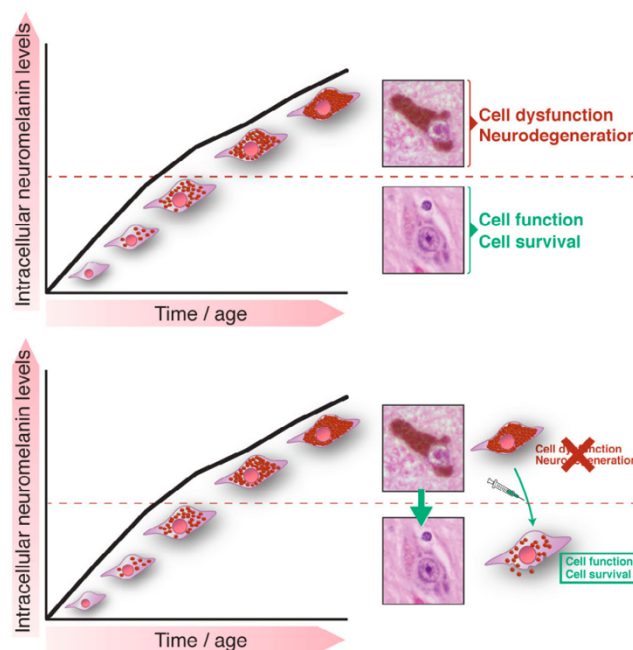


Figure 34. Physiologic and therapeutic implications of a potential pathological threshold of intracellular NM accumulation in DA neurons. *Top*, age-dependent intracellular NM accumulation in human hTyr-overexpressing rodents is associated with PD-like neuronal dysfunction and subsequent degeneration when a certain threshold is surpassed (dotted red line)⁵⁴⁷. *Bottom*, therapeutic strategies aimed at reducing intracellular NM levels below the pathological threshold should avoid, halt, or delay neuronal dysfunction and subsequent degeneration linked to both physiological brain aging and PD. From Vila, 2019⁸³⁴.

To sum up this literature review, the unprecedented use of Tyr for modelling PD constitutes one of the most robust models recapitulating the principal features of the disease. Namely, h-Tyr-overexpressing animals present progressive NM production and accumulation that drives neuronal dysfunction once a specific threshold is reached, ultimately leading to neuronal demise. Furthermore, the model serves as a unique experimental tool that will enable the possible effects of NM generation and

accumulation on neuronal function and viability to be assessed. In this sense, the value and validity of the NM-synthesizing model were already shown in the same publication demonstrating that lowering NM levels below the pathological threshold reduced PD-like inclusion formation, attenuated nigrostriatal neurodegeneration, and alleviated hypokinesia⁵⁴⁷. These results showed the feasibility and therapeutic potential of modulating intracellular NM levels *in vivo*. To develop these ideas in more detail, the present thesis will further assess the robustness of the clinical translatability of these outcomes by presenting two independent and novel approaches aimed at therapeutically diminishing NM levels, with the global target of reducing motor symptomatology.

Taking into account the scarcity of research addressing the involvement of NM in the initiation and propagation PD, we recently postulated that NM-induced cell-autonomous neurotoxic mechanisms may include, among other processes, autophagic dysfunction, reduced mitochondrial respiration, and impaired neurotransmission (Fig. 35)⁸³⁶.

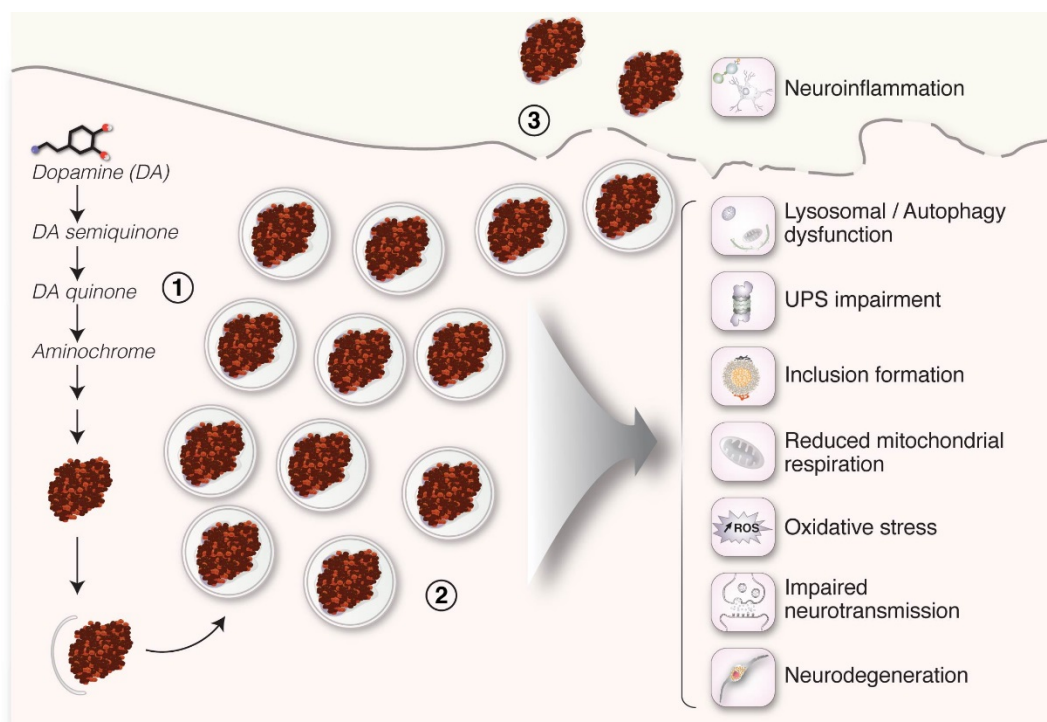


Figure 35. Molecular mechanisms of NM-linked neurotoxicity. (1) DA oxidation entails the generation of *o*-quinones, which can be potentially toxic to neurons. However, the continuous conversion of these oxidized DA species into NM prevents their pathological accumulation in the cytoplasm, consistent with the antioxidant role of NM synthesis. (2) The continuous build-up of NM within undegraded lysosomal-autophagic structures, until they occupy most of the neuronal cytoplasm, may physically interfere with intracellular trafficking/communication and ultimately exhaust the

vesicular storage capacity of the cell, leading to a general failure of cellular proteostasis accompanied by lysosomal/autophagy dysfunction, ubiquitin-proteasome (UPS) impairment, intracellular inclusion body formation, reduced mitochondrial respiration, increased production of reactive oxygen species, impaired neurotransmission, and ultimately leading to neurodegeneration. (3) Extracellular NM released from dying neurons or leaked during phagocytic processes of dead neurons activates microglia that phagocytize this pigment (i.e., neuronophagia) and may trigger an antigenic response able to induce a selective T cell-mediated cytotoxic attack against NM-laden neurons, potentially contributing to the progression of neurodegenerative processes. From Vila, 2019⁸³⁴.

Remarkably, all of these pathological changes are observed both in NM-producing hTyr-overexpressing animals and in PD patients⁵⁴⁷. In this regard, the present dissertation suggests a leading role for NM in the etiopathogenesis and progression of PD, thereby constituting a paradigmatic change where α -synuclein is no longer the principal focus of research attention. Two potential therapeutic strategies are proposed whose aim is to reduce NM levels below the pathological threshold to preserve neuronal integrity and survival.

II. HYPOTHESIS AND OBJECTIVES

GENERAL HYPOTHESIS

The main aim of this study is to open the therapeutic window for modulating NM levels *in vivo* within the framework of PD. This project lays the foundation of a new concept to treat the disease by maintaining or decreasing intracellular NM levels below their pathological threshold, to prevent, halt or delay PD-like neuronal dysfunction and degeneration. In this regard, two different strategies are presented to shape the core structure of this study. In this regard, the specific objectives on which this project rests are:

OBJECTIVE 1. Therapeutic reduction of intracellular NM production by enhancement of dopamine's vesicular encapsulation with VMAT2

HYPOTHESIS 1. Enhancement of dopamine's vesicular encapsulation by VMAT2 overexpression in NM-producing animals will decrease readily available cytosolic DA and DA-derived toxic species that are normally converted to NM. This strategy will slow down the age-dependent intracellular buildup of NM, thus delaying or preventing NM levels from reaching their pathological threshold.

To assess the molecular and motor consequences of VMAT2 overexpression in a NM-accumulating PD rat model as a possible strategy to prevent, delay or attenuate PD pathology. This first global aim can be subdivided into the following specific objectives:

- a) To study DA's metabolism in AAV-hTyr-injected animals upon VMAT2 overexpression
- b) To evaluate NM levels, both intra- and extracellularly in AAV-hTyr-injected animals upon VMAT2 overexpression
- c) To analyze neuronal integrity in the SNpc in AAV-hTyr-injected animals upon VMAT2 overexpression

- d) To assess the inflammatory milieu in AAV-hTyr-injected animals upon VMAT2 overexpression
- e) To determine the status of striatal fibers and striatal DA levels in AAV-hTyr-injected animals upon VMAT2 overexpression.
- f) To appraise the magnitude of motor impairment in AAV-hTyr-injected animals upon VMAT2 overexpression.

OBJECTIVE 2. Therapeutic clearance of NM with tFUS

HYPOTHESIS 2. Treatment of NM-producing animals with tFUS will decrease intra- and extracellular NM levels by a direct (i.e., mechanical/thermal NM fragmentation) effect, thus maintaining or decreasing NM levels below their threshold.

To investigate the biological effects of tFUS application in a NM-accumulating PD rat model as a potential, non-invasive therapy to prevent, delay or attenuate PD pathology. This second global purpose can be subdivided into the following specific goals:

- a) To evaluate tissue integrity upon tFUS application to confirm the biosafety for routine experiments in rats with the implemented protocol
- b) To analyze the effect of tFUS application on both intra- and extracellular NM levels and their characteristic features in AAV-hTyr-injected animals.
- c) To rate the inflammation status of AAV-hTyr-injected animals following tFUS application
- d) To assess neuronal integrity in the SNpc and striatal fibers of AAV-hTyr-injected animals upon tFUS application
- e) To determine the extent of motor impairment in AAV-hTyr-injected animals upon tFUS application

III. MATERIALS AND METHODS

1. MATERIALS

1.1 COMPOUNDS AND REAGENTS

Compound/Reagent	Manufacturer
3-MT	Sigma
3-MT	Sigma
5SCD (350 μ M)	Donated by Professor Kazumasa Wakamatsu and Professor Shosuke Ito at the Fujita Health University in Aichi, Japan
5SCDA (367.65 μ M)	Donated by Professor Kazumasa Wakamatsu and Professor Shosuke Ito at the Fujita Health University in Aichi, Japan
Aminochrome	Sigma
Ammonium acetate (5M)	Applichem
Baytril® (enrofloxacin)	Bayer
Benzonase	Novagen
Bonewax	Ethicon
Bovine serum albumin	Sigma
DA hydrochloride	Sigma
DA-d4 hydroxychloride	Sigma
DAKO® Cytomation fluorescence mounting medium	Agilent Technologies
DOPA	Sigma
DOPAC	Sigma
DPX mounting medium	Sigma
Ethanol absolute	Sigma
Gadolinium contrast medium	Dotarem
GLUture Tissue adhesive	Zoetis
H ₂ O ₂	Sigma
Heparine (25000 IU/5mL)	Choay
Heparine (5000 IU/mL)	Rovi
Hexane	Sigma
Isofluorane	Baxter
KH ₂ HPO ₄	Sigma
LC-MS grade methanol	ThermoFisher Scientific
Meloxicam	Boehringer Ingelheim
Methanol	ThermoFisher Scientific
MS grade formic acid	ThermoFisher Scientific
Na ₂ HPO ₄	Sigma
NaCl	Sigma

NaCl irrigation solution (0.9%)	Dechra
Neo-Predef with tetracaine antibiotic and anti-inflammatory powder	Zoetis
Normal Goat Serum	Vector Laboratories
Paraformaldehyde Solution (4%)	ThermoFisher Scientific
Poly-D-Lysine hydrobromide	Merck
Polyethylene glycol	Sigma
Polyethylenimine	Sigma
Potassium periodate	Acros Organics
Proteinase K	Sigma
Sodium citrate	Sigma
Sucrose	Sigma
Synthetic melanin	Sigma
Tris-base	Sigma
Triton X-100	ThermoFisher Scientific
Ultrasound (acoustic) gel	Konix
Versylene® H ₂ O	Fresenius
Xylene	Sigma

1.2 KITS

Kit	Manufacturer
Pierce® DAB Substrate Kit	ThermoFisher Scientific
Ultra-sensitive ABC Peroxidase Staining Kit	ThermoFisher Scientific
Vector® SG Substrate Kit, Peroxidase	Vector Laboratories

1.3 BUFFERS AND SOLUTIONS

Buffer/Solution	Recipe
1 µM 3-MT dilution	2.0 3-MT + 1 µL formic acid dilution
100 µM ammonium acetate buffer dilution (100 mL)	2 µL 5 M Ammonium acetate buffer dilution in 100 mL H ₂ O (pH 5.8)
2 mM potassium periodate dilution (15 mL)	6.9 mg in 15 mL 100 µM ammonium acetate buffer dilution
25 mM formic acid dilution	1.05 mL MS grade formic acid in 1 L H ₂ O
250 mM formic acid dilution	10.5 mL MS grade formic acid in 1 L H ₂ O
3 µM DA dilution	1.9 mg DA + 1 µL formic acid dilution
3 µM DA-d4 dilution (internal standard)	1.9 mg DA-d4 + 1 µL formic acid dilution
3 µM DOPAC dilution	1.7 mg DOPAC + 1 µL formic acid dilution
3 µM L-DOPA dilution	1.9 mg L-DOPA + 1 µL formic acid dilution
ABC reagent	4 drops Reagent A to 10 mL TBS 1x + 4 drops of Reagent B

Baytril® (5 mg/mL)	2.82 Baytril® mL + 10 mL 0.9% NaCl irrigation solution
Blocking solution (2%) (200 mL)	4 mL NGS + 196 mL
Blocking solution (5%) (200 mL)	10 mL NGS + 190 mL
Endogenous peroxidase blocking solution (200 mL)	6 mL H ₂ O ₂ + 20 mL methanol + 174 mL TBS 1x
Ethanol 70% (200mL)	140 mL ethanol absolute + 60 mL H ₂ O
Ethanol 95% (200 mL)	190 mL ethanol absolute + 10 mL H ₂ O
Internal standard Mix2 (1 mL)	48 µL DOPAC dilution + 952 µL formic acid dilution
Internal standards Mix1 (1 mL)	48 µL DA dilution + 48 µL L-DOPA dilution + 80 µL 3-MT dilution + 96 µL aminochrome dilution + 728 µL formic acid dilution
Internal standards Mix3 (100 µL)	4.6 µL 5SCD dilution + 4.3 µL 5SCDA dilution + 91.1 µL formic acid dilution
Meloxicam (0.5 mg/mL) (10 mL)	1 mL meloxicam + 9 mL 0.9% NaCl irrigation solution
PBS (10x)	Na ₂ HPO ₄ 17.8 g + KH ₂ HPO ₄ 2.4 g + NaCl 90g in 1L H ₂ O (pH 7.4)
PBS (1x)	100 mL PBS 10x + 900 mL H ₂ O
PBS-Triton X-100 (0.2%) (1L)	200 µL Triton X-100 + 980 mL PBS 1x
Pierce® DAB developing solution	1 drop of DAB chromogen solution (10 x) to 1 mL Stable Peroxide Substrate Buffer
Poly-D-Lysine (0.1 mg/mL) solution	500 µl poly-D-lysine + 49,5 mL H ₂ O
Sodium citrate buffer 10mM (1 L)	2.94 g sodium citrate in 1L H ₂ O (pH 6.0)
Sucrose solution 30 % (1L)	30 g sucrose in 1 L H ₂ O
TBS 10x (1 L)	Tris base 121.1g + NaCl 90g in 1L H ₂ O (pH 7.4)
TBS 1x (1 L)	100 mL TBS 10x + 900 mL H ₂ O
Vector® SG developing solution	3 drops reagent 1 (chromogen) in 5 mL PBS + 3 drops reagent 2 (H ₂ O ₂)

1.4 PRIMARY ANTIBODIES

Antigen	Dilution	Manufacturer	Reference	Application
CD68	1:100	Serotec	#MCA341R	IHC
Flag	1:1000	Sigma	#F3165	IHC
GFAP	1:1000	Sigma	#G3893	IHC
Iba-1	1:1000	Wako	#019_19741	IHC
TH (SN)	1:40000	Calbiochem	#657012	IHC
TH (Str)	1:3500	Calbiochem	#657012	IHC
VMAT2	1:500	Progen	#16085	IHC
P62	1:500	Progen	#GP62-C	IF
TH	1:1000	Calbiochem	#657012	IF

1.5 SECONDARY ANTIBODIES

Type (origin)	Dilution	Manufacturer	Reference	Application
Anti-mouse (goat)	1:1000	Vector Laboratories	#BA-9200	IHC
Anti-rabbit (goat)	1:1000	Vector Laboratories	#BA-1000	IHC
Anti-guinea pig Alexa 488 (goat)	1:1000	ThermoFisher Scientific	#A-11073	IF
Anti-rabbit Alexa 594 (goat)	1:1000	ThermoFisher Scientific	#A-11012	IF
Anti-rabbit Alexa 647 (donkey)	1:1000	ThermoFisher Scientific	#A32795	IF

1.6 STAINS

Type (origin)	Dilution	Manufacturer	Reference	Application
Hoechst 33342	1:10000	ThermoFisher Scientific	#H3570	IF

1.7 EQUIPMENT

Equipment	Manufacturer
0.2 µl – 2 µl pipette	Gilson
1 µl – 10 µl pipette	Gilson
100 µl – 1000 µl pipette	Gilson
11.7 MRI	Bruker Biospec
2 µl – 20 µl pipette	Gilson
20 µl – 200 µl pipette	Gilson
Acquity UPLC system	Waters
Acquity® HSS T3 column	Waters
Acquity® HSS T3 VanGuard pre-column	Waters
AX10 Lab A1 microscope	Zeiss
AxioCam ERc5s camera	Zeiss
AxioCam MRc	Zeiss
AxioCam MRc camera	Zeiss
Borosilicate glass capillary	Hamilton
Class II biological safety cabinet A	Telstar
Coated suture	Ethicon
CryoPure® Tubes	Sarstedt
Ductless fume hood	Esco Technologies
Eppendorf® 0.5 mL	Eppendorf
Eppendorf® 1.5 mL	Eppendorf
Eppendorf® 2.0 mL	Eppendorf
Falcon 15 mL Conical Centrifuge Tube	ThermoFisher Scientific

Falcon 50 mL Conical Centrifuge Tube	ThermoFisher Scientific
FUS transducer	Imasonic
Glass cover slip	Leica
Handscope HS5 Numerical oscilloscope	Tiepie Engineering
Heated circulating water bath	Grant Instruments
Hemostat	ThermoFisher Scientific
Hemostatic pean forceps	ThermoFisher Scientific
Heraeus Labofuge 400R Centrifuge	ThermoFisher Scientific
High Speed Drill	Freedom
Imager.D1 microscope	Zeiss
ImmEdge® hydrophobic barrier pen	Vector Laboratories
Kimwipes® wipes	Kimtech Science
LSM 980 with Airyscan laser scanning microscope	Zeiss
NanoDrop 2000	ThermoFisher Scientific
Needle hydrophone HNC 400	Onda Corporation
Norelco Multigroom 3000 Trimmer	Phillips
Noris Pencil – H	Staedtler
Ostro® 96-well plate	Waters
Paintbrush	Leica
Pannoramic 250 Flash III	3D Histech
Paraffin block holders	Leica
Perfection V750 Pro scanner	Epson
Peristaltic pump	Watson Marlow
Polytron® Homogeneizer	Kinematica
Rotary microtome	Leica
Scalpel	ThermoFisher Scientific
Scissors	ThermoFisher Scientific
StainTray® Slide Staining Systems	Simport Scientific
Stereotaxic set-up	Kopf Stereotaxic Instruments
Superfrost Ultra Plus® microscope slides	Menzel Gläser
SW23 shaking water bath	Julabo
Syringe	Hamilton
Tweezers	Excelta
U-shaped coil	IGT
Ultrasonic cleaner	Branson
Water bath	Leica
Xevo TQ-S triple quadrupole mass spectrometer with electrospray ionization interface	Waters
Zeiss Imager.D1	Zeiss

1.8 SOFTWARE

Software	Developer
Aiforia Create (Version 5.1)	Aiforia Technologies Plc
CaseViewer	3D Histech
GraphPad	Dotmatics
Image J	NIH
MassLynx V4.1	Waters
MATLAB	Mathworks
MBF Bioscience StereoInvestigator 11	Micro Brightfield
NanoDrop 2000	ThermoThermoFisher Scientific
PCD controller software	IGT
Photoshop Illustrator	Adobe
Sigma Scan software	Sytate Software
Statistical Parametric Mapping 12	The Wellcome Centre for Human Neuroimaging
Thermoguide software	IGT
Zen	Zeiss

2. METHODS

2.1 ANIMAL HANDLING

Adult male Sprague-Dawley rats (Charles River) were housed two or three per cage with *ad libitum* access to food and water and exposure to a 12 h light/dark cycle. All experimental and surgical procedures were conducted in strict accordance with the European Directive (2010/63/UE) and Spanish regulations (Real Decreto 53/2013; Generalitat de Catalunya Decret 214/97) concerning the protection of animals used for experimental and other scientific purposes. Ethics approval was provided by the Vall d'Hebron Research Institute (VHIR) Ethical Experimentation Committee. While housed at the Centre de NeuroImage de Recherche (Paris, France), animals were subjected to experimental and surgical procedures in accordance with French regulations (APAFIS #18700). Rats were randomly distributed into the different experimental groups, with control and experimental groups processed at the same time' to minimize bias.

2.2 VIRAL VECTOR PRODUCTION

Recombinant AAV (rAAV) vector serotype 2/1 expressing hTyr cDNA driven by the cytomegalovirus (CMV) promoter (AAV-hTyr; concentration 2.6×10^{13} gc/mL) and AAV serotype 2/9 containing human VMAT2 cDNA fused to 3 Flag epitopes under control of the CMV promoter (AAV-hVMAT2; concentration 7.2×10^{12} gc/mL) were produced at the Viral Vector Production Unit of the Autonomous University of Barcelona. Briefly, rAAV vectors were produced by triple transfection of 2×10^8 HEK293 cells with 250 μ g of plasmid AAV (pAAV), 250 μ g of pRepCap, and 500 μ g of pXX6 plasmid mixed with polyethylenimine. The Viral Vector Production Unit generated a pAAV plasmid containing the inverted terminal repeat sequences of the AAV2 genome, a multicloning site to facilitate cloning of expression cassettes, and ampicillin resistance gene for selection. Forty-eight hours after transfection, cells were harvested after centrifugating at ~~for~~ $200 \times g$ for 10 minutes, resuspended in 30 mL of 20 mM NaCl, 2 mM MgCl₂, and 50 mM Tris-HCl (pH 8.5), and lysed by three freeze-thaw cycles. The cell lysate was clarified by centrifugation ($2000 \times g$, 10 min) and rAAV particles were purified from the

supernatant by iodixanol gradient as previously described⁸³⁷. The clarified lysate was treated with 50 U/mL of Benzonase at 37 °C for 1 h and centrifuged at 3000 × g for 20 minutes. The vector-containing supernatant was collected and adjusted to 200 mM NaCl using a 5M stock solution. To precipitate the virus from the clarified cell lysate, polyethylene glycol was added to a final concentration of 8% and the mixture was incubated at 4 °C for 3 h followed by centrifugation at 8000 × g for 15 minutes. The AAV-containing pellets were resuspended in 20 mM NaCl, 2 mM MgCl₂, and 50 mM Tris-HCl (pH 8.5) and incubated for 48 h at 4 °C. The rAAV titration method used was based on the quantitation of encapsidated DNA with the fluorescent dye PicoGreen[®] as described previously⁸³⁸. The following vector concentrations were obtained: AAV-hTyr: 1.7×10^{13} gc/mL (batch a), 2.43×10^{12} gc/mL (batch b); AAV-EV: 2.48×10^{13} gc/mL. Prior to actual experiments, pilot tests were conducted to assess neuronal death upon NM overaccumulation for the different batches.

2.3 STEREOTAXIC INJECTION

Prior to surgery, all surgical instruments were autoclaved, and analgesic (meloxicam, 0.5 mg/mL) and antibiotic (Baytril[®], 5 mg/mL) solutions were prepared. After weighing, animals were placed in an induction chamber and anesthetized with isoflurane in a 1.5% oxygen mixture. For the induction phase (i.e., until the animal was anesthetized, confirmed by loss of the pedal withdrawal reflex), a 5% isoflurane was used and for the maintenance phase (i.e., once the animal was fully anesthetized), which was reduced to 2%. Subsequently, fur was removed from the rat's head (to ensure a surgical procedure as aseptic as possible and also to minimize the risk of post-surgery infection) and the animal was placed on the stereotaxic equipment by gently introducing the ear bars to allow for the head to be securely positioned. Once head stability was checked, analgesic and antibiotic solutions were administered subcutaneously at 2 mg/kg and 10 mg/kg, respectively. At this point, a vacuum system to remove blood and irrigated solutions was turned on, and an incision then made with a scalpel to the center of the rat's head parallel to midline. Once the skull was revealed, 4 hemostatic pean forceps were placed at each end of the incision to fasten skin to achieve a wider opening. To remove blood

from the operated area, hydrogen peroxide was used followed by repeated rinsing with 0.9% NaCl irrigation solution to clean the site, both of which were vacuum-removed.

Subsequently, with the non-cutting side of the scalpel, skull tissue was removed. Once skull sutures were clearly visible and both bregma and lambda visible, skull levelness was checked. To this end, drill tip was placed on lambda and the dorso-ventral coordinates measured, following which the same procedure was repeated at bregma. If the coordinates differed more than ± 0.1 mm, the brain was equilibrated repositioned with the adjustment tool. Once adjusted, the skull was carefully drilled, with the depth of the craniotomy checked regularly. When the skull was thoroughly drilled cleanly, viral vector was injected using a 10 μ L Hamilton syringe fitted with a glass capillary. The injection was carried out unilaterally on the right side of the brain at the following coordinates (flat skull position), right above the SNpc: antero-posterior: -5.29 mm; medio-lateral: -2 mm; dorso-ventral: -7.6 mm below dural surface, calculated relative to bregma according to the stereotaxic atlas of Paxinos and Watson⁸³⁹. Depending on the experiment to be carried out, 2 μ L of a 0.65:1.35 mixture of AAV-hTyr/vehicle, AAV-hTyr/AAV-Flag-hVMAT2, or vehicle/AAV-Flag-hVMAT2 were injected. Infusion was performed at a rate of 0.4 μ L/min and the tip of the glass capillary was left in place for an additional 4 min period before being slowly retracted. Finally, the craniotomy was sealed using bone wax, the incision was closed with surgical suture (three knots per site), tissue adhesive was applied to seal the incision site, and Neo-Predef® power, which has topical antibiotic, anti-inflammatory, and anesthetic properties was dusted over the site. Surgical instruments were cleaned in an ultrasonic cleaner.

2.4 tFUS EXPERIMENTAL SETUP

Prior to commencing surgery, all surgical instruments were autoclaved and analgesic (meloxicam, 0.5 mg/mL) and antibiotic (Baytril®, 5 mg/mL) solutions were prepared. After weighing, animals were placed in an induction chamber and anesthetized with isoflurane in a 1.5% oxygen mixture. For the induction phase (i.e., until the animal was anesthetized, confirmed by loss of the pedal withdrawal reflex), a 5% isoflurane was used and for the maintenance phase (i.e., once the animal was fully anesthetized), which

was reduced to 2%. Subsequently, fur was removed from the rat's head to ensure an optimum acoustic coupling. A 22G catheter was positioned in the caudal vein and a 100 μ L bolus of 10% heparin was delivered to prevent clot formation. The rat was then positioned tail-first in the adapted MRI bed, and the tFUS transducer was positioned on its head. Acoustic coupling of the transducer with the head was achieved by a degassed, deionized water-filled inflatable probe and acoustic gel was applied on the skin and the transducer membrane. Rats were then injected with a 200 μ L bolus of gadolinium contrast medium, followed by a bolus of saline solution.

Three stacks of 2D slices were acquired with an 11.7T MRI, each one at a different orientation (axial, coronal and sagittal), using a 2D Gradient Echo sequence. Imaging parameters were the same for the three acquisitions: field of view (FOV) = 51.2*51.2 mm², with 20 contiguous slices of 1.5 mm thickness, matrix size = 256*256 (200 μ m isotropic in plane resolution), echo time (TE)/repetition time (TR) = 300 ms/4 ms and flip angle $\theta = 60^\circ$. Each scan lasted 1 minute 17 seconds. A tFUS trajectory was then defined using these sequences using Thermoguide software and tFUS was applied with a 20 mm curvature radius, 7-elements, 1.5 MHz transducer. The apparatus was positioned with MR-compatible motors to reach the targeted area. The power of the tFUS ultrasound beam was initially set at 5% corresponding to a Peak Negative Pressure of 1.05 MPa in water, with a duration of 3 ms every 97 ms for 60 repetitions (1 minute). Calibration of the tFUS was performed at the early phase of the project with a HNC 400, SN 1207 needle hydrophone connected to a numerical oscilloscope.

2.5 MRI sequences

MRI images were acquired on an 11.7T MRI with a custom-built U-shaped coil. Anatomical sequences were acquired to locate and SNpc and NM before and after treatment. To correct the future subsequent T1 mapping, B1 mapping was performed using an automated function imaging (AFI)-gradient recall echoes (GRE) sequence with the following characteristics: FOV = 38.4*38.4*38.4 mm³, matrix size = 96*96*96 (400 μ m isotropic resolution), TR/TE = 91/4 ms and flip angle $\theta = 60^\circ$. A stack of 2D Spin Echo T1-weighted sequences with 24 contiguous slices (0.4 mm per slice) was then acquired

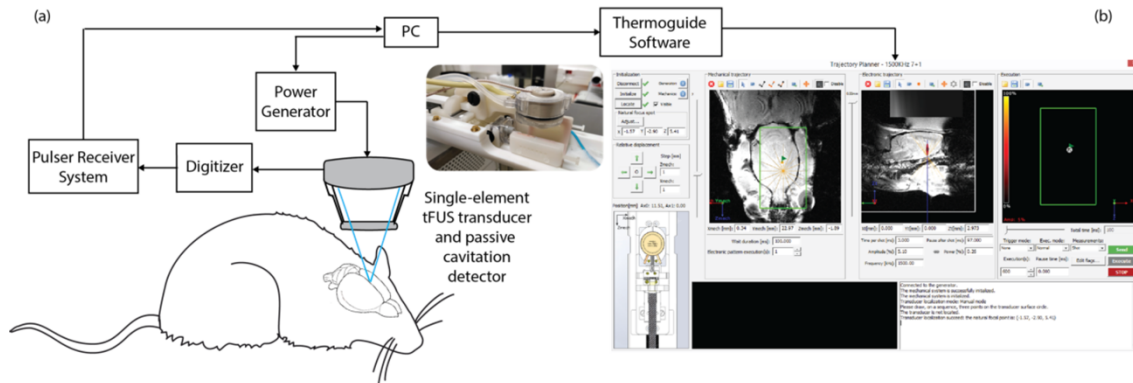
as follows: FOV = 28.8*28.8 mm², matrix size = 192*192 (150 μm isotropic in- 135 plane resolution), TR/TE = 500/6.8 ms and number of excitations (Nex) =12. Following these two acquisitions three Multi-Gradient-Echo (ME-GRE) sequences were acquired, one with magnetization transfer (MT) – to maximize the contrast of macromolecules (such as NM) – and two without. The two acquisitions without MT, acquired with either a flip angle of 6° or 32°, were used to compute the T1 mapping of the whole brain. The images obtained at a flip angle of 6°, with and without MT, were used to calculate the MT ratio and R2* maps, both of which used to locate the SNpc and NM. With the exception of the flip angle, other acquisition parameters remained unchanged: FOV = 25.6*25.6*32.0 mm³, matrix size = 128*128*160 (200 μm isotropic resolution) TR=47 ms, 16 echoes were acquired, the first with TE = 1.71 ms and the last with TE =30.36 ms and a delta-TE of 1.91 ms. Characteristics of the MT pulse were as follows: duration 10.25 ms, irradiation offset = 6kHz, flip angle = 600°.

To set up the tFUS apparatus for treatment, three stacks of 2D slices were acquired, each one with a different orientation (respectively axial, coronal, and sagittal) with a 2D Gradient Echo sequence. Imaging parameters were the same for the three acquisitions: FOV = 51.2*51.2 mm², with 20 contiguous slices of 1.5 mm thickness, matrix size = 256*256 (200 μm isotropic in-plane resolution), TR/TE = 300/4 ms and flip angle $\theta = 60^\circ$. Each scan lasted 1 min 17 s.

2.6 ULTRASOUND SYSTEM

The ultrasound setup consisted of a 7-element, 1.5 MHz, 20 mm radius of curvature FUS transducer (Fig. 36). A Passive Cavitation Detector (PCD) consisting of a broadband mono-element transducer (1.5 MHz center frequency with a -6dB bandwidth > 3Mhz) was inserted in the center of the FUS transducer. The apparatus (tFUS transducer plus its PCD) was positioned with MR-compatible motors to reach the targeted area with the Thermoguide software as shown in figure (Fig. 36). The power of the tFUS ultrasound beam was initially set at 5% corresponding to a Peak Negative Pressure of 1.05 MPa in water, with a duration of 3 ms every 97 ms for 600 repetitions. Calibration measurements were performed with a needle hydrophone connected to a numerical

oscilloscope. The passive cavitation signals were monitored in real-time with PCD controller software. The PCD signals were acquired with a sampling frequency of 16 MHz, then Fourier transformed in windows of 1024 samples (65 μ s). The spectrogram was then displayed in real-time in a roll mode. All frequencies, between 0 and 5 times



the central frequency, were displayed. The acoustic power of the tFUS could be adjusted in real-time by the operator based on the spectrogram.

Figure 36. tFUS apparatus and Thermoguide software used for experiments. (a) Transducer set-up; **(b)** Thermoguide targeting panel: three localization MRI sequences were acquired and transferred to the software to 1) locate the transducer, 2) locate the SNpc and 3) set-up the tFUS parameters (shot length, pause length, power, and number of executions).

2.7 ANATOMICAL SEQUENCES ANALYSIS

All sequences and maps were co-registered to native three-dimensional B1 images using a statistical parametric mapping software package. The quality of registration was checked with visual inspection. R2* maps were computed from a mono-exponential fitting of the ME-GRE acquisitions. T1 maps were also generated from the two ME-GRE sequences acquired without MT at flip angles of 6° and a 32° using the MATLAB toolbox QMRLab⁸⁴⁰. R1 maps were computed similarly to the R2* maps using the T1 data as mentioned above. MT ratios (MTRs) were computed with MATLAB according to the following formula: $MTR = (S_0 - S_{MT})/S_0$, where S_0 is the signal amplitude without MT pulse and S_{MT} is the signal obtained with the MT pulse.

2.8 CYLINDER BEHAVIORAL TEST

Rats were tested for left and right forepaw use with the cylinder test one week before surgery and at 2 and 6 months (m) after viral vector injection for the VMAT2-

overexpressing experiment and 1 m after tFUS application for the tFUS experiment. To perform the cylinder test, rats were first allowed to habituate to the experimental room for at least 1 h before each test. Rats were then placed in a glass cylinder and the total number of left and right forepaw touches performed within 5 min was counted. Data are presented as the percentage of paw usage of the paw contralateral to the injection site. Behavioral equipment was cleaned with 70% ethanol after each test session to avoid olfactory cues. All behavioral tests were performed during the light cycle by an investigator blinded to the experimental groups.

2.9 INTRACARDIAC PERFUSION

Wash and fixative solutions were prepared prior to perfusion. The wash solution was prepared immediately before use by adding 3.75 mL 1% NaNO₂ and 0.11 mL heparin (25000 IU/mL) to 300 mL of 0.9% NaCl irrigation solution. The fixative solution consisted of 4% paraformaldehyde in 0.1M phosphate buffer (pH 7.4). Fixative solution can be stored for no longer than 48 h at 4°C and then brought to room temperature (RT) on the day of perfusion. Prior to perfusion, rats were anesthetized by intraperitoneal overdose with 5% sodium pentobarbital solution (2500 mg/50 mL) according to the animal's weight (50 mg/kg). After around 10 minutes, rats were checked for complete anesthetic state by loss of the pedal pain reflex to ensure the absence of paw movement. If rat still reacted with pedal pain reflex after 15-20 min, additional anesthetic (same amount as first injection) was administered.

With subsequent steps performed with a fume hood, the animal was placed in the supine position on the perfusion stage which in turn was placed in a collection pan for collecting perfusate. With the animal's limbs pinned to facilitate exposure of the peritoneal cavity, forceps were used to grasp the skin over the xiphoid process; scissors were then used to make an incision in the skin to reveal the outer abdominal wall. The abdominal wall was cut laterally and then through the ribs and parallel to the lungs to create a chest "flap". This flap was then retracted, folded back towards the head and the aorta clamped (to restrict circulation in the upper body) with a hemostat. Subsequently, using a forceps to grasp the heart near its apex, a venous catheter was

inserted in the left ventricle and an incision was made in the right atrium to allow drainage. At this point, the heart was rinsed for 5 minutes with wash solution applied with a peristaltic pump (9 mL/min) to remove blood prior to fixation. Subsequently, the perfusate was changed to ice-cold (4°C) paraformaldehyde fixative solution (9 mL/min), which was applied for 15 minutes. The cold temperature of the solution is required to keep tissues in good condition, especially, for further immunohistochemistry procedures. A vigorous muscle contraction is indicative of a correct tissue fixation. Once perfusion was completed, the animal was euthanized by guillotine decapitation, the skull removed with bone rongeurs, and the brain removed with a spatula.

Finally, the brain was prepared for cryoprotection. Here, the fixed brain was placed in a 50 mL conical tube with ice-cold 4% paraformaldehyde and incubated overnight at 4 °C, during which time complete brain equilibration was evident by sinking of the tissue to the bottom of the tube. On the next day, the paraformaldehyde solution was replaced with ice-cold 30% sucrose, and the brain was allowed again to equilibrate completely at 4 °C for at least 48 h, again evidenced by sinking of the tissue to the bottom of the tube. After equilibration, the sucrose solution was removed and the brain was placed in dry ice pre-cooled with 2-methylbutane. At this point, the brain was left for 1 minute, allowing it to reach a temperature between 30 °C and -40 °C. Once frozen, the brain was wrapped in aluminum foil (previously placed on dry ice) and stored at -80 °C until further processing/sectioning. Paraffin embedding to allow fine sectioning of the brain and its long-term preservation at RT, was performed at the VHIR's Drug Delivery and Targeting laboratory facility (principal investigator, Ibane Abasolo).

2.10 MICROTOMY

The microtome blade was inserted into its holder on the microtome, ensuring that the blade was positioned correctly and the hand wheel brake was on. A water bath was heated to a temperature (around 40 °C) a few degrees below the melting point of the paraffin. A paraffin block was taken from an ice tray, dried briefly with a soft tissue, and placed on the block holder. The hand wheel brake was released and the block brought closer to the knife blade using the advance wheel. The trimming button was used to

advance into the paraffin block until the full face of tissue was exposed. Trimming was performed at 30 μm steps. Once trimmed, the paraffin block was placed face down on the ice block and left there until it was thoroughly cooled. This was repeated every 5-10 minutes during the cutting to prevent the tissue from drying out. Subsequently, the trimming blade was changed for a new one and brain slices were cut at a thickness of 5 μm . Each paraffin slice was removed from the microtome using a paintbrush and placed in a water bath. Using a clean paint brush, slices were smoothed out both in the water bath and once placed on a prelabeled (with pencil) glass slide. Finally, the slide was placed in a rack to drain. Throughout the process it was important to maintain a proper flotation technique by avoiding sections with wrinkles, the formation of bubbles and fluctuations of water temperature. Also, to prevent chatter artifact it is important that the block is not too cold or being cut too fast.

NM is not autofluorescent and can be visualized with light microscopy. In this regard, to quantify intracellular and extracellular NM, hematoxylin-eosin staining is adequate as hematoxylin stains the cell nucleus and eosin stains the cell cytoplasm. Selected slides were analyzed at VHIR's Drug Delivery and Targeting laboratory facility.

2.11 IMMUNOCHEMISTRY ON PARAFFIN-EMBEDDED BRAIN SLICES

Slices were deparaffinized and rehydrated. To this end, slides were placed on a rack and incubated at 60 °C for 30 minutes to melt the wax. With work carried out in a fume hood, three washes of 3 minutes each with xylene were performed to solubilize and remove the paraffin. Slides were then washed (two washes, 10 minutes each) in a descending gradient of ethanol percentages (100% (to completely remove xylene), followed by 95% and 70% (to gradually achieve hydration)). Finally, two washes with TBS 1x for 5 minutes were performed to fully hydrate the samples. Importantly, when washing with xylene and 100% ethanol, one bath per wash was employed, with racks holding the slices fully drained between washes to ensure that the previous bath's solution was not transferred to the next wash. Next, slides were placed in endogenous peroxidase blocking solution (3% H_2O_2 and 10% methanol in TBS 1x) for 10 minutes to prevent subsequent interference of the peroxidase-based detection system. After this step, slides were

washed three times for 5 minutes with TBS 1x solution. Subsequently, for the purpose of restoring the secondary and tertiary structure of proteins, heat-induced antigen retrieval for enhanced antibody binding was performed. In this way, antigen epitopes become “unmasked” and available for the desired antibody to bind, thereby increasing detection. Thus, slides were placed in citrate buffer 10mM (pH 6) in a heating bath at 95 °C for 20 minutes. Slides were then cooled at RT for 20 minutes.

Following antigen retrieval, sections were washed 3 times for 5 minutes each wash with TBS 1x solution. At this point, permeabilization (PBS-Triton X-100 (0.2%)) of the sections could be carried out. For established immunocytochemistry protocols, like those employed with the antibodies used in the present project, permeabilization is not indispensable. While permeabilization enhances antibody penetration, it can concomitantly lead to increased background signal due to increased autofluorescence. Afterwards, slides were placed in a black tray and were gently dried with a soft tissue. In order to avoid upcoming solutions to spill and to ensure a constant wet milieu where desired interactions can occur, sections were then circled with a hydrophobic pen, taking much care to not touch them directly. Next, blocking solution (5% NGS in TBS 1x) was added to sections (200 µl/section) and left to incubate for 1 h at RT. Blocking is essential for preventing non-specific binding of antibodies or other reagents to the tissue. Importantly, throughout this and following steps, wells between rails were filled with water to maintain a constant level of moisture. Subsequently, after removing the blocking solution, slides were gently dried and primary antibody solution (primary antibody/ies diluted in 2% blocking solution) was added (200 µl/section). Trays containing slides were covered and incubated at 4°C for 48 h (or 72 h, depending on the antibody used).

After incubation, slides were washed three times for 5 minutes with TBS 1x solution, and the corresponding biotinylated secondary antibody solution (secondary antibody diluted in 2% blocking solution) was added (200 µl/section) and left to incubate at RT for 1 h. At this point, ABC solution was prepared and left on a shaker for 30 minutes. This solution uses the avidin-biotin complex method to amplify the signal intensity during the development process. Meanwhile, slides were washed three times for 5 minutes with TBS 1x solution. Next, the ABC solution was applied and slides left to incubate for

1 h at RT, following which slides were washed three times for 5 minutes with TBS 1x solution. Afterwards, to further amplify the signal with the ABC method, peroxidase activity was developed by means of either DAB (if brown was the desired color for developing) or Vector®SG (if (dark) blue was the desired color for developing) developing solutions, which were prepared in conical tubes covered with aluminum foil to avoid signal intensity loss during development. In both cases, slides were placed on aluminum foil-covered trays and 200 µl of the respective developing solution were added to each section. Importantly, cardboard boxes were used to cover groups of six slides and thus maintain the light-sensitive developing process under dark conditions. The color development duration depends on previous knowledge and expertise with the antibody employed, usually taking 5-15 minutes. The developing solution was removed by means of a vacuum unit and slides were washed three times for 5 minutes with TBS 1x solution. Next, since the mounting medium (DPX) is hydrophobic, sections needed to be dehydrated. To this end, 1-minute-long consecutive immersions in ethanol of increasing gradient (70%, 95% and 100%) were performed. Slides were then transferred to xylene for 5 minutes and, after replacing the xylene, they were mounted by placing a coverslip (previously rinsed with 70% ethanol) with DPX on them. Bubbles were removed by gently pressing with tweezers. Slides were left to dry overnight under a fume hood.

2.12 IMMUNOFLUORESCENCE OF PARAFFIN-EMBEDDED BRAIN SLICES

Slices were first deparaffinated and rehydrated. To this end, slides, placed on a rack, were incubated at 60 °C for 30 minutes to melt the wax. Then, working in a fume hood, three washes of 3 minutes each with xylene were performed in order to solubilize and remove paraffin. The slides were then washed (two washes, 10 minutes each) in descending gradient of ethanol percentage (100% (to completely remove xylene), 95% and 70% (both, to gradually achieve hydration)). Finally, 2 TBS 1X washes of 5 minutes each were performed to fully hydrate the samples. Importantly, when washing with xylene and 100% ethanol one bath per wash was employed and, between washes, racks holding the slices were fully drained to ensure that the previous bath's liquid is not transferred to the next one. Subsequently, with the purpose of restoring secondary and

tertiary structure of proteins, heat-induced antigen retrieval for enhanced antibody binding was performed. This way, antigen's epitopes become "unmasked" and available for the desired antibody to bind, thereby increasing detection. Thus, slides were placed in citrate buffer 10mM (pH 6) in a heating bath and brought to boil at 95 °C for 20 minutes. Slides were then cooled down by placing them at RT for 20 minutes. Following antigen retrieval, sections were washed 3 times for 5 minutes each wash with TBS 1x.

Then, in order to enhance antibody(ies) penetration, sections were permeabilized by washing twice with PBS-Triton X-100 (0.2 %) for 5 minutes each time. Immediately after permeabilization, slides were placed in a black tray and were gently dried with a soft tissue. In order to avoid upcoming solutions to spill and to ensure a constant wet milieu where desired interactions can occur, sections were then circled with a hydrophobic pen, taking much care to not touch them directly. Next, 5% blocking solution was added (200 µl/section) and let incubating for 1 h at RT. Subsequently, after removing the blocking solution, slides were gently dried and primary antibody/ies solution(s) (primary antibody/ies diluted in 2% blocking solution) was added (200 µl/section). Slides-containing trays were covered and let incubating at 4°C for 48 h (alternatively 72 h), depending on the antibody used). After the incubation time, slides were washed three times for 5 minutes each wash with TBS 1x, and the appropriate Alexa Fluor®-conjugated secondary antibody/ies solution(s) (secondary antibody/ies diluted in 2% blocking solution) was added (200 µl/section) and let incubating at RT for 1 h. Subsequently, slides were washed three times for 5 minutes each wash, with TBS 1x. Finally, slides were mounted by placing a coverslip (previously rinsed with 70% ethanol) with fluorescent mounting medium on them. Bubbles were removed by gently pressing with the tweezers handling part. Slides were let dry in the fume hood for 5 minutes and immediately stored at 4°C to avoid fluorescence exhaustion. Importantly, fluorescence immunochemistry protocols do not need the dehydration step used in standard immunochemistry procedures, since the fluorescent mounting medium is not as hydrophobic as DPX.

2.13 CHROMATOGRAPHIC DETERMINATION OF DOPAMINERGIC METABOLITES

2.13.1 CALIBRATION CURVES AND QUALITY CONTROL SAMPLE PREPARATION

In our recent methodological study, a robust and efficient UPLC-MS/MS method was developed and validated (see last part of annex); this methodology has been further improved with a broader metabolite detection range to simultaneously detect and quantify, among other compounds, L-DOPA, DA and its metabolites and oxidation intermediates (in particular, aminochrome, 5SCD and 5SCDA)⁸⁴¹.

Stock solutions of the internal standards were prepared in 25 mM FA, which, if not used immediately, were stored at -80°C . Then, external standards of each metabolite were freshly prepared and used to make three mixtures: Mix1 (DA, L-DOPA, 3-MT, aminochrome), Mix2 (DOPAC) and Mix3 (5SCD, 5SCDA). Aminochrome solution was freshly prepared as described by Lemos-Amado et al⁸⁴². In brief, equal volumes of 1 mM DA dissolved in water and 2 mM KIO_4 dissolved in 100 μM aqueous ammonium acetate buffer (pH 5.8) were mixed at RT with vigorous shaking for 1 min. Successive dilutions were made in 25 mM formic acid. Mixtures were then serially diluted with 25 mM FA to obtain the concentration series used in calibration curves. Finally, internal standard was added to the three mixtures to achieve a final concentration of 500 nM in working mixtures.

To prepare calibration curves, 3 SN or 2 striata from different animals were pooled and homogenized in 4 mL of 250 mM FA. The sample was then distributed into 120 μL aliquots prior to the addition of 40 μM of the appropriate working mixture (Mix1, Mix2 or Mix3). Samples were then centrifuged, and 120 μL of the supernatant and the same amount of 25 mM FA were transferred to an Ostro® protein precipitation and phospholipid removal plate and filtered. Finally, 7 μL were injected into the UPLC-MS/MS system. For brain samples, calibration levels ranged from 1.72–3000 nM for DA, NE, and MIX2 and 0.39–1000 nM for L-DOPA, 3-MT, and AC. For cell samples, calibration levels ranged from 1.72– 3000 nM for both MIX1 and MIX2 with the exception of 3-MT

for which 0.39–1000 nM was used. Four different quality control samples were chosen, covering low to high metabolite concentrations.

2.13.2 SAMPLE PREPARATION

Brain hemispheres were resuspended in 300 μ l of 250 μ M formic acid and homogenized. Twenty microliter samples were taken for protein determination (diluted 1/5 in formic acid) and kept on ice for 15 minutes. Subsequently, 224 μ l samples were mixed with 32 μ l internal standard. After that, suspensions were centrifuged at 18000 rpm at 4°C for 10 minutes. Supernatants were used to determine free neurotransmitter and metabolite levels, while pellets were employed for protein-bound determinations (not carried out in experiments presented in this dissertation). Supernatants were filtered by means of an Ostro® plate, as in the previous step, to remove proteins and phospholipids. Finally, 7 μ l were injected into the UPLC-MS/MS system three times to analyze Mix1, Mix2 and Mix3.

2.13.3 UPLC-MS/MS ANALYSIS

An Acquity UPLC system coupled with a Xevo TQ-S triple quadrupole mass spectrometer with electrospray ionization interface was used. Instrument control, data acquisition, and analysis were performed using MassLynx V4.1. The chromatographic separation of brain and cell samples was performed on an Acquity HSS T3 (1.8 μ m; 2.1 \times 100 mm) column coupled to an Acquity HSS T3 VanGuard pre-column (100 Å, 1.8 μ m, 2.1 mm \times 5 mm). The column temperature was set at 40 °C, and samples were maintained at 6 °C in the thermostatic autosampler. The mobile phase consisted of solvent A (methanol 100%) and solvent B (25 mM FA in water) at a flow of 0.4 mL/min with the following gradient profile: 0.5% B maintained for 0.5 min, 8% B at 2.6 min, 55% B at 2.9min, 60% B at 3.3min, 80% B at 4.3min, 90% B at 4.4 min and maintained for 0.5 min, 0.5% B at 5 min followed by 1 min of equilibration.

The mass spectrometer detector operated under the following parameter settings: source temperature 150 °C, desolvation temperature 450 °C, cone gas flow 50 L/h, desolvation gas flow 1100 L/h, and collision gas flow 0.15 mL/min. Argon was used as

the collision gas. The capillary voltage was set at 0.5 kV for MIX1 and at 2 kV for MIX2 detection. The electrospray ionization source was operated in both positive and negative modes, depending on the analyte. Multiple reaction monitoring acquisition settings for the targeted metabolites are summarized in Table 5.

Table 5. Multiple reaction monitoring (MRM) acquisition settings. ^aParent mass after loss of water. ^b Detected in negative mode. RT, retention time; D, dwell time; CV, cone voltage; CE, collision energy; CpV, capillary voltage.

Analyte	Transition (m/z)	RT (min)	D (ms)	CV (V)	CE (eV)	CpV (kV)
DA4d (IS)	157,83 > 94,8	1,44	52	10	20	0,5
DA	153,93 > 90,57	1,46	52	10	20	0,5
L-DOPA	198,1 > 152,1	1,48	52	15	15	0,5
5SCDA	273,1 > 166,9	1,73	58	20	20	0,5
5SCD	317 > 154,86	2,01	58	24	30	0,5
3-MT ^a	150,7 > 90,96	3,09	52	35	20	0,5
Aminochrome	149,61 > 121,91	3,36	52	25	25	0,5
DOPAC ^b	166,99 > 122,82	3,72	56	18	22	2

Each sample was injected three times into the UPLC-MS/MS system to analyze different sets of compounds (i.e., MIX1, MIX2 and MIX3). Samples with a concentration between limit of detection (LOD) and limit of quantification (LOQ) or bigger than LOQ were considered acceptable; samples with a concentration lower than LOD were considered as the LOD value. Data were normalized to the protein concentration and presented as the percentage of the contralateral concentration or ratio.

2.14 TH STEREOLOGY COUNTING

A Zeiss Imager.D1 microscope coupled to an AxioCam MRc camera was employed for slide visualization. Assessment of the total number of TH-positive neurons, the number of NM-laden neurons (with or without TH), and extracellular NM aggregates in the SNpc was performed according to the fractionator principle, using StereoInvestigator 11. Serial 5 µm-thick paraffin sections covering the entire SNpc were included in the counting procedure (every 17th section for a total of 10-12 sections analyzed/animal). The following sampling parameters were used: (i) a fixed counting frame with a width and length of 50 µm; (ii) a sampling grid size of 115 x 70 µm and (iii) a multiplication factor of 17. The counting frames were placed randomly by the software at the

intersections of the grid within the outlined structure of interest. Objects in both brain hemispheres were independently counted following the unbiased sampling rule using a 100x lens and included in the measurement when they came into focus within the dissector. A coefficient of error of <0.10 was accepted.

Data for the total numbers of TH-positive neurons and NM-containing neurons are expressed as absolute numbers for each hemisphere. To assess the percentage of VMAT2-positive and -negative neurons in the VMAT2-overexpression experiment, a similar approach was applied to a selected SNpc mid-section per animal, taking into consideration VMAT2⁺NM⁺, VMAT2⁺NM⁻ and VMAT2⁻NM⁺ neurons. For both VMAT2-overexpressing and tFUS experiments, the total number of SNpc DA neurons was calculated by considering all TH⁺NM⁺, TH⁻NM⁺ and TH⁺NM⁻ neurons. The percentage of TH downregulation was calculated by considering the total number of TH⁺NM⁺ neurons and the total number of TH⁻NM⁺ neurons with respect to the total number of neurons containing NM. All quantifications were performed by an investigator blinded to the experimental groups.

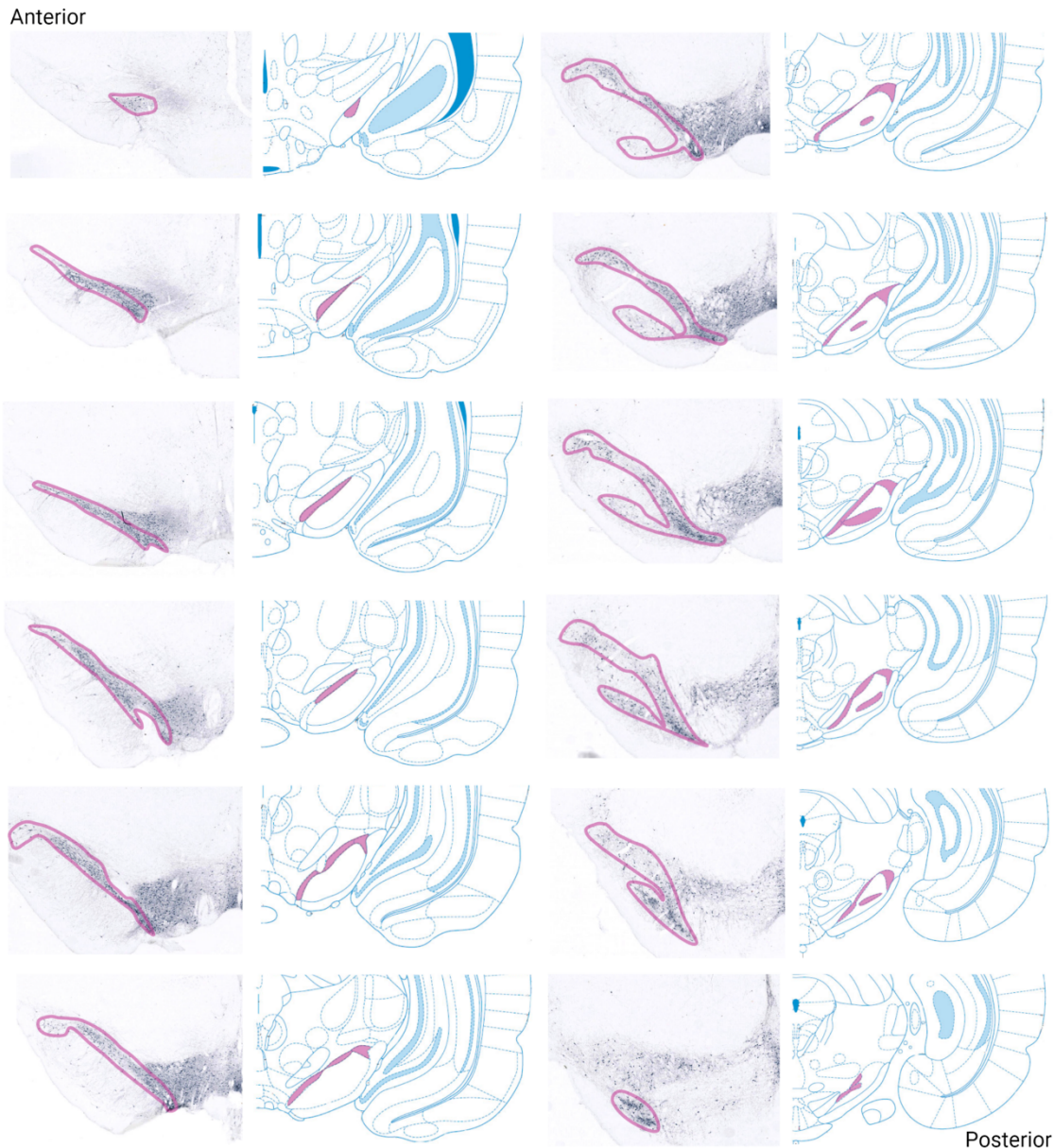


Figure 37. Anatomical levels of rat SN used for quantifications. Twelve serial 5 μm -thick paraffin sections covering the entire rat SNpc (one every 17th section) were immunostained for TH and matched with the corresponding anatomical level from the rat brain atlas⁸⁴³. Pink color indicates the borders of the SNpc in both the atlas and TH-immunostained sections. Figure was created with BioRender.com.

2.15 DENSITOMETRY

The integrity of the nigrostriatal pathway was assessed by quantifying striatal fibers. To this end, sections were scanned in an Epson Perfection V750 PRO scanner and visualized by means of Sigma Scan software. Striatal TH innervation was quantified by optical

densitometry in 10 representative sections of the striatal volume using Image J software. The grey intensity in the STR was compared to the blank, which in this case was the cortex. The optical density was computed using the formula: $\text{optical density} = -\log(\text{intensity str}/\text{intensity cortex})$.

2.16 NEUROMELANIN QUANTIFICATION

Intracellular and extracellular NM levels were quantified in 5 μm -thick paraffin-embedded H&E-stained sections covering the whole SNpc for each animal. In these sections, SNpc DA neurons were identified by the presence of unstained NM brown pigment. Midbrain sections were scanned using the Panoramic P250 Flash III whole slide scanner and section images were acquired with CaseViewer software at an objective magnification of 63x. All NM-positive neurons in a representative SNpc section of each animal were analyzed by means of optical densitometry using ImageJ software to quantify the intracellular density of NM pigment. The pixel brightness values for all individual NM-positive cells (excluding the nucleus) in all acquired images were measured and corrected for non-specific background staining by subtracting values obtained from the neuropil in the same images. All quantifications were performed by an investigator blinded to the experimental groups. Extracellular NM granules were quantified in the same way without the need to subtract any background value. In both intra- and extracellular NM cases, Image J parameters were able to compute the area of the drafted NM pigment as well.

2.17 DEVELOPMENT AND VALIDATION OF ARTIFICIAL INTELLIGENCE-BASED ALGORITHMS FOR AUTOMATED QUANTIFICATION OF NEUROINFLAMMATION

Part of this project was dedicated to the development of different algorithms for the automatized quantification of neuroinflammation with Aiforia® (Aiforia henceforth). Due to the quality of the obtained algorithms, a manuscript covering their validation and comparison to human quantifications is in the process of being published. The principal

findings of that paper can be found below located in the extra chapter. Figure 38 depicts in schematic form the roadmap followed from brain sectioning to the identification and quantification of individual neuroinflammation markers. In this regard, slides were first digitized with the aid of a Panoramic P250 Flash III whole slide scanner with extended focus at a resolution of 0.2 $\mu\text{m}/\text{pixel}$. The extended focus option enables the whole section depth to be in a single focal plane, thus ensuring an optimal whole-tissue image without blurry areas. A total depth of 10 μm was acquired by means of five focal layers with 2 μm intervals. Subsequently, scanned files were uploaded to the Aiforia image processing and management platform and analyzed using a deep convolutional neural network (CNN) algorithm and supervised learning generated by Aiforia Create (Version 5.1).

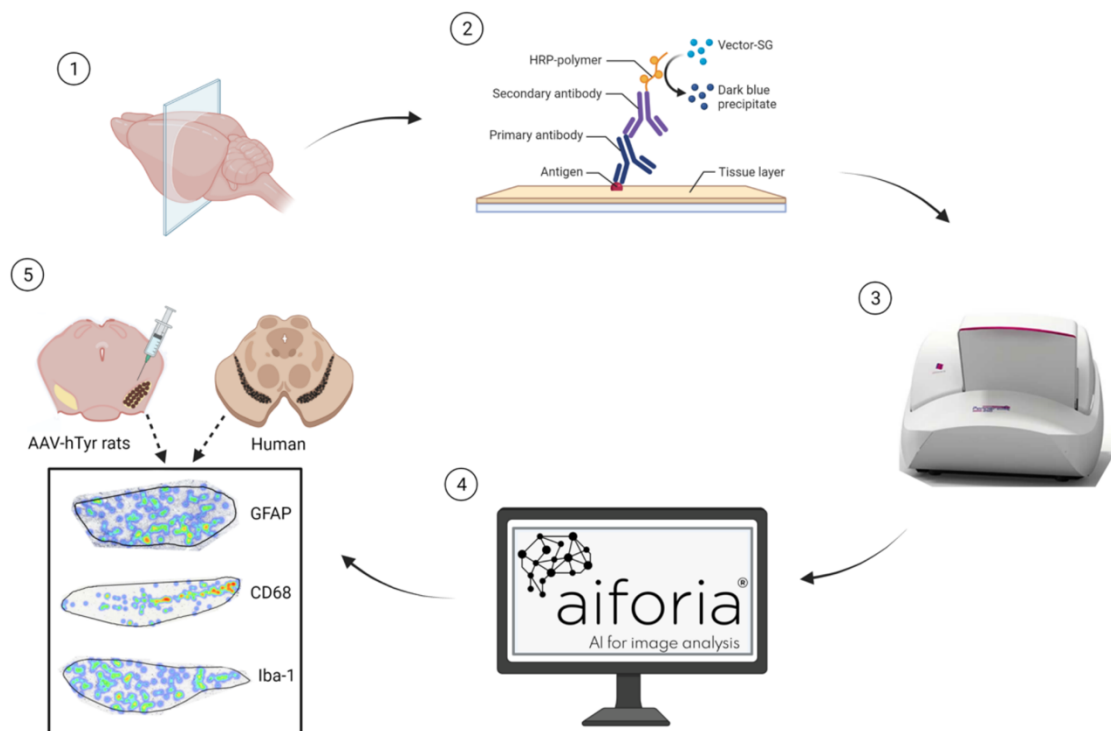


Figure 38. Workflow of the automatized counting method using the Aiforia platform. 1. After perfusion, brains are processed for histology and cut into 5- μm -thick sections. 2. Next, immunohistochemistry with the respective antibody is performed. 3. Slides are subsequently scanned. 4. Slides are uploaded to the Aiforia platform. 5. After delimitation of the area occupied by the SN, the desired regions of interest are defined for the automatic quantification with the respective CNN algorithm (heat maps shown for three different cell types).

The CNN algorithms were trained to recognize the cell bodies of GFAP+ astrocytes and CD68+ infiltrating macrophages, as well as 3 different activation states of Iba-1+ microglial cells from previously digitized images available in the Aiforia Cloud. The astrocyte-recognizing algorithm consisted of one layer discriminating the GFAP+

astrocytic nucleus and strongly marked branches and branchlets from background. The specific hyperparameters for this algorithm were as follows: object size, 20 μm ; minimum object size difference, 25%; complexity, ultra-complex; iterations without progress, 750. The macrophage-recognizing algorithm also consisted of one layer counting CD68+ macrophagic infiltrates associated with extracellular NM (eNM) granules. Specific hyperparameters used for this algorithm, other than default values, included: object size, 15 μm ; minimum object size difference, 25%; complexity, very complex; iterations without progress, 100.

Lastly, the microglia reactivity-discriminating algorithm consisted of three different layers, one for each state: non-reactive, highly-reactive, and mildly-reactive. For this algorithm, hyperparameters that were not default values consisted of: object size, 25 μm ; minimum object size difference, 25%, maximum object overlap, 70%; complexity, ultra-complex; iterations without progress, 750; image augmentation values: scale, luminance and contrast ranging from -10 to 10, and aspect ratio and maximum shear, 10. Algorithm performance was validated against manual counts by two independent blinded observers in 46 brain regions that were not included in the training dataset.

Quantification of Iba-1, CD68 and GFAP-positive cells was performed by means of validated artificial intelligence algorithms in SNpc sections adjacent to those used for stereological cell counts. Iba-1-positive cells were counted separately in 2 different groups according to their activation state: non-reactive (branched shape) and reactive (amoeboid shape). CD68- and GFAP-positive cells were counted individually. All quantifications were performed by an investigator blinded to the experimental groups.

2.17.1 CNN ALGORITHMS ARE A RELIABLE METHOD TO DETECT AND QUANTIFY GFAP-POSITIVE ASTROCYTES, CD68-POSITIVE MACROPHAGES, AND IBA-1-POSITIVE MICROGLIA IN RAT SUBSTANTIA NIGRA

Taking advantage of the Aiforia platform, we herein describe the first fully-automated process for assessing inflammatory changes linked to PD neurodegeneration in human brain tissue and in a NM-accumulating, neurodegenerative PD model. Once the slides were uploaded and the algorithms trained to an extent of minor possible improvement,

we first tested how they performed compared to human observer stereological-based cell counting. We took random regions of interest from rat SN, both ipsilateral and contralateral to AAV-hTyr injection, and counted all three different cell types manually in the digital images. Astrocytes are morphologically heterogeneous and ubiquitous since they represent 20% to 40% of the total number of mammalian brain cells⁸⁴⁴. However, their current classification regarding shape only differentiates between those found in the gray matter (protoplasmic) and in the white matter (fibrous)⁸⁴⁵. On the other hand, based on molecular marker labeling, Emsley and Macklis divided astrocytes into 9 classes, concluding that their morphology is determined by the cytoarchitecture of a given brain region, thereby demonstrating their robust plasticity⁸⁴⁶. In the present case, since astrocytes are distributed across the whole midbrain and their morphology does not suffer strong variations in the presence of eNM, we trained the CNN algorithm to detect astrocytes with a marked GFAP expression independently of soma visibility (Fig. 39A, left panels).

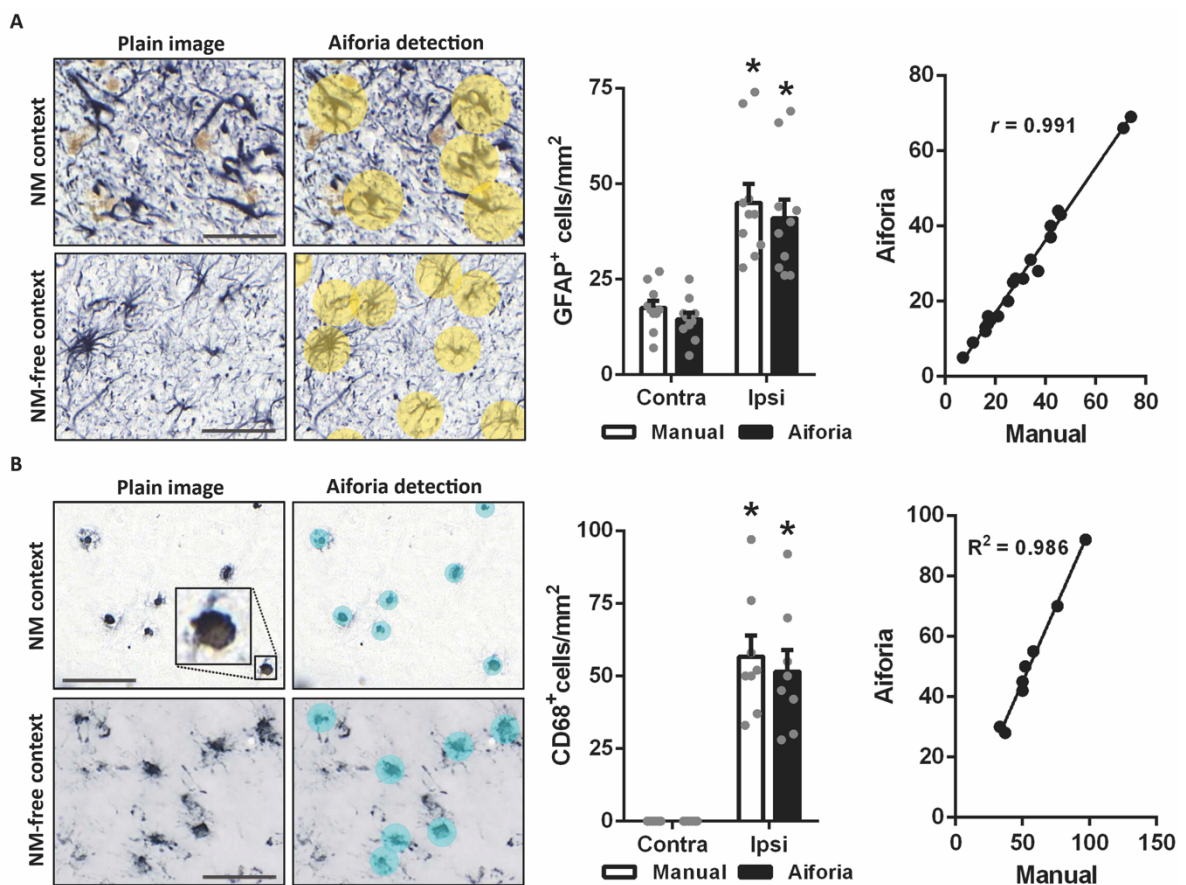


Figure 39. Deep-learning algorithm-based detection of GFAP⁺-astrocytes and CD68⁺-macrophages in an inflammatory milieu in rat. (A) Left, representative images of GFAP-specific algorithm detecting astrocytes in NM and NM-free contexts. Scale bars, 50 μ m. Center, manual cell counts of SNpc GFAP⁺-astrocytes compared to deep

learning-derived quantifications in AAV-hTyr-injected rats 1 month and 2 months after injection. $*p < 0.05$, compared to respective contralateral (non-injected) side. *Right*, Spearman correlation analysis between manual and deep learning-derived quantifications. **(B) Left**, representative images of CD68-specific algorithm detecting astrocytes in NM and NM-free contexts. Scale bars, 50 μm . *Center*, manual cell counts of SNpc CD68⁺-macrophages compared to deep learning-derived quantifications in AAV-hTyr-injected rats 1 month and 2 months after injection. $*p < 0.05$, compared to respective contralateral (non-injected) side. *Right*, Pearson correlation analysis between manual and deep learning-derived quantifications without *Contra* values. In all panels, values are \pm SEM. Statistical analysis: two-way ANOVA; Student-Newman-Keuls post-hoc test. In **A**, $n = 10$ (*Contra*), $n = 10$ (*Ipsi*); in **B**, $n = 8$ (*Contra*), $n = 8$ (*Ipsi*). Photomicrographs correspond to 5- μm -thick sections. *Contra*, contralateral; *Ipsi*, ipsilateral.

Once the algorithm was established, we validated it against stereological counting. When tasked with analyzing 46 regions of interest (randomly scattered along the midbrain, containing zones both with and without NM), human observers counted 534 astrocytes, while the algorithm detected 501, resulting in a strong correlation between both counting approaches (Figure 40A).

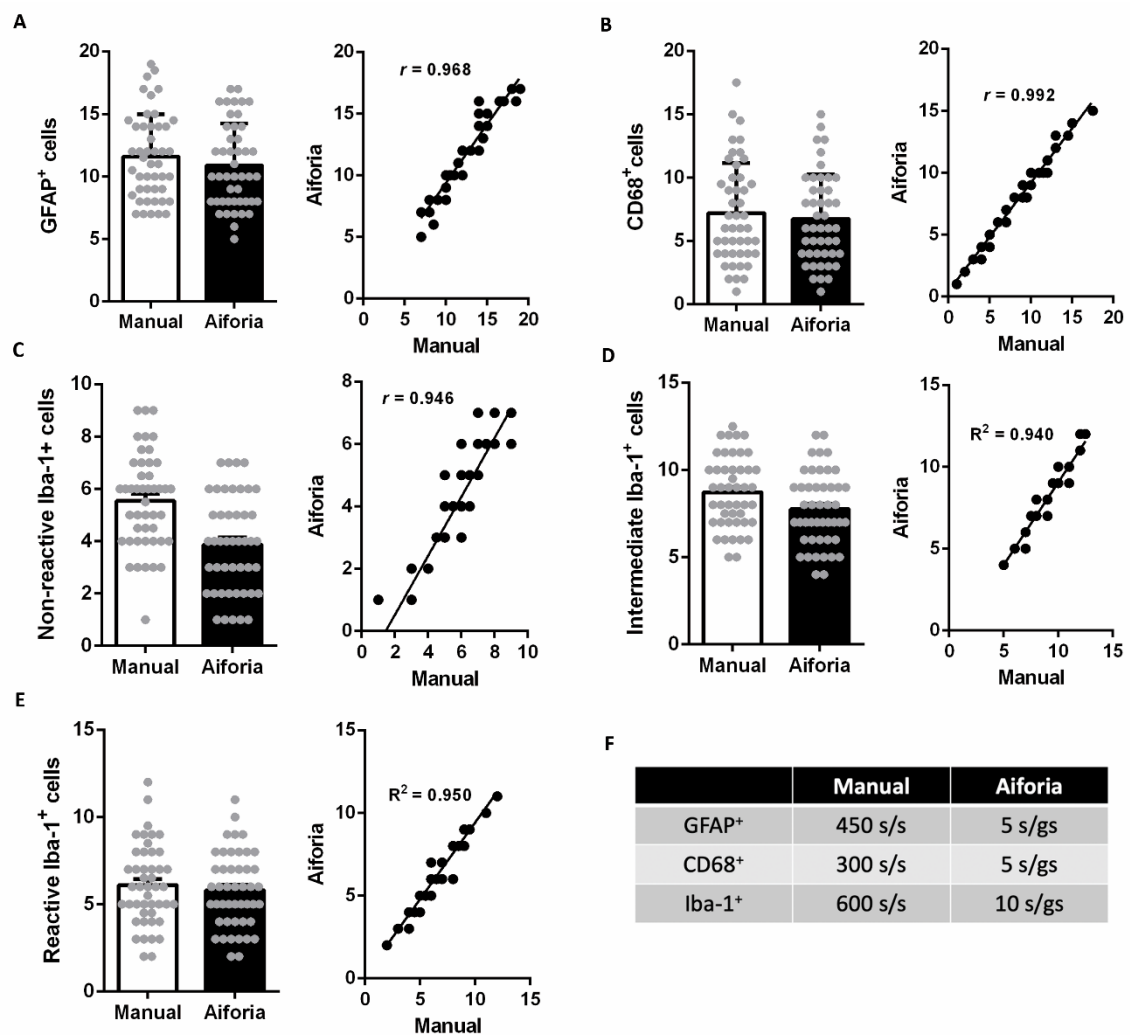


Figure 40. Validation of the Aiforia platform. Three CNN algorithms for GFAP⁺ astrocytes **(A)**, CD68⁺ macrophages **(B)** and three different reactivity states of Iba-1⁺ microglia **(C-E)** detection and automatized counting, were validated by comparing the results to manual counts obtained by two human observers across random regions in the rat SN. In

A-E, *left*, manual quantifications compared to deep learning-derived quantifications; *right*, correlation analysis between both quantifications. In **A-E**, values are mean \pm SEM. $N = 46$ (**A-E**). (**F**) Average time invested in stereology-based neuroinflammation quantification compared to Aiforia-based method. Note that stereology requires complete hands-on application for quantifying each stained slide, while Aiforia-based algorithms are able to perform counting on multiple groups of slices at the same time. s/s, seconds per slide; s/gs, seconds per group of slides

Neuron-supportive astrocytes and only two other immune cell populations are present in the “immune-privileged” central nervous system under steady-state conditions. The latter cell types are represented by parenchymal microglia and non-parenchymal macrophages (location-specific cells and blood-borne monocytes)⁸⁴⁷. While microglia are a unique tissue-resident macrophage population, to gain broader perspective of activated microglia upon eNM insult, we also focused on tissue infiltrating macrophages, which are recruited to active-inflammation sites, deploying the widely-used CD68 marker (Fig. 39B, left panels)⁸⁴⁸. Thus, we developed and validated a CNN-algorithm for detecting CD68⁺ cells across 46 regions randomly scattered along the SN; this resulted in the identification of 309 CD68⁺ macrophages versus 331 compared with manual counting results, providing a very strong correlation between both methods (Figure 40B, right).

Subsequently, we concentrated microglial quantification. Considering the varied morphology of microglia depending on the whether the brain is under physiological or injured/diseased conditions, and in contrast to neurons, astrocytes or macrophages, this characterization resulted in a painstaking task. Microglia perform a constant surveillance role in the normal brain, remaining quiescent under normal conditions, but proliferating and undergoing major morphological and functional alterations⁸⁴⁹ (i.e. phagocytic activity⁸⁵⁰ or antigen presentation^{851,852}) upon insult (i.e., traumatic brain injury⁸⁵³, ischemia⁸⁵⁴ or ongoing neurodegenerative conditions, such as PD⁸⁵⁵ and AD⁸⁵⁶). Microglia have been categorized into three broadly distinct subtypes based on their shape: compact, longitudinally branched, and radially branched⁸⁵⁷. More recently, they have been classified into 4 different clusters with several subtypes⁸⁵⁸. Considering the pleomorphic forms of microglia^{859–862}, and with the aim of simplifying and unifying criteria, we trained the CNN algorithm to distinguish between 3 different morphologies⁸⁶³. First, a basal, healthy resting phenotype characterized by a strong

ramification (at least three sub-branches diverging from a larger one) and an unnoticeable soma (referred to from now on as ‘non-reactive state’; Fig. 41A, left panels). Second, an intermediate state of reactivity, which presents a visible soma and shorter ramifications, widely scattered throughout the brain (referred to from now on as ‘intermediate state’; Fig. 41B, left panels).

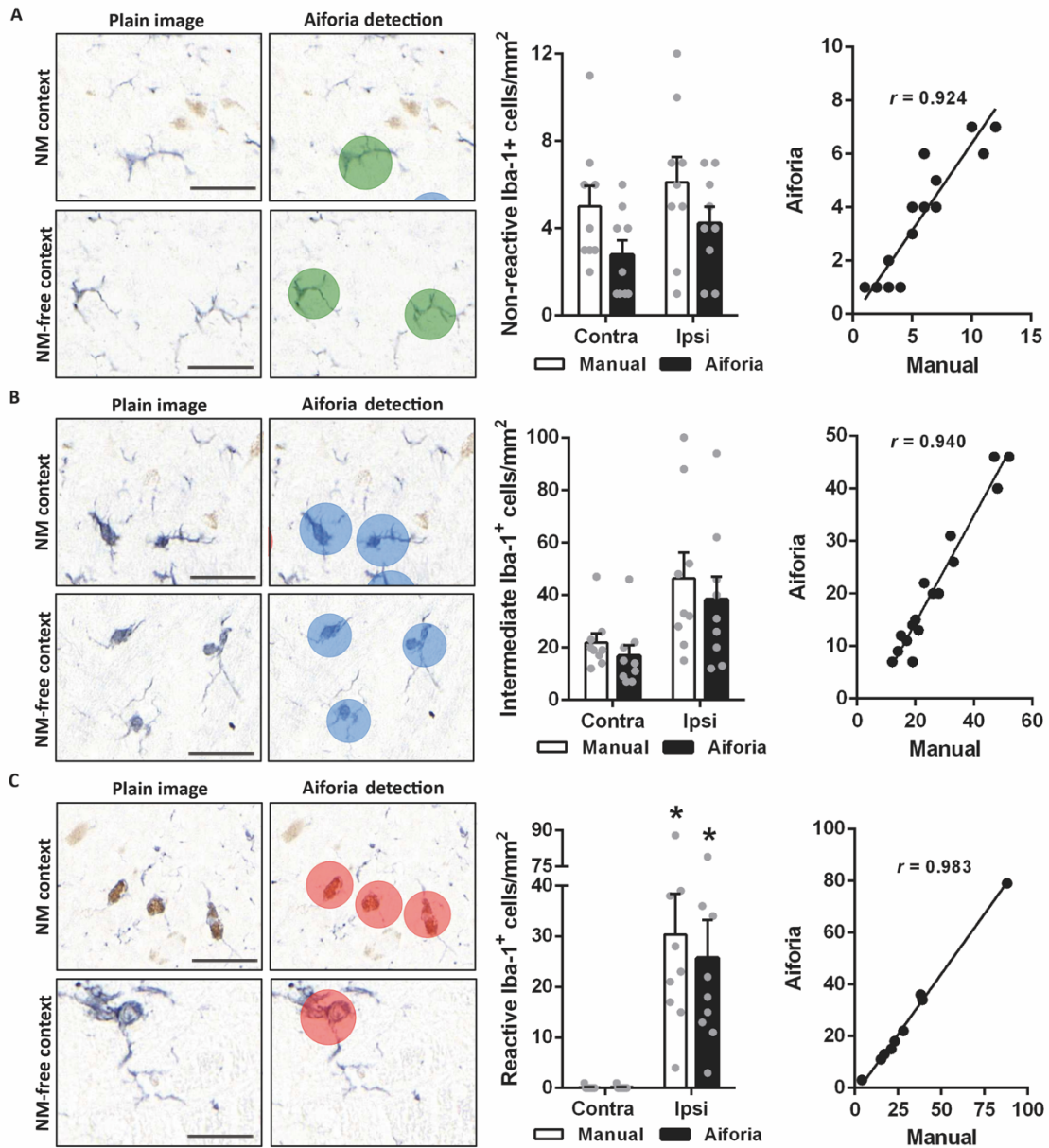


Figure 41. Deep-learning algorithm-based detection of different reactivity states of Iba-1⁺ cells in an inflammatory milieu in rat. (A) Left, representative images of Iba-1⁺-specific algorithm detecting non-reactive Iba-1⁺ microglia in NM and NM-free contexts. Scale bars, 50 μ m. **Center**, manual cell counts of SNpc non-reactive Iba-1⁺ microglia compared to deep learning-derived quantifications in AAV-hTyr-injected rats 1 month and 2 months after injection. **Right**, Spearman correlation analysis between manual and deep learning-derived quantifications. **(B) Left**, representative images of Iba-1⁺-specific algorithm detecting Iba-1⁺ microglia in an intermediate state of reactivity in NM and NM-free contexts. Scale bars, 50 μ m. **Center**, manual cell counts of SNpc intermediate reactive Iba-1⁺-microglia compared to deep learning-derived quantifications in AAV-hTyr-injected rats 1 month and 2 months after injection. **Right**, Spearman correlation analysis between manual and deep learning-derived quantifications. **(C) Left**,

representative images of Iba-1⁺-specific algorithm detecting Iba-1⁺ reactive in NM and NM-free contexts. Scale bars, 50 μ m. *Center*, manual cell counts of SNpc reactive Iba-1⁺-microglia compared to deep learning-derived quantifications in AAV-hTyr-injected rats 1 month and 2 months after injection. * $p < 0.05$, compared to respective contralateral (non-injected) side. *Right*, Spearman correlation analysis between manual and deep learning-derived quantifications without *Contra* values. In all panels, values are \pm SEM. Statistical analysis: two-way ANOVA; Student-Newman-Keuls post-hoc test. In **A-C**, $n = 9$ (*Contra*), $n = 9$ (*Ipsi*). Photomicrographs correspond to 5- μ m-thick sections. *Contra*, contralateral; *Ipsi*, ipsilateral.

Third, a fully amoeboid-shaped state that possesses phagocytic activity, whose processes have completely retracted (referred to from now on as ‘reactive state’; Fig. 41C, left panels). It is important to highlight that both intermediate- and reactive microglia are in close contact/proximity with eNM, although only the reactive microglia are in direct contact with eNM and/or are engulfing neuronal debris (neuronophagic events). On the other hand, non-reactive microglia are predominantly found in areas devoid of the presence of eNM.

We developed and validated the CNN algorithms according to these criteria. Human observers counted a total of 255 non-reactive Iba-1⁺ cells, 396 intermediate state and 281 highly-reactive cells, while the algorithm counted 178 non-reactive Iba-1⁺ cells, 351 intermediate and 265 reactive cells across 46 regions of interest encompassing the SNpc. Again, despite the huge diversity in microglial morphology, the correlation between human-based counts and the algorithms yielded robust correlations, especially for the intermediate and reactive phenotypes (Fig. 40C-E). Strong correlations across all three algorithms are sustained by the good performance metrics of each algorithm against human quantification results, as displayed in Table 6.

Table 6. Results for counting recall, precision and F1-score of the CNN algorithm compared to human observers

	GFAP⁺	CD68⁺	N-r Iba-1⁺	I-r Iba-1⁺	H-r Iba-1⁺
Recall	93.3%	93.5%	69.8%	89.4%	94.8%
Precision	99.4%	99.8%	100%	99.2%	99.6%
F1-score	96.3%	96.6%	82.2%	94.0%	97.2%

Values are mean score percentages from two different observers according to formulae in Table 7. Individual values are found in Supplemental Table1. N-r, non-reactive; I-r, intermediate state; H-r, highly-reactive.

Furthermore, apart from the strong correlations displayed by the generated algorithms, an inherent ability of the Aiforia-based automatized counting system is the possibility of performing batches of analyses simultaneously. In this regard, depending on their complexity, the counting time between algorithms varies slightly (Fig. 40F). In any case, this type of automatized counting boosts both efficiency and reproducibility compared to complete manual or stereology-based quantifications.

2.17.2 CNN ALGORITHMS ARE A RELIABLE METHOD TO ASSESS CHANGES IN INFLAMMATION

Upon validation, we quantified the level of inflammation at two different timepoints (1 month and 2 months) from our previously described time course (from 1 month up to 2 years) after AAV-hTyr injection in rats, coinciding with overt neurodegeneration and onset of PD-like symptoms⁵⁴⁷. It is relevant to point out the difficulty associated with developing these CNN algorithms, especially for GFAP- and Iba-1-related staining. Whereas CD68⁺ stained parenchyma was mostly clear and only stained macrophages were visible, for GFAP⁺ and Iba-1⁺ staining the parenchyma was crowded with non-specific or minute cell debris, partial bodies, or corpuscles from excess of NM-driven neurodegeneration, which notably enhanced the complexity of the algorithms' training procedure (Fig. 42).

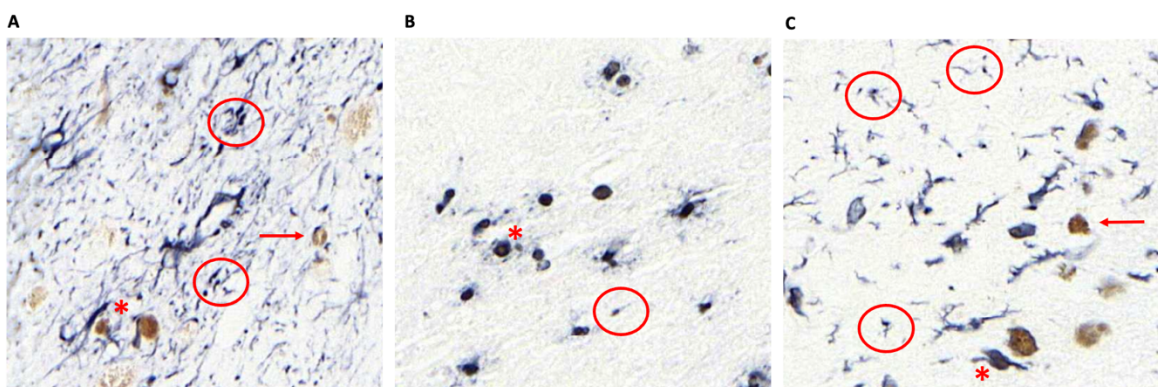


Figure 42. Representation of a typical inflammatory milieu upon eNM stimulation. Images showing reactive parenchyma upon eNM-induced innate immune system exacerbation after staining with (A) GFAP, (B) CD68 and (C) Iba-1. Red asterisks depict direct contact (A) or engulfment (B and C) of eNM granules. Red arrows illustrate *unattended* eNM. Note that in B, the presence of eNM is avidly detected by macrophages. Red circles demonstrate clear examples of non-specific staining (A, C), undefined cell parts or cell debris (A, C) or a stained element that was too small to be included in the training (B).

Therefore, to efficiently identify immune cells, this debris and the large amount of isolated eNM granules were taught in the algorithm to be discriminated as background, thus ensuring the sole identification of stained cells. Furthermore, to achieve maximal discrimination power, counting by the different algorithms was compared to whole-area analysis of stereology-based (henceforth referred to as manual) results of both the injected (ipsilateral) and the non-injected (contralateral) sides.

Following the above procedures, we ensured that our results did not rely on estimations but on exact numbers, thereby avoiding error-prone results adjustments based on slide periodicity or percentage of counted area. Under these terms, independently of the time course pattern itself, the global performance of the three algorithms generated similar results compared to the stereology approaches. Regarding the GFAP⁺-cell-detecting algorithm, despite missing some of the manually-annotated cells, the correlation between both was robust (Fig. 39A, right). In the same manner, astrogliosis between the ipsilateral and contralateral sides was also detected by the automatized algorithm. Of note, astrocytes appear to interact with eNM, but seldom phagocytose/internalize it. In contrast, macrophages only invade/activate in the presence of eNM, resulting in circular structures with eNM granules contained therein (Fig. 39B, left panel). The CD68⁺-cell-detecting algorithm generated a similar quantification of macrophages compared to the manual procedure, with a strong correlation found between both (Fig. 39B, right panel).

Next, we assessed the efficacy of the Iba-1⁺-cell-detecting algorithm to distinguish between the 3 different microglial phenotypes. Astrocytes as well as non-reactive and intermediate state microglia are ubiquitously scattered throughout the whole brain, meaning that their morphology is mostly NM-independent. When in the vicinity of eNM granules, both types of microglia maintain the same morphology, but present a stronger staining. These subtle differences can be detected by the Iba-1⁺-cell-detecting algorithm, which performs robustly compared to manual counting (Fig. 41A and B, right). Non-reactive microglia cells are rarely present in the vicinity or in close contact with eNM granules, whereas a large number of microglia are reactive and it is common to find the intermediate reactive microglia with shorter projections and rounder somas.

The exact antigenic structure of eNM that induces the structural change from mostly branched to almost amoeboid/round is currently unknown. Due to the specificity of the reactive microglia with eNM in terms of their interaction NM (reactive microglia predominantly appear engulfing eNM granules or with already phagocytized granules), algorithmic and manual quantifications gave a robust correlation (Fig. 41C). Of note, the algorithm can recognize reactive microglia not only in the presence of eNM, but also in an NM-free context (41C, lower panels). Taken together, these results demonstrate the feasibility of assessing key neuroinflammatory markers in an excessive NM-evoked PD context.

2.17.3 CNN ALGORITHMS ARE ALSO ABLE TO DETECT INFLAMMATION IN HUMAN BRAIN TISSUE

Once, we had fully confirmed the robustness of the different algorithms, we ran them on human samples to evaluate the feasibility of using AI-mediated identification of different cell types. Since our AAV-hTyr-injected PD model represents an acceleration of the natural course of the disease, we wanted to confirm that the inflammatory pattern in the SNpc of PD patients was equally identifiable. In a PD-specific context, astrocytes produce various neurotrophic molecules, including GDNF, which is especially important for the development and survival of DA neurons^{864,865}, and contribute to the integrity of the BBB, which has been shown to be disrupted in PD patients⁸⁶⁶. Additionally, when an immune response is initiated by microglia, astrocytes surround the area, creating a barrier-like structure that prevents the spread of toxic signals into the surrounding healthy tissue⁸⁶⁷. However, their role upon NM parenchymatic leakage in the PD-neurodegenerated SNpc is poorly understood⁵⁴⁷. In any case, since the exacerbation of human inflammation is not as acute as in AAV-hTyr-injected animals, astrocytes, which appeared in a more ramified fashion, were predominantly found in the vicinity of NM-containing neurons and the overall level of GFAP⁺ staining was fainter (Fig 43, upper left panels). Minimal interaction was found between astrocytes and eNM granules. As with NM-devoid contralateral sites in the rat, the algorithm was able to detect astrocytes outside the SNpc (Fig 43, upper right panels).

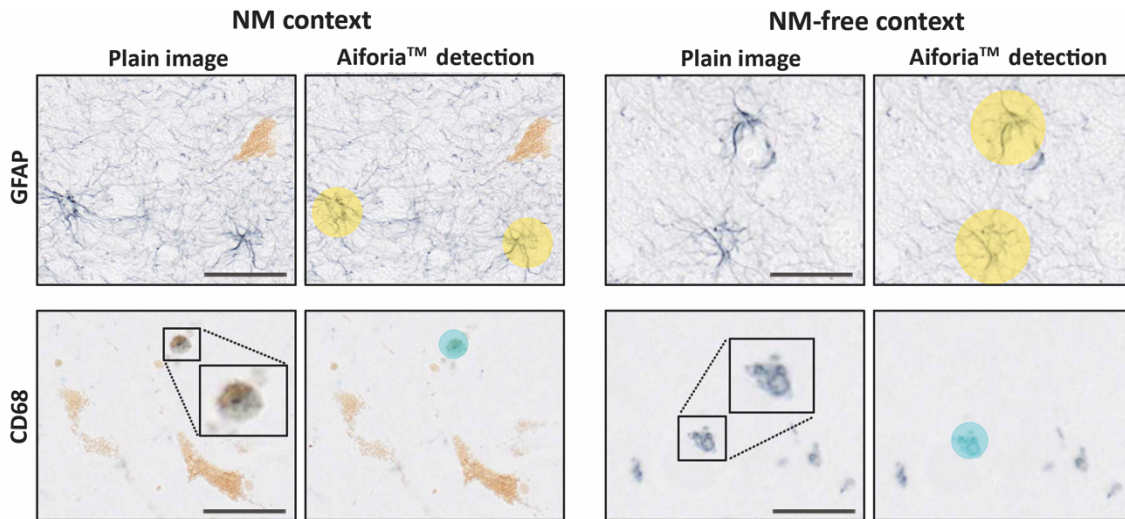


Figure 43. Deep-learning algorithm-based detection of GFAP⁺-astrocytes and CD68⁺-macrophages in a human inflammatory milieu. *Left*, representative images of GFAP- and CD68-specific algorithm-detected astrocytes and macrophages in an NM context. *Right*, representative images of GFAP- and CD68-specific algorithm-detected astrocytes and macrophages in an NM-free context. Scale bars, 50 μ m

Under pathological conditions such as neurodegeneration in PD, microglia are activated, prone to engulf debris and, by sensing pathology, potentially secrete pro- and anti-inflammatory factors⁸⁶⁸. Furthermore, they mediate responses such as inflammation and phagocytosis associated with neurodegeneration and are key players in exacerbating or relieving disease progression⁸⁶⁸. In this regard, from the commonly used markers to document the presence of activated microglia, we decided to use CD68 since it was the only one which entailed a correlation with disease duration⁸⁶⁹. In a similar manner to the detection of CD68-positive cells in rat brain tissue, the algorithm was able to detect human CD68⁺-activated microglia/macrophages with engulfed eNM granules as well as in an NM-free context (Fig.43, lower panels). Of note, microglial phagocytic activity and cytotoxic properties are usually considered to represent end stages of microglial activation, at which point they are phenotypically indistinguishable from blood-borne macrophages⁸⁶⁹. Therefore, although not being able to discriminate between resident microglia and infiltrated macrophages, CD68⁺-staining ensures the specific detection of immunogenic eNM granules in the SNpc and active phagocytic activity elsewhere. As seen in rat microglia, human Iba-1⁺ staining detects any kind of microglia, independently of its activation state⁸⁷⁰. Again, as described above, we defined Iba-1⁺ ramified microglia as cells having a small/almost absent circular body with highly ramified processes. The intermediate/primed phenotype displays a larger cell body and

fewer, thicker ramifications, while the amoeboid phenotype has few or no ramified processes^{863,871,872}. Despite minor morphological differences, the Iba-1⁺-cell-detecting algorithm also performed well in recognizing human microglia with the referred three different phenotypes (Fig. 44).

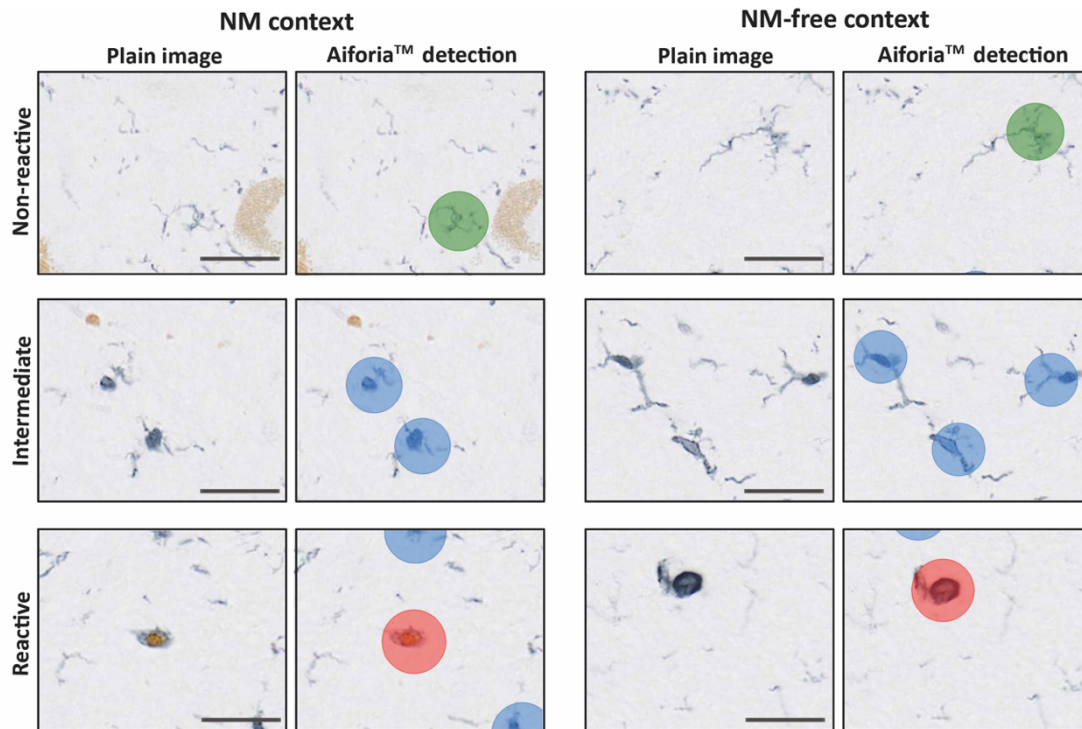


Figure 44. Deep-learning algorithm-based detection of different reactivity states of Iba-1⁺ cells in a human inflammatory milieu. *Left*, representative images of Iba-1⁺-specific algorithm detection of Iba-1⁺ non-reactive, intermediate-reactive, and reactive microglia in an NM context. *Right*, representative images of Iba-1⁺-specific algorithm detection of Iba-1⁺ non-reactive, intermediate-reactive, and reactive microglia in an NM-free context.

In the context of PD, NM has been thoroughly described as a strong immunogenic agent, particularly as an activator of microglia^{547,732,733}. As such, identification of the naturally-induced formation of human eNM granules being phagocytized or already internalized by reactive microglia with macrophagic activity was equally recognized as with the viral hTyr-induced, excessively-accumulated animal model version (Fig. 44, left lower panels). Isolated, small spots of inflammation devoid of NM were also recognized by the Iba-1⁺ algorithm (Fig. 44, right lower panels). All in all, these results confirm that the three different trained algorithms can be employed not only in NM and NM-free contexts, but also between different species, thereby allowing a quick, reliable and efficient automatized quantitative assessment of brain inflammation, PD-affected or not.

2.18 GENERAL STATISTICAL ANALYSIS

Statistical analyses were performed with GraphPad Prism software (v6, GraphPad Software Inc, USA). No statistical methods were used to pre-determine sample size; however the employed sample sizes and those reported in previous publications are similar⁵⁴⁷. Outlier values were identified by the ROUT test and excluded from the analyses when applicable. Selection of the pertinent data representation and statistical test for each experiment was determined after formally testing for normality with the Shapiro-Wilk normality test. Accordingly, differences among means or medians were analyzed either by 1- or 2-way analysis of variance (ANOVA), Kruskal–Wallis ANOVA on ranks or the Mann–Whitney rank sum test as appropriate and indicated in each figure legend. When ANOVA showed significant differences, pairwise comparisons between means were subjected to Tukey’s post-hoc testing for multiple comparisons. Values are expressed either as mean \pm standard error of the mean (SEM) or presented as box plots, with minimum, maximum and median values indicated, depending on the performance of parametric or non-parametric analyses, respectively. In all analyses, the null hypothesis was rejected at the 0.05 level.

2.19 STATISTICAL ANALYSIS OF CNN ALGORITHMS

Spearman or Pearson correlations were used (depending on data normality based on the Shapiro-Wilk test) during algorithm development to compare manually obtained results with CNN-produced results. Recall, precision, and F1-score were computed to compare human versus algorithm counts (Table 7).

Table 7. Formulas for calculating recall, precision and F1-score for the CNN algorithm

Metrics
Recall = $TP/(TP+FN)$
Precision = $TP/(TP+FP)$
F1-score = $2*Recall*Precision / (Recall+ Precision)$

TP, true positive; FN, false negative; FP, false positive

IV. RESULTS

CHAPTER I: *IN VIVO* REDUCTION OF AGE-DEPENDENT NEUROMELANIN ACCUMULATION MITIGATES FEATURES OF PARKINSON'S DISEASE

1. VMAT2 OVEREXPRESSION REDUCES CATECHOL OXIDATION, NM ACCUMULATION AND LB-LIKE INCLUSION FORMATION IN NM-PRODUCING RATS

To determine whether VMAT2 overexpression was able to boost DA vesicular uptake *in vivo*, adult rats received a single unilateral stereotaxic injection of an AAV expressing flagged human VMAT2 (AAV-hVMAT2) above the right SNpc (Fig. 45A). In these animals, conspicuous exogenous VMAT2 expression was observed in the ipsilateral SNpc and STR at 1 month (m) post-AAV injection, as assessed by Flag immunohistochemistry (Fig. 45B). Overexpressed VMAT2 proved to be functionally active, as demonstrated by (i) an enhanced striatal DA storage accompanied by a decreased DA metabolism⁸⁷³ and (ii) an approximately 2-fold increase in the striatal DA:L-DOPA ratio, an index of DA vesicular uptake⁸⁷⁴, measured by UPLC-MS/MS at 2 m post-AAV injection (Fig. 45C and Supplementary Table 1 (annex)).

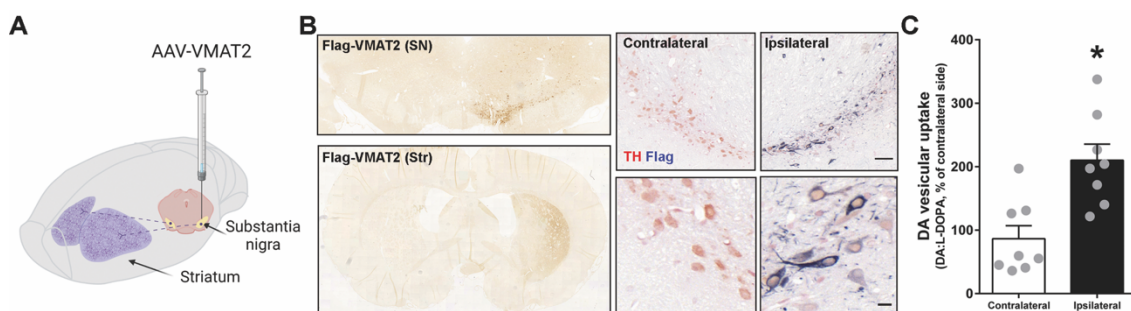


Figure 45. Overexpression of functional VMAT2 in the nigrostriatal pathway of rats. (A) Schematic representation of the site of AAV-hVMAT2 unilateral stereotaxic injection above the SN of the rat brain. (B) *Left*, representative images of nigral (top) and striatal (bottom) Flag-VMAT2 immunolabeling ipsilateral to the AAV-hVMAT2 injection in rats at 1 m post injection. *Right*, representative images of TH-Flag colocalization in ipsilateral SNpc of AAV-hVMAT2-injected rats at 1 m post injection; Scale bar: 50 μm (top), 10 μm (bottom). (C) Quantification of striatal DA vesicular uptake by UPLC-MS/MS in AAV-hVMAT2-injected rats at 2 m post injection, as calculated by the ratio between striatal DA:L-DOPA levels⁸⁷⁴. Values are mean ± SEM. * $p < 0.05$ vs. contralateral (non-injected) side; Two-tailed t-test. $N = 8$ animals per group. Drawing in A was created with BioRender.com.

After confirming that we were able to overexpress functional VMAT2 *in vivo*, we next assessed whether nigrostriatal VMAT2 overexpression in NM-producing rats could

increase DA vesicular uptake and reduce the rate of non-encapsulated DA oxidation into NM precursors. To address this question, AAV-hVMAT2 and AAV-hTYR were co-injected above the rat SNpc (Fig.46, 47, Supplementary Table 2 (annex)), with additional groups of animals receiving equivalent amounts of either AAV-hTYR or AAV-hVMAT2 separately. In AAV-hTYR-injected rats, we previously reported that intracellular NM starts reaching pathological levels at 2 m post-AAV injection, at which time these animals exhibit early functional defects, including impaired DA release and motor deficits, prior to degeneration⁵⁴⁷. Here we found, similar to PD patients^{42,586}, that early functional changes in AAV-hTYR melanized rats are accompanied by a downregulation of endogenous VMAT2 levels, as shown by a reduction of VMAT2 expression within NM-containing neurons (Fig. 46A and Supplementary Table 3 (annex)), and alterations in nigrostriatal DA homeostasis, such as reduced DA vesicular uptake, decreased DA levels, increased DA metabolism and enhanced catechol oxidation (Fig. 46B-E, 48 and Supplementary Tables 4&5 (annex)). Remarkably, all these pathological changes were prevented by overexpressing VMAT2 in these animals (Fig. 46A-E, and Supplementary Tables 4&5 (annex)).

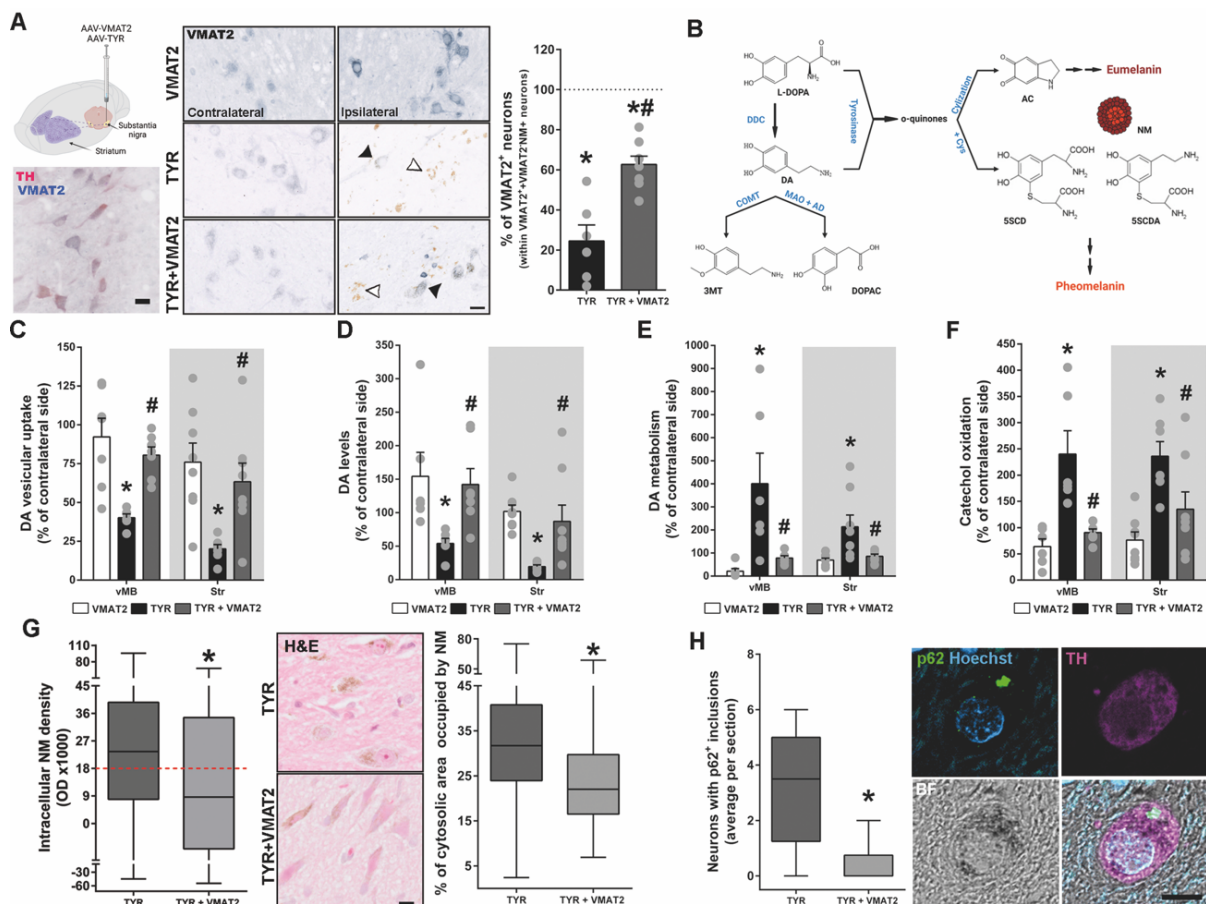


Figure 46. Reduced catechol oxidation, NM accumulation and LB-like pathology by VMAT2 overexpression in NM-producing rats. (A) *Left*, schematic representation of the site of AAV-hVMAT2, AAV-hTYR or AAV-hVMAT2+AAV-hTYR unilateral stereotaxic injection above the SN of the rat brain. *Right*, quantification of ipsilateral SNpc neurons immunopositive for VMAT2 in AAV-hTYR and AAV-hTYR+AAV-hVMAT2-injected rats at 2 m post injection. Total ipsilateral DA neurons include VMAT2+NM+, VMAT2+NM- and VMAT2-NM+ neurons. Representative contralateral and ipsilateral VMAT2-immunostained SNpc sections from these animals are shown in micrographs; Scale bar 20 μ m (B) Schematic representation of DA metabolism and oxidation pathways. DA is synthesized from L-DOPA in the cytoplasm by DDC. Cytosolic DA can be degraded by MAO to produce 3-MT or by MAO followed by AD to produce DOPAC. On the other hand, both cytosolic DA and L-DOPA can be oxidized either spontaneously or by tyrosinase to produce *o*-quinones. These, in turn generate AC, 5SCDA and 5SCD which act as precursors of the eumelanin and pheomelanin components of NM. 5SCD, 5-S-cysteinyl-dopa; 5SCDA, 5-S-cysteinyl-dopamine; AC, aminochrome; AD, aldehyde dehydrogenase; COMT, catechol-O-methyltransferase; DA, dopamine; DDC, dopa decarboxylase; DOPAC, 3,4-dihydroxyphenylacetic acid; L-DOPA, 3,4-dihydroxyphenylalanine; MAO, monoamine oxidase; 3-MT, 3-methoxytyramine; NM, neuromelanin. UPLC-MS/MS quantification of: (C) DA vesicular uptake (calculated as DA:L-DOPA); (D) DA levels; (E) DA metabolism (calculated as [3-MT+DOPAC]:DA); (F) catechol oxidation (calculated as [5SCD:L-DOPA+(5SCDA+AC):DA]) in ventral midbrain (vMB) and striatal samples from AAV-hVMAT2-, AAV-hTYR- and AAV-hTYR+AAV-hVMAT2-injected animals at 2 m post injection. Results represent ipsilateral levels shown as the percentage of the contralateral (non-injected) side. Values are mean \pm SEM. (G) *Left*, quantification of intracellular NM levels by optical densitometry in ipsilateral SNpc DA neurons of AAV-hTYR- and AAV-hTYR+AAV-hVMAT2-injected rats at 2 m post injection. Dotted red line indicates the previously reported pathological threshold of intracellular NM accumulation (5). *Right*, percentage of neuronal cytosolic area occupied by NM in AAV-hTYR- and AAV-hTYR+AAV-hVMAT2-injected rats at 2 m post-injection. Values are median + min to max. *Center*, representative images of 5 μ m-thick H&E-stained nigral sections from these animals (unstained NM in brown); Scale bar: 10 μ m. (H) *Left*, quantification of the number of NM-filled neurons exhibiting p62-positive LB-like cytosolic inclusions in AAV-hTYR- and AAV-hTYR+AAV-hVMAT2-injected rats at 2 m post-injection. Values are median + min to max. *Right*, representative confocal images of a melanized TH⁺ neuron with an LB-like inclusion immunopositive for p62 in the SNpc of an AAV-hTYR-injected rat; BF, brightfield; Scale bar: 10 μ m. In **A**, * p <0.05 VMAT2⁺ vs. VMAT2⁻; # p <0.05 vs. TYR; Two-way ANOVA with Tukey's post-hoc test. N = 6 (TYR), 8 (TYR+VMAT2) animals. In **C-F**, * p <0.05 vs. VMAT2⁻; # p <0.05 vs. TYR; one-way ANOVA with Tukey's post-hoc test. N = 6-8 (VMAT2⁻), 6-8 (TYR), 6-8 (TYR+VMAT2) animals. In **G-H**, * p <0.05 vs. TYR; Mann-Whitney test. N =594 neurons from 8 AAV-hTYR-injected animals and 180 neurons from 8 AAV-hTYR+AAV-hVMAT2-injected animals.

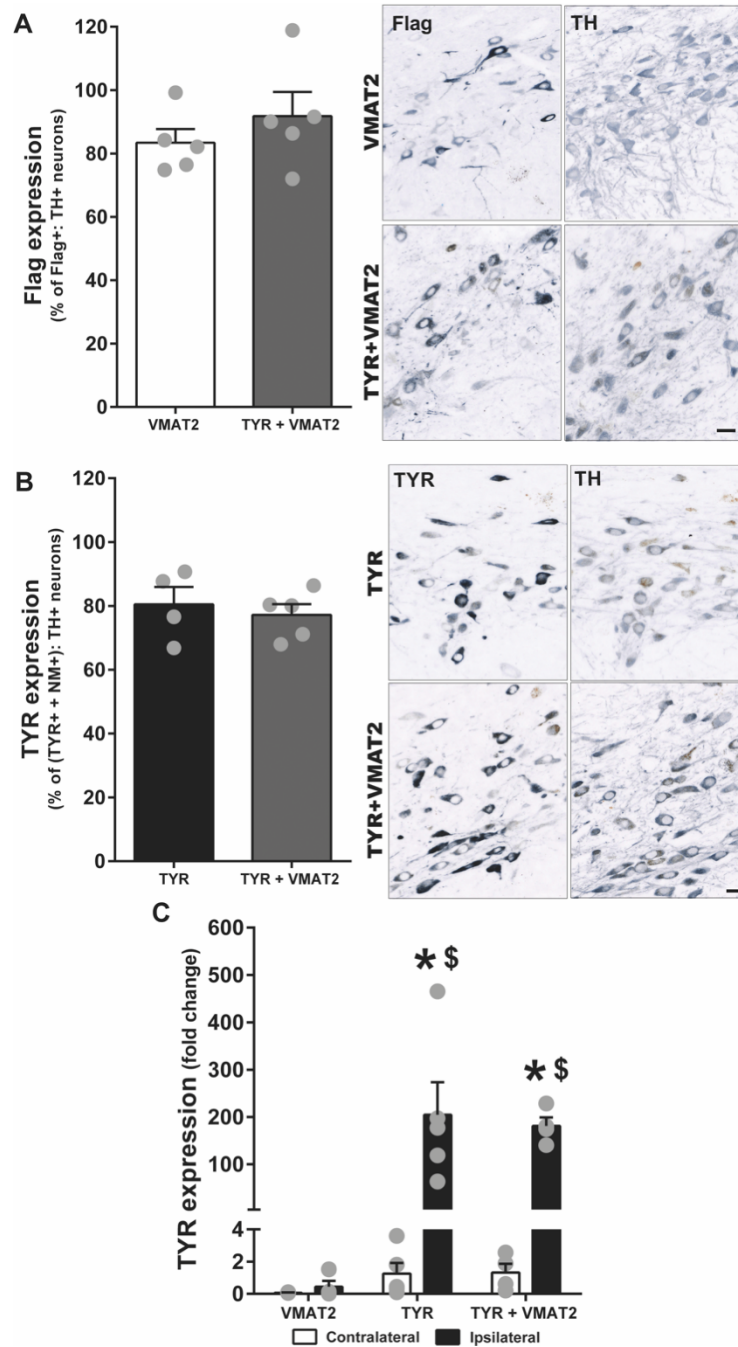


Figure 47. hTYR and hVMAT2 transduction efficiency in AAV-hTYR- and AAV-hVMAT2-injected animals, alone or in combination. (A-B) Percentage of SNpc TH-positive neurons expressing Flag-VMAT2 **(A)** or TYR **(B)** at 1 m post-AAV injection, as assessed in serial 5 μ m-thick adjacent paraffin sections covering the entire SN (every 17th section for a total of 10-12 sections analyzed/animal). Photomicrographs correspond to representative images of adjacent SNpc sections immunostained for either **(A)** Flag or TH (in gray, unstained NM in brown) and **(B)** TYR or TH (in gray, unstained NM in brown). Scale bars: 20 μ m. **(C)** TYR mRNA levels assessed by qPCR in contralateral and ipsilateral vMB samples from VMAT, TYR and TYR+VMAT2 animals. In all panels, values are mean \pm SEM. In **(A-B)**, N.S. (two-tailed t-test). In **(C)**, * p <0.05 vs. ipsilateral VMAT2; $\text{\$}$ p <0.05 vs. respective contralateral side; two-way ANOVA with Tukey's post-hoc test. In **(A-B)** N= 5 (VMAT2), 4 (TYR), 5 (TYR+VMAT2) animals. In **(C)** N= 3-4 (VMAT2), 5 (TYR), 4 (TYR+VMAT2) animals.

When oxidized, tyrosine, L-DOPA or DA produce dopaquinone or DA *o*-quinone that will act as precursors for either the eumelanin (brown) and/or the pheomelanin (reddish) melanic components of NM (Fig. 48). We next assessed whether attenuated catechol oxidation in VMAT2/TYR co-injected animals was associated with a reduced NM production. Quantification of intracellular NM optical density values within individual SNpc neurons, which reflects NM levels^{875,876}, revealed that the intracellular NM density was significantly decreased in SNpc neurons from TYR+VMAT2 rats compared to AAV-hTYR-injected animals (Fig. 46F). While the intracellular NM optical density could be influenced by potential changes in NM composition, independently of the actual levels of NM, we also observed a significant reduction in the percentage of cytosolic neuronal area occupied by NM in TYR+VMAT2 animals compared to their TYR counterparts (Fig. 46F), indicating an actual decrease of NM levels in these animals.

Importantly, VMAT2 overexpression reduced intracellular NM to levels below the pathological NM threshold previously identified in NM-producing animals⁵⁴⁷ (red dotted line in Fig. 46F). Above this threshold, in addition to the functional deficits reported earlier, NM-laden neurons develop LB-like inclusions (Fig. 46G and Supplementary Table 3 (annex)), a hallmark of PD pathology closely associated with NM accumulation^{547,877,878}. LB-like inclusions in NM-producing rats were immunopositive for p62, a common component of LBs in PD brains⁸⁷⁹, and were previously reported to peak at 2 m post-AAV-hTYR injection, thus coinciding with functional alterations and preceding neurodegeneration in these animals⁵⁴⁷. Importantly, the reduction of intracellular NM levels by VMAT2 overexpression was accompanied by attenuated LB-like inclusion formation in these neurons (Fig. 46G, H and Supplementary Table 3 (annex)). Taken together, these results demonstrate that VMAT2 overexpression is able to restore DA homeostasis, reduce NM production/accumulation, and attenuate LB-like pathology *in vivo*.

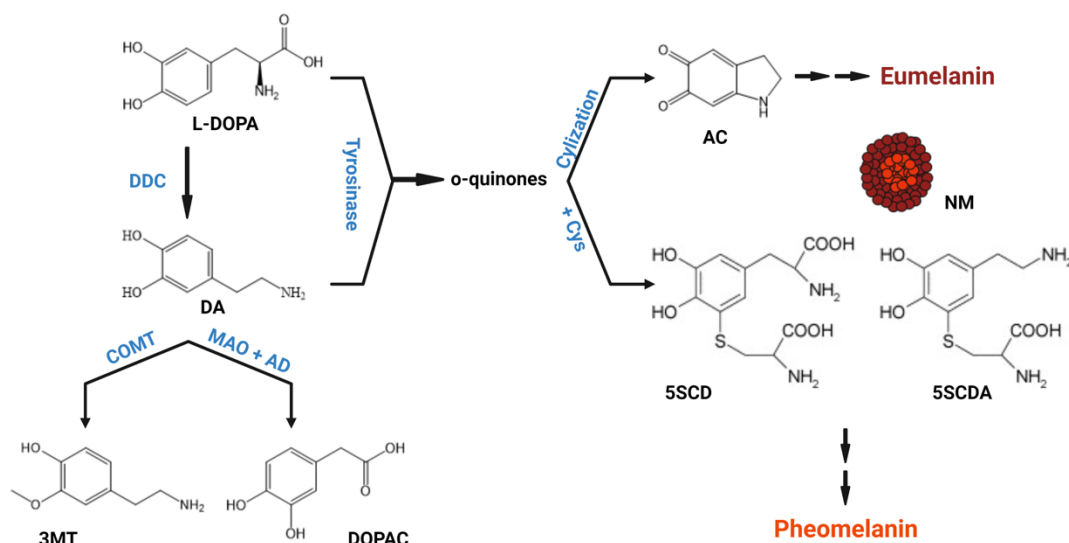


Figure 48. Schematic representation of DA metabolism and oxidation pathways. DA is synthesized from L-DOPA in the cytoplasm by DDC. Cytosolic DA can be degraded by MAO to produce 3-MT or by MAO followed by AD to produce DOPAC. On the other hand, both cytosolic DA and L-DOPA can be oxidized either spontaneously or by tyrosinase to produce o-quinones. These, in turn, generate AC, 5SCDA and 5SCD which will act as precursors of the eumelanin and pheomelanin components of NM. 5SCD, 5-S-cysteinyl-dopa; 5SCDA, 5-S-cysteinyl-dopamine; AC, aminochrome; AD, aldehyde dehydrogenase; COMT, catechol-O-methyltransferase; DA, dopamine; DDC, dopa decarboxylase; DOPAC, 3,4-dihydroxyphenylacetic acid; L-DOPA, 3,4-dihydroxyphenylalanine; MAO, monoamine oxidase; 3-MT, 3-methoxytyramine; NM, neuromelanin. Figure was created with BioRender.com.

2. VMAT2 OVEREXPRESSION PREVENTS NM-LINKED NEURODEGENERATION

Early functional defects observed at 2 m in NM-producing rats are followed by progressive nigrostriatal neurodegeneration beginning at 4 m post-AAV-hTYR injection⁵⁴⁷. To determine whether decreased DA oxidation and the subsequent reduction in NM accumulation achieved by VMAT2 overexpression were associated with preserved neuronal integrity, we assessed the long-term effects of VMAT2 overexpression in NM-producing rats at 6 m post-AAV-hTYR injection, once nigrostriatal degeneration is well-established in this animal model⁵⁴⁷. By this time, NM-producing rats exhibited an approximately 90% reduction in ipsilateral SNpc TH-positive neurons that was markedly attenuated by concomitant VMAT2 overexpression (Fig. 49 and Supplementary Table 6 (annex)). Similar to PD brains, NM-producing rats also exhibited a phenotypic loss of TH expression within NM-laden neurons, which reflects neuronal

dysfunction in the early stages of neurodegeneration⁷¹⁷, as shown by an increased percentage of TH-immunonegative neurons within the total population of NM-containing neurons (Fig. 49B and Supplementary Table 6 (annex)). Interestingly, VMAT2 overexpression significantly attenuated TH downregulation taking place within pigmented neurons, indicating a functional preservation of these neurons (Fig. 49B and Supplementary Table 6 (annex)). To distinguish between the effects of VMAT2 on TH downregulation and on actual cell death, we assessed the number of total SNpc DA neurons (including TH-immunopositive and TH-immunonegative pigmented SNpc neurons), which confirmed the ability of VMAT2 overexpression to prevent NM-linked SNpc DA neurodegeneration in NM-producing rats (Fig. 49C and Supplementary Table 6 (annex)). Overall, these results indicate that VMAT2 overexpression is able to prevent neuronal dysfunction and degeneration linked to excessive NM production/accumulation.

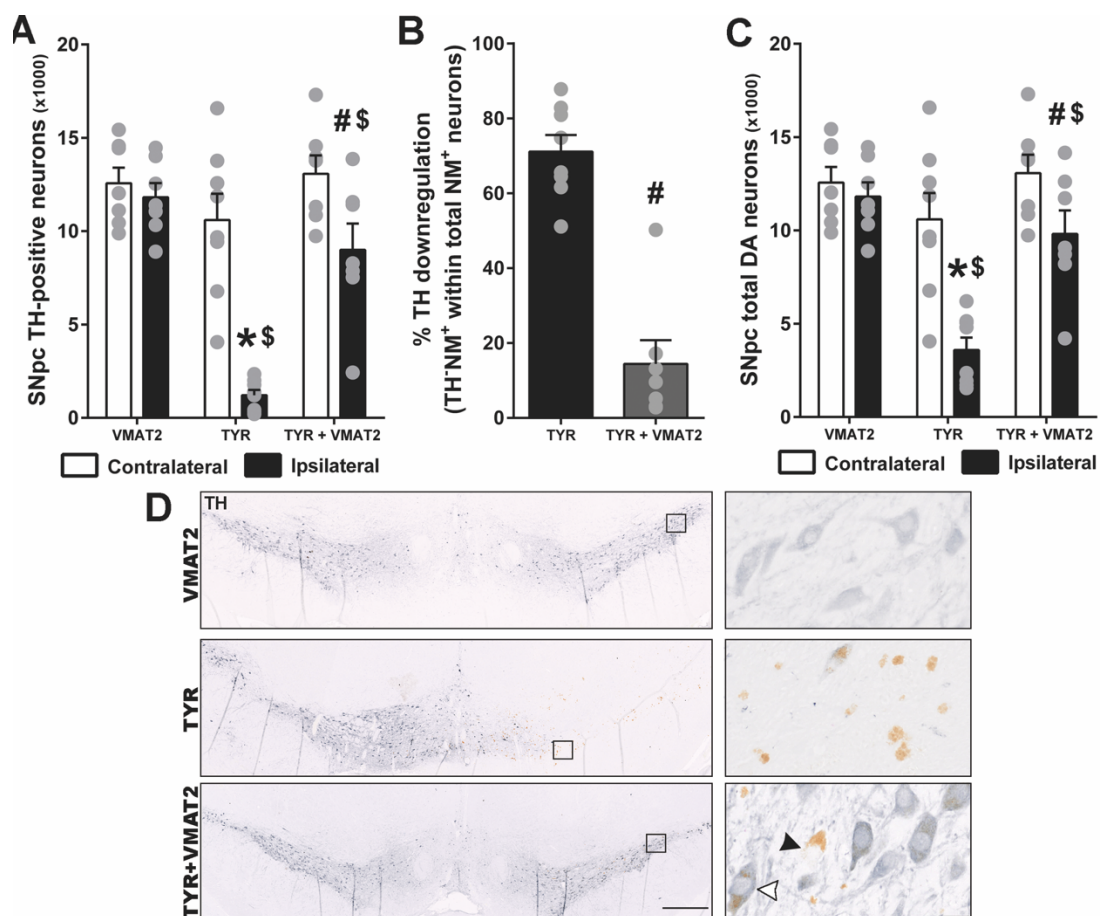


Figure 49. VMAT2 overexpression prevents SNpc neurodegeneration in NM-producing rats. Stereological nigral cell counts of: (A) TH⁺ neurons; (B) TH-NM⁺ neurons vs total NM⁺ neurons (including TH⁺NM⁺ and TH⁻NM⁺ neurons) as an index of TH downregulation; (C) total DA neurons (including TH⁺NM⁺, TH⁺NM⁻ and TH⁻NM⁺ neurons), in AAV-hVMAT2-, AAV-hTYR- and AAV-hTYR+AAV-hVMAT2-injected rats at 6 m post injection. (D) Representative images of TH-stained

neurons (TH in blue, unstained NM in brown), in which TH⁺NM⁺ (black arrowhead) and TH⁺NM⁻ (white arrowhead) neurons are indicated; scale bars: 200 μ m & 20 μ m (insert). Values are mean \pm SEM. * p <0.05 vs. ipsilateral VMAT2; # p <0.05 vs. ipsilateral TYR; § p <0.05 vs. respective contralateral side; & p <0.05 vs. TH⁺NM⁺; Two-way ANOVA with Tukey's post-hoc test. N =7 (AAV-hVMAT2), 8 (AAV-hTYR) and 7 (AAV-hTYR+AAV-hVMAT2) animals.

3. ATTENUATED NEURODEGENERATION BY VMAT2 OVEREXPRESSION IS ASSOCIATED WITH A REDUCTION IN EXTRACELLULAR NM DEBRIS AND INFLAMMATION

Concomitant with SNpc pigmented cell death, PD brains and NM-producing rats exhibit abundant extracellular NM released from dying neurons, some of which is surrounded by, or contained within activated microglia, indicative of an active, ongoing neurodegenerative process (i.e. neuronophagia)^{547,734}. In this context, the marked neuroprotective effect provided by VMAT2 overexpression in NM-producing rats at 6 m post-AAV injection was associated with a drastic reduction of extracellular NM in these animals (Fig. 50A). In agreement with microglial cells being the main players in the recognition, engulfment and clearance of extracellular NM^{728,734}, the number of microglial cells with non-reactive (ramified) and phagocytic/reactive (large amoeboid de-ramified) morphologies was markedly increased in AAV-hTYR-injected rats in association with the presence of extracellular NM and concomitant cell death (Fig. 50B and Supplementary Table 6 (annex)). By attenuating neurodegeneration and subsequent accumulation of extracellular NM, VMAT2 overexpression was associated with a diminished microglial activation in these animals (Fig. 50B and Supplementary Table 6 (annex)). Similarly, VMAT2 overexpression also precluded the recruitment of CD68-positive cells in NM-producing animals, corresponding to tissue-resident or blood-borne macrophages with phagocytic activity that are found in close association with extracellular NM (Fig. 50C and Supplementary Table 6 (annex)). Additional inflammatory changes observed in NM-producing rats included increased astrocyte reactivity that was widely distributed within the SNpc; this was also markedly attenuated by VMAT2 overexpression (Fig. 50D). Taken together, these results reveal that, by reducing cell death and subsequent NM release from dying neurons, VMAT2 overexpression is able to prevent the overall PD-like inflammatory response linked to the accumulation of extracellular NM.

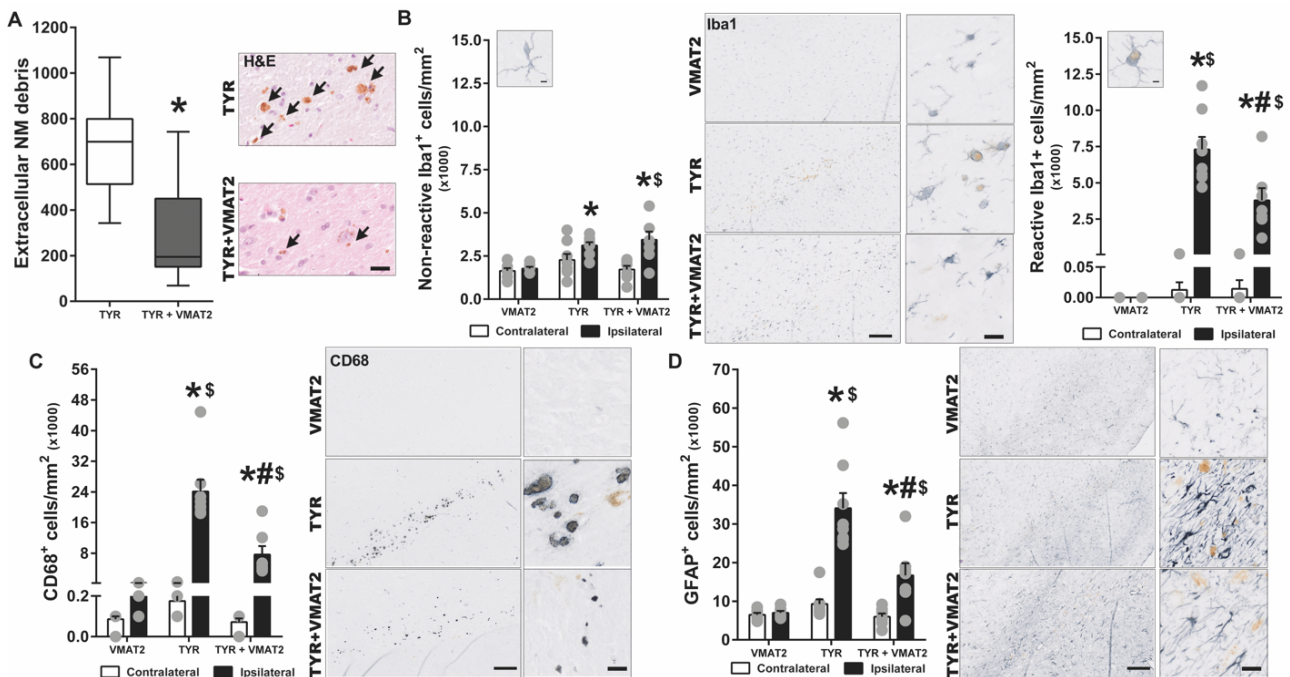


Figure 50. VMAT2 overexpression reduces extracellular NM debris and inflammation in the SNpc of NM-producing rats. Quantification of: (A) extracellular NM clusters; (B) Iba1+ non-reactive (left) and reactive (right) microglia; (C) CD68+ cells; (D) GFAP+ astrocytes, in AAV-hVMAT2-, AAV-hTYR- and AAV-hTYR+AAV-hVMAT2-injected rats at 6 m post injection. Photomicrographs correspond to representative images of (A) H&E-stained SNpc sections (unstained NM in brown) and (B-D) SNpc sections immunostained for Iba1, CD68 or GFAP (in blue, unstained NM in brown). Scale bars: 10 μ m (A, insets in B-D), 200 μ m (B-D). In (A) Values are median + min to max. In B-D, values are mean \pm SEM. * p <0.05 vs. ipsilateral VMAT2; # p <0.05 vs. ipsilateral TYR; $\text{\$}$ p <0.05 vs. contralateral side; Mann-Whitney test (A) or two-way ANOVA with Tukey's post-hoc test (B-D). $N=7$ (VMAT2), 8 (TYR), 7 (TYR+VMAT2) animals.

4. PRESERVATION OF STRIATAL DA LEVELS AND METABOLISM BY VMAT2 OVEREXPRESSION PREVENTS MOTOR DEFICITS IN NM-PRODUCING RATS

We next determined whether the neuroprotective effects of VMAT2 overexpression on SNpc DA neuron cell bodies were accompanied by a preservation of striatal DA levels in NM-producing rats. At 6 m post-AAV-hTYR injection, concomitant to SNpc neurodegeneration, NM-producing rats exhibited a marked reduction of striatal DA levels as assessed by UPLC-MS/MS (Fig. 51A and Supplementary Table 7 (annex)). Consistent with its ability to preserve DA nigral cell bodies, VMAT2 overexpression also prevented the loss of striatal DA in these animals (Fig. 51A and Supplementary Table 7 (annex)). The preservation of striatal DA levels by VMAT2 overexpression was associated with a re-established striatal DA vesicular uptake, reduced DA metabolism and decreased catechol oxidation in these animals (Fig. 51B-D, and Supplementary Table 7

(annex)). Confirming a functional preservation of the nigrostriatal circuit, VMAT2 overexpression prevented contralateral forepaw hypokinesia occurring in NM-producing rats, both at 2 m and 6 m post-AAV injections (Fig. 51E). Collectively, these results demonstrate the ability of VMAT2 overexpression to provide a morphological and functional long-term preservation of the nigrostriatal pathway *in vivo* in a humanized PD model.

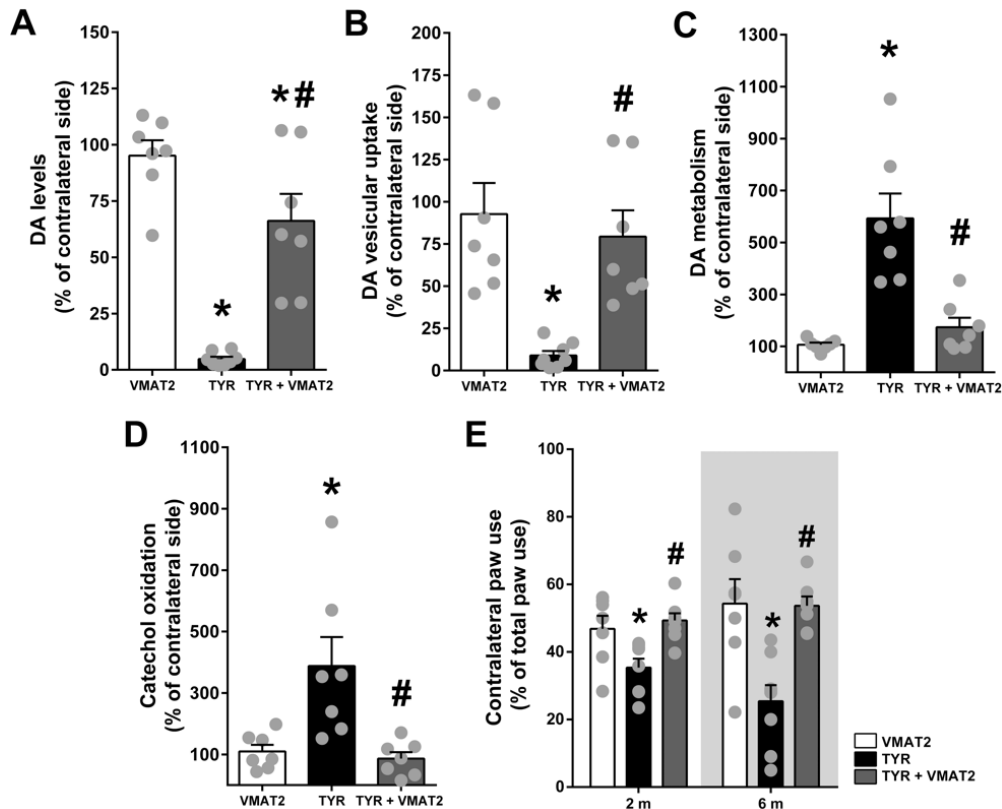


Figure 51. VMAT2 overexpression preserves striatal DA levels and motor function in NM-producing rats. UPLC-MS/MS quantification of striatal (A) DA levels; (B) DA vesicular uptake (calculated as DA:L-DOPA ratio); (C) DA metabolism (calculated as [3-MT+DOPAC]:DA ratio); (D) catechol oxidation (calculated as [5SCD:L-DOPA+(5SCDA+AC):DA] ratio), in AAV-hVMAT2-, AAV-hTYR- and AAV-hTYR+AAV-hVMAT2-injected animals at 6 m post-injection. Results represent ipsilateral levels shown as the percentage of the contralateral (non-injected) side. (E) Contralateral forepaw use was assessed with the cylinder asymmetry test at 2 m and 6 m post-AAV injections. Values are mean \pm SEM. * p <0.05 vs. VMAT2; # p <0.05 vs. TYR, one-way ANOVA with Tukey's post-hoc test. N = 7 (VMAT2), 7-8 (TYR), 7-8 (hTYR+VMAT2) animals.

Figure 52 depicts a complete summary of the aforementioned results.

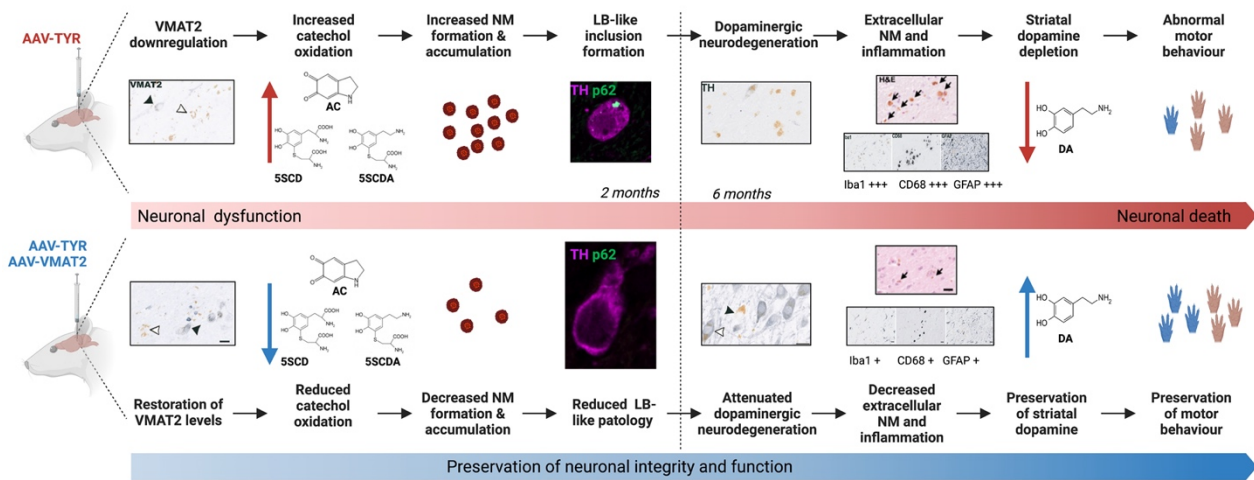


Figure 52. Summary of VMAT2 overexpression-mediated therapeutic effect in NM-accumulating PD rats. VMAT2 overexpression prevented the increase of catechol oxidation observed in the TYR group of animals. As a result, DA neurons of TYR+VMAT2 animals accumulated much less NM. In turn, the reduced level of NM led to decreased neuronal damage (indicated by a reduced number of cytoplasmic inclusions) and to a decreased TH downregulation, which in turn reduced neuronal death. As fewer NM-laden neurons died, less NM was released to the extracellular compartment, reducing extracellular NM-linked inflammation and its associated damage to neuronal fibers. This, in conjunction with the increased neuron survival prevented the loss of striatal dopaminergic fibers. Consequently, VMAT2 overexpression prevented the reduction in striatal DA content and the impairment of motor behavior observed in TYR animals. Figure was created with BioRender.com.

CHAPTER II: MRI-GUIDED TRANSCRANIAL FOCUSED ULTRASOUND ATTENUATES PARKINSON'S DISEASE-LIKE FEATURES IN NEUROMELANIN-PRODUCING RATS

1. EARLY-STAGE MRI-GUIDED TFUS APPLICATION IN NM-PRODUCING PARKINSONIAN RATS

To determine the potential direct effects of tFUS treatment on the PD-like phenotype, we used our recently developed NM-producing rat model, which recapitulates several features of PD, including LB-like inclusion formation, degeneration of nigrostriatal NM-producing neurons, extracellular NM released from dying neurons, inflammatory changes and motor deficits⁵⁴⁷. This model is based on the adeno-associated viral vector-mediated expression of melanin producing enzyme Tyr (AAV-hTyr) in the rat SN. By 1 month post-AAV these animals exhibit intracellular NM levels equivalent to aged human SN⁵⁴⁷. From 1-2 m post-AAV, intracellular NM reaches levels equivalent to those observed in ILBD subjects and PD patients. Likewise, these animals start exhibiting a PD-like phenotype that becomes fully established by 4 m post-injection⁵⁴⁷ (Fig. 53).

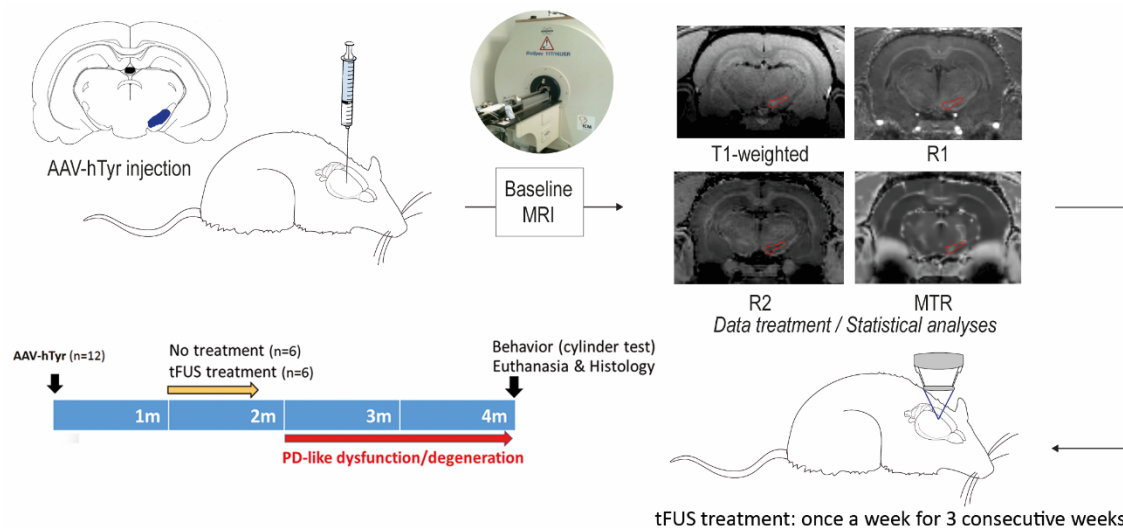


Figure 53. Schematic representation of the experimental design for the tFUS treatments in parkinsonian NM-producing rats (see text for details).

Based on these temporal dynamics, we decided to apply tFUS treatment between 1 and 2 m post-AAV, analogous to early PD stages, and assess the long-term behavioral and histological effects at 4 m post-AAV. Accordingly, AAV-hTyr-injected and control naïve

rats (we have previously shown that AAV-empty vector (EV) does not produce any phenotype) were divided into 2 experimental groups for either tFUS or sham treatment (n=6 animals per treatment and group). By taking advantage of the presence of NM in AAV-hTyr-injected rats, NM-sensitive MRI was performed to guide the application of tFUS into the SN. In all experimental groups, MRI-guided tFUS/sham treatments were performed once a week for 3 consecutive weeks at an $I_{\text{spta}} = 1.1\text{W}/\text{cm}^2$. At 4 m post-AAV-hTyr injection, corresponding to ~2.5 m after the last tFUS application, animals were assessed for contralateral paw akinesia (cylinder test) and processed for neuropathological examination. Overall, MRI-guided tFUS application in the SN of NM-producing rats proved feasible, reproducible, localized, and could thus be used to further investigate the influence of this treatment on the PD-like phenotype in this animal model.

2. TFUS REDUCES INTRACELLULAR NM LEVELS AND EXTRACELLULAR NM DEBRIS IN NM-PRODUCING PARKINSONIAN RATS

Because of the reported capacity of tFUS to reduce UV-induced skin melanin hyperpigmentation³¹⁴, we assessed here whether tFUS focused at the melanized SN could decrease the age-dependent accumulation of nigral NM. This was determined by measuring both intracellular NM levels and extracellular NM debris released from dying neurons in NM-producing parkinsonian rats at 4 m post-AAV-hTyr injection, once these animals have reached pathological NM levels linked to conspicuous nigrostriatal degeneration. In these animals, tFUS treatment was associated with a significant reduction in intracellular NM density, reflecting the actual concentration/levels of NM, and a decreased percentage of cytosolic neuronal area occupied by NM (Fig. 54A).

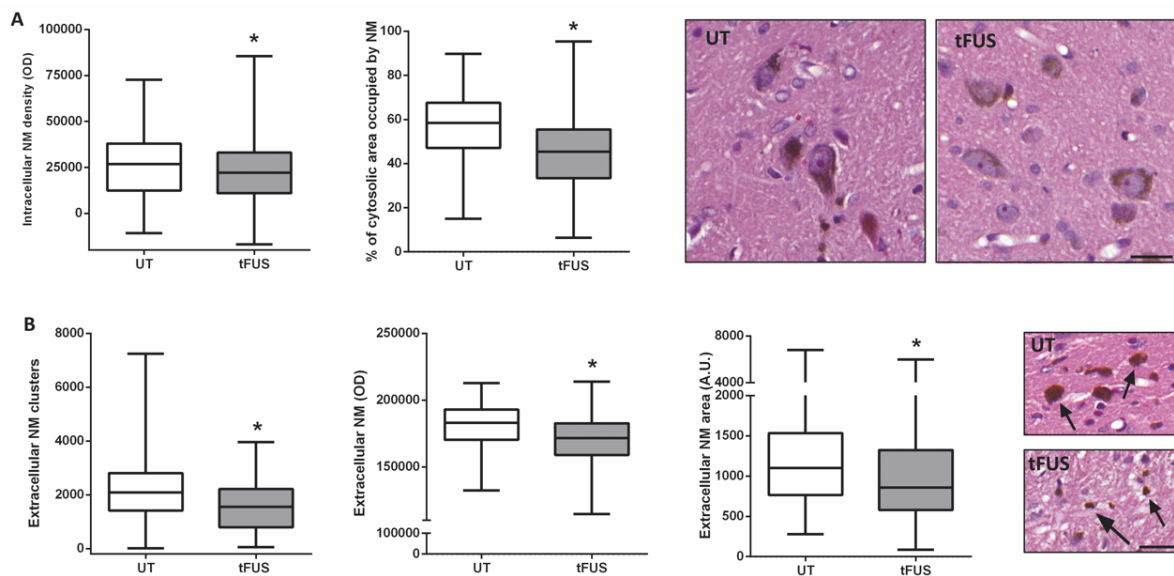


Figure 54. tFUS reduces intracellular and extracellular NM accumulations in NM-producing parkinsonian rats. (A) Quantification of intracellular NM levels by optical densitometry (*left*) and the percentage of neuronal cytosolic area occupied by NM (*right*) in ipsilateral SN DA neurons of AAV-hTyr-injected rats at 4 m post-injection, in untreated rats (“UT”) or rats treated with tFUS (“tFUS”). *Micrographs*, representative images of 5 μm -thick H&E-stained SN sections from these animals (unstained NM in brown). **(B)** Quantification of the number (*left*), density (*center*) and size (*right*) of extracellular NM debris in ipsilateral SN of AAV-hTyr-injected rats at 4 m post injection, in untreated rats (“UT”) or rats treated with tFUS (“tFUS”). *Micrographs*, representative images of 5 μm -thick H&E-stained SN sections from these animals (arrows, unstained extracellular NM debris, in brown). In all panels, $*p < 0.05$ vs untreated; Mann-Whitney test. In **A**, $N = 206$ neurons from 6 untreated animals and 822 neurons from 6 tFUS-treated animals. In **B** (*center* & *right*), $N = 1002$ NM clusters per group, from 6 untreated animals and 6 tFUS-treated animals. Scale bars: 20 μm .

The reduction in intracellular NM levels by tFUS was accompanied by concomitant decreases in extracellular NM debris, including reductions in the number, size and density of extracellular NM clusters (Fig. 54B). Overall, these results indicate that tFUS treatment lessens age-dependent NM accumulation, both at intracellular and extracellular level, linked to the PD-like pathology occurring in NM-producing animals.

3. REDUCTION OF EXTRACELLULAR NM DEBRIS BY TFUS IS LINKED TO AN ATTENUATION OF PD-LIKE NEUROINFLAMMATION

Extracellular NM debris released from dying neurons, as observed in NM-producing parkinsonian rats, is a common PD feature often associated with activated microglia, and is indicative of an active, ongoing neurodegenerative process (i.e., neuronophagia). Microglial cells are indeed considered the main players in the recognition, engulfment and clearance of extracellular NM^{728,734}. Accordingly, the tFUS-induced attenuation of

extracellular NM was associated with a diminished microglial activation, as indicated by a reduction in the number of Iba1-positive microglial cells with a phagocytic/reactive (large amoeboid de-ramified) morphology in NM-producing parkinsonian rats following tFUS treatment (Fig. 55A).

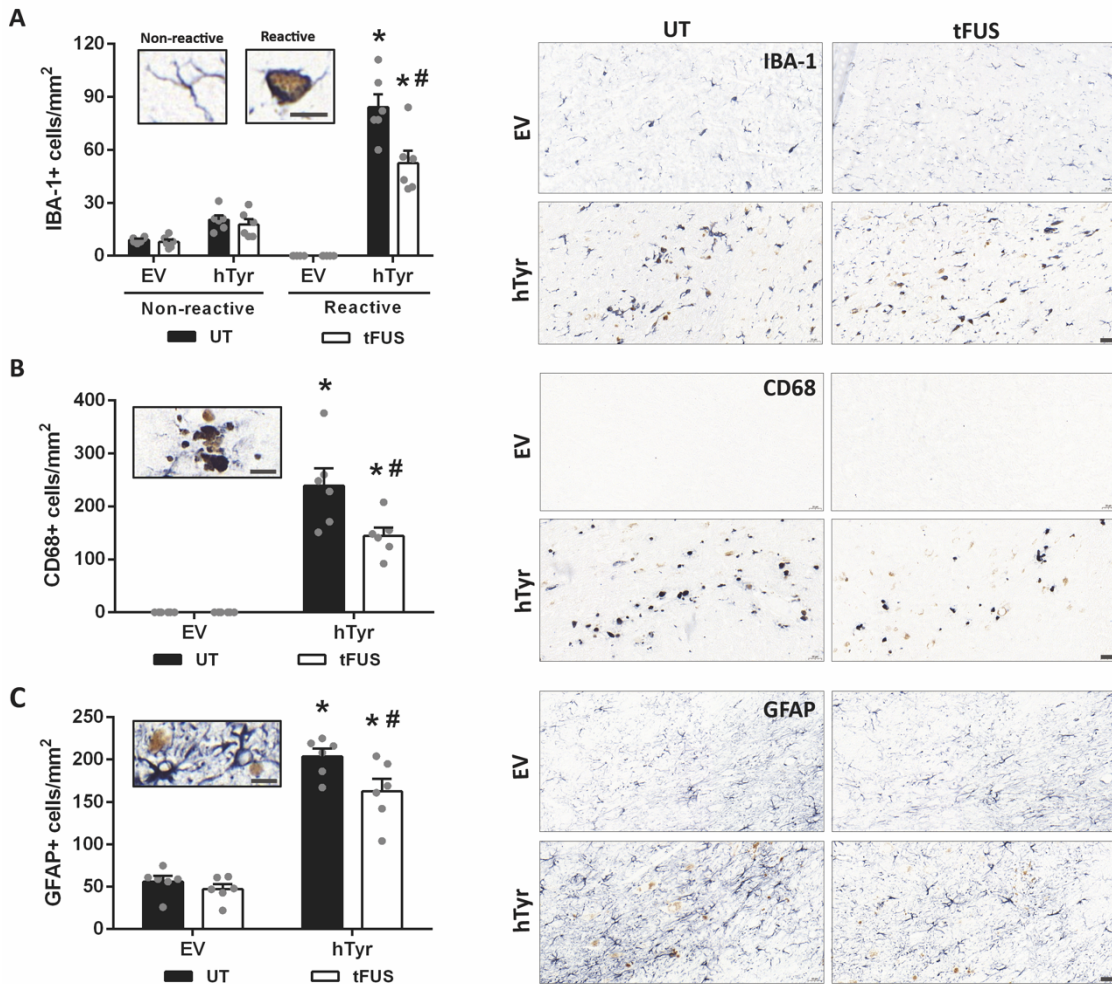


Figure 55. tFUS diminishes PD-like inflammatory changes in NM-producing parkinsonian rats. (A) Quantification of Iba-1-positive microglial cells with a non-reactive (ramified) and phagocytic/reactive (large amoeboid de-ramified) morphologies in the ipsilateral SNpc of AAV-hTyr-injected rats at 4 m post injection, and their naive non-melanized counterparts, either untreated (“UT”) or treated with tFUS (“tFUS”). *Micrographs*, representative images of 5 μ m-thick immunostained SNpc sections with Iba-1 in blue and unstained NM in brown. **(B)** Quantification of CD68-positive macrophages in the ipsilateral SNpc of AAV-hTyr-injected rats at 4 m post injection, and their EV-injected non-melanized counterparts, either untreated (“UT”) or treated with tFUS (“tFUS”). *Micrographs*, representative images of 5 μ m-thick immunostained SNpc sections with CD68 in dark-blue and unstained NM in brown. **C.** Quantification of GFAP-positive astrocytes in the ipsilateral SNpc of AAV-hTyr-injected rats at 4 m post injection, and their EV-injected non-melanized counterparts, either untreated (“UT”) or treated with tFUS (“tFUS”). *Micrographs*, representative images of 5 μ m-thick H&E-stained SNpc sections from these animals (GFAP in blue, NM in brown). In all panels, values shown are mean \pm SEM. In **A**, * p <0.05 vs respective non-reactive state; # p <0.05 vs “UT” reactive state; Two-way ANOVA with Tukey’s post-hoc test. In **B** & **C**, * p <0.05 vs respective naive group; # p <0.05 vs “UT” AAV-hTyr-injected animals; Two-way ANOVA with Tukey’s post-hoc test. In all panels, N=6 animals per group. Scale bars: 10 μ m (inserts), 20 μ m (SNpc micrographs).

Similarly, tFUS treatment also precluded the recruitment of CD68-positive cells in NM-producing parkinsonian animals, corresponding to tissue-resident or blood-borne macrophages with phagocytic activity that are found in close association with extracellular NM (Fig. 55B), as occurs in PD brains⁵⁴⁷. Additional inflammatory changes observed in NM-producing parkinsonian rats included increased astrocyte reactivity, widely distributed within the SNpc, which was also markedly attenuated by tFUS treatment (Fig. 55C). In contrast, no neuroinflammatory traces were observed in the SNpc of tFUS-treated control (EV) animals, indicating that tFUS *per se* does not induce brain inflammation (Fig. 55A-C). Taken together, these results indicate that, by reducing extracellular NM accumulation, tFUS treatment is able to prevent the overall PD-like inflammatory response linked to extracellular NM debris.

4. tFUS ATTENUATES NM-LINKED NIGRAL NEURODEGENERATION

To determine whether the tFUS-induced reductions in intracellular and extracellular NM levels and neuroinflammation might impact on nigral neuronal viability, we assessed DA neuronal integrity in tFUS-treated parkinsonian rats. First, we established that tFUS itself is not deleterious to neurons, as indicated by a lack of effect of tFUS on the morphology and number of dopaminergic nigral neurons in EV-injected non-melanized rats (Fig. 56A). In NM-producing parkinsonian animals, tFUS significantly attenuated the loss of DA TH-positive SN neurons that took place by 4 m post-AAV-hTyr injection in these animals (Fig. 56A). Part of this effect could be attributed to an attenuation by tFUS of the phenotypic loss of TH expression that occurs within NM-laden neurons at early stages of neurodegeneration (Fig. 56B). To distinguish between the effects of tFUS on TH downregulation and on actual cell death, we also assessed the total number of SN DA neurons, including TH-immunopositive and TH-immunonegative pigmented nigral neurons (Fig. 56C). This analysis revealed a preservation of total DA neurons by tFUS in NM-producing parkinsonian rats compared to untreated animals (Fig. 56C). In addition, preserved neurons in tFUS-treated rats exhibited fewer LB-like cytoplasmic inclusions and less cellular atrophy/shrinkage than those from untreated animals, which, together with the attenuated TH downregulation reported above, indicates a functional preservation of these neurons following tFUS treatment. Overall, these results indicate

that tFUS mitigates the PD-like neuronal dysfunction and degeneration linked to excessive NM accumulation.

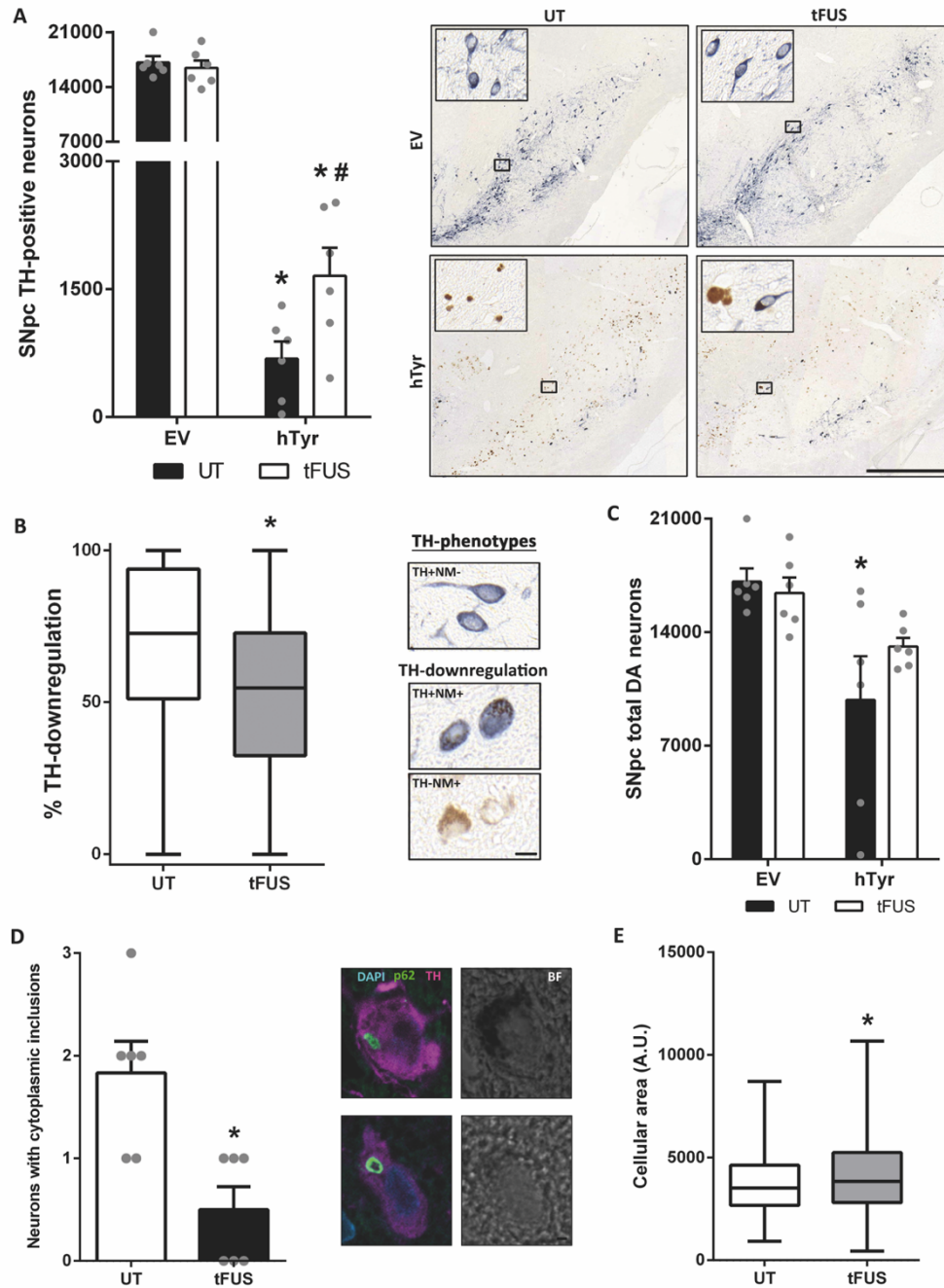


Figure 56. tFUS attenuates SN neurodegeneration in NM-producing parkinsonian rats. (A) Stereological cell counts of TH-positive neurons in the ipsilateral SN of AAV-hTyr-injected rats at 4 m post injection, and their naive non-melanized counterparts, either untreated (“UT”) or treated with tFUS (“tFUS”). *Micrographs*, representative images of 5 μm -thick TH-immunostained ipsilateral SN sections, with TH in blue and unstained NM in brown; Scale bar: 500 μm . **(B)** Percentage of pigmented neurons with downregulated TH expression assessed by immunohistochemistry. **(C)** Stereological cell counts of total number of SN DA neurons (including TH+NM+, TH+NM- and TH-NM+). **(D)** Quantification of the number of NM-laden neurons exhibiting p62-positive LB-like cytosolic inclusions in the ipsilateral SN of AAV-hTyr-injected rats at 4 m post injection, either untreated (“UT”) or treated with tFUS (“tFUS”). *Micrographs*, representative confocal images of a melanized TH+ neuron with an LB-like inclusion immunopositive for p62 in the SN of an AAV-hTyr-injected rat; BF, brightfield; Scale bar: 10 μm . **(E)** Quantification of the cellular area of NM-containing neurons in the ipsilateral SN of AAV-hTyr-injected rats at 4 m post injection, either untreated (“UT”) or

treated with tFUS (“tFUS”). In **A** & **C** values are mean \pm SEM. In **A**, * p <0.05 vs respective naive animals; # p <0.05 vs untreated AAV-hTyr-injected animals. In **B**, **D** & **E**, * p <0.05 vs UT animals. In **C**, * p <0.05 vs UT EV-injected animals.; **A** & **C**, Two-way ANOVA with Tukey’s post-hoc test; **B**, **D** & **E**, Mann-Whitney test. **A-D**, N=6 animals per group. In **E**, N=206 neurons from 6 untreated animals and 822 neurons from 6 tFUS-treated animals.

5. PRESERVATION OF MOTOR FUNCTION BY TFUS TREATMENT OF NM-PRODUCING PARKINSONIAN RATS

We next determined whether the neuroprotective effects exerted by tFUS on SN DA neurons were accompanied by functional improvements in NM-producing parkinsonian rats. Consistent with its effect at preserving nigral cell bodies, tFUS treatment was associated with a reduced loss of striatal DA fibers in these animals (Fig. 57A). This protective effect was mostly limited to the (dorso)lateral STR which receives its DA innervation exclusively from the SN and is considered to be the equivalent of the putamen in humans⁸⁸⁰. This striatal subregion presents the most profound DA depletion in patients with PD⁸⁸¹ and appears to be critical for motor function⁸⁸². In agreement with this, tFUS treatment markedly attenuated contralateral forepaw hypokinesia in NM-producing rats up to 4 m post-AAV injection, as assessed by the cylinder test (Fig. 57B). The level of motor function preservation for each animal significantly correlated with the level of preservation of striatal DA fibers (Fig. 57C). Overall, these results indicate that tFUS treatment at prodromal/early (pre-symptomatic) PD stages provides a long-term functional preservation of the nigrostriatal circuit in parkinsonian rats.

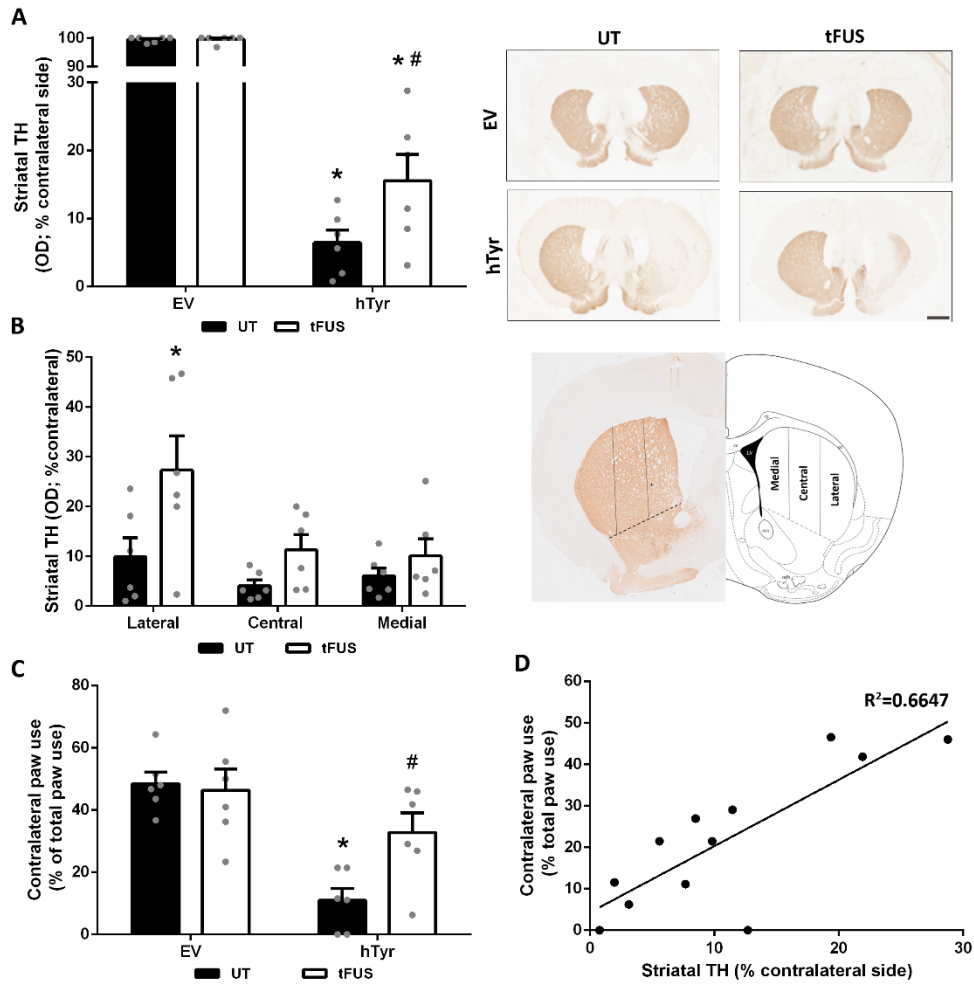


Figure 57. tFUS preserves (dorso)striatal TH-positive fibers and long-term motor function. (A) Optical densitometry of striatal TH-positive fibers in AAV-hTyr-injected rats at 4 m post injection, and their naive non-melanized counterparts, either untreated (“UT”) or treated with tFUS (“tFUS”). *Micrographs*, representative images of 5 μ m-thick TH-immunostained ipsilateral striatal sections (TH in brown; Scale bar: 1 mm). * p <0.05 vs respective naive animals; # p <0.05 vs untreated (“UT”) AAV-hTyr-injected animals; Two-way ANOVA with Tukey’s post-hoc test. **(B)** Optical densitometry (OD) of TH-positive striatal subregions (i.e., lateral, central, medial, as indicated in diagram) in AAV-hTyr-injected rats at 4 m post injection either untreated (“UT”) or treated with tFUS (“tFUS”). * p ≤0.05 vs respective untreated animals; Two-way ANOVA with Tukey’s post-hoc test. **(C)** Contralateral forepaw use of AAV-EV and AAV-hTyr-injected rats, and their naive non-melanized counterparts, either untreated (“UT”) or treated with tFUS at 4 m post injection. * p <0.05 vs untreated control; # p <0.05 vs untreated 1 m; Two-way ANOVA with Tukey’s post-hoc test. **(D)** Pearson correlation analysis between striatal TH OD (% contralateral side) and contralateral paw use. In all panels, values are mean are \pm SEM. In all panels, N=6 animals per experimental group.

V. DISCUSSION

Since the seminal publication of *An Essay on the Shaking Palsy* by James Parkinson two centuries ago, our understanding of the genetics, pathogenesis and clinical heterogeneity of PD has evolved significantly. Nowadays, it is widely accepted that PD involves more than the degeneration of DA neurons of the SNpc, and its manifestations extend beyond the cardinal motor features of tremor, rigidity, and bradykinesia. In this sense, the development of PD is shaped by a complex interplay between genes and the environment, while the presence of multiple pathways involving genes, proteins, organelles, and neural networks could directly influence the wide range of heterogeneous symptoms. Since PD presents a systematic chronic course with progressive disability, it also entails a considerable socioeconomic burden. Thus, over the past generation, the global encumbrance of PD has more than doubled due to larger numbers of affected people along with potential contributions from longer disease duration and environmental factors. Furthermore, demographic and other potential factors are poised to notably augment the future financial implications of PD¹⁶². Society thus faces a pressing need to develop therapeutic strategies to combat PD that either halt disease progression once it has been diagnosed, slow it down or, ideally, to prevent its appearance.

As PD is an established multifactorial disease, it has many therapeutically targetable sites. Historically, individual pathological pathways have been targeted for symptomatic improvement and disease modification with variable success. In this sense, while DA therapies remain the benchmark for symptomatic alleviation of PD, many unmet needs remain concerning the treatment of DA-resistant motor and non-motor symptomatology. Also, there is an urgent need for the development of therapies that can modify the clinical course of the disease or preempt neuronal death. The latter should mandatorily be accompanied by a robust susceptibility risk biomarker able to predict and/or identify preclinical PD subjects. Currently available biomarkers for PD are either diagnostic or prognostic, with most of them relying on the identification of either different α -synuclein species (both in the blood and cerebrospinal fluid (CSF)), or altered lysosomal enzyme activities (in the CSF), or, more robustly, a combination of both⁸⁸³. A noteworthy alternative therapeutic approach is the application of α -synuclein immunotherapy, one of which has recently advanced to phase 2 studies⁸⁸⁴.

In this sense, many pharmacological agents and strategies specifically designed to address PD have failed in multiple clinical trials over the past decades to provide patient improvement without major side-effects. These studies faced critical challenges including the clinical heterogeneity of the population, patient selection (for example, inclusion of patients with coexisting neurodegenerative or vascular diseases, which might markedly skew the results of the drug studied) and, most importantly, the lack of an adequate preclinical PD model. Due to the absence of such a model, another major challenge in PD therapy is the identification of the best window for disease-modifying therapeutic strategies to be applied. Since it has been postulated that a major percentage of neuronal death occurs before overt symptomatology arises³⁹, the generation of animal models mimicking progressive PD development and the discovery of reliable biomarkers seem indispensable elements to lay robust foundations for the future development of PD therapies.

Nevertheless, these unmet needs are closer to being addressed than ever before. With the generation of our AAV-hTyr-overexpressing PD model (we are also about to publish a transgenic hTyr mouse model), a revolutionary tool is now available to address the PD therapy field with renewed scope. By overexpressing hTyr in the SNpc, we have not only managed to generate the first animal model displaying progressive NM accumulation, but also, we were able to recapitulate principal PD hallmarks both at the molecular (neurodegeneration in the SNpc, decreased DA in the STR, LB-like inclusion formation) and mechanistic (motor symptomatology) levels. These outstanding features demonstrate, for the first time *in vivo*, the fact that NM is a direct contributor to PD pathology independently of α -synuclein, thereby disrupting the long-held theory that α -synuclein is the principal driving factor of PD. Whereas pre-formed (either from *postmortem* or other animal species) NM has been used in the past for studying its biochemistry and in an attempt to elucidate its double-edged deleterious component, the hTyr-overexpressing model is unique in the objective of modelling PD by mimicking gradual NM accumulation as seen in humans, which ultimately leads to neurodegeneration. In the present dissertation, leveraging this unique feature, we have successfully managed to reduce NM levels and to observe the concomitant beneficial effects of this approach.

MITIGATION OF PARKINSON'S DISEASE-LIKE FEATURES IN NEUROMELANIN-PRODUCING RATS AFTER VMAT2-OVEREXPRESSION

The modulation of VMAT2 activity has been in the spotlight as a potential therapeutic strategy for a wide range of diseases involving disturbances of DA metabolism and/or signaling; from addiction, schizophrenia or depression, to neurodegenerative diseases such as PD^{52,885,886}. However, while some well-characterized pharmacological inhibitors of VMAT2 are available, such as reserpine and tetrabenazine, positive modulators of VMAT2 function are currently lacking⁸⁸⁷. Here, we found that viral vector-mediated VMAT2 overexpression provides therapeutic benefit in parkinsonian NM-producing rats by maintaining DA homeostasis, reducing potentially toxic DA oxidized species and preventing excessive age-dependent NM accumulation. The latter, in particular, shows for the first time that age-dependent NM production and subsequent intracellular buildup can be slowed down for therapeutic purposes *in vivo*. Indeed, until the recent description of the first rodent model of NM production⁵⁴⁷, NM had not been taken into account in the experimental modeling of PD *in vivo*, despite the fact that this pigment has long been established as a major vulnerability factor underlying PD-linked neurodegeneration⁸³⁶.

This new melanized animal model revealed that the continuous, age-dependent intracellular build-up of NM within autophagic structures ultimately leads to a general failure of cellular proteostasis associated with major PD-like features, including motor deficits, LB-like inclusion formation, and nigrostriatal neurodegeneration⁵⁴⁷. Here we show that all these pathological PD-like features can be prevented or attenuated in these animals by inducing VMAT2 overexpression to reduce intracellular NM levels below a pathological threshold (Figure 52, summary). Relevant to PD, it has been reported in *postmortem* human brains that midbrain DA neurons with the highest VMAT2 protein expression exhibit the lowest NM levels and are the least vulnerable to PD-linked neurodegeneration⁵⁹⁰. Conversely, the most vulnerable human midbrain DA

neurons accumulate the most NM and have the lowest VMAT2 levels⁵⁹⁰. Because VMAT2 overexpression reduces intracellular NM levels by decreasing free cytosolic DA that can subsequently be oxidized to NM, the beneficial effects of VMAT2 could be related to reduced levels of potentially toxic oxidized DA species that serve as NM precursors. In particular, tyrosine, L-DOPA or DA-derived *o*-quinones, which are rapidly transformed into NM, have long been proposed as potential pathological factors in PD⁵⁸⁷. In fact, NM synthesis is regarded as a protective antioxidant mechanism that traps cytosolic quinones and semiquinones in lysosome-associated organelles so that they are no longer reactive with cytosolic components⁷²⁶. However, while high concentrations of DA can be acutely toxic *in vitro*⁷⁵³, the chronic enhancement of DA levels and oxidation does not cause DA nerve terminal or cell body loss *in vivo*⁸⁸⁸⁻⁸⁹⁰. For instance, chronic L-DOPA treatment^{888,889} or genetic enhancement of TH activity⁸⁹⁰ in rodents, both of which result in increased levels of DA and oxidized DA species, are not toxic to regular, wild-type animals but only to animals displaying additional PD-related alterations, such as DJ-1 deficiency⁸⁸⁸ or A53T α -synuclein overexpression⁸⁹⁰.

Relevant to humans, there is no clinical evidence for L-DOPA being neurotoxic and thus accentuate the progression of PD symptoms⁸⁹¹. In addition, antioxidant strategies have systematically failed to provide any therapeutic benefit in PD clinical trials⁸⁹². Even if NM synthesis *per se* was initially neuroprotective, its long-term accumulation until it occupies most of the neuronal cytoplasm has deleterious consequences by physically interfering with intracellular communication⁸⁹³⁻⁸⁹⁵ and impairing proteostasis^{547,836}. In fact, L-DOPA seems to be toxic *in vitro* only at doses associated with NM formation⁷⁵³, an effect that has been attributed to interference with intracellular neurotrophin signaling by NM, and not to an acute toxic effect of L-DOPA *per se*⁸⁹⁶. Consistent with a macromolecular crowding effect linked to progressive NM accumulation, in-depth ultrastructural analyses have revealed that LP in NM-containing neurons from PD brains mostly consists of a crowded environment of vesicular structures and dysmorphic organelles⁸⁷⁸. In agreement with this, we found here that decreased intracellular NM levels by VMAT2 overexpression was associated with a reduced PD-like inclusion formation *in vivo*. In any case, any putative contribution of these species to NM-linked

PD pathology could be therapeutically targeted by VMAT2 overexpression, as the latter reduces both oxidized DA species and age-dependent NM accumulation.

Regulation of the balance of cytosolic DA levels is complex and involves an interplay between different processes. On the one hand, DAT-mediated reuptake of extracellular DA⁸⁹⁷⁻⁸⁹⁹, leaking from synaptic vesicles and TH-mediated DA synthesis, increases cytosolic DA levels. On the other hand, VMAT2-mediated DA encapsulation into synaptic vesicles and MAO-mediated DA metabolism decrease cytosolic DA levels⁹⁰⁰. While Tyr can mediate L-DOPA synthesis from tyrosine⁹⁰⁰ and thus accelerate DA production, the overall levels of cytosolic DA should not be highly increased due to the feedback-inhibition of cytosolic DA on TH^{873,901} and the transient condition of cytosolic DA, which is rapidly metabolized or oxidized. In fact, TYR also promotes the continuous oxidation of cytosolic DA into NM. In addition, the progressive accumulation of NM ultimately impairs neuronal function, causing a downregulation of VMAT2 and TH that may contribute to the decreased DA vesicular uptake and vesicular DA levels⁹⁰² observed in these animals. Furthermore, we have previously reported that striatal DAT levels are decreased by ~70% in AAV-hTYR-injected animals by 2 m post-AAV-hTYR injection⁵⁴⁷, which concurs with neuroimaging in *in vivo* analyses of PD patients exhibiting reductions in DAT striatal density in early stages of the disease⁹⁰³. In this context, it is important to recall that DAT is also expressed in astrocytes and macrophages, which contribute to DA clearance from the synaptic cleft^{898,899}. The increased number of CD68- and GFAP-positive cells in AAV-hTYR-injected animals could thus favor an increased DA uptake and metabolism in glial cells; this is consistent with increased 3-MT levels observed in the ventral midbrain of AAV-hTYR-injected animals at 2 m post-AAV injection (Supplemental Table 4) and could restrict the amount of DA available to be re-uptaken by neuronal DAT. All these changes in DA metabolism, combined with the progressive buildup of NM within the neuronal cytosol, may potentially contribute to the vulnerability of the dopaminergic system in TYR animals and in PD patients.

In addition to the attenuation of nigrostriatal neurodegeneration, VMAT2 overexpression also mitigated the phenotypic loss of TH expression that occurs within

NM-laden neurons at early stages of degeneration. Indeed, despite the general notion that the number of DA neurons are reduced in PD, NM-containing neurons from both PD patients and parkinsonian NM-producing rats exhibit an early phenotypic loss of TH expression, which is associated with impaired DA release and early motor deficits, prior to degeneration^{547,800}. In agreement with this, genetic disruption of mitochondrial complex I in mice was recently reported to induce progressive parkinsonism in which TH downregulation and defective DA release both in striatal terminals and SNpc neuronal cell bodies preceded neurodegeneration⁸³². The occurrence of neuronal dysfunction before overt cell death, and its restoration by VMAT2, may have important therapeutic implications as the latter provides a therapeutic window in which neuronal function can be restored before the actual loss of the cell.

The preservation of neuronal function by VMAT2 overexpression was not limited to the protection of nigrostriatal DA fibers and a maintenance of TH protein expression, but also to a direct effect at maintaining DA homeostasis/metabolism, all of which resulted in an early and long-lasting preservation of the motor function in NM-producing parkinsonian rats. Importantly, VMAT2 overexpression by itself did not alter the normal motor function in non-parkinsonian (control) animals. This is in agreement with previous studies in VMAT2-overexpressing transgenic mice⁹⁰⁴, despite the reported effects of VMAT2 overexpression at enhancing vesicular uptake and capacity leading to increases in DA quantal size and DA release⁶⁰¹. Indeed, while the latter could theoretically result in behavioral changes, VMAT2 overexpression in transgenic mice did not result in any dramatic behavioral phenotype, as measured by motor, sensory, affective, appetitive, or social assays⁹⁰⁴, which concurs with our results in AAV-hVMAT2-overexpressing animals. From a translational point of view, these observations support the feasibility and safety of increasing VMAT2 function as a potential therapeutic strategy in humans.

Overall, our results demonstrate for the first time the feasibility and therapeutic potential of modulating NM production *in vivo* by modifying DA homeostasis/metabolism with VMAT2. These results open the possibility of targeting NM production to prevent or delay PD by slowing down the progressive accumulation

of NM that occurs with age. Such a strategy would represent a conceptually novel therapeutic approach for PD and, in a broader sense, brain aging. There are, however, some limitations to this study. For instance, by concomitantly injecting AAV-hVMAT2 and AAV-hTYR, the production of NM was slowed from its initial synthesis, thus being able to prevent or delay disease onset. It remains to be determined whether in a PD patient in which intracellular NM has already reached pathological levels, VMAT2 would be able to halt or delay disease progression. Finally, while we have shown a beneficial effect of VMAT2 overexpression for up to 6 months post-AAV injection, we do not know how much longer this beneficial effect could potentially last. Indeed, VMAT2 overexpression may slow down but not completely halt NM production, meaning that NM could continue to steadily accumulate with age despite VMAT2 overexpression, although at a slower rate. To overcome this limitation, VMAT2 overexpression could be potentially combined with strategies aimed at eliminating intracellular NM once it has already been produced, such as by overexpression of the autophagy master regulator TFEB, which we recently showed promotes the clearance of NM-filled autophagic structures⁹⁰⁵.

ATTENUATION OF PARKINSON'S DISEASE-LIKE FEATURES IN NEUROMELANIN-PRODUCING RATS AFTER TRANSCRANIAL FOCUSED ULTRASOUND APPLICATION

tFUS has already been successfully applied in PD patients to permanently ablate the thalamus^{298,299}, STN^{300,301} and globus pallidus interna³⁰² in the search for motor symptoms alleviation. However, scarce literature data are available regarding other potential functions of tFUS in PD research. In the present study, based on our previous results, we applied tFUS one month after AAV-hTyr injection, when PD-like symptomatology had not started yet. To evaluate the safety of tFUS *in vivo* and according to previously reported studies, we deployed HE staining to assess the presence of hemorrhage or tissue damage, and TH staining to visualize neurons in brain sections^{329,906,907}. In addition, we also demonstrated here the absence of hemorrhage or cytotoxic damage with normal neuronal density in tFUS-untreated animals, not AAV-hTyr injected animals, thus confirming the safety of the applied protocol.

In this way, initial results for the cylinder motor test in both tFUS-treated rats suggested a strong protection for the pre-symptomatic group. This considerable difference in such a small period of only 1 month can be hardly explained without a therapeutic effect of tFUS essentially focused at the injected SNpc. Several hypotheses have been postulated regarding the duration of the tFUS effect according to different transducer frequencies and pulse repetition frequencies³²⁴. In broad terms, mechanisms that have been postulated include: thermal effects³²⁴, acoustic cavitation³²⁶, acoustic radiation forces^{337,338} and plasma deformation³³⁸. In non-human primates, Pouget et al. described that a 20 s sonication induced a 20-minute-long effect, while Verhagen et al were able to prolong the tFUS neurostimulative effect to 2 h when a 40 s sonication was performed. In the present study, by employing a novel, rodent-specific tFUS apparatus, we applied sonication with a 3 ms duration every 97 ms for 600 repetitions (10 minutes) at $I_{psta} = 1.1 \text{ W/cm}^2$. Since this value is slightly above the limit for diagnostic imaging (0.7 W/cm^2), the tFUS intensity applied herein can be considered as intermediate/high.

Given the scarcity of published studies, and since the intensity values are within ranges used for neurostimulation/modulation and for tissue ablation, none of the known tFUS effects can be completely ruled out as explanations for the observed findings. Indeed, such a long-term beneficial impact of tFUS application has no comparison in literature regardless of the animal model used. Only one study reported a long-term change of neural activity upon tFUS treatment, whereby ischemic stroke-induced mice that received a 20 min sonication presented an improved sensorimotor performance lasting for 4 weeks after treatment⁹⁰⁸. In this study, with half the sonication time, the animals presented with significant improvement at the behavioral level and a reduction of the PD-like pathology induced by hTyr overexpression.

Indeed, the applied tFUS intensity was enough to generate a long-lasting reduction of both intracellular and extracellular NM levels, which translated into a reduction of parenchymal inflammation and a preservation of the SNpc neuronal population, respectively. Also, the PD-like classical neuronal dysfunctional state, marked by the presence of cytoplasmic inclusions, was also revealed to be alleviated upon tFUS treatment. Proportionally, eNM levels presented a stronger reduction than intracellular

levels, thereby suggesting that one of the mechanisms by which tFUS exerts its beneficial action is by the mechanical fragmentation of eNM granules, shredding eNM in smaller and less dense granules. Interestingly, tFUS – in its high intensity version – has already been shown to decrease ultraviolet light-induced hyperpigmentation in experimental animal models by the mechanical elimination of melanin and pigmented debris from the epidermis and upper dermis³¹⁴. Our findings revealed that not only the macroscopic hyperpigmentation reduction can be enhanced with higher intensity tFUS application, but also confirmed histologically that SNpc-focused tFUS is able to induce a significant reduction in melanin deposition. In a complementary way, high-intensity tFUS has been also used for skin tightening and rejuvenation^{909,910}. Therefore, the possibility that our adjusted tFUS protocol has been able to target a deep brain region such as the SNpc and decrease both intracellular and extracellular NM granules seems plausible.

More relevantly, the reduction of eNM levels significantly altered their three main features, namely, cluster amounts, pigment intensity, and area. Specifically, the finding that eNM levels were significantly diminished could be explained by the fact that tFUS-fragmented eNM aggregates are rendered smaller and, in turn, are more likely to be phagocytosed by microglia, while macrophagic activity is also favored⁷³⁰. Wilms and Zhang studies^{728,730} were the first to provide evidence to Zecca's hypothesis that NM released from dying neurons can activate microglia, thereby promoting the degeneration of neighboring neurons⁵³. Nevertheless, the applicability of their models was limited because the exogenous application of NM, although of human origin, may constitute an overly aggressive approach with reduced translational capacity. On the other hand, by harnessing the potential of the NM-accumulation model, we were able to confirm that eNM was associated with sustained microglial/macrophage activation, with NM fragments, as well as entire NM-filled residual neurons being surrounded by, or wholly contained within, activated microglia/macrophages⁵⁴⁷.

Here, we demonstrated that inflammation in the SNpc was significantly reduced by tFUS treatment, as indicated by a lower infiltration of macrophages and reduced numbers of both microglia and astroglia. A potential tFUS-induced reduction of neuroinflammation

was previously postulated, but was not as thoroughly confirmed as shown here⁹¹¹. From our previous study, we know that, analogous to PD brains, NM-filled microglia from AAV-hTyr-injected animals appear to migrate to blood vessels to exit the brain along with the NM pigment as a clear indicator of an active clearance process⁵⁴⁷. In case that tFUS treatment could have been coupled via microbubbles to BBB opening, it would have added invaluable data to confirm a predominant mechanism for eNM removal. Relevant data supporting the potential effect of tFUS-mediated BBB opening in the removal of excess eNM include the elimination of β -amyloid plaques in an AD model³¹³.

Strikingly, the significant reduction of intracellular NM levels in tFUS-treated animals was accompanied by a concomitant reduction in the percentage of cytosolic area occupation by NM. The decrease in intracellular NM levels was not enough to go below the pathological threshold previously described⁵⁴⁷, but nevertheless was sufficient to significantly preserve the neuronal population. Accordingly, fibers projecting to the STR were partially conserved upon tFUS application. This global preservation of neuronal integrity translated into a robust enhancement of locomotor function. While this is the first study analyzing the potential motor-improvement effects of tFUS in a NM-accumulating model, literature reports are available assessing the potential beneficial effect of tFUS on neuronal preservation and locomotor function improvement. By applying low-intensity tFUS, Chen et al³²⁹., Dong et al.³³⁰ and Sung⁹¹¹ et al. and reported an attenuation of neurotoxin-induced neuronal death and improved motor behavior in mice after repeated short 10, 10 and 5 minute applications of sonication, respectively. As mentioned above, despite not being fully understood, the mechanism(s) underlying such an important neuroprotective effect of tFUS application are thought to be exerted via the beneficial actions of thermal and/or mechanical effects.

Interestingly, since the SN in PD patients is known to be subjected to a low perfusion state⁹¹² and since it is known that under hypoxic conditions the pH of the extracellular milieu drops⁹¹³, thereby promoting neurotoxic iron oxidation through interactions with ROS such as superoxide⁹¹⁴, it has been postulated that tFUS application could ameliorate brain microcirculation and reduce this effect⁹¹⁵. Furthermore, it is known that NM acts

as a buffer against potentially toxic ions such as Fe^{2+} ⁷⁰². In this regard, given that dying or already dead DA neurons in PD release loosely bound iron leading to Fe^{2+} deposition⁹¹⁶, tFUS application in the present study may have exerted a beneficial action by protecting DA neurons from Fe^{2+} deposition and—subsequent mitochondrial impairment as well as by the mechanical break-down of both intracellular and extracellular NM granules.

The beneficial effect of tFUS on motor dysfunction in the presence of excessive NM accumulation could be explained by the preservation of striatal fibers and an enhancement of the release of striatal DA, which would enable neurons to cope with the strong DA deficiency in striatal axon terminals due to massive neuronal loss⁹⁰⁷. Since DA's half-life in brain is thought to be in the range of a few minutes, the sustained amelioration of the motor symptoms must be derived from another prolonged mechanism. A potential tFUS-induced neuronal repair mechanism was postulated and could be another reason for the significant recovery of the neuronal population and motor behavior performance after tFUS application in NM-accumulating animals⁹⁰⁷. In this regard, since PD is also known to exhibit alterations in axonal transport motor proteins⁹¹⁷ and spontaneous behavioral recovery and of TH activity in the STR have been described in 6-OHDA-induced lesions to the SNpc⁹¹⁸, the potential for tFUS-induced repair and axonal preservation (concomitant with general neuronal preservation) could induce sprouting and/or compensatory mechanisms that may explain the motor symptomatology recovery despite the scarce neuronal preservation.

AUTOMATED QUANTIFICATION OF NEUROINFLAMMATION

Neuroinflammation requires a coordinated response between microglia and other cells of the central nervous system, such as astrocytes, as well as peripheral immune cells infiltrating the brain⁹¹⁹. Herein, we established a completely cloud-based set of deep CNN algorithms to automatically quantify neuroinflammation. Moreover, these algorithms were validated in an age-dependent NM-accumulating PD model. The Aiforia software platform enables an automatic, rapid, and reproducible analysis of cell

numbers with minimal hands-on activity, presenting several advantages over other counting methods. First, the Aiforia system allows counting to be performed on a battery of scanned slides, whereas the stereology approach requires the counting of one slide at a time and is thus more time-consuming (Fig. 40F). Second, the stereology approach has the drawback of potential human bias. When dealing with hundreds or thousands of cells to count, unbiased estimations of cell populations in a specific brain area are key measurements in neuroscience, comparative physiology, among other disciplines.

Despite yielding highly accurate estimates of cell body numbers, stereological counting with the optical fractionator method relies on a process that is randomized and where the decision of which cells are included in the count is subjective⁹²⁰. The observer who is performing the counting bases the choice on the cell shape, size, and staining intensity on accepted stereology rules. Besides, usually only a small number of cells of interest in the target structure are counted and the total number is mathematically estimated. These characteristics render the stereological method susceptible to human bias. Nevertheless, potential (high) error in these estimations can be reduced by increasing the number of counting frames and the size of the analyzed area, but this is an arduous and time-consuming procedure. To date, some approaches and techniques have been developed with the aim of improving stereological counting. For example, the coupling of light microscopy with free access software such as Image J, although more time-consuming, has emerged as a reliable economic alternative to commercial stereology equipment⁹²¹. Still, complementing stereology with an automated and motorized stage has been demonstrated to reduce counting time by up to 10%⁹²². Furthermore, recent methods such as the proportionator⁹²³ and an optimized automatic optical fractionator⁹²⁴ have been implemented to achieve a reduction in subjective bias and an acceleration of the counting analysis. Nonetheless all these examples entail, inevitably, the need for expensive and bulky physical equipment, and the use of mathematical strategies to generate cell number estimations.

In the present work, as presented by Penttinen *et al.* for counting TH+ neurons⁹²⁵ and by Perosa *et al.* for the quantitative assessment of histopathological markers of AD, we

used a hardware-free, fully cloud-based, context-intelligent CNN to count three different cell types involved in neuroinflammation: (i) microglia, the brain's professional phagocytes; (ii) astroglia, the brain's resident immune system; and (iii) active macrophages, which only infiltrate the brain parenchyma in case of severe inflammatory processes. While microglia protect the brain by phagocytosing pathogens, dead cells, dying cells, debris and protein aggregates⁹²⁶, astrocytes on the other hand provide trophic support for neurons, among a vast array of other homeostatic maintenance functions⁸⁶⁷. Nevertheless, both cell types can be overactivated under certain pathologic conditions and become neurotoxic^{815,927}. One of these deleterious circumstances includes the presence of eNM granules in the parenchyma, inducing a strong immunogenic response^{547,730} and the recruitment macrophages that infiltrate the active site of neuroinflammation^{928,929}. These algorithms 'learn' and perform counting by themselves, yielding fast, robust, and reproducible analyses between sections.

Despite its numerous advantages, the Aiforia platform has some limitations that deserve consideration. As the system is validated by the human observer, the only possible bias is in drawing the outline of the region of interest (ROI) in the digital image. According to our vast experience in SN neuronal counting with stereology^{547,905,930}, the shape of the area and the irregular distribution of cells along it, even with cautious definition of the ROI, may cause the random sampling to miss high-cell density regions. Stereology considers the space between analyzed sections, enabling the estimation of total cell numbers, which the CNN algorithms presented herein don't. Another remarkable feature present in stereology that Aiforia does not contemplate is the independence of background/non-specific staining. As described above, astrocytes and particularly microglia are highly pleomorphic, this being exacerbated in the presence of eNM and giving rise to a strong GFAP⁺ and Iba-1⁺ staining in both cases. As a consequence, the respective counting algorithms struggle to differentiate actual cells from other cell debris, other miniscule elements, or undefined shapes. However, macrophage (either resident microglia or infiltrating immune cells) detection did not entail this difficulty since CD68⁺ staining produced a clear background. Therefore, it is important to highlight that this platform requires specific training for all potential staining intensities for the

same cell types. Also, specific algorithms must be prepared for different development and counterstaining strategies.

To test the quality of the developed algorithms, we compared the counting obtained with the manual stereology-based neuroinflammation assessment upon eNM insult in the NM-accumulation based AAV-hTyr PD model. Since the number of immune events in the total ROI is relatively low compared to the standard neuronal cell counts, and in order to make the human vs machine counting comparison as accurate as possible, we manually counted the whole SN region delimited by the extent of eNM granules dispersed within it. Our data showed a strong correlation between the results obtained for the two methods, attesting to the validity of the developed CNN algorithms. In any case, it is important to stress the necessity of teaching the algorithm all marker-specific staining ranges and to maximize the reproducibility of the immunochemistry process between batches to minimize the false positive rate and, especially, the false negative rate. In addition, CNN algorithm performance can be constantly ameliorated by further rounds of training. A clear demonstration of this comes from the results of counting the contralateral AAV-hTyr-injected SN. There, inflammation was absent and the global staining was fainter compared to the corresponding ipsilateral side. Despite these limitations, the quality of the generated CNN algorithms was evidenced by the strong correlation shown between manual counting results and the algorithm-counted direct indicators of macrophagic activity revealing neuroinflammation in the AAV-hTyr-injected SN, namely reactive microglia and infiltrating macrophages.

Despite these minor drawbacks, the relevance of this work surpasses basic research in preclinical models (these algorithms have been also applied to the characterization of a mouse model, with a manuscript currently in preparation) since the algorithms, with minimal finetuning, have also been applied to the analysis of human samples (both in an NM-specific, PD-focused context and in an NM-free, PD-independent context). These algorithms could therefore serve as a powerful tool to robustly assess the neuroinflammation status of *postmortem* patient brains, providing valuable information about the disease progression state upon death. After ischemic heart disease, stroke and respiratory illnesses, and neurodegenerative diseases⁹³¹, all of which have a strong

neuroinflammatory involvement⁹³², rank among the most prevalent causes of death worldwide. In addition, neurodegenerative diseases are expected to undergo a marked surge in number in the upcoming years⁹³³ given increased life expectancy and since age is their principal risk factor. Therefore, there is an urgent need to develop tools to rapidly assess both neuronal degeneration and neuroinflammation during *postmortem* neuropathological assessment to improve diagnostic accuracy and provide direct information about disease progression and endpoint state.

In conclusion, we present three one-of-a-kind, deep CNN algorithms to count individual astrocytes, macrophages and microglia in both rat and human midbrains. All algorithms are precise, fast and reproducible, requiring minimal human activity other than slide scans and initial software training. Furthermore, we demonstrate here that the algorithms can be indistinctly applied to assess differences in inflammation not only in the NM-accumulating PD model, but also in *postmortem* PD brains. Also, since the algorithms rely mainly on cell morphology, they are poised to be easily adapted to other neurodegenerative disorders and to other animal species to distinguish variations in inflammatory states between different sexes, brain regions and health conditions. In addition, the Aiforia platform is completely cloud-based, meaning it is accessible from everywhere, thereby avoiding the need for expensive and bulky equipment required for stereology and of the often-intricate software and methods required for counting estimations. As it is available to the neuroscience community, the Aiforia platform supports whole slide scanning from principal manufacturers and offers a wide scope of potential applications, like the algorithms presented herein, ensuring non-human biased, physical-space-saving, simple, automated, reproducible and fast quantifications, both for immunochemistry and immunofluorescence.

VI. CONCLUSIONS

1. VMAT2 overexpression enhances dopamine vesicular uptake *in vivo*, thereby reducing cytoplasmic dopamine.
2. VMAT2 overexpression reduces cytosolic dopamine, resulting in a decrease of its potentially neurotoxic-derived intermediate oxidation metabolites.
3. Fewer neuromelanin precursors in response to VMAT2 overexpression means reduced levels of intracellular neuromelanin, keeping it below the pathological threshold.
4. SNpc dopaminergic neurons preserve their integrity as demonstrated by a reduced Lewy body-like pathology upon VMAT2 overexpression.
5. Upon VMAT2 overexpression, reduced levels of oxidative metabolism, intracellular neuromelanin levels, and cytoplasmic inclusions translate to reduced levels of neurodegeneration in the SNpc.
6. VMAT2-overexpression-driven neuronal preservation entails a reduction in extracellular neuromelanin levels and reduced inflammation.
7. VMAT2-overexpression-related SNpc neuronal survival preserves striatal fibers and, concomitantly, restores striatal dopamine.
8. VMAT2-overexpression-driven global nigrostriatal pathway preservation ensures a significant improvement in motor function.
9. tFUS rat-specific equipment can deliver ultrasound waves in a safe, non-invasive manner.
10. tFUS application, by itself, reduces both intracellular and extracellular neuromelanin levels.
11. tFUS application, by itself, diminishes inflammation in the SNpc.
12. tFUS application, by itself, preserves neuronal integrity and, in turn, protects nigral neurons from excessive neuromelanin accumulation.
13. tFUS-induced nigral protection results in the preservation of striatal dopaminergic fibers.

14. Global, tFUS-induced PD-like phenotype rescue, translates to a substantial improvement of motor performance.

15. The modulation of neuromelanin levels by both VMAT2 overexpression and tFUS application, entails a widespread beneficial effect to neuromelanin-accumulating Parkinson's Disease animal models, both at the molecular and phenotypic levels, thereby serving as potential treatments for early stages of PD if successfully translated into clinical practice.

16. Artificial intelligence-based algorithms allow neuroinflammation to be quantified in rodents and humans in an automated and reliable manner.

VII. BIBLIOGRAPHY

1. Parkinson, J. An essay on the shaking palsy. 1817. *Whitting-ham Rowl. Sherwood, Needly Jones, London.* (1817).
2. Dorsey, E. R. & Bloem, B. R. The Parkinson Pandemic-A Call to Action. *JAMA Neurol.* **75**, 9–10 (2018).
3. Blauwendraat, C., Nalls, M. A. & Singleton, A. B. The genetic architecture of Parkinson's disease. *Lancet. Neurol.* **19**, 170–178 (2020).
4. Hughes, A. J., Daniel, S. E., Kilford, L. & Lees, A. J. Accuracy of clinical diagnosis of idiopathic Parkinson's disease: a clinico-pathological study of 100 cases. *J. Neurol. Neurosurg. Psychiatry* **55**, 181–184 (1992).
5. Bernheimer, H., Birkmayer, W., Hornykiewicz, O., Jellinger, K. & Seitelberger, F. Brain dopamine and the syndromes of Parkinson and Huntington. Clinical, morphological and neurochemical correlations. *J. Neurol. Sci.* **20**, 415–455 (1973).
6. Hornykiewicz, O. & Kish, S. J. Biochemical pathophysiology of Parkinson's disease. *Adv. Neurol.* **45**, 19–34 (1987).
7. Halliday, G. M., Leverenz, J. B., Schneider, J. S. & Adler, C. H. The neurobiological basis of cognitive impairment in Parkinson's disease. *Mov. Disord.* **29**, 634–650 (2014).
8. Ferrazzoli, D. *et al.* Dopamine Replacement Therapy, Learning and Reward Prediction in Parkinson's Disease: Implications for Rehabilitation. *Front. Behav. Neurosci.* **10**, 121 (2016).
9. Alexander, G. E., Crutcher, M. D. & DeLong, M. R. Basal ganglia-thalamocortical circuits: parallel substrates for motor, oculomotor, 'prefrontal' and 'limbic' functions. *Prog. Brain Res.* **85**, 119–146 (1990).
10. Middleton, F. A. & Strick, P. L. Basal ganglia and cerebellar loops: motor and cognitive circuits. *Brain Res. Brain Res. Rev.* **31**, 236–250 (2000).
11. Nambu, A., Tokuno, H. & Takada, M. Functional significance of the cortico-subthalamo-pallidal 'hyperdirect' pathway. *Neurosci. Res.* **43**, 111–117 (2002).
12. Poewe, W. *et al.* Parkinson disease. *Nat. Rev. Dis. Prim.* **3**, 17013 (2017).
13. Chung, C. Y., Koprach, J. B., Siddiqi, H. & Isacson, O. Dynamic changes in presynaptic and axonal transport proteins combined with striatal neuroinflammation precede dopaminergic neuronal loss in a rat model of AAV alpha-synucleinopathy. *J. Neurosci. Off. J. Soc. Neurosci.* **29**, 3365–3373 (2009).
14. Fahn, S. & Sulzer, D. Neurodegeneration and neuroprotection in Parkinson disease. *NeuroRx* **1**, 139–154 (2004).
15. W., S. C. Lewy bodies. *Proc. Natl. Acad. Sci.* **103**, 1661–1668 (2006).
16. Lewy, F. H. Paralysis agitans. in *Handbuch der Neurologie, hsg. von Max Lewandowsky, Dritter Band, Spezielle Neurologie II. Für Später Vormerken* (ed. Lewandowsky, M.) 920–958 (Springer Berlin, 1912).
17. Tretiakoff, K. Contribution a l'Étude de l'Anatomiepathologique du Locus Niger de Soemmering Avec Quelques Deductions Relatives a la Pathogenie des Troubles Dotonus Musculaire de La Maladie de Parkinson. (Paris, 1919).
18. Braak, E. *et al.* α -Synuclein immunopositive Parkinson's disease-related inclusion bodies in lower brain stem nuclei. *Acta Neuropathol.* **101**, 195–201 (2001).
19. Braak, H. & Del Tredici, K. Neuropathological Staging of Brain Pathology in Sporadic Parkinson's disease: Separating the Wheat from the Chaff. *J.*

- Parkinsons. Dis.* **7**, S71–S85 (2017).
20. Braak, H. *et al.* Staging of brain pathology related to sporadic Parkinson's disease. *Neurobiol. Aging* **24**, 197–211 (2003).
 21. Braak, H. & Del Tredici, K. Neuroanatomy and pathology of sporadic Parkinson's disease. *Adv. Anat. Embryol. Cell Biol.* **201**, 1–119 (2009).
 22. Conway, K. A., Rochet, J. C., Bieganski, R. M. & Lansbury, P. T. J. Kinetic stabilization of the alpha-synuclein protofibril by a dopamine-alpha-synuclein adduct. *Science* **294**, 1346–1349 (2001).
 23. Nath, S., Goodwin, J., Engelborghs, Y. & Pountney, D. L. Raised calcium promotes α -synuclein aggregate formation. *Mol. Cell. Neurosci.* **46**, 516–526 (2011).
 24. Sulzer, D. & Surmeier, D. J. Neuronal vulnerability, pathogenesis, and Parkinson's disease. *Mov. Disord.* **28**, 41–50 (2013).
 25. Gilman, S. *et al.* Second consensus statement on the diagnosis of multiple system atrophy. *Neurology* **71**, 670–676 (2008).
 26. Giguère, N., Burke Nanni, S. & Trudeau, L.-E. On Cell Loss and Selective Vulnerability of Neuronal Populations in Parkinson's Disease. *Front. Neurol.* **9**, 455 (2018).
 27. Bazelon, M., Fenichel, G. M. & Randall, J. Studies on neuromelanin. I. A melanin system in the human adult brainstem. *Neurology* **17**, 512–519 (1967).
 28. Fedorow, H. *et al.* Neuromelanin in human dopamine neurons : Comparison with peripheral melanins and relevance to Parkinson ' s disease. *Prog. Neurobiol.* **75**, 109–124 (2005).
 29. Saper, C. B., Sorrentino, D. M., German, D. C. & de Lacalle, S. Medullary catecholaminergic neurons in the normal human brain and in Parkinson's disease. *Ann. Neurol.* **29**, 577–584 (1991).
 30. Surmeier, D. J. & Sulzer, D. The pathology roadmap in Parkinson disease. *Prion* **7**, 85–91 (2013).
 31. Armstrong, M. J. & Okun, M. S. Diagnosis and Treatment of Parkinson Disease: A Review. *JAMA - J. Am. Med. Assoc.* **323**, 548–560 (2020).
 32. Berg, D. *et al.* MDS research criteria for prodromal Parkinson's disease. *Mov. Disord.* **30**, 1600–1611 (2015).
 33. Galbiati, A., Verga, L., Giora, E., Zucconi, M. & Ferini-Strambi, L. The risk of neurodegeneration in REM sleep behavior disorder: A systematic review and meta-analysis of longitudinal studies. *Sleep Med. Rev.* **43**, 37–46 (2019).
 34. Howell, M. J. & Schenck, C. H. Rapid Eye Movement Sleep Behavior Disorder and Neurodegenerative Disease. *JAMA Neurol.* **72**, 707–712 (2015).
 35. Darweesh, S. K. L. *et al.* Professional occupation and the risk of Parkinson's disease. *Eur. J. Neurol.* **25**, 1470–1476 (2018).
 36. Fereshtehnejad, S.-M. *et al.* Evolution of prodromal Parkinson's disease and dementia with Lewy bodies: a prospective study. *Brain* **142**, 2051–2067 (2019).
 37. Fearnley, J. M. & Lees, A. J. Ageing and Parkinson's disease: substantia nigra regional selectivity. *Brain* **114** (Pt 5), 2283–2301 (1991).
 38. Przuntek, H. and Müller, T. *Diagnosis and Treatment of Parkinson's Disease - State of the Art.* (Springer-Verlag Wien New York, 1999). doi:10.1007/978-3-7091-6360-3.
 39. Marsden, C. D. Parkinson's disease. *Lancet* **335**, 948–949 (1990).

40. Ross, G. W. *et al.* Parkinsonian signs and substantia nigra neuron density in decedents elders without PD. *Ann. Neurol.* **56**, 532–539 (2004).
41. Lang, A. E. & Lozano, A. M. Parkinson's disease. First of two parts. *N. Engl. J. Med.* **339**, 1044–1053 (1998).
42. Dauer, W. & Przedborski, S. Parkinson's disease: mechanisms and models. *Neuron* **39**, 889–909 (2003).
43. Surmeier, D. J., Obeso, J. A. & Halliday, G. M. Selective neuronal vulnerability in Parkinson disease. *Nat. Rev. Neurosci.* **18**, 101–113 (2017).
44. Rudow, G. *et al.* Morphometry of the human substantia nigra in ageing and Parkinson's disease. *Acta Neuropathol.* **115**, 461 (2008).
45. Buchman, A. S. *et al.* Nigral pathology and parkinsonian signs in elders without Parkinson disease. *Ann. Neurol.* **71**, 258–266 (2012).
46. Reeve, A., Simcox, E. & Turnbull, D. Ageing and Parkinson's disease: Why is advancing age the biggest risk factor? *Ageing Res. Rev.* **14**, 19–30 (2014).
47. Ma, S. Y., Røytt, M., Collan, Y. & Rinne, J. O. Unbiased morphometrical measurements show loss of pigmented nigral neurones with ageing. *Neuropathol. Appl. Neurobiol.* **25**, 394–399 (1999).
48. Pakkenberg, B. & Gundersen, H. J. Neocortical neuron number in humans: effect of sex and age. *J. Comp. Neurol.* **384**, 312–320 (1997).
49. Hirsch, E. C., Graybiel, A. M., Duyckaerts, C. & Javoy-Agid, F. Neuronal loss in the pedunculopontine tegmental nucleus in Parkinson disease and in progressive supranuclear palsy. *Proc. Natl. Acad. Sci.* **84**, 5976–5980 (1987).
50. Matsuda, W. *et al.* Single Nigrostriatal Dopaminergic Neurons Form Widely Spread and Highly Dense Axonal Arborizations in the Neostriatum. *J. Neurosci.* **29**, 444 LP – 453 (2009).
51. Michel, P. P. *et al.* Role of activity-dependent mechanisms in the control of dopaminergic neuron survival. *J. Neurochem.* **101**, 289–297 (2007).
52. Segura-Aguilar, J. *et al.* Protective and toxic roles of dopamine in Parkinson's disease. *J. Neurochem.* **129**, 898–915 (2014).
53. Zecca, L., Zucca, F. A., Wilms, H. & Sulzer, D. Neuromelanin of the substantia nigra: A neuronal black hole with protective and toxic characteristics. *Trends in Neurosciences* vol. 26 578–580 (2003).
54. Zecca, L., Youdim, M. B. H., Riederer, P., Connor, J. R. & Crichton, R. R. Iron, brain ageing and neurodegenerative disorders. *Nat. Rev. Neurosci.* **5**, 863–873 (2004).
55. Hare, D. J. *et al.* An iron-dopamine index predicts risk of parkinsonian neurodegeneration in the substantia nigra pars compacta. *Chem. Sci.* **5**, 2160–2169 (2014).
56. Ren, Y., Liu, W., Jiang, H., Jiang, Q. & Feng, J. Selective vulnerability of dopaminergic neurons to microtubule depolymerization. *J. Biol. Chem.* **280**, 34105–34112 (2005).
57. Pacelli, C. *et al.* Elevated Mitochondrial Bioenergetics and Axonal Arborization Size Are Key Contributors to the Vulnerability of Dopamine Neurons. *Curr. Biol.* **25**, 2349–2360 (2015).
58. Gesi, M. *et al.* The role of the locus coeruleus in the development of Parkinson's disease. *Neurosci. Biobehav. Rev.* **24**, 655–668 (2000).
59. Baloyannis, S. J., Costa, V. & Baloyannis, I. S. Morphological alterations of the

- synapses in the locus coeruleus in Parkinson's disease. *J. Neurol. Sci.* **248**, 35–41 (2006).
60. Fereshtehnejad, S.-M., Zeighami, Y., Dagher, A. & Postuma, R. B. Clinical criteria for subtyping Parkinson's disease: biomarkers and longitudinal progression. *Brain* **140**, 1959–1976 (2017).
 61. De Pablo-Fernández, E., Lees, A. J., Holton, J. L. & Warner, T. T. Prognosis and Neuropathologic Correlation of Clinical Subtypes of Parkinson Disease. *JAMA Neurol.* **76**, 470–479 (2019).
 62. Hoehn, M. M. & Yahr, M. D. Parkinsonism: onset, progression and mortality. *Neurology* **17**, 427–442 (1967).
 63. Goetz, C. G. *et al.* Movement Disorder Society-Sponsored Revision of the Unified Parkinson's Disease Rating Scale (MDS-UPDRS): Scale presentation and clinimetric testing results. *Mov. Disord.* **23**, 2129–2170 (2008).
 64. Antony, P. M. A., Diederich, N. J., Krüger, R. & Balling, R. The hallmarks of Parkinson's disease. *FEBS J.* **280**, 5981–5993 (2013).
 65. Larsen, S. B., Hanss, Z. & Krüger, R. The genetic architecture of mitochondrial dysfunction in Parkinson's disease. *Cell Tissue Res.* **373**, 21–37 (2018).
 66. Day, J. O. & Mullin, S. The genetics of parkinson's disease and implications for clinical practice. *Genes (Basel)*. **12**, (2021).
 67. Marras, C. & Lang, A. Parkinson's disease subtypes: Lost in translation? *J. Neurol. Neurosurg. Psychiatry* **84**, 409–415 (2013).
 68. Thomas, B. & Beal, M. F. Parkinson's disease. *Hum. Mol. Genet.* **16 Spec No**, R183-94 (2007).
 69. Polymeropoulos, M. H. *et al.* Mapping of a gene for Parkinson's disease to chromosome 4q21-q23. *Science (80-.)*. **274**, 1197–1199 (1996).
 70. Polymeropoulos, M. H. *et al.* Mutation in the alpha-synuclein gene identified in families with Parkinson's disease. *Science (80-.)*. **276**, 2045–2047 (1997).
 71. Bonifati, V. Genetics of Parkinson's disease - state of the art, 2013. *Park. Relat. Disord.* **20**, S23–S28 (2014).
 72. Bender, A. *et al.* High levels of mitochondrial DNA deletions in substantia nigra neurons in aging and Parkinson disease. *Nat. Genet.* **38**, 515–517 (2006).
 73. Klein, C. & Westenberger, A. Genetics of Parkinson's Disease. (2012).
 74. Oliveira, L. M. A. *et al.* Elevated α -synuclein caused by SNCA gene triplication impairs neuronal differentiation and maturation in Parkinson's patient-derived induced pluripotent stem cells. *Cell Death Dis.* **6**, e1994 (2015).
 75. Ibáñez, P. *et al.* Causal relation between alpha-synuclein gene duplication and familial Parkinson's disease. *Lancet (London, England)* **364**, 1169–1171 (2004).
 76. Ibáñez, P. *et al.* Alpha-synuclein gene rearrangements in dominantly inherited parkinsonism: frequency, phenotype, and mechanisms. *Arch. Neurol.* **66**, 102–108 (2009).
 77. Bruggemann, N. *et al.* Re: Alpha-synuclein gene duplication is present in sporadic Parkinson disease. *Neurology* vol. 71 1294; author reply 1294 (2008).
 78. Singleton, A. B. *et al.* alpha-Synuclein locus triplication causes Parkinson's disease. *Science* **302**, 841 (2003).
 79. Nishioka, K. *et al.* Clinical heterogeneity of alpha-synuclein gene duplication in Parkinson's disease. *Ann. Neurol.* **59**, 298–309 (2006).
 80. Fuchs, J. *et al.* Phenotypic variation in a large Swedish pedigree due to SNCA

- duplication and triplication. *Neurology* **68**, 916–922 (2007).
81. Winkler, S. *et al.* α -Synuclein and Parkinson disease susceptibility. *Neurology* **69**, 1745 LP – 1750 (2007).
 82. Ross, O. A. *et al.* Genomic investigation of alpha-synuclein multiplication and parkinsonism. *Ann. Neurol.* **63**, 743–750 (2008).
 83. Bertoncini, C. W., Fernandez, C. O., Griesinger, C., Jovin, T. M. & Zweckstetter, M. Familial mutants of alpha-synuclein with increased neurotoxicity have a destabilized conformation. *J. Biol. Chem.* **280**, 30649–30652 (2005).
 84. Chen, L. & Feany, M. B. Alpha-synuclein phosphorylation controls neurotoxicity and inclusion formation in a *Drosophila* model of Parkinson disease. *Nat. Neurosci.* **8**, 657–663 (2005).
 85. Eleuteri, S. & Albanese, A. VPS35-Based Approach: A Potential Innovative Treatment in Parkinson’s Disease. *Front. Neurol.* **10**, 1–11 (2019).
 86. Snyder, H. *et al.* Aggregated and monomeric alpha-synuclein bind to the S6’ proteasomal protein and inhibit proteasomal function. *J. Biol. Chem.* **278**, 11753–11759 (2003).
 87. Cuervo, A. M., Stefanis, L., Fredenburg, R., Lansbury, P. T. & Sulzer, D. Impaired degradation of mutant alpha-synuclein by chaperone-mediated autophagy. *Science* **305**, 1292–1295 (2004).
 88. Olanow, C. W. & Prusiner, S. B. Is Parkinson’s disease a prion disorder? *Proc. Natl. Acad. Sci. U. S. A.* **106**, 12571–12572 (2009).
 89. Bernal-Conde, L. D. *et al.* Alpha-Synuclein Physiology and Pathology: A Perspective on Cellular Structures and Organelles. *Front. Neurosci.* **13**, 1–22 (2020).
 90. Brice, A. Genetics of Parkinson’s disease: LRRK2 on the rise. *Brain* **128**, 2760–2762 (2005).
 91. Lesage, S. *et al.* LRRK2 G2019S as a cause of Parkinson’s disease in North African Arabs. *The New England journal of medicine* vol. 354 422–423 (2006).
 92. Ozelius, L. J. *et al.* LRRK2 G2019S as a cause of Parkinson’s disease in Ashkenazi Jews. *The New England journal of medicine* vol. 354 424–425 (2006).
 93. Haugarvoll, K. *et al.* Lrrk2 R1441C parkinsonism is clinically similar to sporadic Parkinson disease. *Neurology* **70**, 1456–1460 (2008).
 94. Ren, C. *et al.* G2019S Variation in LRRK2: An Ideal Model for the Study of Parkinson’s Disease? . *Frontiers in Human Neuroscience* vol. 13 (2019).
 95. Giasson, B. I. *et al.* Biochemical and pathological characterization of Lrrk2. *Ann. Neurol.* **59**, 315–322 (2006).
 96. Islam, M. S. & Moore, D. J. Mechanisms of LRRK2-dependent neurodegeneration: role of enzymatic activity and protein aggregation. *Biochem. Soc. Trans.* **45**, 163–172 (2017).
 97. Goldwurm, S. *et al.* Evaluation of LRRK2 G2019S penetrance: relevance for genetic counseling in Parkinson disease. *Neurology* **68**, 1141–1143 (2007).
 98. Wallings, R., Manzoni, C. & Bandopadhyay, R. Cellular processes associated with LRRK2 function and dysfunction. *FEBS J.* **282**, 2806–2826 (2015).
 99. Rivero-Ríos, P., Romo-Lozano, M., Fasiczka, R., Naaldijk, Y. & Hilfiker, S. LRRK2-Related Parkinson’s Disease Due to Altered Endolysosomal Biology With Variable Lewy Body Pathology: A Hypothesis . *Frontiers in Neuroscience* vol. 14 (2020).

100. Chen, C.-Y. *et al.* (G2019S) LRRK2 activates MKK4-JNK pathway and causes degeneration of SN dopaminergic neurons in a transgenic mouse model of PD. *Cell Death Differ.* **19**, 1623–1633 (2012).
101. Longo, F. *et al.* Age-dependent dopamine transporter dysfunction and Serine129 phospho- α -synuclein overload in G2019S LRRK2 mice. *Acta Neuropathol. Commun.* **5**, 22 (2017).
102. Zimprich, A. *et al.* Mutations in LRRK2 cause autosomal-dominant parkinsonism with pleomorphic pathology. *Neuron* **44**, 601–607 (2004).
103. Lin, X. *et al.* Leucine-rich repeat kinase 2 regulates the progression of neuropathology induced by Parkinson's-disease-related mutant alpha-synuclein. *Neuron* **64**, 807–827 (2009).
104. Herzig, M. C. *et al.* High LRRK2 levels fail to induce or exacerbate neuronal alpha-synucleinopathy in mouse brain. *PLoS One* **7**, e36581 (2012).
105. Liu, G., Aliaga, L. & Cai, H. α -synuclein, LRRK2 and their interplay in Parkinson's disease. *Future Neurol.* **7**, 145–153 (2012).
106. Vilarinho-Güell, C. *et al.* VPS35 mutations in Parkinson disease. *Am. J. Hum. Genet.* **89**, 162–167 (2011).
107. Zimprich, A. *et al.* A mutation in VPS35, encoding a subunit of the retromer complex, causes late-onset Parkinson disease. *Am. J. Hum. Genet.* **89**, 168–175 (2011).
108. Guella, I. *et al.* The Asp620asn mutation in VPS35 is not a common cause of familial Parkinson's disease. *Movement disorders : official journal of the Movement Disorder Society* vol. 27 800–801 (2012).
109. Kumar, K. R. *et al.* Frequency of the D620N mutation in VPS35 in Parkinson disease. *Arch. Neurol.* **69**, 1360–1364 (2012).
110. Sheerin, U.-M. *et al.* Screening for VPS35 mutations in Parkinson's disease. *Neurobiol. Aging* **33**, 838.e1-838.e8385 (2012).
111. Hierro, A. *et al.* Functional architecture of the retromer cargo-recognition complex. *Nature* **449**, 1063–1067 (2007).
112. Harbour, M. E. *et al.* The cargo-selective retromer complex is a recruiting hub for protein complexes that regulate endosomal tubule dynamics. *J. Cell Sci.* **123**, 3703–3717 (2010).
113. Zavodszky, E. *et al.* Mutation in VPS35 associated with Parkinson's disease impairs WASH complex association and inhibits autophagy. *Nat. Commun.* **5**, 3828 (2014).
114. Ishizu, N. *et al.* Impaired striatal dopamine release in homozygous Vps35 D620N knock-in mice. *Hum. Mol. Genet.* **25**, 4507–4517 (2016).
115. Xi, C. *et al.* Parkinson's disease-linked D620N VPS35 knockin mice manifest tau neuropathology and dopaminergic neurodegeneration. *Proc. Natl. Acad. Sci.* **116**, 5765–5774 (2019).
116. Wu, S. *et al.* The Dopamine Transporter Recycles via a Retromer-Dependent Postendocytic Mechanism: Tracking Studies Using a Novel Fluorophore-Coupling Approach. *J. Neurosci.* **37**, 9438–9452 (2017).
117. Mir, R. *et al.* The Parkinson's disease VPS35[D620N] mutation enhances LRRK2-mediated Rab protein phosphorylation in mouse and human. *Biochem. J.* **475**, 1861–1883 (2018).
118. Miura, E. *et al.* VPS35 dysfunction impairs lysosomal degradation of α -synuclein

- and exacerbates neurotoxicity in a Drosophila model of Parkinson's disease. *Neurobiol. Dis.* **71**, 1–13 (2014).
119. Tang, F.-L. *et al.* VPS35 in Dopamine Neurons Is Required for Endosome-to-Golgi Retrieval of Lamp2a, a Receptor of Chaperone-Mediated Autophagy That Is Critical for α -Synuclein Degradation and Prevention of Pathogenesis of Parkinson's Disease. *J. Neurosci.* **35**, 10613–10628 (2015).
 120. Lücking, C. B. *et al.* Association between early-onset Parkinson's disease and mutations in the parkin gene. *N. Engl. J. Med.* **342**, 1560–1567 (2000).
 121. Klein, C. & Lohmann-Hedrich, K. Impact of recent genetic findings in Parkinson's disease. *Curr. Opin. Neurol.* **20**, 453–464 (2007).
 122. Zhang, Y. *et al.* Parkin functions as an E2-dependent ubiquitin- protein ligase and promotes the degradation of the synaptic vesicle-associated protein, CDCrel-1. *Proc. Natl. Acad. Sci. U. S. A.* **97**, 13354–13359 (2000).
 123. Rothfuss, O. *et al.* Parkin protects mitochondrial genome integrity and supports mitochondrial DNA repair. *Hum. Mol. Genet.* **18**, 3832–3850 (2009).
 124. Schlossmacher, M. G. *et al.* Parkin localizes to the Lewy bodies of Parkinson disease and dementia with Lewy bodies. *Am. J. Pathol.* **160**, 1655–1667 (2002).
 125. Gouider-Khouja, N. *et al.* Autosomal recessive parkinsonism linked to parkin gene in a Tunisian family. Clinical, genetic and pathological study. *Parkinsonism Relat. Disord.* **9**, 247–251 (2003).
 126. Miyakawa, S. *et al.* Lewy body pathology in a patient with a homozygous parkin deletion. *Mov. Disord.* **28**, 388–391 (2013).
 127. Samaranch, L. *et al.* PINK1-linked parkinsonism is associated with Lewy body pathology. *Brain* **133**, 1128–1142 (2010).
 128. Steele, J. C. *et al.* Defining neurodegeneration on Guam by targeted genomic sequencing. *Ann. Neurol.* **77**, 458–468 (2015).
 129. Nybø, C. J., Gustavsson, E. K., Farrer, M. J. & Aasly, J. O. Neuropathological findings in PINK1-associated Parkinson's disease. *Park. Relat. Disord.* **78**, 105–108 (2020).
 130. Takanashi, M., Li, Y. & Hattori, N. Absence of Lewy pathology associated with PINK1 homozygous mutation. *Neurology* **86**, 2212–2213 (2016).
 131. Narenda, D., Tanaka, A., Suen, D.-F. & Youle, R. J. Parkin is recruited selectively to impaired mitochondria and promotes their autophagy. *J. Cell Biol.* **183**, 795–803 (2008).
 132. Narenda, D. P. *et al.* PINK1 is selectively stabilized on impaired mitochondria to activate Parkin. *PLoS Biol.* **8**, e1000298 (2010).
 133. Pankratz, N. *et al.* Mutations in DJ-1 are rare in familial Parkinson disease. *Neurosci. Lett.* **408**, 209–213 (2006).
 134. Taipa, R. *et al.* DJ-1 linked parkinsonism (PARK7) is associated with Lewy body pathology. *Brain* **139**, 1680–1687 (2016).
 135. M., C.-A. R. *et al.* The Parkinson's disease protein DJ-1 is neuroprotective due to cysteine-sulfinic acid-driven mitochondrial localization. *Proc. Natl. Acad. Sci.* **101**, 9103–9108 (2004).
 136. Junn, E. *et al.* Interaction of DJ-1 with Daxx inhibits apoptosis signal-regulating kinase 1 activity and cell death. *Proc. Natl. Acad. Sci. U. S. A.* **102**, 9691–9696 (2005).
 137. Xiong, H. *et al.* Parkin, PINK1, and DJ-1 form a ubiquitin E3 ligase complex

- promoting unfolded protein degradation. *J. Clin. Invest.* **119**, 650–660 (2009).
138. Anderson, P. C. & Daggett, V. Molecular basis for the structural instability of human DJ-1 induced by the L166P mutation associated with Parkinson's disease. *Biochemistry* **47**, 9380–9393 (2008).
 139. Takahashi-Niki, K., Niki, T., Taira, T., Iguchi-Ariga, S. M. M. & Ariga, H. Reduced anti-oxidative stress activities of DJ-1 mutants found in Parkinson's disease patients. *Biochem. Biophys. Res. Commun.* **320**, 389–397 (2004).
 140. Malgieri, G. & Eliezer, D. Structural effects of Parkinson's disease linked DJ-1 mutations. *Protein Sci.* **17**, 855–868 (2008).
 141. Ramirez, A. *et al.* Hereditary parkinsonism with dementia is caused by mutations in ATP13A2, encoding a lysosomal type 5 P-type ATPase. *Nat. Genet.* **38**, 1184–1191 (2006).
 142. van Veen, S. *et al.* ATP13A2 deficiency disrupts lysosomal polyamine export. *Nature* **578**, 419–424 (2020).
 143. de Lau, L. M. L. & Breteler, M. M. B. Epidemiology of Parkinson's disease. *Lancet Neurol.* **5**, 525–535 (2006).
 144. Ascherio, A. & Schwarzschild, M. A. The epidemiology of Parkinson's disease: risk factors and prevention. *Lancet Neurol.* **15**, 1257–1272 (2016).
 145. Belvisi, D. *et al.* Risk factors of Parkinson disease. *Neurology* **95**, e2500 LP-e2508 (2020).
 146. Brady, R. O., Kanfer, J. N., Bradley, R. M. & Shapiro, D. Demonstration of a deficiency of glucocerebrosidase in Gaucher's disease. *J. Clin. Invest.* **45**, 1112–1115 (1966).
 147. Neudorfer, O. *et al.* Occurrence of Parkinson's syndrome in type I Gaucher disease. *QJM* **89**, 691–694 (1996).
 148. Sidransky, E. *et al.* Multicenter analysis of glucocerebrosidase mutations in Parkinson's disease. *N. Engl. J. Med.* **361**, 1651–1661 (2009).
 149. Clark, L. N. *et al.* Association of glucocerebrosidase mutations with dementia with lewy bodies. *Arch. Neurol.* **66**, 578–583 (2009).
 150. Dawson, T. M., Ko, H. S. & Dawson, V. L. Genetic animal models of Parkinson's disease. *Neuron* **66**, 646–661 (2010).
 151. Billingsley, K. J., Bandres-Ciga, S., Saez-Atienzar, S. & Singleton, A. B. Genetic risk factors in Parkinson's disease. *Cell Tissue Res.* **373**, 9–20 (2018).
 152. Twelves, D., Perkins, K. S. M. & Counsell, C. Systematic review of incidence studies of Parkinson's disease. *Mov. Disord.* **18**, 19–31 (2003).
 153. von Campenhausen, S. *et al.* Prevalence and incidence of Parkinson's disease in Europe. *Eur. Neuropsychopharmacol.* **15**, 473–490 (2005).
 154. de Rijk, M. C. *et al.* Prevalence of Parkinson's disease in the elderly: the Rotterdam Study. *Neurology* **45**, 2143–2146 (1995).
 155. de Rijk, M. C. *et al.* Prevalence of Parkinson's disease in Europe: A collaborative study of population-based cohorts. Neurologic Diseases in the Elderly Research Group. *Neurology* **54**, S21-3 (2000).
 156. Bloem, B. R., Okun, M. S. & Klein, C. Parkinson's disease. *Lancet* **397**, 2284–2303 (2021).
 157. Storstein, O. T. A. Epidemiology of Parkinson's disease Diagnosis of PD. *J. Neural Transm.* (2017) doi:10.1007/s00702-017-1686-y.
 158. Pinter, B. *et al.* Mortality in Parkinson's disease: A 38-year follow-up study. *Mov.*

- Disord.* **30**, 266–269 (2015).
159. Vos, T. *et al.* Years lived with disability (YLDs) for 1160 sequelae of 289 diseases and injuries 1990–2010: a systematic analysis for the Global Burden of Disease Study 2010. *Lancet (London, England)* **380**, 2163–2196 (2012).
 160. Murray, C. J. L. *et al.* Disability-adjusted life years (DALYs) for 291 diseases and injuries in 21 regions, 1990–2010: a systematic analysis for the Global Burden of Disease Study 2010. *Lancet (London, England)* **380**, 2197–2223 (2012).
 161. Leibson, C. L. *et al.* Direct medical costs associated with Parkinson’s disease: a population-based study. *Mov. Disord.* **21**, 1864–1871 (2006).
 162. Ray Dorsey, E. *et al.* Global, regional, and national burden of Parkinson’s disease, 1990–2016: a systematic analysis for the Global Burden of Disease Study 2016. *Lancet Neurol.* **17**, 939–953 (2018).
 163. Macleod, A. D., Taylor, K. S. M. & Counsell, C. E. Mortality in Parkinson’s disease: a systematic review and meta-analysis. *Mov. Disord.* **29**, 1615–1622 (2014).
 164. Hely, M. A., Reid, W. G. J., Adena, M. A., Halliday, G. M. & Morris, J. G. L. The Sydney multicenter study of Parkinson’s disease: the inevitability of dementia at 20 years. *Mov. Disord.* **23**, 837–844 (2008).
 165. Moscovich, M. *et al.* Death certificate data and causes of death in patients with parkinsonism. *Parkinsonism Relat. Disord.* **41**, 99–103 (2017).
 166. Pennington, S., Snell, K., Lee, M. & Walker, R. The cause of death in idiopathic Parkinson’s disease. *Parkinsonism Relat. Disord.* **16**, 434–437 (2010).
 167. Kusumi, M., Nakashima, K., Harada, H., Nakayama, H. & Takahashi, K. Epidemiology of Parkinson’s Disease in Yonago City, Japan: Comparison with a Study Carried Out 12 Years Ago. *Neuroepidemiology* **15**, 201–207 (1996).
 168. Van Den Eeden, S. K. *et al.* Incidence of Parkinson’s disease: variation by age, gender, and race/ethnicity. *Am. J. Epidemiol.* **157**, 1015–1022 (2003).
 169. Baldereschi, M. *et al.* Parkinson’s disease and parkinsonism in a longitudinal study: two-fold higher incidence in men. ILSA Working Group. Italian Longitudinal Study on Aging. *Neurology* **55**, 1358–1363 (2000).
 170. Pringsheim, T., Jette, N., Frolkis, A. & Steeves, T. D. L. The prevalence of Parkinson’s disease: a systematic review and meta-analysis. *Mov. Disord.* **29**, 1583–1590 (2014).
 171. Hirsch, L., Jette, N., Frolkis, A., Steeves, T. & Pringsheim, T. The Incidence of Parkinson’s Disease: A Systematic Review and Meta-Analysis. *Neuroepidemiology* **46**, 292–300 (2016).
 172. Taylor, K. S. M., Cook, J. A. & Counsell, C. E. Heterogeneity in male to female risk for Parkinson’s disease. *Journal of neurology, neurosurgery, and psychiatry* vol. 78 905–906 (2007).
 173. de Lau, L. M. L., Verbaan, D., Marinus, J. & van Hilten, J. J. Survival in Parkinson’s disease. Relation with motor and non-motor features. *Parkinsonism Relat. Disord.* **20**, 613–616 (2014).
 174. Feigin, V. L. *et al.* Global, regional, and national burden of neurological disorders, 1990–2016: a systematic analysis for the Global Burden of Disease Study 2016. *Lancet Neurol.* **18**, 459–480 (2019).
 175. Wooten, G. F., Currie, L. J., Bovbjerg, V. E., Lee, J. K. & Patrie, J. Are men at greater risk for Parkinson’s disease than women? *J. Neurol. Neurosurg. Psychiatry* **75**, 637–639 (2004).

176. Maeda, T. *et al.* Clinical manifestations of nonmotor symptoms in 1021 Japanese Parkinson's disease patients from 35 medical centers. *Parkinsonism Relat. Disord.* **38**, 54–60 (2017).
177. Xu, J., Gong, D. D., Man, C. F. & Fan, Y. Parkinson's disease and risk of mortality: meta-analysis and systematic review. *Acta Neurol. Scand.* **129**, 71–79 (2014).
178. Abbas, M. M., Xu, Z. & Tan, L. C. S. Epidemiology of Parkinson's Disease—East Versus West. *Mov. Disord. Clin. Pract.* **5**, 14–28 (2018).
179. Meoni, S., Macerollo, A. & Moro, E. Sex differences in movement disorders. *Nat. Rev. Neurol.* **16**, 84–96 (2020).
180. Diem-Zangerl, A. *et al.* Mortality in Parkinson's disease: a 20-year follow-up study. *Mov. Disord.* **24**, 819–825 (2009).
181. Haaxma, C. A. *et al.* Gender differences in Parkinson's disease. *J. Neurol. Neurosurg. Psychiatry* **78**, 819–824 (2007).
182. Cantuti-Castelvetri, I. *et al.* Effects of gender on nigral gene expression and parkinson disease. *Neurobiol. Dis.* **26**, 606–614 (2007).
183. Simunovic, F., Yi, M., Wang, Y., Stephens, R. & Sonntag, K. C. Evidence for gender-specific transcriptional profiles of nigral dopamine neurons in Parkinson disease. *PLoS One* **5**, e8856–e8856 (2010).
184. Rijpkema, M. *et al.* Normal sexual dimorphism in the human basal ganglia. *Hum. Brain Mapp.* **33**, 1246–1252 (2012).
185. Gillies, G. E., Pienaar, I. S., Vohra, S. & Qamhawi, Z. Sex differences in Parkinson's disease. *Front. Neuroendocrinol.* **35**, 370–384 (2014).
186. Smith, K. M. & Dahodwala, N. Sex differences in Parkinson's disease and other movement disorders. *Exp. Neurol.* **259**, 44–56 (2014).
187. Litim, N., Morissette, M. & Di Paolo, T. Neuroactive gonadal drugs for neuroprotection in male and female models of Parkinson's disease. *Neurosci. Biobehav. Rev.* **67**, 79–88 (2016).
188. Sawada, H. & Shimohama, S. Estrogens and Parkinson disease: novel approach for neuroprotection. *Endocrine* **21**, 77–79 (2003).
189. Liu, R. *et al.* Female reproductive factors, menopausal hormone use, and Parkinson's disease. *Mov. Disord.* **29**, 889–896 (2014).
190. Benedetti, M. D. *et al.* Hysterectomy, menopause, and estrogen use preceding Parkinson's disease: An exploratory case-control study. *Mov. Disord.* **16**, 830–837 (2001).
191. Simon, K. C., Chen, H., Gao, X., Schwarzschild, M. A. & Ascherio, A. Reproductive factors, exogenous estrogen use, and risk of Parkinson's disease. *Mov. Disord.* **24**, 1359–1365 (2009).
192. Moisan, F. *et al.* Parkinson disease male-to-female ratios increase with age: French nationwide study and meta-analysis. *J. Neurol. Neurosurg. Psychiatry* **87**, 952–957 (2016).
193. Cereda, E., Barichella, M., Cassani, E., Caccialanza, R. & Pezzoli, G. Reproductive factors and clinical features of Parkinson's disease. *Parkinsonism Relat. Disord.* **19**, 1094–1099 (2013).
194. Beyer, C., Pilgrim, C. & Reisert, I. Dopamine content and metabolism in mesencephalic and diencephalic cell cultures: sex differences and effects of sex steroids. *J. Neurosci.* **11**, 1325–1333 (1991).
195. Lavalaye, J., Booij, J., Reneman, L., Habraken, J. B. & van Royen, E. A. Effect of

- age and gender on dopamine transporter imaging with [123I]FP-CIT SPET in healthy volunteers. *Eur. J. Nucl. Med.* **27**, 867–869 (2000).
196. Latourelle, J. C. *et al.* Large-scale identification of clinical and genetic predictors of motor progression in patients with newly diagnosed Parkinson's disease: a longitudinal cohort study and validation. *Lancet. Neurol.* **16**, 908–916 (2017).
 197. Scott, N. W., Macleod, A. D. & Counsell, C. E. Motor complications in an incident Parkinson's disease cohort. *Eur. J. Neurol.* **23**, 304–312 (2016).
 198. Zappia, M. *et al.* Sex differences in clinical and genetic determinants of levodopa peak-dose dyskinesias in Parkinson disease: an exploratory study. *Arch. Neurol.* **62**, 601–605 (2005).
 199. Bjornestad, A. *et al.* Risk and course of motor complications in a population-based incident Parkinson's disease cohort. *Parkinsonism Relat. Disord.* **22**, 48–53 (2016).
 200. Hassin-Baer, S. *et al.* Gender effect on time to levodopa-induced dyskinesias. *J. Neurol.* **258**, 2048–2053 (2011).
 201. Colombo, D. *et al.* The 'gender factor' in wearing-off among patients with Parkinson's disease: a post hoc analysis of DEEP study. *ScientificWorldJournal.* **2015**, 787451 (2015).
 202. Lubomski, M., Louise Rushworth, R., Lee, W., Bertram, K. L. & Williams, D. R. Sex differences in Parkinson's disease. *J. Clin. Neurosci. Off. J. Neurosurg. Soc. Australas.* **21**, 1503–1506 (2014).
 203. De Pablo-Fernández, E., Lees, A. J., Holton, J. L. & Warner, T. T. Neuropathological progression of clinical Parkinson disease subtypes. *Nat. Rev. Neurol.* **15**, 361 (2019).
 204. Sauerbier, A., Lenka, A., Aris, A. & Pal, P. K. Nonmotor Symptoms in Parkinson's Disease: Gender and Ethnic Differences. *Int. Rev. Neurobiol.* **133**, 417–446 (2017).
 205. Martinez-Martin, P. *et al.* Gender-related differences in the burden of non-motor symptoms in Parkinson's disease. *J. Neurol.* **259**, 1639–1647 (2012).
 206. Song, Y., Gu, Z., An, J. & Chan, P. Gender differences on motor and non-motor symptoms of de novo patients with early Parkinson's disease. *Neurol. Sci. Off. J. Ital. Neurol. Soc. Ital. Soc. Clin. Neurophysiol.* **35**, 1991–1996 (2014).
 207. Nicoletti, A. *et al.* Gender effect on non-motor symptoms in Parkinson's disease: are men more at risk? *Parkinsonism Relat. Disord.* **35**, 69–74 (2017).
 208. Leentjens, A. F. G. *et al.* Symptomatology and markers of anxiety disorders in Parkinson's disease: a cross-sectional study. *Mov. Disord.* **26**, 484–492 (2011).
 209. Szcwzyk-Krolikowski, K. *et al.* The influence of age and gender on motor and non-motor features of early Parkinson's disease: initial findings from the Oxford Parkinson Disease Center (OPDC) discovery cohort. *Parkinsonism Relat. Disord.* **20**, 99–105 (2014).
 210. Kovacs, M. *et al.* Impact of Sex on the Nonmotor Symptoms and the Health-Related Quality of Life in Parkinson's Disease. *Parkinsons. Dis.* **2016**, 7951840 (2016).
 211. Picillo, M. *et al.* The PRIAMO study: urinary dysfunction as a marker of disease progression in early Parkinson's disease. *Eur. J. Neurol.* **24**, 788–795 (2017).
 212. Picillo, M. *et al.* Gender differences in non-motor symptoms in early, drug naive Parkinson's disease. *J. Neurol.* **260**, 2849–2855 (2013).

213. Liu, R. *et al.* Potential sex differences in nonmotor symptoms in early drug-naive Parkinson disease. *Neurology* **84**, 2107–2115 (2015).
214. Lewitt, P. A. Levodopa for the treatment of Parkinson's disease. *N. Engl. J. Med.* **359**, 2468–2476 (2008).
215. Gray, R. *et al.* Long-term effectiveness of dopamine agonists and monoamine oxidase B inhibitors compared with levodopa as initial treatment for Parkinson's disease (PD MED): a large, open-label, pragmatic randomised trial. *Lancet (London, England)* **384**, 1196–1205 (2014).
216. Fox, S. H. *et al.* The Movement Disorder Society Evidence-Based Medicine Review Update: Treatments for the motor symptoms of Parkinson's disease. *Mov. Disord.* **26 Suppl 3**, S2-41 (2011).
217. Ferreira, J. J. *et al.* Opicapone as an adjunct to levodopa in patients with Parkinson's disease and end-of-dose motor fluctuations: a randomised, double-blind, controlled trial. *Lancet. Neurol.* **15**, 154–165 (2016).
218. Sweeney, P. J. Parkinson's disease: managing symptoms and preserving function. *Geriatrics* **50**, 24–31 (1995).
219. Connolly, B. S. & Lang, A. E. Pharmacological treatment of Parkinson disease: a review. *JAMA* **311**, 1670–1683 (2014).
220. Calabresi, P., Ghiglieri, V., Mazzocchetti, P., Corbelli, I. & Picconi, B. Levodopa-induced plasticity: a double-edged sword in Parkinson's disease? *Philos. Trans. R. Soc. London. Ser. B, Biol. Sci.* **370**, (2015).
221. Nishijima, H. *et al.* Morphologic changes of dendritic spines of striatal neurons in the levodopa-induced dyskinesia model. *Mov. Disord.* **29**, 336–343 (2014).
222. Barbeau, A. Editorial: Long-term assessment of levodopa therapy in Parkinson's disease. *Can. Med. Assoc. J.* **112**, 1379–1380 (1975).
223. Marsden, C. D. & Parkes, J. D. Success and problems of long-term levodopa therapy in Parkinson's disease. *Lancet (London, England)* **1**, 345–349 (1977).
224. Kikuchi, S. Motor fluctuations in Parkinson's disease. *J. Neurol.* **254**, 32–40 (2007).
225. Lawrence, A. D., Evans, A. H. & Lees, A. J. Compulsive use of dopamine replacement therapy in Parkinson's disease: reward systems gone awry? *Lancet. Neurol.* **2**, 595–604 (2003).
226. Baba, Y., Putzke, J. D., Whaley, N. R., Wszolek, Z. K. & Uitti, R. J. Gender and the Parkinson's disease phenotype. *J. Neurol.* **252**, 1201–1205 (2005).
227. Nyholm, D., Karlsson, E., Lundberg, M. & Askmark, H. Large differences in levodopa dose requirement in Parkinson's disease: men use higher doses than women. *Eur. J. Neurol.* **17**, 260–266 (2010).
228. Arabia, G. *et al.* Body weight, levodopa pharmacokinetics and dyskinesia in Parkinson's disease. *Neurol. Sci. Off. J. Ital. Neurol. Soc. Ital. Soc. Clin. Neurophysiol.* **23 Suppl 2**, S53-4 (2002).
229. Martinelli, P. *et al.* Levodopa pharmacokinetics and dyskinesias: are there sex-related differences? *Neurol. Sci. Off. J. Ital. Neurol. Soc. Ital. Soc. Clin. Neurophysiol.* **24**, 192–193 (2003).
230. Sharma, J. C., Macnamara, L., Hasoon, M., Vassallo, M. & Ross, I. Cascade of levodopa dose and weight-related dyskinesia in Parkinson's disease (LD-WD-PD cascade). *Parkinsonism Relat. Disord.* **12**, 499–505 (2006).
231. Sharma, J. C., Ross, I. N., Rascol, O. & Brooks, D. Relationship between weight,

- levodopa and dyskinesia: the significance of levodopa dose per kilogram body weight. *Eur. J. Neurol.* **15**, 493–496 (2008).
232. Kumagai, T. *et al.* Sex differences in the pharmacokinetics of levodopa in elderly patients with Parkinson disease. *Clin. Neuropharmacol.* **37**, 173–176 (2014).
 233. Montaurier, C. *et al.* Mechanisms of body weight gain in patients with Parkinson's disease after subthalamic stimulation. *Brain* **130**, 1808–1818 (2007).
 234. Sampaio, T. F. *et al.* MAO-B and COMT Genetic Variations Associated With Levodopa Treatment Response in Patients With Parkinson's Disease. *J. Clin. Pharmacol.* **58**, 920–926 (2018).
 235. San Luciano, M. *et al.* Sex differences in LRRK2 G2019S and idiopathic Parkinson's Disease. *Ann. Clin. Transl. Neurol.* **4**, 801–810 (2017).
 236. Hely, M. A., Morris, J. G. L., Reid, W. G. J. & Trafficante, R. Sydney Multicenter Study of Parkinson's disease: non-L-dopa-responsive problems dominate at 15 years. *Mov. Disord.* **20**, 190–199 (2005).
 237. Luquin, M.-R., Kulisevsky, J., Martinez-Martin, P., Mir, P. & Tolosa, E. S. Consensus on the Definition of Advanced Parkinson's Disease: A Neurologists-Based Delphi Study (CEPA Study). *Parkinsons. Dis.* **2017**, 4047392 (2017).
 238. Chaudhuri, K. R. & Schapira, A. H. V. Non-motor symptoms of Parkinson's disease: dopaminergic pathophysiology and treatment. *Lancet. Neurol.* **8**, 464–474 (2009).
 239. Storch, A. *et al.* Nonmotor fluctuations in Parkinson disease: severity and correlation with motor complications. *Neurology* **80**, 800–809 (2013).
 240. Lim, S.-Y., Fox, S. H. & Lang, A. E. Overview of the extranigral aspects of Parkinson disease. *Arch. Neurol.* **66**, 167–172 (2009).
 241. Kalia, L. V, Brotchie, J. M. & Fox, S. H. Novel nondopaminergic targets for motor features of Parkinson's disease: review of recent trials. *Mov. Disord. Off. J. Mov. Disord. Soc.* **28**, 131–144 (2013).
 242. Seppi, K. *et al.* The Movement Disorder Society Evidence-Based Medicine Review Update: Treatments for the non-motor symptoms of Parkinson's disease. *Mov. Disord.* **26 Suppl 3**, S42-80 (2011).
 243. Connolly, B. & Fox, S. H. Treatment of cognitive, psychiatric, and affective disorders associated with Parkinson's disease. *Neurother. J. Am. Soc. Exp. Neurother.* **11**, 78–91 (2014).
 244. Weintraub, D. & Burn, D. J. Parkinson's disease: the quintessential neuropsychiatric disorder. *Mov. Disord.* **26**, 1022–1031 (2011).
 245. Perez-Lloret, S., Rey, M. V., Pavy-Le Traon, A. & Rascol, O. Emerging drugs for autonomic dysfunction in Parkinson's disease. *Expert Opin. Emerg. Drugs* **18**, 39–53 (2013).
 246. Mak, M. K., Wong-Yu, I. S., Shen, X. & Chung, C. L. Long-term effects of exercise and physical therapy in people with Parkinson disease. *Nat. Rev. Neurol.* **13**, 689–703 (2017).
 247. Chung, C. L. H., Thilarajah, S. & Tan, D. Effectiveness of resistance training on muscle strength and physical function in people with Parkinson's disease: a systematic review and meta-analysis. *Clin. Rehabil.* **30**, 11–23 (2015).
 248. Mehrholz, J. *et al.* Treadmill training for patients with Parkinson Disease. An abridged version of a Cochrane Review. *Eur. J. Phys. Rehabil. Med.* **52**, 704–713 (2016).

249. Lötze, D., Ostermann, T. & Büssing, A. Argentine tango in Parkinson disease – a systematic review and meta-analysis. *BMC Neurol.* **15**, 226 (2015).
250. Zhang, S., Liu, D., Ye, D., Li, H. & Chen, F. Can music-based movement therapy improve motor dysfunction in patients with Parkinson’s disease? Systematic review and meta-analysis. *Neurol. Sci.* **38**, 1629–1636 (2017).
251. Yang, Y., Li, X.-Y., Gong, L., Zhu, Y.-L. & Hao, Y.-L. Tai Chi for Improvement of Motor Function, Balance and Gait in Parkinson’s Disease: A Systematic Review and Meta-Analysis. *PLoS One* **9**, e102942 (2014).
252. Tomlinson, C. L. *et al.* Physiotherapy versus placebo or no intervention in Parkinson’s disease. *Cochrane Database Syst. Rev.* (2013) doi:10.1002/14651858.CD002817.pub4.
253. Calabresi, P., Castrioto, A., Di Filippo, M. & Picconi, B. New experimental and clinical links between the hippocampus and the dopaminergic system in Parkinson’s disease. *Lancet. Neurol.* **12**, 811–821 (2013).
254. Cotzias, G. C., Papavasiliou, P. S. & Gellene, R. Modification of Parkinsonism--chronic treatment with L-dopa. *N. Engl. J. Med.* **280**, 337–345 (1969).
255. Valldeoriola, F. *et al.* Bilateral subthalamic stimulation monotherapy in advanced Parkinson’s disease: long-term follow-up of patients. *Mov. Disord.* **17**, 125–132 (2002).
256. Deuschl, G. *et al.* A randomized trial of deep-brain stimulation for Parkinson’s disease. *N. Engl. J. Med.* **355**, 896–908 (2006).
257. Tseng, H.-M., Su, P. C., Liu, H.-M., Liou, H.-H. & Yen, R.-F. Bilateral subthalamotomy for advanced Parkinson disease. *Surg. Neurol.* **68 Suppl 1**, S43-50; discussion S50-1 (2007).
258. Perlmutter, J. S. *et al.* Blood flow responses to deep brain stimulation of thalamus. *Neurology* **58**, 1388–1394 (2002).
259. Limousin, P. *et al.* Effect of parkinsonian signs and symptoms of bilateral subthalamic nucleus stimulation. *Lancet (London, England)* **345**, 91–95 (1995).
260. Krack, P. *et al.* Five-year follow-up of bilateral stimulation of the subthalamic nucleus in advanced Parkinson’s disease. *N. Engl. J. Med.* **349**, 1925–1934 (2003).
261. Tabbal, S. D. *et al.* Safety and efficacy of subthalamic nucleus deep brain stimulation performed with limited intraoperative mapping for treatment of Parkinson’s disease. *Neurosurgery* **61**, 119–127 (2007).
262. Bronstein, J. M. *et al.* Deep brain stimulation for Parkinson disease: an expert consensus and review of key issues. *Arch. Neurol.* **68**, 165 (2011).
263. Deuschl, G. & Agid, Y. Subthalamic neurostimulation for Parkinson’s disease with early fluctuations: balancing the risks and benefits. *Lancet. Neurol.* **12**, 1025–1034 (2013).
264. Odekerken, V. J. J. *et al.* Subthalamic nucleus versus globus pallidus bilateral deep brain stimulation for advanced Parkinson’s disease (NSTAPS study): a randomised controlled trial. *Lancet. Neurol.* **12**, 37–44 (2013).
265. Stern, M. B., Follett, K. A. & Weaver, F. M. Randomized trial of deep brain stimulation for Parkinson disease: thirty-six-month outcomes; turning tables: should GPi become the preferred DBS target for Parkinson disease? Author response. *Neurology* vol. 80 225 (2013).
266. Odekerken, V. J. J. *et al.* GPi vs STN deep brain stimulation for Parkinson disease:

- Three-year follow-up. *Neurology* **86**, 755–761 (2016).
267. McIntosh, E., Gray, A. & Aziz, T. Estimating the costs of surgical innovations: the case for subthalamic nucleus stimulation in the treatment of advanced Parkinson's disease. *Mov. Disord.* **18**, 993–999 (2003).
 268. Bergman, H., Wichmann, T. & DeLong, M. R. Reversal of experimental parkinsonism by lesions of the subthalamic nucleus. *Science* **249**, 1436–1438 (1990).
 269. Iacono, R. P. *et al.* The results, indications, and physiology of posteroventral pallidotomy for patients with Parkinson's disease. *Neurosurgery* **36**, 1117–1118 (1995).
 270. Su, P. C., Tseng, H.-M., Liu, H.-M., Yen, R.-F. & Liou, H.-H. Treatment of advanced Parkinson's disease by subthalamotomy: One-year results. *Mov. Disord.* **18**, 531–538 (2003).
 271. Alvarez, L. *et al.* Bilateral subthalamotomy in Parkinson's disease: initial and long-term response. *Brain* **128**, 570–583 (2005).
 272. Schuurman, P. R. *et al.* A Comparison of Continuous Thalamic Stimulation and Thalamotomy for Suppression of Severe Tremor. *N. Engl. J. Med.* **342**, 461–468 (2000).
 273. Dierssen, G., Bergman, L. L., Gionio, G. & Cooper, I. S. Hemiballism Following Surgery for Parkinson's Disease: A Clinicoanatomical Study of a Case. *Arch. Neurol.* **5**, 627–637 (1961).
 274. Guridi, J. & Obeso, J. A. The subthalamic nucleus, hemiballismus and Parkinson's disease: reappraisal of a neurosurgical dogma. *Brain* **124**, 5–19 (2001).
 275. De Fabregues, O. *et al.* Long-term safety and effectiveness of levodopa-carbidopa intestinal gel infusion. *Brain Behav.* **7**, e00758–e00758 (2017).
 276. Fernandez, H. H. *et al.* Long-term safety and efficacy of levodopa-carbidopa intestinal gel in advanced Parkinson's disease. *Mov. Disord.* **33**, 928–936 (2018).
 277. Manson, A. J. *et al.* Intravenous apomorphine therapy in Parkinson's disease: Clinical and pharmacokinetic observations. *Brain* **124**, 331–340 (2001).
 278. Katzenschlager, R. *et al.* Apomorphine subcutaneous infusion in patients with Parkinson's disease with persistent motor fluctuations (TOLEDO): a multicentre, double-blind, randomised, placebo-controlled trial. *Lancet. Neurol.* **17**, 749–759 (2018).
 279. Ntetsika, T., Papathoma, P.-E. & Markaki, I. Novel targeted therapies for Parkinson's disease. *Mol. Med.* **27**, 17 (2021).
 280. Meng, Y., Hynynen, K. & Lipsman, N. Applications of focused ultrasound in the brain: from thermoablation to drug delivery. *Nat. Rev. Neurol.* **17**, 7–22 (2021).
 281. Dayan, E., Censor, N., Buch, E. R., Sandrini, M. & Cohen, L. G. Noninvasive brain stimulation: from physiology to network dynamics and back. *Nat. Neurosci.* **16**, 838–844 (2013).
 282. Bestmann, S. & Walsh, V. Transcranial electrical stimulation. *Curr. Biol.* **27**, R1258–R1262 (2017).
 283. Polanía, R., Nitsche, M. A. & Ruff, C. C. Studying and modifying brain function with non-invasive brain stimulation. *Nat. Neurosci.* **21**, 174–187 (2018).
 284. FRY, W. J. Intense ultrasound in investigations of the central nervous system. *Adv. Biol. Med. Phys.* **6**, 281–348 (1958).
 285. Tufail, Y. *et al.* Transcranial Pulsed Ultrasound Stimulates Intact Brain Circuits.

- Neuron* **66**, 681–694 (2010).
286. Dallapiazza, R. F. *et al.* Noninvasive neuromodulation and thalamic mapping with low-intensity focused ultrasound. *J. Neurosurg. JNS* **128**, 875–884 (2018).
 287. Folloni, D. *et al.* Manipulation of Subcortical and Deep Cortical Activity in the Primate Brain Using Transcranial Focused Ultrasound Stimulation. *Neuron* **101**, 1109–1116.e5 (2019).
 288. Deffieux, T. *et al.* Low-Intensity Focused Ultrasound Modulates Monkey Visuomotor Behavior. *Curr. Biol.* **23**, 2430–2433 (2013).
 289. Ballantine, H. T., Bell, E. & Manlapaz, J. Progress and Problems in the Neurological Applications of Focused Ultrasound. *J. Neurosurg.* **17**, 858–876 (1960).
 290. Lele, P. P. Effects of focused ultrasonic radiation on peripheral nerve, with observations on local heating. *Exp. Neurol.* **8**, 47–83 (1963).
 291. Yoo, S.-S. *et al.* Focused ultrasound modulates region-specific brain activity. *Neuroimage* **56**, 1267–1275 (2011).
 292. Liu, L. *et al.* Protective effect of low-intensity transcranial ultrasound stimulation after differing delay following an acute ischemic stroke. *Brain Res. Bull.* **146**, 22–27 (2019).
 293. Stern, J. M. *et al.* Safety of focused ultrasound neuromodulation in humans with temporal lobe epilepsy. *Brain Stimul.* **14**, 1022–1031 (2021).
 294. Verhagen, L. *et al.* Offline impact of transcranial focused ultrasound on cortical activation in primates. *Elife* **8**, e40541 (2019).
 295. Dinno, M. A. *et al.* The significance of membrane changes in the safe and effective use of therapeutic and diagnostic ultrasound. *Phys. Med. Biol.* **34**, 1543–1552 (1989).
 296. Dalecki, D. Mechanical Bioeffects of Ultrasound. *Annu. Rev. Biomed. Eng.* **6**, 229–248 (2004).
 297. Tyler, W. J. *et al.* Remote excitation of neuronal circuits using low-intensity, low-frequency ultrasound. *PLoS One* **3**, e3511 (2008).
 298. Schlesinger, I. *et al.* MRI Guided Focused Ultrasound Thalamotomy for Moderate-to-Severe Tremor in Parkinson’s Disease. *Park. Dis.* 219149 (2015) doi:10.1155/2015/219149.
 299. Sperling, S. A. *et al.* Focused ultrasound thalamotomy in Parkinson disease: Nonmotor outcomes and quality of life. *Neurology* **91**, e1275–e1284 (2018).
 300. Magara, A. *et al.* First experience with MR-guided focused ultrasound in the treatment of Parkinson’s disease. *J. Ther. ultrasound* **2**, 11 (2014).
 301. Martínez-Fernández, R. *et al.* Focused ultrasound subthalamotomy in patients with asymmetric Parkinson’s disease: a pilot study. *Lancet Neurol.* **17**, 54–63 (2018).
 302. Na, Y. C., Chang, W. S., Jung, H. H., Kweon, E. J. & Chang, J. W. Unilateral magnetic resonance-guided focused ultrasound pallidotomy for Parkinson disease. *Neurology* **85**, 549–551 (2015).
 303. Perlmutter, J. S. & Ushe, M. Parkinson’s Disease — What’s the FUS? *N. Engl. J. Med.* **383**, 2582–2584 (2020).
 304. Kalia, L. V, Kalia, S. K. & Lang, A. E. Disease-modifying strategies for Parkinson’s disease. *Mov. Disord.* **30**, 1442–1450 (2015).
 305. Yulug, B., Hanoglu, L. & Kilic, E. The neuroprotective effect of focused

- ultrasound: New perspectives on an old tool. *Brain Res. Bull.* **131**, 199–206 (2017).
306. McDannold, N., Vykhodtseva, N. & Hynynen, K. Blood-brain barrier disruption induced by focused ultrasound and circulating preformed microbubbles appears to be characterized by the mechanical index. *Ultrasound Med. Biol.* **34**, 834–840 (2008).
 307. Yang, F.-Y. & Lee, P.-Y. Efficiency of drug delivery enhanced by acoustic pressure during blood-brain barrier disruption induced by focused ultrasound. *Int. J. Nanomedicine* **7**, 2573–2582 (2012).
 308. Samiotaki, G., Acosta, C., Wang, S. & Konofagou, E. E. Enhanced delivery and bioactivity of the neurturin neurotrophic factor through focused ultrasound-mediated blood-brain barrier opening in vivo. *J. Cereb. Blood Flow Metab.* **35**, 611–622 (2015).
 309. Wang, X. *et al.* Intracerebral administration of ultrasound-induced dissolution of lipid-coated GDNF microbubbles provides neuroprotection in a rat model of Parkinson’s disease. *Brain Res. Bull.* **103**, 60–65 (2014).
 310. Fan, C.-H. *et al.* Noninvasive, Targeted, and Non-Viral Ultrasound-Mediated GDNF-Plasmid Delivery for Treatment of Parkinson’s Disease. *Sci. Rep.* **6**, 19579 (2016).
 311. Lin, C.-Y. *et al.* Non-invasive, neuron-specific gene therapy by focused ultrasound-induced blood-brain barrier opening in Parkinson’s disease mouse model. *J. Control. Release* **235**, 72–81 (2016).
 312. Jordão, J. F. *et al.* Antibodies targeted to the brain with image-guided focused ultrasound reduces amyloid-beta plaque load in the TgCRND8 mouse model of Alzheimer’s disease. *PLoS One* **5**, e10549 (2010).
 313. Leinenga, G. & Götz, J. Scanning ultrasound removes amyloid- β and restores memory in an Alzheimer’s disease mouse model. *Sci. Transl. Med.* **7**, 278ra33 (2015).
 314. Choi, S. Y. *et al.* High intensity focused ultrasound as a potential new modality for the treatment of pigmentary skin disorder. *Ski. Res. Technol. Off. J. Int. Soc. Bioeng. Ski. [and] Int. Soc. Digit. Imaging Ski. [and] Int. Soc. Ski. Imaging* **22**, 131–136 (2016).
 315. Gavrillov, L. R. *et al.* The effect of focused ultrasound on the skin and deep nerve structures of man and animal. *Prog. Brain Res.* **43**, 279–292 (1976).
 316. Velling, V. A. & Shklyaruk, S. P. Modulation of the functional state of the brain with the aid of focused ultrasonic action. *Neurosci. Behav. Physiol.* **18**, 369–375 (1988).
 317. Bachtold, M. R., Rinaldi, P. C., Jones, J. P., Reines, F. & Price, L. R. Focused ultrasound modifications of neural circuit activity in a mammalian brain. *Ultrasound Med. Biol.* **24**, 557–565 (1998).
 318. ter Haar, G. Therapeutic applications of ultrasound. *Prog. Biophys. Mol. Biol.* **93**, 111–129 (2007).
 319. Haar, G. Ter & Coussios, C. High intensity focused ultrasound: physical principles and devices. *Int. J. Hyperth. Off. J. Eur. Soc. Hyperthermic Oncol. North Am. Hyperth. Gr.* **23**, 89–104 (2007).
 320. Mouratidis, P. X. E., Rivens, I., Civale, J., Symonds-Tayler, R. & Ter Haar, G. ‘Relationship between thermal dose and cell death for “rapid” ablative and

- “slow” hyperthermic heating’. *Int. J. Hyperth. Off. J. Eur. Soc. Hyperthermic Oncol. North Am. Hyperth. Gr.* **36**, 229–243 (2019).
321. Cosgrove, D. Ultrasound contrast agents: an overview. *Eur. J. Radiol.* **60**, 324–330 (2006).
 322. Ferrara, K., Pollard, R. & Borden, M. Ultrasound microbubble contrast agents: fundamentals and application to gene and drug delivery. *Annu. Rev. Biomed. Eng.* **9**, 415–447 (2007).
 323. Sukovich, J. R. *et al.* In vivo histotripsy brain treatment. *J. Neurosurg.* 1–8 (2018) doi:10.3171/2018.4.JNS172652.
 324. Fomenko, A., Neudorfer, C., Dallapiazza, R. F., Kalia, S. K. & Lozano, A. M. Low-intensity ultrasound neuromodulation: An overview of mechanisms and emerging human applications. *Brain Stimul.* **11**, 1209–1217 (2018).
 325. Pasquinelli, C., Hanson, L. G., Siebner, H. R., Lee, H. J. & Thielscher, A. Safety of transcranial focused ultrasound stimulation: A systematic review of the state of knowledge from both human and animal studies. *Brain Stimul.* **12**, 1367–1380 (2019).
 326. Sassaroli, E. & Vykhodtseva, N. Acoustic neuromodulation from a basic science prospective. *J. Ther. ultrasound* **4**, 17 (2016).
 327. Burgess, A. *et al.* Alzheimer disease in a mouse model: MR imaging-guided focused ultrasound targeted to the hippocampus opens the blood-brain barrier and improves pathologic abnormalities and behavior. *Radiology* **273**, 736–745 (2014).
 328. Nisbet, R. M. *et al.* Combined effects of scanning ultrasound and a tau-specific single chain antibody in a tau transgenic mouse model. *Brain* **140**, 1220–1230 (2017).
 329. Chen, X. *et al.* Neuroprotective Effect of Low-Intensity Pulsed Ultrasound on the Mouse MPTP/MPP+ Model of Dopaminergic Neuron Injury. *Ultrasound Med. Biol.* **47**, 2321–2330 (2021).
 330. Dong, Y. *et al.* Assessment of Neuroprotective Effects of Low-Intensity Transcranial Ultrasound Stimulation in a Parkinson’s Disease Rat Model by Fractional Anisotropy and Relaxation Time T2(*) Value. *Front. Neurosci.* **15**, 590354 (2021).
 331. Hynynen, K., McDannold, N., Vykhodtseva, N. & Jolesz, F. A. Noninvasive MR imaging-guided focal opening of the blood-brain barrier in rabbits. *Radiology* **220**, 640–646 (2001).
 332. Xhima, K., Nabbouh, F., Hynynen, K., Aubert, I. & Tandon, A. Noninvasive delivery of an α -synuclein gene silencing vector with magnetic resonance-guided focused ultrasound. *Mov. Disord.* **33**, 1567–1579 (2018).
 333. Karakatsani, M. E. *et al.* Amelioration of the nigrostriatal pathway facilitated by ultrasound-mediated neurotrophic delivery in early Parkinson’s disease. *J. Control. release Off. J. Control. Release Soc.* **303**, 289–301 (2019).
 334. Lipsman, N. *et al.* Blood–brain barrier opening in Alzheimer’s disease using MR-guided focused ultrasound. *Nat. Commun.* **9**, 2336 (2018).
 335. Abrahao, A. *et al.* First-in-human trial of blood-brain barrier opening in amyotrophic lateral sclerosis using MR-guided focused ultrasound. *Nat. Commun.* **10**, 4373 (2019).
 336. Gasca-Salas, C. *et al.* Blood-brain barrier opening with focused ultrasound in

- Parkinson's disease dementia. *Nat. Commun.* **12**, 779 (2021).
337. G., B. S., Zhenwei, S. & Roderick, M. Mechanosensitivity is mediated directly by the lipid membrane in TRAAK and TREK1 K⁺ channels. *Proc. Natl. Acad. Sci.* **111**, 3614–3619 (2014).
 338. Tyler, W. J. Noninvasive neuromodulation with ultrasound? A continuum mechanics hypothesis. *Neurosci. a Rev. J. bringing Neurobiol. Neurol. psychiatry* **17**, 25–36 (2011).
 339. Guo, H. *et al.* Ultrasound Produces Extensive Brain Activation via a Cochlear Pathway. *Neuron* **98**, 1020-1030.e4 (2018).
 340. Sato, T., Shapiro, M. G. & Tsao, D. Y. Ultrasonic Neuromodulation Causes Widespread Cortical Activation via an Indirect Auditory Mechanism. *Neuron* **98**, 1031-1041.e5 (2018).
 341. Lindvall, O. *et al.* Grafts of fetal dopamine neurons survive and improve motor function in Parkinson's disease. *Science* **247**, 574–577 (1990).
 342. Piccini, P. *et al.* Dopamine release from nigral transplants visualized in vivo in a Parkinson's patient. *Nat. Neurosci.* **2**, 1137–1140 (1999).
 343. Freed, C. R. *et al.* Transplantation of embryonic dopamine neurons for severe Parkinson's disease. *N. Engl. J. Med.* **344**, 710–719 (2001).
 344. Hagell, P. *et al.* Dyskinesias following neural transplantation in Parkinson's disease. *Nat. Neurosci.* **5**, 627–628 (2002).
 345. Olanow, C. W. *et al.* A double-blind controlled trial of bilateral fetal nigral transplantation in Parkinson's disease. *Ann. Neurol.* **54**, 403–414 (2003).
 346. Brundin, P. & Kordower, J. H. Neuropathology in transplants in Parkinson's disease: implications for disease pathogenesis and the future of cell therapy. *Prog. Brain Res.* **200**, 221–241 (2012).
 347. Kefalopoulou, Z. *et al.* Long-term clinical outcome of fetal cell transplantation for Parkinson disease: two case reports. *JAMA Neurol.* **71**, 83–87 (2014).
 348. Barker, R. A. Designing stem-cell-based dopamine cell replacement trials for Parkinson's disease. *Nat. Med.* **25**, 1045–1053 (2019).
 349. Barker, R. A., Drouin-Ouellet, J. & Parmar, M. Cell-based therapies for Parkinson disease—past insights and future potential. *Nat. Rev. Neurol.* **11**, 492–503 (2015).
 350. Barker, R. A., Parmar, M., Studer, L. & Takahashi, J. Human Trials of Stem Cell-Derived Dopamine Neurons for Parkinson's Disease: Dawn of a New Era. *Cell Stem Cell* **21**, 569–573 (2017).
 351. Kordower, J. H. & Bjorklund, A. Trophic factor gene therapy for Parkinson's disease. *Mov. Disord.* **28**, 96–109 (2013).
 352. Gill, S. S. *et al.* Direct brain infusion of glial cell line-derived neurotrophic factor in Parkinson disease. *Nat. Med.* **9**, 589–595 (2003).
 353. Lang, A. E. *et al.* Randomized controlled trial of intraputamenal glial cell line-derived neurotrophic factor infusion in Parkinson disease. *Ann. Neurol.* **59**, 459–466 (2006).
 354. Kordower, J. H. *et al.* Delivery of neurturin by AAV2 (CERE-120)-mediated gene transfer provides structural and functional neuroprotection and neurorestoration in MPTP-treated monkeys. *Ann. Neurol.* **60**, 706–715 (2006).
 355. Bartus, R. T. & Johnson, E. M. J. Clinical tests of neurotrophic factors for human neurodegenerative diseases, part 1: Where have we been and what have we

- learned? *Neurobiol. Dis.* **97**, 156–168 (2017).
356. Bartus, R. T. & Johnson, E. M. J. Clinical tests of neurotrophic factors for human neurodegenerative diseases, part 2: Where do we stand and where must we go next? *Neurobiol. Dis.* **97**, 169–178 (2017).
 357. Palfi, S. *et al.* Long-Term Follow-Up of a Phase I/II Study of ProSavin, a Lentiviral Vector Gene Therapy for Parkinson’s Disease. *Hum. Gene Ther. Clin. Dev.* **29**, 148–155 (2018).
 358. Mittermeyer, G. *et al.* Long-term evaluation of a phase 1 study of AADC gene therapy for Parkinson’s disease. *Hum. Gene Ther.* **23**, 377–381 (2012).
 359. Nutt, J. G. *et al.* Aromatic L-Amino Acid Decarboxylase Gene Therapy Enhances Levodopa Response in Parkinson’s Disease. *Mov. Disord.* **35**, 851–858 (2020).
 360. Christine, C. W. *et al.* Safety of AADC Gene Therapy for Moderately Advanced Parkinson Disease. *Neurology* **98**, e40 LP-e50 (2022).
 361. LeWitt, P. A. *et al.* AAV2-GAD gene therapy for advanced Parkinson’s disease: a double-blind, sham-surgery controlled, randomised trial. *Lancet. Neurol.* **10**, 309–319 (2011).
 362. Niethammer, M. *et al.* Long-term follow-up of a randomized AAV2-GAD gene therapy trial for Parkinson’s disease. *JCI Insight* **2**, (2017).
 363. Tieu, K. A guide to neurotoxic animal models of Parkinson’s disease. *Cold Spring Harb. Perspect. Med.* **1**, 1–20 (2011).
 364. Stoker TB, G. J. *Parkinson’s Disease: Pathogenesis and Clinical Aspects.* (Codon Publications, 2018). doi:10.15586/codonpublications.parkinsonsdisease.2018.
 365. Langston, J. W. & Ballard, P. A. J. Parkinson’s disease in a chemist working with 1-methyl-4-phenyl-1,2,5,6-tetrahydropyridine. *The New England journal of medicine* vol. 309 310 (1983).
 366. Chiba, K., Trevor, A. & Castagnoli, N. J. Metabolism of the neurotoxic tertiary amine, MPTP, by brain monoamine oxidase. *Biochem. Biophys. Res. Commun.* **120**, 574–578 (1984).
 367. Cui, M. *et al.* The organic cation transporter-3 is a pivotal modulator of neurodegeneration in the nigrostriatal dopaminergic pathway. *Proc. Natl. Acad. Sci. U. S. A.* **106**, 8043–8048 (2009).
 368. Javitch, J. A., D’Amato, R. J., Strittmatter, S. M. & Snyder, S. H. Parkinsonism-inducing neurotoxin, N-methyl-4-phenyl-1,2,3,6 -tetrahydropyridine: uptake of the metabolite N-methyl-4-phenylpyridine by dopamine neurons explains selective toxicity. *Proc. Natl. Acad. Sci. U. S. A.* **82**, 2173–2177 (1985).
 369. Nicklas, W. J., Vyas, I. & Heikkila, R. E. Inhibition of NADH-linked oxidation in brain mitochondria by 1-methyl-4-phenyl-pyridine, a metabolite of the neurotoxin, 1-methyl-4-phenyl-1,2,5,6-tetrahydropyridine. *Life Sci.* **36**, 2503–2508 (1985).
 370. Ramsay, R. R., Salach, J. I., Dadgar, J. & Singer, T. P. Inhibition of mitochondrial NADH dehydrogenase by pyridine derivatives and its possible relation to experimental and idiopathic parkinsonism. *Biochem. Biophys. Res. Commun.* **135**, 269–275 (1986).
 371. Mizuno, Y., Sone, N. & Saitoh, T. Effects of 1-methyl-4-phenyl-1,2,3,6-tetrahydropyridine and 1-methyl-4-phenylpyridinium ion on activities of the enzymes in the electron transport system in mouse brain. *J. Neurochem.* **48**, 1787–1793 (1987).

372. Przedborski, S. *et al.* The parkinsonian toxin MPTP: action and mechanism. *Restor. Neurol. Neurosci.* **16**, 135–142 (2000).
373. Jackson-Lewis, V., Jakowec, M., Burke, R. E. & Przedborski, S. Time course and morphology of dopaminergic neuronal death caused by the neurotoxin 1-methyl-4-phenyl-1,2,3,6-tetrahydropyridine. *Neurodegeneration* **4**, 257–269 (1995).
374. Vázquez-Claverie, M. *et al.* Acute and chronic 1-methyl-4-phenyl-1,2,3,6-tetrahydropyridine administrations elicit similar microglial activation in the substantia nigra of monkeys. *J. Neuropathol. Exp. Neurol.* **68**, 977–984 (2009).
375. Forno, L. S., DeLanney, L. E., Irwin, I. & Langston, J. W. Similarities and differences between MPTP-induced parkinsonism and Parkinson's disease. Neuropathologic considerations. *Adv. Neurol.* **60**, 600–608 (1993).
376. Forno, L. S., Langston, J. W., DeLanney, L. E., Irwin, I. & Ricaurte, G. A. Locus ceruleus lesions and eosinophilic inclusions in MPTP-treated monkeys. *Ann. Neurol.* **20**, 449–455 (1986).
377. Fornai, F. *et al.* Parkinson-like syndrome induced by continuous MPTP infusion: convergent roles of the ubiquitin-proteasome system and alpha-synuclein. *Proc. Natl. Acad. Sci. U. S. A.* **102**, 3413–3418 (2005).
378. Anderson, G. *et al.* Loss of enteric dopaminergic neurons and associated changes in colon motility in an MPTP mouse model of Parkinson's disease. *Exp. Neurol.* **207**, 4–12 (2007).
379. Ungerstedt, U. 6-Hydroxy-dopamine induced degeneration of central monoamine neurons. *Eur. J. Pharmacol.* **5**, 107–110 (1968).
380. Curtius, H. C., Wolfensberger, M., Steinmann, B., Redweik, U. & Siegfried, J. Mass fragmentography of dopamine and 6-hydroxydopamine. Application to the determination of dopamine in human brain biopsies from the caudate nucleus. *J. Chromatogr.* **99**, 529–540 (1974).
381. Jonsson, G. Chemical neurotoxins as denervation tools in neurobiology. *Annu. Rev. Neurosci.* **3**, 169–187 (1980).
382. Luthman, J., Fredriksson, A., Sundström, E., Jonsson, G. & Archer, T. Selective lesion of central dopamine or noradrenaline neuron systems in the neonatal rat: motor behavior and monoamine alterations at adult stage. *Behav. Brain Res.* **33**, 267–277 (1989).
383. Saner, A. & Thoenen, H. Model experiments on the molecular mechanism of action of 6-hydroxydopamine. *Mol. Pharmacol.* **7**, 147–154 (1971).
384. Jeon, B. S., Jackson-Lewis, V. & Burke, R. E. 6-Hydroxydopamine lesion of the rat substantia nigra: time course and morphology of cell death. *Neurodegener. a J. Neurodegener. Disord. neuroprotection, neuroregeneration* **4**, 131–137 (1995).
385. Sauer, H. & Oertel, W. H. Progressive degeneration of nigrostriatal dopamine neurons following intrastriatal terminal lesions with 6-hydroxydopamine: a combined retrograde tracing and immunocytochemical study in the rat. *Neuroscience* **59**, 401–415 (1994).
386. Branchi, I. *et al.* Nonmotor symptoms in Parkinson's disease: investigating early-phase onset of behavioral dysfunction in the 6-hydroxydopamine-lesioned rat model. *J. Neurosci. Res.* **86**, 2050–2061 (2008).
387. Tadaiesky, M. T. *et al.* Emotional, cognitive and neurochemical alterations in a premotor stage model of Parkinson's disease. *Neuroscience* **156**, 830–840

- (2008).
388. Jonsson, G. *Chemical lesioning techniques: Monoamine neurotoxins*. In *Handbook of chemical neuroanatomy Vol 1: Methods in chemical neuroanatomy*. (Elsevier, Amsterdam, 1983).
 389. Bezard, E., Imbert, C. & Gross, C. E. Experimental models of Parkinson's disease: from the static to the dynamic. *Rev. Neurosci.* **9**, 71–90 (1998).
 390. Bezard, E. & Przedborski, S. A tale on animal models of Parkinson's disease. *Mov. Disord.* **26**, 993–1002 (2011).
 391. Ungerstedt, U. & Arbuthnott, G. W. Quantitative recording of rotational behavior in rats after 6-hydroxy-dopamine lesions of the nigrostriatal dopamine system. *Brain Res.* **24**, 485–493 (1970).
 392. Snyder, S. H. & D'Amato, R. J. Neurology: Predicting Parkinson's disease. *Nature* **317**, 198–199 (1985).
 393. Shimizu, K. *et al.* Carrier-mediated processes in blood–brain barrier penetration and neural uptake of paraquat. *Brain Res.* **906**, 135–142 (2001).
 394. Corasaniti, M. T., Defilippo, R., Rodinò, P., Nappi, G. & Nisticò, G. Evidence that paraquat is able to cross the blood-brain barrier to a different extent in rats of various age. *Funct. Neurol.* **6**, 385–391 (1991).
 395. Richardson, J. R., Quan, Y., Sherer, T. B., Greenamyre, J. T. & Miller, G. W. Paraquat neurotoxicity is distinct from that of MPTP and rotenone. *Toxicol. Sci.* **88**, 193–201 (2005).
 396. Cochemé, H. M. & Murphy, M. P. Complex I Is the Major Site of Mitochondrial Superoxide Production by Paraquat *. *J. Biol. Chem.* **283**, 1786–1798 (2008).
 397. Day, B. J., Patel, M., Calavetta, L., Chang, L. Y. & Stamler, J. S. A mechanism of paraquat toxicity involving nitric oxide synthase. *Proc. Natl. Acad. Sci. U. S. A.* **96**, 12760–12765 (1999).
 398. Brooks, A. I., Chadwick, C. A., Gelbard, H. A., Cory-Slechta, D. A. & Federoff, H. J. Paraquat elicited neurobehavioral syndrome caused by dopaminergic neuron loss. *Brain Res.* **823**, 1–10 (1999).
 399. McCormack, A. L. *et al.* Environmental risk factors and Parkinson's disease: selective degeneration of nigral dopaminergic neurons caused by the herbicide paraquat. *Neurobiol. Dis.* **10**, 119–127 (2002).
 400. Thiruchelvam, M. *et al.* Age-related irreversible progressive nigrostriatal dopaminergic neurotoxicity in the paraquat and maneb model of the Parkinson's disease phenotype. *Eur. J. Neurosci.* **18**, 589–600 (2003).
 401. Thiruchelvam, M., Richfield, E. K., Baggs, R. B., Tank, A. W. & Cory-Slechta, D. A. The nigrostriatal dopaminergic system as a preferential target of repeated exposures to combined paraquat and maneb: implications for Parkinson's disease. *J. Neurosci.* **20**, 9207–9214 (2000).
 402. Cicchetti, F. *et al.* Systemic exposure to paraquat and maneb models early Parkinson's disease in young adult rats. *Neurobiol. Dis.* **20**, 360–371 (2005).
 403. Ossowska, K. *et al.* A slowly developing dysfunction of dopaminergic nigrostriatal neurons induced by long-term paraquat administration in rats: an animal model of preclinical stages of Parkinson's disease? *Eur. J. Neurosci.* **22**, 1294–1304 (2005).
 404. Hertzman, C., Wiens, M., Bowering, D., Snow, B. & Calne, D. Parkinson's disease: a case-control study of occupational and environmental risk factors. *Am. J. Ind.*

- Med.* **17**, 349–355 (1990).
405. Kamel, F. *et al.* Pesticide exposure and self-reported Parkinson's disease in the agricultural health study. *Am. J. Epidemiol.* **165**, 364–374 (2007).
 406. Manning-Bog, A. B. *et al.* The herbicide paraquat causes up-regulation and aggregation of alpha-synuclein in mice: paraquat and alpha-synuclein. *J. Biol. Chem.* **277**, 1641–1644 (2002).
 407. Fernagut, P. O. *et al.* Behavioral and histopathological consequences of paraquat intoxication in mice: effects of alpha-synuclein over-expression. *Synapse* **61**, 991–1001 (2007).
 408. Heikkila, R. E., Nicklas, W. J., Vyas, I. & Duvoisin, R. C. Dopaminergic toxicity of rotenone and the 1-methyl-4-phenylpyridinium ion after their stereotaxic administration to rats: implication for the mechanism of 1-methyl-4-phenyl-1,2,3,6-tetrahydropyridine toxicity. *Neurosci. Lett.* **62**, 389–394 (1985).
 409. Ferrante, R. J., Schulz, J. B., Kowall, N. W. & Beal, M. F. Systemic administration of rotenone produces selective damage in the striatum and globus pallidus, but not in the substantia nigra. *Brain Res.* **753**, 157–162 (1997).
 410. Fleming, S. M. *et al.* Behavioral and immunohistochemical effects of chronic intravenous and subcutaneous infusions of varying doses of rotenone. *Exp. Neurol.* **187**, 418–429 (2004).
 411. Lapointe, N. *et al.* Rotenone induces non-specific central nervous system and systemic toxicity. *FASEB J. Off. Publ. Fed. Am. Soc. Exp. Biol.* **18**, 717–719 (2004).
 412. Zhu, C. *et al.* Variable effects of chronic subcutaneous administration of rotenone on striatal histology. *J. Comp. Neurol.* **478**, 418–426 (2004).
 413. Cannon, J. R. *et al.* A highly reproducible rotenone model of Parkinson's disease. *Neurobiol. Dis.* **34**, 279–290 (2009).
 414. P., B. T., C., R. P., C., C. A., Lesley, R. & S., L. L. Pesticides and Parkinson's Disease—Is There a Link? *Environ. Health Perspect.* **114**, 156–164 (2006).
 415. Tanner, C. M. *et al.* Rotenone, paraquat, and Parkinson's disease. *Environ. Health Perspect.* **119**, 866–872 (2011).
 416. Ogawa, N., Hirose, Y., Ohara, S., Ono, T. & Watanabe, Y. A simple quantitative bradykinesia test in MPTP-treated mice. *Res. Commun. Chem. Pathol. Pharmacol.* **50**, 435–441 (1985).
 417. McCormack, A. L. & Di Monte, D. A. Effects of l-dopa and other amino acids against paraquat-induced nigrostriatal degeneration. *J. Neurochem.* **85**, 82–86 (2003).
 418. Maniyath, S. P., Solaiappan, N. & Rathinasamy, M. Neurobehavioural Changes in a Hemiparkinsonian Rat Model Induced by Rotenone. *J. Clin. Diagn. Res.* **11**, AF01–AF05 (2017).
 419. Carlsson, A., Lindqvist, M. & Magnusson, T. 3,4-Dihydroxyphenylalanine and 5-Hydroxytryptophan as Reserpine Antagonists. *Nature* **180**, 1200 (1957).
 420. Carlsson, A. The occurrence, distribution and physiological role of catecholamines in the nervous system. *Pharmacol. Rev.* **11**, 490–493 (1959).
 421. Herrera, A. J., Castaño, A., Venero, J. L., Cano, J. & Machado, A. The single intranigral injection of LPS as a new model for studying the selective effects of inflammatory reactions on dopaminergic system. *Neurobiol. Dis.* **7**, 429–447 (2000).

422. Spector, S., Sjoerdsma, A. & Udenfriend, S. Blockade of endogenous norepinephrine synthesis by alpha-methyl-tyrosine, an inhibitor of tyrosine hydroxylase. *J. Pharmacol. Exp. Ther.* **147**, 86–95 (1965).
423. Nagatsu, T. Isoquinoline neurotoxins in the brain and Parkinson's disease. *Neurosci. Res.* **29**, 99–111 (1997).
424. Nagatsu, T. & Yoshida, M. An endogenous substance of the brain, tetrahydroisoquinoline, produces parkinsonism in primates with decreased dopamine, tyrosine hydroxylase and bipterin in the nigrostriatal regions. *Neurosci. Lett.* **87**, 178–182 (1988).
425. Krasnova, I. N. & Cadet, J. L. Methamphetamine toxicity and messengers of death. *Brain Res. Rev.* **60**, 379–407 (2009).
426. Meredith, G. E., Sonsalla, P. K. & Chesselet, M.-F. Animal models of Parkinson's disease progression. *Acta Neuropathol.* **115**, 385–398 (2008).
427. Norris, E. H. *et al.* Pesticide exposure exacerbates alpha-synucleinopathy in an A53T transgenic mouse model. *Am. J. Pathol.* **170**, 658–666 (2007).
428. Xiong, Y. *et al.* Robust kinase- and age-dependent dopaminergic and norepinephrine neurodegeneration in LRRK2 G2019S transgenic mice. *Proc. Natl. Acad. Sci. U. S. A.* **115**, 1635–1640 (2018).
429. Dhungel, N. *et al.* Parkinson's disease genes VPS35 and EIF4G1 interact genetically and converge on α -synuclein. *Neuron* **85**, 76–87 (2015).
430. Goldberg, M. S. *et al.* Parkin-deficient mice exhibit nigrostriatal deficits but not loss of dopaminergic neurons. *J. Biol. Chem.* **278**, 43628–43635 (2003).
431. Chen, L. *et al.* Age-dependent motor deficits and dopaminergic dysfunction in DJ-1 null mice. *J. Biol. Chem.* **280**, 21418–21426 (2005).
432. Kitada, T. *et al.* Impaired dopamine release and synaptic plasticity in the striatum of PINK1-deficient mice. *Proc. Natl. Acad. Sci. U. S. A.* **104**, 11441–11446 (2007).
433. Ginns, E. I. *et al.* Neuroinflammation and α -synuclein accumulation in response to glucocerebrosidase deficiency are accompanied by synaptic dysfunction. *Mol. Genet. Metab.* **111**, 152–162 (2014).
434. Bento, C. F., Ashkenazi, A., Jimenez-Sanchez, M. & Rubinsztein, D. C. The Parkinson's disease-associated genes ATP13A2 and SYT11 regulate autophagy via a common pathway. *Nat. Commun.* **7**, 11803 (2016).
435. Wang, C. *et al.* Synaptotagmin-11 is a critical mediator of parkin-linked neurotoxicity and Parkinson's disease-like pathology. *Nat. Commun.* **9**, 81 (2018).
436. Oliver, C. *et al.* Pharmacological Rescue of Mitochondrial Deficits in iPSC-Derived Neural Cells from Patients with Familial Parkinson's Disease. *Sci. Transl. Med.* **4**, 141ra90-141ra90 (2012).
437. Laperle, A. H. *et al.* iPSC modeling of young-onset Parkinson's disease reveals a molecular signature of disease and novel therapeutic candidates. *Nat. Med.* **26**, 289–299 (2020).
438. Smits, L. M. *et al.* Modeling Parkinson's disease in midbrain-like organoids. *npj Park. Dis.* **5**, (2019).
439. Uemura, N. *et al.* Inoculation of α -synuclein preformed fibrils into the mouse gastrointestinal tract induces Lewy body-like aggregates in the brainstem via the vagus nerve. *Mol. Neurodegener.* **13**, 21 (2018).

440. Kim, S. *et al.* Transneuronal Propagation of Pathologic α -Synuclein from the Gut to the Brain Models Parkinson's Disease. *Neuron* **103**, 627-641.e7 (2019).
441. Li, J.-Y. *et al.* Lewy bodies in grafted neurons in subjects with Parkinson's disease suggest host-to-graft disease propagation. *Nat. Med.* **14**, 501–503 (2008).
442. Volpicelli-Daley, L. A., Luk, K. C. & Lee, V. M.-Y. Addition of exogenous α -synuclein preformed fibrils to primary neuronal cultures to seed recruitment of endogenous α -synuclein to Lewy body and Lewy neurite-like aggregates. *Nat. Protoc.* **9**, 2135–2146 (2014).
443. Volpicelli-Daley, L. A., Kirik, D., Stoyka, L. E., Standaert, D. G. & Harms, A. S. How can rAAV- α -synuclein and the fibril α -synuclein models advance our understanding of Parkinson's disease? *J. Neurochem.* **139 Suppl**, 131–155 (2016).
444. Luk, K. C. *et al.* Pathological α -synuclein transmission initiates Parkinson-like neurodegeneration in nontransgenic mice. *Science* **338**, 949–953 (2012).
445. Recasens, A. *et al.* Lewy body extracts from Parkinson disease brains trigger α -synuclein pathology and neurodegeneration in mice and monkeys. *Ann. Neurol.* **75**, 351–362 (2014).
446. Grassi, D. *et al.* Identification of a highly neurotoxic α -synuclein species inducing mitochondrial damage and mitophagy in Parkinson's disease. *Proc. Natl. Acad. Sci. U. S. A.* **115**, E2634–E2643 (2018).
447. Zarranz, J. J. *et al.* The new mutation, E46K, of alpha-synuclein causes Parkinson and Lewy body dementia. *Ann. Neurol.* **55**, 164–173 (2004).
448. Fleming, S. M., Fernagut, P.-O. & Chesselet, M.-F. Genetic mouse models of parkinsonism: strengths and limitations. *NeuroRx* **2**, 495–503 (2005).
449. Chesselet, M.-F. In vivo alpha-synuclein overexpression in rodents: a useful model of Parkinson's disease? *Exp. Neurol.* **209**, 22–27 (2008).
450. K., L. M. *et al.* Human α -synuclein-harboring familial Parkinson's disease-linked Ala-53 \rightarrow Thr mutation causes neurodegenerative disease with α -synuclein aggregation in transgenic mice. *Proc. Natl. Acad. Sci.* **99**, 8968–8973 (2002).
451. Chesselet, M.-F., Fleming, S., Mortazavi, F. & Meurers, B. Strengths and limitations of genetic mouse models of Parkinson's disease. *Parkinsonism Relat. Disord.* **14 Suppl 2**, S84–S87 (2008).
452. Konnova, Elena; Swanberg, M. *Parkinson's Disease*. (Codon Publications, 2018).
453. Chesselet, M.-F. *et al.* A progressive mouse model of Parkinson's disease: the Thy1-aSyn ('Line 61') mice. *Neurother. J. Am. Soc. Exp. Neurother.* **9**, 297–314 (2012).
454. Giasson, B. I. *et al.* Neuronal α -Synucleinopathy with Severe Movement Disorder in Mice Expressing A53T Human α -Synuclein. *Neuron* **34**, 521–533 (2002).
455. Wakamatsu, M. *et al.* Selective loss of nigral dopamine neurons induced by overexpression of truncated human alpha-synuclein in mice. *Neurobiol. Aging* **29**, 574–585 (2008).
456. Klivenyi, P. *et al.* Mice lacking alpha-synuclein are resistant to mitochondrial toxins. *Neurobiol. Dis.* **21**, 541–548 (2006).
457. Martin, L. J. *et al.* Parkinson's disease alpha-synuclein transgenic mice develop neuronal mitochondrial degeneration and cell death. *J. Neurosci. Off. J. Soc. Neurosci.* **26**, 41–50 (2006).
458. Ekstrand, M. I. *et al.* Progressive parkinsonism in mice with respiratory-chain-

- deficient dopamine neurons. *Proc. Natl. Acad. Sci. U. S. A.* **104**, 1325–1330 (2007).
459. Van der Perren, A., Van den Haute, C. & Baekelandt, V. Viral vector-based models of Parkinson's disease. *Curr. Top. Behav. Neurosci.* **22**, 271–301 (2015).
 460. Decressac, M., Mattsson, B., Lundblad, M., Weikop, P. & Björklund, A. Progressive neurodegenerative and behavioural changes induced by AAV-mediated overexpression of α -synuclein in midbrain dopamine neurons. *Neurobiol. Dis.* **45**, 939–953 (2012).
 461. Kirik, D. *et al.* Parkinson-Like Neurodegeneration Induced by Targeted Overexpression of α -Synuclein in the Nigrostriatal System. *J. Neurosci.* **22**, 2780 LP – 2791 (2002).
 462. Oliveras-Salva, M. *et al.* rAAV2/7 vector-mediated overexpression of alpha-synuclein in mouse substantia nigra induces protein aggregation and progressive dose-dependent neurodegeneration. *Mol. Neurodegener.* **8**, 44 (2013).
 463. Deniz, K. *et al.* Nigrostriatal α -synucleinopathy induced by viral vector-mediated overexpression of human α -synuclein: A new primate model of Parkinson's disease. *Proc. Natl. Acad. Sci.* **100**, 2884–2889 (2003).
 464. Koprach, J. *et al.* Characterization and reproducibility of a macaque model of Parkinson's disease alpha-synucleinopathy. *Parkinsonism Relat. Disord.* **46**, e3–e4 (2018).
 465. R., A. D. & Esther, S. LRRK2 kinase in Parkinson's disease. *Science (80-.).* **360**, 36–37 (2018).
 466. Blesa, J. & Przedborski, S. Parkinson's disease: animal models and dopaminergic cell vulnerability . *Frontiers in Neuroanatomy* vol. 8 (2014).
 467. Henderson, J. L. *et al.* Discovery and Preclinical Profiling of 3-[4-(Morpholin-4-yl)-7H-pyrrolo[2,3-d]pyrimidin-5-yl]benzotrile (PF-06447475), a Highly Potent, Selective, Brain Penetrant, and in Vivo Active LRRK2 Kinase Inhibitor. *J. Med. Chem.* **58**, 419–432 (2015).
 468. Li, Y. *et al.* Mutant LRRK2R1441G BAC transgenic mice recapitulate cardinal features of Parkinson's disease. *Nat. Neurosci.* **12**, 826–828 (2009).
 469. Dusonchet, J. *et al.* A Rat Model of Progressive Nigral Neurodegeneration Induced by the Parkinson's Disease-Associated G2019S Mutation in LRRK2. *J. Neurosci.* **31**, 907 LP – 912 (2011).
 470. Lee, B. D. *et al.* Inhibitors of leucine-rich repeat kinase-2 protect against models of Parkinson's disease. *Nat. Med.* **16**, 998–1000 (2010).
 471. Palacino, J. J. *et al.* Mitochondrial dysfunction and oxidative damage in parkin-deficient mice. *J. Biol. Chem.* **279**, 18614–18622 (2004).
 472. Goldberg, M. S. *et al.* Nigrostriatal dopaminergic deficits and hypokinesia caused by inactivation of the familial Parkinsonism-linked gene DJ-1. *Neuron* **45**, 489–496 (2005).
 473. Andres-Mateos, E. *et al.* DJ-1 gene deletion reveals that DJ-1 is an atypical peroxiredoxin-like peroxidase. *Proc. Natl. Acad. Sci. U. S. A.* **104**, 14807–14812 (2007).
 474. Haque, M. E. *et al.* Inactivation of Pink1 gene in vivo sensitizes dopamine-producing neurons to 1-methyl-4-phenyl-1,2,3,6-tetrahydropyridine (MPTP) and can be rescued by autosomal recessive Parkinson disease genes, Parkin or

- DJ-1. *J. Biol. Chem.* **287**, 23162–23170 (2012).
475. Kim, R. H. *et al.* Hypersensitivity of DJ-1-deficient mice to 1-methyl-4-phenyl-1,2,3,6-tetrahydropyridine (MPTP) and oxidative stress. *Proc. Natl. Acad. Sci. U. S. A.* **102**, 5215–5220 (2005).
476. Lu, X.-H. *et al.* Bacterial artificial chromosome transgenic mice expressing a truncated mutant parkin exhibit age-dependent hypokinetic motor deficits, dopaminergic neuron degeneration, and accumulation of proteinase K-resistant alpha-synuclein. *J. Neurosci.* **29**, 1962–1976 (2009).
477. Yasuda, T. *et al.* Neuronal specificity of alpha-synuclein toxicity and effect of Parkin co-expression in primates. *Neuroscience* **144**, 743–753 (2007).
478. Berzelius, J. J. *Lehrbuch Chemie.* (1840).
479. LILLIE, R. D. The basophilia of melanins. *J. Histochem. Cytochem. Off. J. Histochem. Soc.* **3**, 453–454 (1955).
480. LILLIE, R. D. Metal reduction reactions of the melanins: histochemical studies. *J. Histochem. Cytochem. Off. J. Histochem. Soc.* **5**, 325–333 (1957).
481. Zhong, J., Frases, S., Wang, H., Casadevall, A. & Stark, R. E. Following fungal melanin biosynthesis with solid-state NMR: Biopolymer molecular structures and possible connections to cell-wall polysaccharides. *Biochemistry* **47**, 4701–4710 (2008).
482. Ito, S. & Wakamatsu, K. Chemistry of mixed melanogenesis - Pivotal roles of dopaquinone. *Photochem. Photobiol.* **84**, 582–592 (2008).
483. Lees, A. J., Selikhova, M., Andrade, L. A. & Duyckaerts, C. The black stuff and Konstantin Nikolaevich Tretiakoff. *Mov. Disord.* **23**, 777–783 (2008).
484. Bogerts, B. A brainstem atlas of catecholaminergic neurons in man, using melanin as a natural marker. *J. Comp. Neurol.* **197**, 63–80 (1981).
485. SAPER, C. B. & PETITO, C. K. CORRESPONDENCE OF MELANIN-PIGMENTED NEURONS IN HUMAN BRAIN WITH A1–A14 CATECHOLAMINE CELL GROUPS. *Brain* **105**, 87–101 (1982).
486. Halliday, G. M. *et al.* Distribution of monoamine-synthesizing neurons in the human medulla oblongata. *J. Comp. Neurol.* **273**, 301–317 (1988).
487. Cowen, D. The melanoneurons of the human cerebellum (nucleus pigmentosus cerebellaris) and homologues in the monkey. *J. Neuropathol. Exp. Neurol.* **45**, 205–221 (1986).
488. Hild, W. *Das Neuron. In Möllendorf, W. v. a. B. (Ed.) Handbuch der Mikroskopischen Anatomie des Menschen. Viertes Band; Nervensystem; Viertes Teil; Das Neuron, Die Nervenzelle, Die Nervenfaser.* W. (Springer-Verlag, Berlin, 1959).
489. Price, J. L. & Amaral, D. G. An autoradiographic study of the projections of the central nucleus of the monkey amygdala. *J. Neurosci.* **1**, 1242–1259 (1981).
490. Petito, C. K. Melanin-Pigmented Neurons in Human Brain With a1-a14. *Cell* **87**–101 (1982).
491. Gaspar, P. *et al.* Tyrosine hydroxylase and methionine-enkephalin in the human mesencephalon: Immunocytochemical localization and relationships. *J. Neurol. Sci.* **58**, 247–267 (1983).
492. Zucca, F. A. *et al.* Neuromelanin organelles are specialized autolysosomes that accumulate undegraded proteins and lipids in aging human brain and are likely involved in Parkinson's disease. *npj Parkinson's Dis.* (2018) doi:10.1038/s41531-

- 018-0050-8.
493. Zecca, L. *et al.* The absolute concentration of nigral neuromelanin, assayed by a new sensitive method, increases throughout the life and is dramatically decreased in Parkinson's disease. *FEBS Lett.* **510**, 216–220 (2002).
 494. Halliday, G. M. *et al.* Evidence for specific phases in the development of human neuromelanin. *J. Neural Transm.* **113**, 721–728 (2006).
 495. FitzGerald, P. M., Jankovic, J. & Percy, A. K. Rett syndrome and associated movement disorders. *Mov. Disord.* **5**, 195–202 (1990).
 496. Jellinger, K., Armstrong, D., Zoghbi, H. Y. & Percy, A. K. Neuropathology of Rett syndrome. *Acta Neuropathol.* **76**, 142–158 (1988).
 497. Dunn, H. G. *et al.* Rett syndrome: investigation of nine patients, including PET scan. *Can. J. Neurol. Sci. Le J. Can. des Sci. Neurol.* **29**, 345–357 (2002).
 498. Barden, H. & Levine, S. Histochemical observations on rodent brain melanin. *Brain Res. Bull.* **10**, 847–851 (1983).
 499. Moses, H. L., Ganote, C. E., Beaver, D. L. & Schuffman, S. S. Light and electron microscopic studies of pigment in human and rhesus monkey substantia nigra and locus coeruleus. *Anat. Rec.* **155**, 167–183 (1966).
 500. Schwyn, R. C., King, J. S. & Fox, C. A. Pigments in the red nucleus and substantia nigra in man and in representative old and new world monkeys. *Bol. Estud. Med. Biol.* **26**, 139–160 (1970).
 501. Marsden, C. D. Pigmentation in the nucleus substantiae nigrae of mammals. *J. Anat.* **95**, 256–261 (1961).
 502. Herrero, M. T. *et al.* Neuromelanin accumulation with age in catecholaminergic neurons from *Macaca fascicularis* brainstem. *Dev. Neurosci.* **15**, 37–48 (1993).
 503. Sacchini, S. *et al.* Locus coeruleus complex of the family Delphinidae. *Sci. Rep.* **8**, 5486 (2018).
 504. Brayda-Bruno, M. & Levi, A. C. Ultrastructure of neuromelanin granules in dog substantia nigra at different ages. *Boll. Soc. Ital. Biol. Sper.* **55**, 1902–1908 (1979).
 505. Cozzi, B., Pellegrini, M. & Droghi, A. Neuromelanin in the substantia nigra of adult horses. *Anat. Anz.* **166**, 53–61 (1988).
 506. Scherer, H. J. Vergleichende Pathologie des Nervensystems der Säugetiere, unter besonderer Berücksichtigung der Primaten. *Georg Thiem Verlag, Leipzig* **44**, 1906–1945 (1994).
 507. Lindquist, N. G., Larsson, B. S. & Lydén-Sokolowski, A. Autoradiography of [14C]paraquat or [14C]diquat in frogs and mice: accumulation in neuromelanin. *Neurosci. Lett.* **93**, 1–6 (1988).
 508. Schroeder, R. L., Double, K. L. & Gerber, J. P. Using *Sepia* melanin as a PD model to describe the binding characteristics of neuromelanin - A critical review. *J. Chem. Neuroanat.* **64–65**, 20–32 (2015).
 509. Guillot, T. S. & Miller, G. W. Protective actions of the vesicular monoamine transporter 2 (VMAT2) in monoaminergic neurons. *Molecular Neurobiology* vol. 39 149–170 (2009).
 510. Cartier, E. A. *et al.* A biochemical and functional protein complex involving dopamine synthesis and transport into synaptic vesicles. *J. Biol. Chem.* **285**, 1957–1966 (2010).
 511. Segura-Aguilar, J. & Paris, I. Mechanisms of Dopamine Oxidation and Parkinson's

- Disease - Handbook of Neurotoxicity. in (ed. Kostrzewa, R. M.) 865–883 (Springer New York, 2014). doi:10.1007/978-1-4614-5836-4_16.
512. Li, L. & Chin, L. The molecular machinery of synaptic vesicle exocytosis. *Cell. Mol. Life Sci.* **60**, 942–960 (2003).
 513. Trifaró, J. M., Vitale, M. L. & Rodríguez Del Castillo, A. Cytoskeleton and molecular mechanisms in neurotransmitter release by neurosecretory cells. *Eur. J. Pharmacol.* **225**, 83–104 (1992).
 514. Jackson, M. B. & Chapman, E. R. Fusion pores and fusion machines in Ca²⁺-triggered exocytosis. *Annu. Rev. Biophys. Biomol. Struct.* **35**, 135–160 (2006).
 515. Colliver, T. L., Pyott, S. J., Achalabun, M. & Ewing, A. G. VMAT-Mediated changes in quantal size and vesicular volume. *J. Neurosci.* **20**, 5276–5282 (2000).
 516. Pothos, E. N. Regulation of dopamine quantal size in midbrain and hippocampal neurons. *Behav. Brain Res.* **130**, 203–207 (2002).
 517. Männistö, P. T. Catechol O-methyltransferase: characterization of the protein, its gene, and the preclinical pharmacology of COMT inhibitors. *Adv. Pharmacol.* **42**, 324–328 (1998).
 518. Chen, N. & Reith, M. E. Structure and function of the dopamine transporter. *Eur. J. Pharmacol.* **405**, 329–339 (2000).
 519. Fon, E. A. *et al.* Vesicular transport regulates monoamine storage and release but is not essential for amphetamine action. *Neuron* **19**, 1271–1283 (1997).
 520. Linert, W. *et al.* Dopamine, 6-hydroxydopamine, iron, and dioxygen--their mutual interactions and possible implication in the development of Parkinson's disease. *Biochim. Biophys. Acta* **1316**, 160–168 (1996).
 521. Westlund, K. N., Denney, R. M., Rose, R. M. & Abell, C. W. Localization of distinct monoamine oxidase A and monoamine oxidase B cell populations in human brainstem. *Neuroscience* **25**, 439–456 (1988).
 522. Saura, J. *et al.* Increased monoamine oxidase B activity in plaque-associated astrocytes of Alzheimer brains revealed by quantitative enzyme radioautography. *Neuroscience* **62**, 15–30 (1994).
 523. Strolin Benedetti, M., Dostert, P. & Tipton, K. F. Developmental aspects of the monoamine-degrading enzyme monoamine oxidase. *Dev. Pharmacol. Ther.* **18**, 191–200 (1992).
 524. Tzvetkov, N. T. *et al.* Crystal structures, binding interactions, and ADME evaluation of brain penetrant N-substituted indazole-5-carboxamides as subnanomolar, selective monoamine oxidase B and dual MAO-A/B inhibitors. *Eur. J. Med. Chem.* **127**, 470–492 (2017).
 525. Mallajosyula, J. K., Chinta, S. J., Rajagopalan, S., Nicholls, D. G. & Andersen, J. K. Metabolic control analysis in a cellular model of elevated MAO-B: relevance to Parkinson's disease. *Neurotox. Res.* **16**, 186–193 (2009).
 526. Xu, C. L. & Sim, M. K. Reduction of dihydroxyphenylacetic acid by a novel enzyme in the rat brain. *Biochem. Pharmacol.* **50**, 1333–1337 (1995).
 527. Weinreb, O., Amit, T., Riederer, P., Youdim, M. B. H. & Mandel, S. A. Neuroprotective profile of the multitarget drug rasagiline in Parkinson's disease. *Int. Rev. Neurobiol.* **100**, 127–149 (2011).
 528. Goodman, J. E., Jensen, L. T., He, P. & Yager, J. D. Characterization of human soluble high and low activity catechol-O-methyltransferase catalyzed catechol estrogen methylation. *Pharmacogenetics* **12**, 517–528 (2002).

529. Bai, H.-W., Shim, J.-Y., Yu, J. & Zhu, B. T. Biochemical and molecular modeling studies of the O-methylation of various endogenous and exogenous catechol substrates catalyzed by recombinant human soluble and membrane-bound catechol-O-methyltransferases. *Chem. Res. Toxicol.* **20**, 1409–1425 (2007).
530. Ball, P., Knuppen, R., Haupt, M. & Breuer, H. Interactions between estrogens and catechol amines. 3. Studies on the methylation of catechol estrogens, catechol amines and other catechols by the catechol-O-methyltransferases of human liver. *J. Clin. Endocrinol. Metab.* **34**, 736–746 (1972).
531. Myöhänen, T. T., Schendzielorz, N. & Männistö, P. T. Distribution of catechol-O-methyltransferase (COMT) proteins and enzymatic activities in wild-type and soluble COMT deficient mice. *J. Neurochem.* **113**, 1632–1643 (2010).
532. Männistö, P. T. *et al.* Characteristics of catechol O-methyl-transferase (COMT) and properties of selective COMT inhibitors. *Prog. drug Res. Fortschritte der Arzneimittelforschung. Prog. des Rech. Pharm.* **39**, 291–350 (1992).
533. Roth, J. A. Membrane-bound catechol-O-methyltransferase: a reevaluation of its role in the O-methylation of the catecholamine neurotransmitters. *Rev. Physiol. Biochem. Pharmacol.* **120**, 1–29 (1992).
534. Guldberg, H. C. & Marsden, C. A. Catechol-O-methyl transferase: pharmacological aspects and physiological role. *Pharmacol. Rev.* **27**, 135–206 (1975).
535. Marin, C. & Obeso, J. A. Catechol-O-methyltransferase inhibitors in preclinical models as adjuncts of L-dopa treatment. *Int. Rev. Neurobiol.* **95**, 191–205 (2010).
536. Zürcher, G., Colzi, A. & Da Prada, M. Ro 40-7592: inhibition of COMT in rat brain and extracerebral tissues. *J. Neural Transm. Suppl.* **32**, 375–380 (1990).
537. Huotari, M. *et al.* Effect of dopamine uptake inhibition on brain catecholamine levels and locomotion in catechol-O-methyltransferase-disrupted mice. *J. Pharmacol. Exp. Ther.* **303**, 1309–1316 (2002).
538. Muñoz, P., Huenchuguala, S., Paris, I. & Segura-Aguilar, J. Dopamine oxidation and autophagy. *Parkinsons. Dis.* **2012**, 920953 (2012).
539. Paris, I. *et al.* Copper neurotoxicity is dependent on dopamine-mediated copper uptake and one-electron reduction of aminochrome in a rat substantia nigra neuronal cell line. *J. Neurochem.* **77**, 519–529 (2001).
540. Paris, I. *et al.* Monoamine transporter inhibitors and norepinephrine reduce dopamine-dependent iron toxicity in cells derived from the substantia nigra. *J. Neurochem.* **92**, 1021–1032 (2005).
541. Segura-Aguilar, J. & Lind, C. On the mechanism of the Mn³(+)-induced neurotoxicity of dopamine: prevention of quinone-derived oxygen toxicity by DT diaphorase and superoxide dismutase. *Chem. Biol. Interact.* **72**, 309–324 (1989).
542. Hastings, T. G. Enzymatic oxidation of dopamine: the role of prostaglandin H synthase. *J. Neurochem.* **64**, 919–924 (1995).
543. Thompson, C. M., Capdevila, J. H. & Strobel, H. W. Recombinant Cytochrome P450 2D18 Metabolism of Dopamine and Arachidonic Acid. *J. Pharmacol. Exp. Ther.* **294**, 1120–1130 (2000).
544. Galzigna, L., De Iulii, A. & Zanatta, L. Enzymatic dopamine peroxidation in substantia nigra of human brain. *Clin. Chim. Acta.* **300**, 131–138 (2000).
545. Foppoli, C., Coccia, R., Cini, C. & Rosei, M. A. Catecholamines oxidation by

- xanthine oxidase. *Biochim. Biophys. Acta* **1334**, 200–206 (1997).
546. Jimenez, M. *et al.* Chemical intermediates in dopamine oxidation by tyrosinase, and kinetic studies of the process. *Arch. Biochem. Biophys.* **235**, 438–448 (1984).
 547. Carballo-Carbajal, I. *et al.* Brain tyrosinase overexpression implicates age-dependent neuromelanin production in Parkinson's disease pathogenesis. *Nat. Commun.* **10**, (2019).
 548. Segura-Aguilar, J. On the Role of Aminochrome in Mitochondrial Dysfunction and Endoplasmic Reticulum Stress in Parkinson's Disease. *Front. Neurosci.* **13**, 1–6 (2019).
 549. Paris, I. *et al.* Aminochrome induces disruption of actin, alpha-, and beta-tubulin cytoskeleton networks in substantia-nigra-derived cell line. *Neurotox. Res.* **18**, 82–92 (2010).
 550. Napolitano, A., Manini, P. & d'Ischia, M. Oxidation chemistry of catecholamines and neuronal degeneration: an update. *Curr. Med. Chem.* **18**, 1832–1845 (2011).
 551. Baez, S., Linderson, Y. & Segura-Aguilar, J. Superoxide dismutase and catalase enhance autoxidation during one-electron reduction of aminochrome by NADPH-cytochrome P-450 reductase. *Biochem. Mol. Med.* **54**, 12–18 (1995).
 552. Arriagada, C. *et al.* On the neurotoxicity mechanism of leucoaminochrome o-semiquinone radical derived from dopamine oxidation: mitochondria damage, necrosis, and hydroxyl radical formation. *Neurobiol. Dis.* **16**, 468–477 (2004).
 553. Fuentes, P., Paris, I., Nassif, M., Caviedes, P. & Segura-Aguilar, J. Inhibition of VMAT-2 and DT-Diaphorase Induce Cell Death in a Substantia Nigra-Derived Cell Line An Experimental Cell Model for Dopamine Toxicity Studies. *Chem. Res. Toxicol.* **20**, 776–783 (2007).
 554. Paris, I. *et al.* Autophagy Protects Against Aminochrome-Induced Cell Death in Substantia Nigra-Derived Cell Line. *Toxicol. Sci.* **121**, 376–388 (2011).
 555. Lozano, J., Muñoz, P., Nore, B. F., Ledoux, S. P. & Segura-Aguilar, J. Stable expression of short interfering RNA for DT-diaphorase induces neurotoxicity. *Chem. Res. Toxicol.* **23** 9, 1492–1496 (2010).
 556. Muñoz, P., Paris, I., Sanders, L. H., Greenamyre, J. T. & Segura-Aguilar, J. Overexpression of VMAT-2 and DT-diaphorase protects substantia nigra-derived cells against aminochrome neurotoxicity. *Biochim. Biophys. Acta* **1822**, 1125–1136 (2012).
 557. Herrera-Soto, A. *et al.* On the Role of DT-Diaphorase Inhibition in Aminochrome-Induced Neurotoxicity In Vivo. *Neurotox. Res.* **32**, 134–140 (2017).
 558. Meléndez, C., Muñoz, P. & Segura-Aguilar, J. DT-Diaphorase Prevents Aminochrome-Induced Lysosome Dysfunction in SH-SY5Y Cells. *Neurotox. Res.* **35**, 255–259 (2019).
 559. Segura-Aguilar, J. & Huenchuguala, S. Aminochrome Induces Irreversible Mitochondrial Dysfunction by Inducing Autophagy Dysfunction in Parkinson's Disease. *Frontiers in Neuroscience* vol. 12 (2018).
 560. Huenchuguala, S. *et al.* Glutathione transferase mu 2 protects glioblastoma cells against aminochrome toxicity by preventing autophagy and lysosome dysfunction. *Autophagy* **10**, 618–630 (2014).
 561. Huenchuguala, S., Sjödin, B., Mannervik, B. & Segura-Aguilar, J. Novel Alpha-Synuclein Oligomers Formed with the Aminochrome-Glutathione Conjugate Are Not Neurotoxic. *Neurotox. Res.* **35**, 432–440 (2019).

562. Baez, S., Segura-Aguilar, J., Widersten, M., Johansson, A. S. & Mannervik, B. Glutathione transferases catalyse the detoxication of oxidized metabolites (o-quinones) of catecholamines and may serve as an antioxidant system preventing degenerative cellular processes. *Biochem. J.* **324** (Pt 1, 25–28 (1997).
563. Segura-Aguilar, J., Baez, S., Widersten, M., Welch, C. J. & Mannervik, B. Human class Mu glutathione transferases, in particular isoenzyme M2-2, catalyze detoxication of the dopamine metabolite aminochrome. *J. Biol. Chem.* **272**, 5727–5731 (1997).
564. Shen, X. M., Xia, B., Wrona, M. Z. & Dryhurst, G. Synthesis, redox properties, in vivo formation, and neurobehavioral effects of N-acetylcysteinyl conjugates of dopamine: possible metabolites of relevance to Parkinson's disease. *Chem. Res. Toxicol.* **9** 7, 1117–1126 (1996).
565. Ito, S. & Protá, G. A facile one-step synthesis of cysteinyl-dopas using mushroom tyrosinase. *Experientia* **33**, 1118–1119 (1977).
566. Agrup, G., Hansson, C., Rorsman, H. & Rosengren, E. The effect of cysteine on oxidation of tyrosine dopa, and cysteinyl-dopas. *Arch. Dermatol. Res.* **272**, 103–115 (1981).
567. MD, A. C. & Fornstedt, B. Catechol metabolites in the cerebrospinal fluid as possible markers in the early diagnosis of Parkinson's disease. *Neurology* **41**, 50–51 (1991).
568. Cheng, F. C., Kuo, J. S., Chia, L. G. & Dryhurst, G. Elevated 5-S-cysteinyl-dopamine/homovanillic acid ratio and reduced homovanillic acid in cerebrospinal fluid: possible markers for and potential insights into the pathoetiology of Parkinson's disease. *J. Neural Transm.* **103**, 433–446 (1996).
569. Rosengren, E., Linder-Eliasson, E. & Carlsson, A. Detection of 5-S-cysteinyl-dopamine in human brain. *J. Neural Transm.* **63**, 247–253 (1985).
570. Carstam, R., Brinck, C., Hindemith-Augustsson, A., Rorsman, H. & Rosengren, E. The neuromelanin of the human substantia nigra. *BBA - Mol. Basis Dis.* **1097**, 152–160 (1991).
571. Dagnino-Subiabre, A. *et al.* Glutathione transferase M2-2 catalyzes conjugation of dopamine and dopa o-quinones. *Biochem. Biophys. Res. Commun.* **274**, 32–36 (2000).
572. Mosca, L. *et al.* 5-S-Cysteinyl-dopamine effect on the human dopaminergic neuroblastoma cell line SH-SY5Y. *Neurochem. Int.* **49**, 262–269 (2006).
573. Ito, S., Kato, T., Maruta, K., Fujita, K. & Kurahashi, T. Determination of DOPA, dopamine, and 5-S-cysteinyl-DOPA in plasma, urine, and tissue samples by high-performance liquid chromatography with electrochemical detection. *J. Chromatogr.* **311**, 154–159 (1984).
574. Stewart, R. M., Miller, S. & Gunder, M. Urinary 5-S-cysteinyl-dopa in Parkinsonism after DOPA and carbidopa. *Acta Derm. Venereol.* **63**, 97–101 (1983).
575. Protá, G. Structure and biogenesis of pheomelanins. *Pigment. Its Genes. Biol. Control. New York Applet. Century Crofts.* 615–630 (1972).
576. Protá, G. Recent advances in the chemistry of melanogenesis in mammals. *J. Invest. Dermatol.* **75**, 122–127 (1980).
577. Zucca, F. A. *et al.* Interactions of iron, dopamine and neuromelanin pathways in brain aging and Parkinson's disease. *Prog. Neurobiol.* **155**, 96–119 (2017).

578. Eiden, L. E., Schäfer, M. K.-H., Weihe, E. & Schütz, B. The vesicular amine transporter family (SLC18): amine/proton antiporters required for vesicular accumulation and regulated exocytotic secretion of monoamines and acetylcholine. *Pflügers Arch.* **447**, 636–640 (2004).
579. Zucker, M., Weizman, A. & Rehavi, M. Characterization of high-affinity [3H]TBZOH binding to the human platelet vesicular monoamine transporter. *Life Sci.* **69**, 2311–2317 (2001).
580. Anlauf, M. *et al.* Expression of the two isoforms of the vesicular monoamine transporter (VMAT1 and VMAT2) in the endocrine pancreas and pancreatic endocrine tumors. *J. Histochem. Cytochem. Off. J. Histochem. Soc.* **51**, 1027–1040 (2003).
581. Lawal, H. O. & Krantz, D. E. SLC18: Vesicular neurotransmitter transporters for monoamines and acetylcholine. *Molecular Aspects of Medicine* vol. 34 360–372 (2013).
582. Erickson, J. D. & Eiden, L. E. Functional Identification and Molecular Cloning of a Human Brain Vesicle Monoamine Transporter. *J. Neurochem.* **61**, 2314–2317 (1993).
583. Liu, Y. & Edwards, R. H. The role of vesicular transport proteins in synaptic transmission and neural degeneration. *Annual Review of Neuroscience* vol. 20 125–156 (1997).
584. Miller, G. W. *et al.* Immunochemical analysis of vesicular monoamine transporter (VMAT2) protein in Parkinson's disease. *Exp. Neurol.* **156**, 138–148 (1999).
585. Sala, G. *et al.* Vesicular monoamine transporter 2 mRNA levels are reduced in platelets from patients with Parkinson's disease. *J. Neural Transm.* **117**, 1093–1098 (2010).
586. Piffl, C. *et al.* Is Parkinson's disease a vesicular dopamine storage disorder? Evidence from a study in isolated synaptic vesicles of human and nonhuman primate striatum. *J. Neurosci. Off. J. Soc. Neurosci.* **34**, 8210–8218 (2014).
587. Monzani, E. *et al.* Dopamine, Oxidative Stress and Protein–Quinone Modifications in Parkinson's and Other Neurodegenerative Diseases. *Angew. Chemie - Int. Ed.* **58**, 6512–6527 (2019).
588. Pillaiyar, T., Manickam, M. & Jung, S.-H. Downregulation of melanogenesis: drug discovery and therapeutic options. *Drug Discov. Today* **22**, 282–298 (2017).
589. Chen, L. *et al.* Unregulated Cytosolic Dopamine Causes Neurodegeneration Associated with Oxidative Stress in Mice. *J. Neurosci.* **28**, 425–433 (2008).
590. Liang, C. L., Nelson, O., Yazdani, U., Pasbakhsh, P. & German, D. C. Inverse Relationship between the Contents of Neuromelanin Pigment and the Vesicular Monoamine Transporter-2: Human Midbrain Dopamine Neurons. *J. Comp. Neurol.* **473**, 97–106 (2004).
591. Glatt, C. E., Wahner, A. D., White, D. J., Ruiz-Linares, A. & Ritz, B. Gain-of-function haplotypes in the vesicular monoamine transporter promoter are protective for Parkinson disease in women. *Hum. Mol. Genet.* **15**, 299–305 (2006).
592. Bucher, M. L. *et al.* Acquired dysregulation of dopamine homeostasis reproduces features of Parkinson's disease. *NPJ Park. Dis* **6(1):34.**, (2020).
593. Goldstein, D. S. *et al.* Determinants of buildup of the toxic dopamine metabolite

- DOPAL in Parkinson's disease. *J. Neurochem.* **126**, 591–603 (2013).
594. Wang, Y. M. *et al.* Knockout of the vesicular monoamine transporter 2 gene results in neonatal death and supersensitivity to cocaine and amphetamine. *Neuron* **19**, 1285–1296 (1997).
595. Takahashi, N. *et al.* VMAT2 knockout mice: Heterozygotes display reduced amphetamine-conditioned reward, enhanced amphetamine locomotion, and enhanced MPTP toxicity. *Proc. Natl. Acad. Sci. U. S. A.* **94**, 9938–9943 (1997).
596. Mooslehner, K. A. *et al.* Mice with very low expression of the vesicular monoamine transporter 2 gene survive into adulthood: potential mouse model for parkinsonism. *Mol. Cell. Biol.* **21**, 5321–5331 (2001).
597. Caudle, W. M. *et al.* Reduced vesicular storage of dopamine causes progressive nigrostriatal neurodegeneration. *J. Neurosci.* **27**, 8138–8148 (2007).
598. Taylor, T. N. *et al.* Nonmotor symptoms of Parkinson's disease revealed in an animal model with reduced monoamine storage capacity. *J. Neurosci.* **29**, 8103–8113 (2009).
599. Chang, H.-Y. *et al.* Overexpression of the *Drosophila* vesicular monoamine transporter increases motor activity and courtship but decreases the behavioral response to cocaine. *Mol. Psychiatry* **11**, 99–113 (2006).
600. Lawal, H. O. *et al.* The *Drosophila* vesicular monoamine transporter reduces pesticide-induced loss of dopaminergic neurons. *Neurobiol. Dis.* **40**, 102–112 (2010).
601. Lohr, K. M. *et al.* Increased vesicular monoamine transporter enhances dopamine release and opposes Parkinson disease-related neurodegeneration in vivo. *Proc. Natl. Acad. Sci. U. S. A.* **111**, 9977–9982 (2014).
602. Lohr, K. M. *et al.* Vesicular Monoamine Transporter 2 (VMAT2) Level Regulates MPTP Vulnerability and Clearance of Excess Dopamine in Mouse Striatal Terminals. *Toxicol. Sci.* **153**, 79–88 (2016).
603. Schapira, A. H. *et al.* Mitochondrial complex I deficiency in Parkinson's disease. *Lancet (London, England)* vol. 1 1269 (1989).
604. Holper, L., Ben-Shachar, D. & Mann, J. J. Multivariate meta-analyses of mitochondrial complex I and IV in major depressive disorder, bipolar disorder, schizophrenia, Alzheimer disease, and Parkinson disease. *Neuropsychopharmacol. Off. Publ. Am. Coll. Neuropsychopharmacol.* **44**, 837–849 (2019).
605. Lopez-Fabuel, I. *et al.* Mitochondrial respiratory chain disorganization in Parkinson's disease-relevant PINK1 and DJ1 mutants. *Neurochem. Int.* **109**, 101–105 (2017).
606. Devi, L., Raghavendran, V., Prabhu, B. M., Avadhani, N. G. & Anandatheerthavarada, H. K. Mitochondrial import and accumulation of alpha-synuclein impair complex I in human dopaminergic neuronal cultures and Parkinson disease brain. *J. Biol. Chem.* **283**, 9089–9100 (2008).
607. Chinta, S. J., Mallajosyula, J. K., Rane, A. & Andersen, J. K. Mitochondrial alpha-synuclein accumulation impairs complex I function in dopaminergic neurons and results in increased mitophagy in vivo. *Neurosci. Lett.* **486**, 235–239 (2010).
608. Martínez, J. H. *et al.* Alpha-synuclein mitochondrial interaction leads to irreversible translocation and complex I impairment. *Arch. Biochem. Biophys.* **651**, 1–12 (2018).

609. Nakamura, K. *et al.* Direct membrane association drives mitochondrial fission by the Parkinson disease-associated protein alpha-synuclein. *J. Biol. Chem.* **286**, 20710–20726 (2011).
610. Auluck, P. K., Chan, H. Y. E., Trojanowski, J. Q., Lee, V. M. Y. & Bonini, N. M. Chaperone suppression of alpha-synuclein toxicity in a *Drosophila* model for Parkinson's disease. *Science* **295**, 865–868 (2002).
611. Selkoe DJ. Folding proteins in fatal ways. *Nature* **426**, 900–904 (2003).
612. Taylor, J. P., Hardy, J. & Fischbeck, K. H. Toxic proteins in neurodegenerative disease. *Science* **296**, 1991–1995 (2002).
613. Lindholm, D., Wootz, H. & Korhonen, L. ER stress and neurodegenerative diseases. *Cell Death Differ.* **13**, 385–392 (2006).
614. Rao, R. V & Bredesen, D. E. Misfolded proteins, endoplasmic reticulum stress and neurodegeneration. *Curr. Opin. Cell Biol.* **16**, 653–662 (2004).
615. Hoozemans, J. J. M. *et al.* Activation of the unfolded protein response in Parkinson's disease. *Biochem. Biophys. Res. Commun.* **354**, 707–711 (2007).
616. Heman-Ackah, S. M. *et al.* Alpha-synuclein induces the unfolded protein response in Parkinson's disease SNCA triplication iPSC-derived neurons. *Hum. Mol. Genet.* **26**, 4441–4450 (2017).
617. Liu, M. *et al.* α -synuclein induces apoptosis of astrocytes by causing dysfunction of the endoplasmic reticulum-Golgi compartment. *Mol. Med. Rep.* **18**, 322–332 (2018).
618. García-Sanz, P. *et al.* N370S-GBA1 mutation causes lysosomal cholesterol accumulation in Parkinson's disease. *Mov. Disord.* **32**, 1409–1422 (2017).
619. Williams, A. MPTP toxicity: clinical features. *J. Neural Transm. Suppl.* **20**, 5–9 (1986).
620. Brundin, P. & Melki, R. Prying into the Prion Hypothesis for Parkinson's Disease. *J. Neurosci.* **37**, 9808–9818 (2017).
621. Asanuma, M., Miyazaki, I., Diaz-Corrales, F. J. & Ogawa, N. Quinone formation as dopaminergic neuron-specific oxidative stress in the pathogenesis of sporadic Parkinson's disease and neurotoxin-induced parkinsonism. *Acta Med. Okayama* **58**, 221–233 (2004).
622. Hauser, D. N., Dukes, A. A., Mortimer, A. D. & Hastings, T. G. Dopamine quinone modifies and decreases the abundance of the mitochondrial selenoprotein glutathione peroxidase 4. *Free Radic. Biol. Med.* **65**, 419–427 (2013).
623. Van Laar, V. S., Mishizen, A. J., Cascio, M. & Hastings, T. G. Proteomic identification of dopamine-conjugated proteins from isolated rat brain mitochondria and SH-SY5Y cells. *Neurobiol. Dis.* **34**, 487–500 (2009).
624. LaVoie, M. J., Ostaszewski, B. L., Weihofen, A., Schlossmacher, M. G. & Selkoe, D. J. Dopamine covalently modifies and functionally inactivates parkin. *Nat. Med.* **11**, 1214–1221 (2005).
625. Berman, S. B. & Hastings, T. G. Dopamine oxidation alters mitochondrial respiration and induces permeability transition in brain mitochondria: implications for Parkinson's disease. *J. Neurochem.* **73**, 1127–1137 (1999).
626. Xu, Y., Stokes, A. H., Roskoski, R. J. & Vrana, K. E. Dopamine, in the presence of tyrosinase, covalently modifies and inactivates tyrosine hydroxylase. *J. Neurosci. Res.* **54**, 691–697 (1998).
627. Whitehead, R. E., Ferrer, J. V, Javitch, J. A. & Justice, J. B. Reaction of oxidized

- dopamine with endogenous cysteine residues in the human dopamine transporter. *J. Neurochem.* **76**, 1242–1251 (2001).
628. Zahid, M. *et al.* Formation of dopamine quinone-DNA adducts and their potential role in the etiology of Parkinson's disease. *IUBMB Life* **63**, 1087–1093 (2011).
 629. Dibenedetto, D., Rossetti, G., Caliandro, R. & Carloni, P. A Molecular Dynamics Simulation-Based Interpretation of Nuclear Magnetic Resonance Multidimensional Heteronuclear Spectra of α -Synuclein-Dopamine Adducts. *Biochemistry* **52**, 6672–6683 (2013).
 630. Norris, E. H. *et al.* Reversible Inhibition of α -Synuclein Fibrillization by Dopaminochrome-mediated Conformational Alterations*. *J. Biol. Chem.* **280**, 21212–21219 (2005).
 631. Zafar, K. S., Siegel, D. & Ross, D. A Potential Role for Cyclized Quinones Derived from Dopamine, DOPA, and 3,4-Dihydroxyphenylacetic Acid in Proteasomal Inhibition. *Mol. Pharmacol.* **70**, 1079 LP – 1086 (2006).
 632. Zhou, Z. D. & Lim, T. M. Dopamine (DA) induced irreversible proteasome inhibition via DA derived quinones. *Free Radic. Res.* **43**, 417–430 (2009).
 633. Aguirre, P. *et al.* The dopamine metabolite aminochrome inhibits mitochondrial complex I and modifies the expression of iron transporters DMT1 and FPN1. *BioMetals* **25**, 795–803 (2012).
 634. Huenchuguala, S., Muñoz, P. & Segura-Aguilar, J. The Importance of Mitophagy in Maintaining Mitochondrial Function in U373MG Cells. Bafilomycin A1 Restores Aminochrome-Induced Mitochondrial Damage. *ACS Chem. Neurosci.* **8**, 2247–2253 (2017).
 635. Briceño, A. *et al.* Aminochrome Toxicity is Mediated by Inhibition of Microtubules Polymerization Through the Formation of Adducts with Tubulin. *Neurotox. Res.* **29**, 381–393 (2016).
 636. Xiong, R., Siegel, D. & Ross, D. Quinone-induced protein handling changes: Implications for major protein handling systems in quinone-mediated toxicity. *Toxicol. Appl. Pharmacol.* **280**, 285–295 (2014).
 637. Santos, C. C. *et al.* Aminochrome induces microglia and astrocyte activation. *Toxicol. In Vitro* **42**, 54–60 (2017).
 638. de Araújo, F. M. *et al.* Aminochrome decreases NGF, GDNF and induces neuroinflammation in organotypic midbrain slice cultures. *Neurotoxicology* **66**, 98–106 (2018).
 639. Herrera, A. *et al.* Aminochrome induces dopaminergic neuronal dysfunction: a new animal model for Parkinson's disease. *Cell. Mol. Life Sci.* **73**, 3583–3597 (2016).
 640. Bisaglia, M., Soriano, M. E., Arduini, I., Mammi, S. & Bubacco, L. Molecular characterization of dopamine-derived quinones reactivity toward NADH and glutathione: implications for mitochondrial dysfunction in Parkinson disease. *Biochim. Biophys. Acta* **1802**, 699–706 (2010).
 641. Anderson, D. G., Mariappan, S. V. S., Buettner, G. R. & Doorn, J. A. Oxidation of 3,4-Dihydroxyphenylacetaldehyde, a Toxic Dopaminergic Metabolite, to a Semiquinone Radical and an ortho-Quinone*. *J. Biol. Chem.* **286**, 26978–26986 (2011).
 642. Goldstein, D. S., Kopin, I. J. & Sharabi, Y. Catecholamine autotoxicity.

- Implications for pharmacology and therapeutics of Parkinson disease and related disorders. *Pharmacol. Ther.* **144**, 268–282 (2014).
643. Norris, E. H. *et al.* Reversible inhibition of alpha-synuclein fibrillization by dopaminochrome-mediated conformational alterations. *J. Biol. Chem.* **280**, 21212–21219 (2005).
 644. Linsenbardt, A. J., Wilken, G. H., Westfall, T. C. & Macarthur, H. Cytotoxicity of dopaminochrome in the mesencephalic cell line, MN9D, is dependent upon oxidative stress. *Neurotoxicology* **30**, 1030–1035 (2009).
 645. Ochs, S. D., Westfall, T. C. & Macarthur, H. The separation and quantification of aminochromes using high-pressure liquid chromatography with electrochemical detection. *J. Neurosci. Methods* **142**, 201–208 (2005).
 646. Hashimoto, T. *et al.* An endogenous metabolite of dopamine, 3,4-dihydroxyphenylethanol, acts as a unique cytoprotective agent against oxidative stress-induced injury. *Free Radic. Biol. Med.* **36**, 555–564 (2004).
 647. Hearing, V. J. The melanosome: the perfect model for cellular responses to the environment. *Pigment cell research* vol. 13 Suppl 8 23–34 (2000).
 648. Raper, H. S. The Tyrosinase-tyrosine Reaction: Production from Tyrosine of 5: 6-Dihydroxyindole and 5: 6-Dihydroxyindole-2-carboxylic Acid-the Precursors of Melanin. *Biochem. J.* **21**, 89–96 (1927).
 649. Prota, G., Crescenzi, S., Misuraca, G., Nicolaus, R. A. New intermediates in phaemelanogenesis in vitro. *Experientia* 1058–1509 (1970).
 650. Cooksey, C. J. *et al.* Evidence of the indirect formation of the catecholic intermediate substrate responsible for the autoactivation kinetics of tyrosinase. *J. Biol. Chem.* **272**, 26226–26235 (1997).
 651. Ozeki, H., Ito, S., Wakamatsu, K. & Ishiguro, I. Chemical characterization of pheomelanogenesis starting from dihydroxyphenylalanine or tyrosine and cysteine. Effects of tyrosinase and cysteine concentrations and reaction time. *Biochim. Biophys. Acta* **1336**, 539–548 (1997).
 652. Xu, Y. *et al.* Tyrosinase mRNA is expressed in human substantia nigra. *Brain Res. Mol. Brain Res.* **45**, 159–162 (1997).
 653. Greggio, E. *et al.* Tyrosinase exacerbates dopamine toxicity but is not genetically associated with Parkinson's disease. *J. Neurochem.* **93**, 246–256 (2005).
 654. Miranda, M., Botti, D., Bonfigli, A., Ventura, T. & Arcadi, A. Tyrosinase-like activity in normal human substantia nigra. *Gen. Pharmacol.* **15**, 541–544 (1984).
 655. Ikemoto, K. *et al.* Does tyrosinase exist in neuromelanin-pigmented neurons in the human substantia nigra? *Neurosci. Lett.* **253**, 198–200 (1998).
 656. Tribl, F., Arzberger, T., Riederer, P. & Gerlach, M. Tyrosinase is not detected in human catecholaminergic neurons by immunohistochemistry and Western blot analysis. *J. Neural Transm. Suppl.* 51–55 (2007) doi:10.1007/978-3-211-73574-9_8.
 657. Nicolaus, R.A., Piatelli, M. Structure of melanins and melanogenesis. *Am. J. Pol. Sci.* **58**, **1133**, (1962).
 658. Piattelli, M., Fattorusso, E., Magno, S. & Nicolaus, R. A. The structure of melanins and melanogenesis-II. *Tetrahedron* **18**, 941–949 (1962).
 659. Mason, H. S. The structure of melanin. In: Montagna, W., Hu, F. (Eds.), *The pigmentary System: Advances in Biology of Skin. Pergamon Press. Oxford* 293–312 (1967).

660. Swan, G. A. Structure, chemistry, and biosynthesis of the melanins. *Fortschritte der Chemie Org. Naturstoffe = Prog. Chem. Org. Nat. Prod. Prog. dans la Chim. des Subst. Org. Nat.* **31**, 521–582 (1974).
661. Ito, S. Reexamination of the structure of eumelanin. *Biochim. Biophys. Acta* **883**, 155–161 (1986).
662. Novellino, L., Napolitano, A. & Protà, G. Isolation and characterization of mammalian eumelanins from hair and irides. *Biochim. Biophys. Acta* **1475**, 295–306 (2000).
663. Odh, G. *et al.* Neuromelanin of the Human Substantia Nigra: A Mixed-Type Melanin. *J. Neurochem.* **62**, (1994).
664. Bush, W. D. *et al.* The surface oxidation potential of human neuromelanin reveals a spherical architecture with a pheomelanin core and a eumelanin surface. *Proc. Natl. Acad. Sci. U. S. A.* **103**, 14785–14789 (2006).
665. Ito, S. Encapsulation of a reactive core in neuromelanin. *Proc. Natl. Acad. Sci. U. S. A.* **103**, 14647–14648 (2006).
666. Wakamatsu, K., Fujikawa, K., Zucca, F. A., Zecca, L. & Ito, S. The structure of neuromelanin as studied by chemical degradative methods. *J. Neurochem.* **86**, 1015–1023 (2003).
667. Aime, S., Fasano, M., Bergamasco, B., Lopiano, L. & Valente, G. Evidence for a glycidic-lipidic matrix in human neuromelanin, potentially responsible for the enhanced iron sequestering ability of substantia nigra. *J. Neurochem.* **62**, 369–371 (1994).
668. Aime, S., Fasano, M., Bergamasco, B., Lopiano, L. & Quattrocchio, G. Nuclear magnetic resonance spectroscopy characterization and iron content determination of human mesencephalic neuromelanin. *Adv. Neurol.* **69**, 263–270 (1996).
669. Aime, S. *et al.* Isolation and ¹³C-NMR characterization of an insoluble proteinaceous fraction from substantia nigra of patients with Parkinson's disease. *Mov. Disord.* **15**, 977–981 (2000).
670. Double, K. L. *et al.* Structural characteristics of human substantia nigra neuromelanin and synthetic dopamine melanins. *J. Neurochem.* **75**, 2583–2589 (2000).
671. Zecca, L. *et al.* Interaction of human substantia nigra neuromelanin with lipids and peptides. *J. Neurochem.* **74**, 1758–1765 (2000).
672. Pezzella, A. *et al.* Identification of Partially Degraded Oligomers of 5,6-Dihydroxyindole-2-carboxylic Acid in Sepia Melanin by Matrix-assisted Laser Desorption/Ionization Mass Spectrometry. *Rapid Commun. Mass Spectrom.* **11**, 368–372 (1997).
673. Cheng, J., Moss, S. C., Eisner, M. & Zschack, P. X-ray characterization of melanins--I. *Pigment Cell Res.* **7**, 255–262 (1994).
674. Zajac, G. W. *et al.* The fundamental unit of synthetic melanin: a verification by tunneling microscopy of X-ray scattering results. *Biochim. Biophys. Acta - Gen. Subj.* **1199**, 271–278 (1994).
675. Crippa, R. *et al.* Structure of human neuromelanin by X-ray diffraction: comparison with synthetics. *Pigment Cell Res* **5**, (1996).
676. Dzierzega-Leczna, A. *et al.* GC/MS analysis of thermally degraded neuromelanin from the human substantia nigra. *J. Am. Soc. Mass Spectrom.* **15**, 920–926

- (2004).
677. Enochs, W. S., Nilges, M. J. & Swartz, H. M. Purified human neuromelanin, synthetic dopamine melanin as a potential model pigment, and the normal human substantia nigra: characterization by electron paramagnetic resonance spectroscopy. *J. Neurochem.* **61**, 68–79 (1993).
 678. Aime, S. *et al.* EPR investigations of the iron domain in neuromelanin. *Biochim. Biophys. Acta - Mol. Basis Dis.* **1361**, 49–58 (1997).
 679. Zecca, L. *et al.* Interaction of neuromelanin and iron in substantia nigra and other areas of human brain. *Neuroscience* **73**, 407–415 (1996).
 680. Tribl, F. *et al.* ‘Subcellular Proteomics’ of Neuromelanin Granules Isolated from the Human Brain*. *Mol. Cell. Proteomics* **4**, 945–957 (2005).
 681. Han, X. Multi-dimensional mass spectrometry-based shotgun lipidomics and the altered lipids at the mild cognitive impairment stage of Alzheimer’s disease. *Biochim. Biophys. Acta* **1801**, 774–783 (2010).
 682. Engelen, M. *et al.* Neuromelanins of Human Brain Have Soluble and Insoluble Components with Dolichols Attached to the Melanic Structure. *PLoS One* **7**, e48490 (2012).
 683. Licker, V. *et al.* Proteomic analysis of human substantia nigra identifies novel candidates involved in Parkinson’s disease pathogenesis. *Proteomics* **14**, 784–794 (2014).
 684. Plum, S. *et al.* Proteomics in neurodegenerative diseases: Methods for obtaining a closer look at the neuronal proteome. *Proteomics. Clin. Appl.* **9**, 848–871 (2015).
 685. Plum, S. *et al.* Proteomic characterization of neuromelanin granules isolated from human substantia nigra by laser-microdissection. *Sci. Rep.* **6**, 37139 (2016).
 686. Sulzer, D. *et al.* Neuromelanin biosynthesis is driven by excess cytosolic catecholamines not accumulated by synaptic vesicles. *Proc. Natl. Acad. Sci.* **97**, 11869–11874 (2000).
 687. Sulzer, D. *et al.* Neuronal pigmented autophagic vacuoles: lipofuscin, neuromelanin, and ceroid as macroautophagic responses during aging and disease. *J. Neurochem.* **106**, 24–36 (2008).
 688. Zecca, L. *et al.* Iron and other metals in neuromelanin, substantia nigra, and putamen of human brain. *J. Neurochem.* **62**, 1097–1101 (1994).
 689. Zecca, L. *et al.* Combined biochemical separation and INAA for the determination of iron other metals in Neuromelanin of human brain Substantia Nigra. *J. Radioanal. Nucl. Chem.* **249**, 449–454 (2001).
 690. Shima, T. *et al.* Binding of iron to neuromelanin of human substantia nigra and synthetic melanin: an electron paramagnetic resonance spectroscopy study. *Free Radic. Biol. Med.* **23**, 110–119 (1997).
 691. Zecca, L. *et al.* New melanic pigments in the human brain that accumulate in aging and block environmental toxic metals. *Proc. Natl. Acad. Sci. U. S. A.* **105**, 17567–17572 (2008).
 692. Bohic, S. *et al.* Intracellular chemical imaging of the developmental phases of human neuromelanin using synchrotron X-ray microspectroscopy. *Anal. Chem.* **80**, 9557–9566 (2008).
 693. Double, K. L. *et al.* Iron-binding characteristics of neuromelanin of the human substantia nigra. *Biochem. Pharmacol.* **66**, 489–494 (2003).

694. Kropf, A. J. *et al.* X-ray absorption fine-structure spectroscopy studies of Fe sites in natural human neuromelanin and synthetic analogues. *Biophys. J.* **75**, 3135–3142 (1998).
695. Sofic, E. *et al.* Increased iron (III) and total iron content in post mortem substantia nigra of parkinsonian brain. *J. Neural Transm.* **74**, 199–205 (1988).
696. Zhang, F. & Dryhurst, G. Effects of L-cysteine on the oxidation chemistry of dopamine: new reaction pathways of potential relevance to idiopathic Parkinson's disease. *J. Med. Chem.* **37**, 1084–1098 (1994).
697. Gerlach, M. *et al.* A post mortem study on neurochemical markers of dopaminergic, GABA-ergic and glutamatergic neurons in basal ganglia-thalamocortical circuits in Parkinson syndrome. *Brain Res.* **741**, 142–152 (1996).
698. Fedorow, H. *et al.* Investigation of the lipid component of neuromelanin. *J. Neural Transm.* **113**, 735–739 (2006).
699. Zucca, F. A. *et al.* Neuromelanin organelles are specialized autolysosomes that accumulate undegraded proteins and lipids in aging human brain and are likely involved in Parkinson's disease. *npj Park. Dis.* **4**, (2018).
700. LaVoie, M. J. & Hastings, T. G. Dopamine quinone formation and protein modification associated with the striatal neurotoxicity of methamphetamine: evidence against a role for extracellular dopamine. *J. Neurosci.* **19**, 1484–1491 (1999).
701. Sulzer, D. & Zecca, L. Intraneuronal dopamine-quinone synthesis: a review. *Neurotox. Res.* **1**, 181–195 (2000).
702. Zecca, L. *et al.* The role of iron and copper molecules in the neuronal vulnerability of locus coeruleus and substantia nigra during aging. *Proc. Natl. Acad. Sci. U. S. A.* **101**, 9843–9848 (2004).
703. Venkateshappa, C. *et al.* Increased oxidative damage and decreased antioxidant function in aging human substantia nigra compared to striatum: implications for Parkinson's disease. *Neurochem. Res.* **37**, 358–369 (2012).
704. Zecca, L. *et al.* *New melanic pigments in the human brain that accumulate in aging and block environmental toxic metals.* www.pnas.org/cgi/content/full/ (2008).
705. Zareba, M., Bober, A., Korytowski, W., Zecca, L. & Sarna, T. The effect of a synthetic neuromelanin on yield of free hydroxyl radicals generated in model systems. *Biochim. Biophys. Acta* **1271**, 343–348 (1995).
706. Zecca, L. *et al.* Neuromelanin can protect against iron-mediated oxidative damage in system modeling iron overload of brain aging and Parkinson's disease. *J. Neurochem.* **106**, 1866–1875 (2008).
707. Korytowski, W., Sarna, T. & Zareba, M. Antioxidant action of neuromelanin: the mechanism of inhibitory effect on lipid peroxidation. *Arch. Biochem. Biophys.* **319**, 142–148 (1995).
708. Lindquist, N. G., Larsson, B. S. & Lydén-Sokolowski, A. Neuromelanin and its possible protective and destructive properties. *Pigment cell Res.* **1**, 133–136 (1987).
709. J., D. R., P., L. Z. & H., S. S. Selectivity of the Parkinsonian Neurotoxin MPTP: Toxic Metabolite MPP+ Binds to Neuromelanin. *Science (80-)*. **231**, 987–989 (1986).
710. Ostergren, A., Annas, A., Skog, K., Lindquist, N. G. & Brittebo, E. B. Long-term

- retention of neurotoxic beta-carbolines in brain neuromelanin. *J. Neural Transm.* **111**, 141–157 (2004).
711. Naoi, M., Maruyama, W. & Dostert, P. Binding of 1,2(N)-dimethyl-6,7-dihydroxy-isoquinolinium ion to melanin: effects of ferrous and ferric ion on the binding. *Neurosci. Lett.* **171**, 9–12 (1994).
 712. Lindquist, N. G. Accumulation in vitro of 35 S-chlorpromazine in the neuromelanin of human substantia nigra and locus coeruleus. *Arch. Int. Pharmacodyn. Ther.* **200**, 190–195 (1972).
 713. Salazar, M., Sokoloski, T. D. & Patil, P. N. Binding of dopaminergic drugs by the neuromelanin of the substantia nigra, synthetic melanins and melanin granules. *Fed. Proc.* **37**, 2403–2407 (1978).
 714. Lydén, A., Larsson, B. & Lindquist, N. G. Studies on the melanin affinity of haloperidol. *Arch. Int. Pharmacodyn. Ther.* **259**, 230–243 (1982).
 715. Karlsson, O. & Lindquist, N. G. Melanin and neuromelanin binding of drugs and chemicals: toxicological implications. *Arch. Toxicol.* **90**, 1883–1891 (2016).
 716. Marsden, C. D. Neuromelanin and Parkinson's disease. *J. Neural Transm. Suppl.* **19**, 121–141 (1983).
 717. Hirsch, E., Graybiel, A. M. & Agid, Y. A. Melanized dopaminergic neurons are differentially susceptible to degeneration in Parkinson's disease. *Nature* **334**, 345–348 (1988).
 718. Youdim, M. B., Ben-Shachar, D. & Riederer, P. Is Parkinson's disease a progressive siderosis of substantia nigra resulting in iron and melanin induced neurodegeneration? *Acta Neurol. Scand. Suppl.* **126**, 47–54 (1989).
 719. Mann, D. M. & Yates, P. O. Possible role of neuromelanin in the pathogenesis of Parkinson's disease. *Mech. Ageing Dev.* **21**, 193–203 (1983).
 720. Kastner, A., Hirsch, E. C., Javoy-Agid, F. & Agid, Y. *Is the Vulnerability of Neurons in the Substantia Nigra of Patients with Parkinson's Disease Related to Their Neuromelanin Content?* (1992).
 721. Shamoto-Nagai, M. *et al.* Neuromelanin inhibits enzymatic activity of 26S proteasome in human dopaminergic SH-SY5Y cells. *J. Neural Transm.* **111**, 1253–1265 (2004).
 722. Shamoto-Nagai, M. *et al.* Neuromelanin induces oxidative stress in mitochondria through release of iron: mechanism behind the inhibition of 26S proteasome. *J. Neural Transm.* **113**, 633–644 (2006).
 723. McGeer, P. L., Itagaki, S., Boyes, B. E. & McGeer, E. G. Reactive microglia are positive for HLA-DR in the substantia nigra of Parkinson's and Alzheimer's disease brains. *Neurology* **38**, 1285–1291 (1988).
 724. Banati, R. B., Daniel, S. E. & Blunt, S. B. Glial pathology but absence of apoptotic nigral neurons in long-standing Parkinson's disease. *Mov. Disord.* **13**, 221–227 (1998).
 725. Langston, J. W. *et al.* Evidence of active nerve cell degeneration in the substantia nigra of humans years after 1-methyl-4-phenyl-1,2,3,6-tetrahydropyridine exposure. *Ann. Neurol.* **46**, 598–605 (1999).
 726. Zucca, F. A. *et al.* Neuromelanin of the human substantia nigra: An update. *Neurotox. Res.* **25**, 13–23 (2014).
 727. Ferger, B., Leng, A., Mura, A., Hengerer, B. & Feldon, J. Genetic ablation of tumor necrosis factor-alpha (TNF-alpha) and pharmacological inhibition of TNF-

- synthesis attenuates MPTP toxicity in mouse striatum. *J. Neurochem.* **89**, 822–833 (2004).
728. Wilms, H. *et al.* Activation of microglia by human neuromelanin is NF-kappaB dependent and involves p38 mitogen-activated protein kinase: implications for Parkinson's disease. *FASEB J. Off. Publ. Fed. Am. Soc. Exp. Biol.* **17**, 500–502 (2003).
729. Cebrián, C. *et al.* MHC-I expression renders catecholaminergic neurons susceptible to T-cell-mediated degeneration. *Nat. Commun.* **5**, 3633 (2014).
730. Zhang, W. *et al.* Neuromelanin activates microglia and induces degeneration of dopaminergic neurons: Implications for progression of parkinson's disease. *Neurotox. Res.* **19**, 63–72 (2011).
731. Zecca, L. *et al.* Human neuromelanin induces neuroinflammation and neurodegeneration in the rat substantia nigra: implications for Parkinson's disease. *Acta Neuropathol.* **116**, 47–55 (2008).
732. Viceconte, N., Burguillos, M. A., Herrera, A. J., Pablos, R. M. De & Joseph, B. Neuromelanin activates proinflammatory microglia through a caspase-8-dependent mechanism. 1–15 (2015) doi:10.1186/s12974-014-0228-x.
733. Zhang, W. *et al.* Human neuromelanin: an endogenous microglial activator for dopaminergic neuron death. *Front. Biosci. (Elite Ed).* **5**, 1–11 (2013).
734. Beach, T. G. *et al.* Marked microglial reaction in normal aging human substantia nigra: Correlation with extraneuronal neuromelanin pigment deposits. *Acta Neuropathol.* **114**, 419–424 (2007).
735. Oberländer, U. *et al.* Neuromelanin is an immune stimulator for dendritic cells in vitro. *BMC Neurosci.* **12**, 116 (2011).
736. Wykes, M., Pombo, A., Jenkins, C. & MacPherson, G. G. Dendritic cells interact directly with naive B lymphocytes to transfer antigen and initiate class switching in a primary T-dependent response. *J. Immunol.* **161**, 1313–1319 (1998).
737. Earle, K. M. Studies on Parkinson's disease including x-ray fluorescent spectroscopy of formalin fixed brain tissue. *J. Neuropathol. Exp. Neurol.* **27** **1**, 1–14 (1968).
738. Dexter, D. T. *et al.* Increased nigral iron content in postmortem parkinsonian brain. *Lancet* **330**, 1219–1220 (1987).
739. Dexter, D. T. *et al.* Increased nigral iron content and alterations in other metal ions occurring in brain in Parkinson's disease. *J. Neurochem.* **52**, 1830–1836 (1989).
740. Double, K. L. *et al.* Influence of neuromelanin on oxidative pathways within the human substantia nigra. *Neurotoxicol. Teratol.* **24**, 621–628 (2002).
741. Swartz, H. M., Sarna, T. & Zecca, L. Modulation by neuromelanin of the availability and reactivity of metal ions. *Ann. Neurol.* **32** **Suppl**, S69–75 (1992).
742. Enochs, W. S., Sarna, T., Zecca, L., Riley, P. A. & Swartz, H. M. The roles of neuromelanin, binding of metal ions, and oxidative cytotoxicity in the pathogenesis of Parkinson's disease: a hypothesis. *J. Neural Transm. Park. Dis. Dement. Sect.* **7**, 83–100 (1994).
743. Fasano, M., Bergamasco, B. & Lopiano, L. Modifications of the iron–neuromelanin system in Parkinson's disease. *J. Neurochem.* **96**, 909–916 (2006).
744. Zecca, L., Zucca, F. A., Albertini, A., Rizzio, E. & Fariello, R. G. A proposed dual

- role of neuromelanin in the pathogenesis of Parkinson's disease. *Neurology* **67**, (2006).
745. Ehringer, H. & Hornykiewicz, O. [Distribution of noradrenaline and dopamine (3-hydroxytyramine) in the human brain and their behavior in diseases of the extrapyramidal system]. *Klin. Wochenschr.* **38**, 1236–1239 (1960).
 746. Iseki, E. Dementia with Lewy bodies: reclassification of pathological subtypes and boundary with Parkinson's disease or Alzheimer's disease. *Neuropathology* **24**, 72–78 (2004).
 747. Halliday, G. M., Hardman, C. D., Cordato, N. J., Hely, M. A. & Morris, J. G. A role for the substantia nigra pars reticulata in the gaze palsy of progressive supranuclear palsy. *Brain* **123** (Pt 4, 724–732 (2000).
 748. Ozawa, T. *et al.* The spectrum of pathological involvement of the striatonigral and olivopontocerebellar systems in multiple system atrophy: clinicopathological correlations. *Brain* **127**, 2657–2671 (2004).
 749. Dickson, D. W. Neuropathologic differentiation of progressive supranuclear palsy and corticobasal degeneration. *J. Neurol.* **246 Suppl**, I16-15 (1999).
 750. Hardman, C. D. *et al.* Comparison of the basal ganglia in rats, marmosets, macaques, baboons, and humans: volume and neuronal number for the output, internal relay, and striatal modulating nuclei. *J. Comp. Neurol.* **445**, 238–255 (2002).
 751. Halliday, G. M. *et al.* Midbrain neuropathology in idiopathic Parkinson's disease and diffuse Lewy body disease. *J. Clin. Neurosci. Off. J. Neurosurg. Soc. Australas.* **3**, 52–60 (1996).
 752. Damier, P., Hirsch, E. C., Agid, Y. & Graybiel, A. M. The substantia nigra of the human brain. II. Patterns of loss of dopamine-containing neurons in Parkinson's disease. *Brain* **122** (Pt 8, 1437–1448 (1999).
 753. Mosharov, E. V *et al.* Interplay between cytosolic dopamine, calcium, and alpha-synuclein causes selective death of substantia nigra neurons. *Neuron* **62**, 218–229 (2009).
 754. M., L. K. *et al.* Increased vesicular monoamine transporter enhances dopamine release and opposes Parkinson disease-related neurodegeneration in vivo. *Proc. Natl. Acad. Sci.* **111**, 9977–9982 (2014).
 755. Fahn, S. & Group, and the P. S. Does levodopa slow or hasten the rate of progression of Parkinson's disease? *J. Neurol.* **252**, iv37–iv42 (2005).
 756. Lipski, J. *et al.* L-DOPA: A scapegoat for accelerated neurodegeneration in Parkinson's disease? *Prog. Neurobiol.* **94**, 389–407 (2011).
 757. Haacke, E. M. *et al.* Correlation of putative iron content as represented by changes in R2* and phase with age in deep gray matter of healthy adults. *J. Magn. Reson. Imaging* **32**, 561–576 (2010).
 758. Bilgic, B., Pfefferbaum, A., Rohlfing, T., Sullivan, E. V & Adalsteinsson, E. MRI estimates of brain iron concentration in normal aging using quantitative susceptibility mapping. *Neuroimage* **59**, 2625–2635 (2012).
 759. Daugherty, A. & Raz, N. Age-related differences in iron content of subcortical nuclei observed in vivo: A meta-analysis. *Neuroimage* **70**, 113–121 (2013).
 760. Bolam, J. P. & Pissadaki, E. K. Living on the edge with too many mouths to feed: Why dopamine neurons die. *Mov. Disord.* **27**, 1478–1483 (2012).
 761. Kienzl, E., Jellinger, K., Stachelberger, H. & Linert, W. Iron as catalyst for

- oxidative stress in the pathogenesis of Parkinson's disease? *Life Sci.* **65**, 1973–1976 (1999).
762. Friedman, A., Galazka-Friedman, J. & Bauminger, E. R. Iron as a trigger of neurodegeneration in Parkinson's disease. *Handb. Clin. Neurol.* **83**, 493–505 (2007).
763. Bean, B. P. The action potential in mammalian central neurons. *Nat. Rev. Neurosci.* **8**, 451–465 (2007).
764. Chan, C. S. *et al.* 'Rejuvenation' protects neurons in mouse models of Parkinson's disease. *Nature* **447**, 1081–1086 (2007).
765. Guzman, J. N. *et al.* Oxidant stress evoked by pacemaking in dopaminergic neurons is attenuated by DJ-1. *Nature* **468**, 696–700 (2010).
766. Surmeier, D. J. *et al.* Calcium and Parkinson's disease. *Biochem. Biophys. Res. Commun.* **483**, 1013–1019 (2017).
767. Reeve, A., Simcox, E. & Turnbull, D. Ageing and Parkinson's disease: why is advancing age the biggest risk factor? *Ageing Res. Rev.* **14**, 19–30 (2014).
768. Sanchez-Padilla, J. *et al.* Mitochondrial oxidant stress in locus coeruleus is regulated by activity and nitric oxide synthase. *Nat. Neurosci.* **17**, 832–840 (2014).
769. Goldberg, J. A. *et al.* Calcium entry induces mitochondrial oxidant stress in vagal neurons at risk in Parkinson's disease. *Nat. Neurosci.* **15**, 1414–1421 (2012).
770. Pissadaki, E. K. & Bolam, J. P. The energy cost of action potential propagation in dopamine neurons: clues to susceptibility in Parkinson's disease. *Front. Comput. Neurosci.* **7**, 13 (2013).
771. Uhl, G. R., Hedreen, J. C. & Price, D. L. Parkinson's disease: loss of neurons from the ventral tegmental area contralateral to therapeutic surgical lesions. *Neurology* **35**, 1215–1218 (1985).
772. Maingay, M., Romero-Ramos, M., Carta, M. & Kirik, D. Ventral tegmental area dopamine neurons are resistant to human mutant alpha-synuclein overexpression. *Neurobiol. Dis.* **23**, 522–532 (2006).
773. Sofic, E., Lange, K. W., Jellinger, K. & Riederer, P. Reduced and oxidized glutathione in the substantia nigra of patients with Parkinson's disease. *Neurosci. Lett.* **142**, 128–130 (1992).
774. Sian, J. *et al.* Alterations in glutathione levels in Parkinson's disease and other neurodegenerative disorders affecting basal ganglia. *Ann. Neurol.* **36**, 348–355 (1994).
775. Pearce, R. K., Owen, A., Daniel, S., Jenner, P. & Marsden, C. D. Alterations in the distribution of glutathione in the substantia nigra in Parkinson's disease. *J. Neural Transm.* **104**, 661–677 (1997).
776. Burke, R. E. & O'Malley, K. Axon degeneration in Parkinson's disease. *Exp. Neurol.* **246**, 72–83 (2013).
777. O'Malley, K. L. The role of axonopathy in Parkinson's disease. *Exp. Neurobiol.* **19**, 115–119 (2010).
778. Tagliaferro, P. & Burke, R. E. Retrograde Axonal Degeneration in Parkinson Disease. **6**, 1–15 (2016).
779. Gegg, M. E. *et al.* Glucocerebrosidase deficiency in substantia nigra of parkinson disease brains. *Ann. Neurol.* **72**, 455–463 (2012).
780. Murphy, K. E. & Halliday, G. M. Glucocerebrosidase deficits in sporadic

- Parkinson disease. *Autophagy* **10**, 1350–1351 (2014).
781. MacLeod, D. *et al.* The familial Parkinsonism gene LRRK2 regulates neurite process morphology. *Neuron* **52**, 587–593 (2006).
 782. Sheng, C. *et al.* DJ-1 deficiency perturbs microtubule dynamics and impairs striatal neurite outgrowth. *Neurobiol. Aging* **34**, 489–498 (2013).
 783. Ashrafi, G. & Schwarz, T. L. PINK1- and PARK2-mediated local mitophagy in distal neuronal axons. *Autophagy* **11**, 187–189 (2015).
 784. Matheoud, D. *et al.* Parkinson's Disease-Related Proteins PINK1 and Parkin Repress Mitochondrial Antigen Presentation. *Cell* **166**, 314–327 (2016).
 785. Dahlström, A. & Fuxe, K. Localization of monoamines in the lower brain stem. *Experientia* **20**, 398–399 (1964).
 786. Gibb, W. R. & Lees, A. J. Anatomy, pigmentation, ventral and dorsal subpopulations of the substantia nigra, and differential cell death in Parkinson's disease. *J. Neurol. Neurosurg. Psychiatry* **54**, 388–396 (1991).
 787. Damier, P., Hirsch, E. C., Agid, Y. & Graybiel, A. M. The substantia nigra of the human brain. I. Nigrosomes and the nigral matrix, a compartmental organization based on calbindin D(28K) immunohistochemistry. *Brain* **122** (Pt 8, 1421–1436 (1999).
 788. Brichta, L. & Greengard, P. Molecular determinants of selective dopaminergic vulnerability in Parkinson's disease: an update. *Front. Neuroanat.* **8**, 152 (2014).
 789. Halliday, G. M. *et al.* Alpha-synuclein redistributes to neuromelanin lipid in the substantia nigra early in Parkinson's disease. *Brain* **128**, 2654–2664 (2005).
 790. McRitchie, D. A., Hardman, C. D. & Halliday, G. M. Cytoarchitectural distribution of calcium binding proteins in midbrain dopaminergic regions of rats and humans. *J. Comp. Neurol.* **364**, 121–150 (1996).
 791. Gibb, W. R. Melanin, tyrosine hydroxylase, calbindin and substance P in the human midbrain and substantia nigra in relation to nigrostriatal projections and differential neuronal susceptibility in Parkinson's disease. *Brain Res.* **581**, 283–291 (1992).
 792. Greene, J. G., Dingledine, R. & Greenamyre, J. T. Gene expression profiling of rat midbrain dopamine neurons: implications for selective vulnerability in parkinsonism. *Neurobiol. Dis.* **18**, 19–31 (2005).
 793. Kamath, T. *et al.* Single-cell genomic profiling of human dopamine neurons identifies a population that selectively degenerates in Parkinson's disease. *Nat. Neurosci.* **25**, 588–595 (2022).
 794. Haining, R. L. & Achat-mendes, C. Neuromelanin , one of the most overlooked molecules in modern medicine , is not a spectator. **12**, 2017–2020 (2017).
 795. DelleDonne, A. *et al.* Incidental Lewy body disease and preclinical Parkinson disease. *Arch. Neurol.* **65**, 1074–1080 (2008).
 796. Bennett, D. A. *et al.* Prevalence of parkinsonian signs and associated mortality in a community population of older people. *N. Engl. J. Med.* **334**, 71–76 (1996).
 797. Prettyman, R. Extrapyramidal signs in cognitively intact elderly people. *Age Ageing* **27**, 557–560 (1998).
 798. Xing, Y., Sapuan, A., Dineen, R. A. & Auer, D. P. Life span pigmentation changes of the substantia nigra detected by neuromelanin-sensitive MRI. *Mov. Disord.* **33**, 1792–1799 (2018).
 799. Chu, Y. & Kordower, J. H. Age-associated increases of alpha-synuclein in

- monkeys and humans are associated with nigrostriatal dopamine depletion: Is this the target for Parkinson's disease? *Neurobiol. Dis.* **25**, 134–149 (2007).
800. Kordower, J. H. *et al.* Disease duration and the integrity of the nigrostriatal system in Parkinson's disease. *Brain* **136**, 2419–2431 (2013).
 801. Conde, J. R. & Streit, W. J. Microglia in the aging brain. *J. Neuropathol. Exp. Neurol.* **65**, 199–203 (2006).
 802. Kim, W. G. *et al.* Regional difference in susceptibility to lipopolysaccharide-induced neurotoxicity in the rat brain: role of microglia. *J. Neurosci.* **20**, 6309–6316 (2000).
 803. Crichton, R.R., Ward, R. J. *Metal-based Neurodegeneration: From Molecular Mechanisms to Clinical Consequences.* (2013).
doi:<https://doi.org/10.1002/9781118553480.ch04>.
 804. Dlouhy, A. C. & Outten, C. E. The iron metallome in eukaryotic organisms. *Met. Ions Life Sci.* **12**, 241–278 (2013).
 805. Ramos, P. *et al.* Iron levels in the human brain: a post-mortem study of anatomical region differences and age-related changes. *J. trace Elem. Med. Biol. organ Soc. Miner. Trace Elem.* **28**, 13–17 (2014).
 806. Farrall, A. J. & Wardlaw, J. M. Blood-brain barrier: ageing and microvascular disease -systematic review and meta-analysis. *Neurobiol. Aging* **30**, 337–352 (2009).
 807. Zucca, F. A. *et al.* Neuromelanin and iron in human locus coeruleus and substantia nigra during aging: consequences for neuronal vulnerability. *J. Neural Transm.* **113**, 757–767 (2006).
 808. Good, P. F., Olanow, C. W. & Perl, D. P. Neuromelanin-containing neurons of the substantia nigra accumulate iron and aluminum in Parkinson's disease: a LAMMA study. *Brain Res.* **593**, 343–346 (1992).
 809. Jellinger, K. *et al.* Iron-melanin complex in substantia nigra of parkinsonian brains: an x-ray microanalysis. *J. Neurochem.* **59**, 1168–1171 (1992).
 810. Castellani, R. J., Siedlak, S. L., Perry, G. & Smith, M. A. Sequestration of iron by Lewy bodies in Parkinson's disease. *Acta Neuropathol.* **100**, 111–114 (2000).
 811. Faucheux, B. A. *et al.* Neuromelanin associated redox-active iron is increased in the substantia nigra of patients with Parkinson's disease. *J. Neurochem.* **86**, 1142–1148 (2003).
 812. Faucheux, B. A., Bonnet, A. M., Agid, Y. & Hirsch, E. C. Blood vessels change in the mesencephalon of patients with Parkinson's disease. *Lancet (London, England)* vol. 353 981–982 (1999).
 813. Kortekaas, R. *et al.* Blood-brain barrier dysfunction in parkinsonian midbrain in vivo. *Ann. Neurol.* **57**, 176–179 (2005).
 814. Al-Bachari, S., Naish, J. H., Parker, G. J. M., Emsley, H. C. A. & Parkes, L. M. Blood-Brain Barrier Leakage Is Increased in Parkinson's Disease . *Frontiers in Physiology* vol. 11 (2020).
 815. Block, M. L., Zecca, L. & Hong, J.-S. Microglia-mediated neurotoxicity: uncovering the molecular mechanisms. *Nat. Rev. Neurosci.* **8**, 57–69 (2007).
 816. Rathore, K. I., Redensek, A. & David, S. Iron homeostasis in astrocytes and microglia is differentially regulated by TNF- α and TGF- β 1. *Glia* **60**, 738–750 (2012).
 817. Urrutia, P. *et al.* Inflammation alters the expression of DMT1, FPN1 and

- hepcidin, and it causes iron accumulation in central nervous system cells. *J. Neurochem.* **126**, 541–549 (2013).
818. Mastroberardino, P. G. *et al.* A novel transferrin/TfR2-mediated mitochondrial iron transport system is disrupted in Parkinson's disease. *Neurobiol. Dis.* **34**, 417–431 (2009).
 819. Hochstrasser, H. *et al.* Ceruloplasmin gene variations and substantia nigra hyperechogenicity in Parkinson disease. *Neurology* **63**, 1912–1917 (2004).
 820. Olivieri, S. *et al.* Ceruloplasmin oxidation, a feature of Parkinson's disease CSF, inhibits ferroxidase activity and promotes cellular iron retention. *J. Neurosci.* **31**, 18568–18577 (2011).
 821. Ayton, S. *et al.* Ceruloplasmin dysfunction and therapeutic potential for Parkinson disease. *Ann. Neurol.* **73**, 554–559 (2013).
 822. Salazar, J. *et al.* Divalent metal transporter 1 (DMT1) contributes to neurodegeneration in animal models of Parkinson's disease. *Proc. Natl. Acad. Sci. U. S. A.* **105**, 18578–18583 (2008).
 823. Guerreiro, R. J. *et al.* Association of HFE common mutations with Parkinson's disease, Alzheimer's disease and mild cognitive impairment in a Portuguese cohort. *BMC Neurol.* **6**, 24 (2006).
 824. Faucheux, B. A. *et al.* Expression of lactoferrin receptors is increased in the mesencephalon of patients with Parkinson disease. *Proc. Natl. Acad. Sci. U. S. A.* **92**, 9603–9607 (1995).
 825. Jellinger, K., Paulus, W., Grundke-Iqbal, I., Riederer, P. & Youdim, M. B. Brain iron and ferritin in Parkinson's and Alzheimer's diseases. *J. Neural Transm. Park. Dis. Dement. Sect.* **2**, 327–340 (1990).
 826. Morris, C. M. & Edwardson, J. A. Iron histochemistry of the substantia nigra in Parkinson's disease. *Neurodegener. a J. Neurodegener. Disord. neuroprotection, neuroregeneration* **3**, 277–282 (1994).
 827. Teoh, C. Y. & Davies, K. J. A. Potential roles of protein oxidation and the immunoproteasome in MHC class I antigen presentation: the 'PrOxI' hypothesis. *Arch. Biochem. Biophys.* **423**, 88–96 (2004).
 828. Brochard, V. *et al.* Infiltration of CD4+ lymphocytes into the brain contributes to neurodegeneration in a mouse model of Parkinson disease. *J. Clin. Invest.* **119**, 182–192 (2009).
 829. Galiano-Landeira, J., Torra, A., Vila, M. & Bové, J. CD8 T cell nigral infiltration precedes synucleinopathy in early stages of Parkinson's disease. *Brain* **143**, 3717–3733 (2020).
 830. Schröder, J. B. *et al.* Immune Cell Activation in the Cerebrospinal Fluid of Patients With Parkinson's Disease. *Frontiers in Neurology* vol. 9 (2018).
 831. Sulzer, D. *et al.* T cells from patients with Parkinson's disease recognize α -synuclein peptides. *Nat. Publ. Gr.* **546**, 656–661 (2017).
 832. González-Rodríguez, P. *et al.* Disruption of mitochondrial complex I induces progressive parkinsonism. *Nature* **599**, 650–656 (2021).
 833. Sánchez-Ferrer, A., Rodríguez-López, J. N., García-Cánovas, F. & García-Carmona, F. Tyrosinase: a comprehensive review of its mechanism. *Biochim. Biophys. Acta* **1247**, 1–11 (1995).
 834. Vila, M. Neuromelanin, Aging, and Neuronal Vulnerability in Parkinson's Disease Neuromelanin and PD: A 100-Year-Old Relationship Synthesis of

- Neuromelanin : Mechanisms and Significance. *Mov. Disord.* **34**, 1440–1451 (2019).
835. Beach, T. G. *et al.* Substantia Nigra Marinesco Bodies Are Associated with Decreased Striatal Expression of Dopaminergic Markers. *J. Neuropathol. Exp. Neurol.* **63**, 329–337 (2004).
836. Vila, M. Neuromelanin, aging, and neuronal vulnerability in Parkinson’s disease. *Mov. Disord.* **34**, 1440–1451 (2019).
837. Zolotukhin, S. *et al.* Recombinant adeno-associated virus purification using novel methods improves infectious titer and yield. *Gene Ther.* **6**, 973–985 (1999).
838. Piedra, J. *et al.* Development of a rapid, robust, and universal picogreen-based method to titer adeno-associated vectors. *Hum. Gene Ther. Methods* **26**, 35–42 (2015).
839. Paxinos, G. & Watson, C. *The Rat Brain in Stereotaxic Coordinates*. (Academic Press, 1982).
840. Karakuzu, A. *et al.* qMRLab: Quantitative MRI analysis, under one umbrella. *J. Open Source Softw.* **5**, 2343 (2020).
841. Gonzalez-Sepulveda, M. *et al.* Validation of a reversed phase UPLC-MS/MS method to determine dopamine metabolites and oxidation intermediates in neuronal differentiated SH-SY5Y cells and brain tissue. *ACS Chem. Neurosci.* **11**, 2679–2687 (2020).
842. Lemos-Amado, F. *et al.* Electrospray tandem mass spectrometry of aminochromes. *Rapid Commun. Mass Spectrom.* **15**, 2466–2471 (2001).
843. Paxinos, G. & Watson, C. *The Rat Brain in Stereotaxic Coordinates, 5th edition*. *Journal of Chemical Information and Modeling* vol. 53 (2004).
844. Herculano-Houzel, S. The glia/neuron ratio: how it varies uniformly across brain structures and species and what that means for brain physiology and evolution. *Glia* **62**, 1377–1391 (2014).
845. Retzius, G. Die neuroglia des gehirns beim menschen und bei säugethieren. *Biol. Untersuch.* **6**, 1–24 (1894).
846. Emsley, J. G. & Macklis, J. D. Astroglial heterogeneity closely reflects the neuronal-defined anatomy of the adult murine CNS. *Neuron Glia Biol.* **2**, 175–186 (2006).
847. Prinz, M., Priller, J., Sisodia, S. S. & Ransohoff, R. M. Heterogeneity of CNS myeloid cells and their roles in neurodegeneration. *Nat. Neurosci.* **14**, 1227–1235 (2011).
848. Ferenbach, D. & Hughes, J. Macrophages and dendritic cells: what is the difference? *Kidney Int.* **74**, 5–7 (2008).
849. Cuadros, M. A. & Navascués, J. The origin and differentiation of microglial cells during development. *Prog. Neurobiol.* **56**, 173–189 (1998).
850. Sierra, A., Abiega, O., Shahraz, A. & Neumann, H. Janus-faced microglia: beneficial and detrimental consequences of microglial phagocytosis. *Frontiers in Cellular Neuroscience* vol. 7 (2013).
851. McGeer, P. L., Itagaki, S., Tago, H. & McGeer, E. G. Occurrence of HLA-DR reactive microglia in Alzheimer’s disease. *Ann. N. Y. Acad. Sci.* **540**, 319–323 (1988).
852. Jimenez-Ferrer, I., Jewett, M., Tontanahal, A., Romero-Ramos, M. & Swanberg, M. Allelic difference in Mhc2ta confers altered microglial activation and

- susceptibility to α -synuclein-induced dopaminergic neurodegeneration. *Neurobiol. Dis.* **106**, 279–290 (2017).
853. Wiessner, C. *et al.* Expression of transforming growth factor-beta 1 and interleukin-1 beta mRNA in rat brain following transient forebrain ischemia. *Acta Neuropathol.* **86**, 439–446 (1993).
 854. Fujita, T., Yoshimine, T., Maruno, M. & Hayakawa, T. Cellular dynamics of macrophages and microglial cells in reaction to stab wounds in rat cerebral cortex. *Acta Neurochir. (Wien)*. **140**, 275–279 (1998).
 855. Perry, V. H. Innate inflammation in Parkinson's disease. *Cold Spring Harb. Perspect. Med.* **2**, a009373 (2012).
 856. Henneman, W. J. P. *et al.* Hippocampal atrophy rates in Alzheimer disease: added value over whole brain volume measures. *Neurology* **72**, 999–1007 (2009).
 857. Lawson, L. J., Perry, V. H., Dri, P. & Gordon, S. Heterogeneity in the distribution and morphology of microglia in the normal adult mouse brain. *Neuroscience* **39**, 151–170 (1990).
 858. Fernández-Arjona, M. del M., Grondona, J. M., Granados-Durán, P., Fernández-Llebrez, P. & López-Ávalos, M. D. Microglia morphological categorization in a rat model of neuroinflammation by hierarchical cluster and principal components analysis. *Front. Cell. Neurosci.* **11**, 1–22 (2017).
 859. Das, G. D. Gitter cells and their relationship to macrophages in the developing cerebellum: an electron microscopic study. *Virchows Arch. B, Cell Pathol.* **20**, 299–305 (1976).
 860. Thomas, W. E. Brain macrophages: evaluation of microglia and their functions. *Brain Res. Brain Res. Rev.* **17**, 61–74 (1992).
 861. Nakajima, K. & Kohsaka, S. Functional roles of microglia in the brain. *Neurosci. Res.* **17**, 187–203 (1993).
 862. Kreutzberg, G. W. Microglia: a sensor for pathological events in the CNS. *Trends Neurosci.* **19**, 312–318 (1996).
 863. Doorn, K. J. *et al.* Microglial phenotypes and toll-like receptor 2 in the substantia nigra and hippocampus of incidental Lewy body disease cases and Parkinson's disease patients. *Acta Neuropathol. Commun.* **2**, 90 (2014).
 864. Lin, L. F., Doherty, D. H., Lile, J. D., Bektesh, S. & Collins, F. GDNF: a glial cell line-derived neurotrophic factor for midbrain dopaminergic neurons. *Science* **260**, 1130–1132 (1993).
 865. Schaar, D. G., Sieber, B. A., Dreyfus, C. F. & Black, I. B. Regional and cell-specific expression of GDNF in rat brain. in *Experimental neurology* vol. 124 368–371 (1993).
 866. Gray, M. T. & Woulfe, J. M. Striatal blood-brain barrier permeability in Parkinson's disease. *J. Cereb. blood flow Metab. Off. J. Int. Soc. Cereb. Blood Flow Metab.* **35**, 747–750 (2015).
 867. Sofroniew, M. V & Vinters, H. V. Astrocytes: biology and pathology. *Acta Neuropathol.* **119**, 7–35 (2010).
 868. Ho, M. S. Microglia in Parkinson's Disease BT - Neuroglia in Neurodegenerative Diseases. in *Advances in Experimental Medicine and Biology*, vol 1175 (eds. Verkhatsky, A., Ho, M. S., Zorec, R. & Parpura, V.) 335–353 (Springer Singapore, 2019). doi:10.1007/978-981-13-9913-8_13.

869. Croisier, E., Moran, L. B., Dexter, D. T., Pearce, R. K. B. & Graeber, M. B. Microglial inflammation in the parkinsonian substantia nigra: Relationship to alpha-synuclein deposition. *J. Neuroinflammation* **2**, 1–8 (2005).
870. Eckert, L. L. Parkinson's disease and a dopamine-derived neurotoxin, 3,4-Dihydroxyphenylacetaldehyde : implications for proteins, microglia, and neurons. (University of Iowa, 2012). doi:10.17077/etd.5twcno7l.
871. Doorn, K. J. *et al.* Increased amoeboid microglial density in the olfactory bulb of Parkinson's and Alzheimer's patients. *Brain Pathol.* **24**, 152–165 (2014).
872. Torres-Platas, S. G. *et al.* Morphometric characterization of microglial phenotypes in human cerebral cortex. *J. Neuroinflammation* **11**, 12 (2014).
873. González-Sepúlveda, M. *et al.* Spontaneous changes in brain striatal dopamine synthesis and storage dynamics *ex vivo* reveal end-product feedback-inhibition of tyrosine hydroxylase. *Neuropharmacology* **212**, (2022).
874. Goldstein, D. S. *et al.* Determinants of buildup of the toxic dopamine metabolite DOPAL in Parkinson's disease. *J. Neurochem.* **126**, 591–603 (2013).
875. Fedorow, H. *et al.* Evidence for specific phases in the development of human neuromelanin. **27**, 506–512 (2006).
876. Kastner, A. *et al.* Is the Vulnerability of Neurons in the Substantia Nigra of Patients with Parkinson's Disease Related to Their Neuromelanin Content? *J. Neurochem.* **59**, 1080–1089 (1992).
877. Halliday, G. M. *et al.* α -Synuclein redistributes to neuromelanin lipid in the substantia nigra early in Parkinson's disease. *Brain* **128**, 2654–2664 (2005).
878. Shahmoradian, S. H. *et al.* Lewy pathology in Parkinson's disease consists of crowded organelles and lipid membranes. *Nat. Neurosci.* **22**, 1099–1109 (2019).
879. Kuusisto, E., Parkkinen, L. & Alafuzoff, I. Morphogenesis of Lewy bodies: dissimilar incorporation of alpha-synuclein, ubiquitin, and p62. *J. Neuropathol. Exp. Neurol.* **62**, 1241–1253 (2003).
880. Kirik, D., Rosenblad, C. & Björklund, A. Characterization of Behavioral and Neurodegenerative Changes Following Partial Lesions of the Nigrostriatal Dopamine System Induced by Intra-striatal 6-Hydroxydopamine in the Rat. *Exp. Neurol.* **152**, 259–277 (1998).
881. Kish, S. J., Shannak, K. & Hornykiewicz, O. Uneven pattern of dopamine loss in the striatum of patients with idiopathic Parkinson's disease. Pathophysiologic and clinical implications. *N. Engl. J. Med.* **318**, 876–880 (1988).
882. Lanciego, J. L., Luquin, N. & Obeso, J. A. Functional neuroanatomy of the basal ganglia. *Cold Spring Harb. Perspect. Med.* **2**, a009621 (2012).
883. Parnetti, L. *et al.* CSF and blood biomarkers for Parkinson's disease. *Lancet Neurol.* **18**, 573–586 (2019).
884. Volc, D. *et al.* Safety and immunogenicity of the α -synuclein active immunotherapeutic PD01A in patients with Parkinson's disease: a randomised, single-blinded, phase 1 trial. *Lancet Neurol.* **19**, 591–600 (2020).
885. Volkow, N. D., Wise, R. A. & Baler, R. The dopamine motive system: implications for drug and food addiction. *Nat. Rev. Neurosci.* **18**, 741–752 (2017).
886. Grace, A. A. Dysregulation of the dopamine system in the pathophysiology of schizophrenia and depression. *Nat. Rev. Neurosci.* vol. 17 524–532 (2016).
887. Osherovich, L. Priming the PD pump. *Sci. Exch.* **7**, 755 (2014).
888. Disease, P. S. *et al.* Dopamine oxidation mediates mitochondrial and lysosomal

- dysfunction in Parkinson's disease. **1261**, 1255–1261 (2017).
889. Murer, M. G. *et al.* Chronic levodopa is not toxic for remaining dopamine neurons, but instead promotes their recovery, in rats with moderate nigrostriatal lesions. *Ann. Neurol.* **43**, 561–575 (1998).
 890. Mor, D. E. *et al.* Dopamine induces soluble α -synuclein oligomers and nigrostriatal degeneration. *Nat. Neurosci.* **20**, 1560–1568 (2017).
 891. The Parkinson Study Group. Levodopa and the Progression of Parkinson's Disease. *N. Engl. J. Med.* **351**, 2498–2508 (2004).
 892. Duarte-Jurado, A. P. *et al.* Antioxidant Therapeutics in Parkinson's Disease: Current Challenges and Opportunities. *Antioxidants (Basel, Switzerland)* **10**, 1–19 (2021).
 893. Graham, D. Oxidative Pathways for Catecholamines in the Genesis of Neuromelanin and Cytotoxic Quinones. *Mol. Pharmacol.* **14**, (1978).
 894. Mann, D. M. A. & Yates, P. O. Possible role of neuromelanin in the pathogenesis of Parkinson's disease. *Mech. Ageing Dev.* **21**, 193–203 (1983).
 895. Ellis, R. J. Macromolecular crowding: obvious but underappreciated. *Trends Biochem. Sci.* **26**, 597–604 (2001).
 896. Sulzer, D. *et al.* Neuromelanin biosynthesis is driven by excess cytosolic catecholamines not accumulated by synaptic vesicles. www.pnas.org.
 897. Giros, B. & Caron, M. G. Molecular characterization of the dopamine transporter. *Trends Pharmacol. Sci.* **14**, 43–49 (1993).
 898. Gaskill, P. J., Carvallo, L., Eugenin, E. A. & Berman, J. W. Characterization and function of the human macrophage dopaminergic system: Implications for CNS disease and drug abuse. *J. Neuroinflammation* **9**, 1 (2012).
 899. Segura-Aguilar, J. *et al.* Neuroprotection against Aminochrome Neurotoxicity: Glutathione Transferase M2-2 and DT-Diaphorase. *Antioxidants* **11**, 1–15 (2022).
 900. Meiser, J., Weindl, D. & Hiller, K. Complexity of dopamine metabolism. *Cell Commun. Signal.* **11**, 1–18 (2013).
 901. Spector, S., Gordon, R., Sjoerdsma, A. & Udenfriend, S. End-product inhibition of tyrosine hydroxylase as a possible mechanism for regulation of norepinephrine synthesis. *Mol. Pharmacol.* **3**, 549–55 (1967).
 902. Mosharov, E. V., Gong, L. W., Khanna, B., Sulzer, D. & Lindau, M. Intracellular patch electrochemistry: regulation of cytosolic catecholamines in chromaffin cells. *J. Neurosci.* **23**, 5835–5845 (2003).
 903. Iranzo, A. *et al.* Dopamine transporter imaging deficit predicts early transition to synucleinopathy in idiopathic rapid eye movement sleep behavior disorder. *Ann. Neurol.* **82**, 419–428 (2017).
 904. Branco, R. C. *et al.* Vesicular monoamine transporter 2 mediates fear behavior in mice. *Genes. Brain. Behav.* **19**, e12634 (2020).
 905. Torra, A. *et al.* Overexpression of TFE3 Drives a Pleiotropic Neurotrophic Effect and Prevents Parkinson's Disease-Related Neurodegeneration. *Mol. Ther.* **26**, 1552–1567 (2018).
 906. Zhou, H. *et al.* Wearable Ultrasound Improves Motor Function in an MPTP Mouse Model of Parkinson's Disease. *IEEE Trans. Biomed. Eng.* **66**, 3006–3013 (2019).
 907. Xu, T. *et al.* Ultrasonic stimulation of the brain to enhance the release of dopamine – A potential novel treatment for Parkinson's disease. *Ultrason.*

- Sonochem.* **63**, 104955 (2020).
908. Baek, H., Pahk, K. J., Kim, M.-J., Youn, I. & Kim, H. Modulation of Cerebellar Cortical Plasticity Using Low-Intensity Focused Ultrasound for Poststroke Sensorimotor Function Recovery. *Neurorehabil. Neural Repair* **32**, 777–787 (2018).
 909. Suh, D. H. *et al.* Intense focused ultrasound tightening in Asian skin: clinical and pathologic results. *Dermatologic Surg. Off. Publ. Am. Soc. Dermatologic Surg. [et al.]* **37**, 1595–1602 (2011).
 910. Lee, H. S. *et al.* Multiple pass ultrasound tightening of skin laxity of the lower face and neck. *Dermatologic Surg. Off. Publ. Am. Soc. Dermatologic Surg. [et al.]* **38**, 20–27 (2012).
 911. Sung, C.-Y., Chiang, P.-K., Tsai, C.-W. & Yang, F.-Y. Low-Intensity Pulsed Ultrasound Enhances Neurotrophic Factors and Alleviates Neuroinflammation in a Rat Model of Parkinson’s Disease. *Cereb. Cortex* **32**, 176–185 (2021).
 912. Wei, X. *et al.* Combined Diffusion Tensor Imaging and Arterial Spin Labeling as Markers of Early Parkinson’s disease. *Sci. Rep.* **6**, 33762 (2016).
 913. Timofeev, I., Nortje, J., Al-Rawi, P. G., Hutchinson, P. J. A. & Gupta, A. K. Extracellular brain pH with or without hypoxia is a marker of profound metabolic derangement and increased mortality after traumatic brain injury. *J. Cereb. blood flow Metab. Off. J. Int. Soc. Cereb. Blood Flow Metab.* **33**, 422–427 (2013).
 914. Haacke, E. M. *et al.* Imaging iron stores in the brain using magnetic resonance imaging. *Magn. Reson. Imaging* **23**, 1–25 (2005).
 915. Yuan, Y., Wang, Z., Liu, M. & Shoham, S. Cortical hemodynamic responses induced by low-intensity transcranial ultrasound stimulation of mouse cortex. *Neuroimage* **211**, 116597 (2020).
 916. Double, K. L. & Halliday, G. M. New face of neuromelanin BT - Parkinson’s Disease and Related Disorders. in (eds. Riederer, P., Reichmann, H., Youdim, M. B. H. & Gerlach, M.) 119–123 (Springer Vienna, 2006).
 917. Chu, Y. *et al.* Alterations in axonal transport motor proteins in sporadic and experimental Parkinson’s disease. *Brain* **135**, 2058–2073 (2012).
 918. Arkadir, D., Bergman, H. & Fahn, S. Redundant dopaminergic activity may enable compensatory axonal sprouting in Parkinson disease. *Neurology* **82**, 1093 LP – 1098 (2014).
 919. Mammana, S. *et al.* The role of macrophages in neuroinflammatory and neurodegenerative pathways of alzheimer’s disease, amyotrophic lateral sclerosis, and multiple sclerosis: Pathogenetic cellular effectors and potential therapeutic targets. *Int. J. Mol. Sci.* **19**, 1–20 (2018).
 920. West, M. J., Slomianka, L. & Gundersen, H. J. G. Unbiased stereological estimation of the total number of neurons in the subdivisions of the rat hippocampus using the optical fractionator. *Anat. Rec.* **231**, 482–497 (1991).
 921. Ip, C. W., Cheong, D. & Volkmann, J. Stereological Estimation of Dopaminergic Neuron Number in the Mouse Substantia Nigra Using the Optical Fractionator and Standard Microscopy Equipment. *J. Vis. Exp.* **127**, (2017).
 922. Tapias, V., Greenamyre, J. T. & Watkins, S. C. Automated imaging system for fast quantitation of neurons, cell morphology and neurite morphometry in vivo and in vitro. *Neurobiol. Dis.* **54**, 158–168 (2013).

923. Keller, K. K. *et al.* Improving efficiency in stereology: A study applying the proportionator and the autodisector on virtual slides. *J. Microsc.* **251**, 68–76 (2013).
924. Mouton, P. R. *et al.* Unbiased estimation of cell number using the automatic optical fractionator. *J. Chem. Neuroanat.* **80**, A1–A8 (2017).
925. Penttinen, A. M. *et al.* Implementation of deep neural networks to count dopamine neurons in substantia nigra. *Eur. J. Neurosci.* **48**, 2354–2361 (2018).
926. Wolf, S. A., Boddeke, H. W. G. M. & Kettenmann, H. Microglia in Physiology and Disease. *Annu. Rev. Physiol.* **79**, 619–643 (2017).
927. Liddelw, S. A. *et al.* Neurotoxic reactive astrocytes are induced by activated microglia. *Nature* **541**, 481–487 (2017).
928. Holness, C. L. & Simmons, D. L. Molecular cloning of CD68, a human macrophage marker related to lysosomal glycoproteins. *Blood* **81**, 1607–1613 (1993).
929. Fadini, G. P. *et al.* Monocyte-macrophage polarization balance in pre-diabetic individuals. *Acta Diabetol.* **50**, 977–982 (2013).
930. Rabaneda-Lombarte, N. *et al.* The CD200R1 microglial inhibitory receptor as a therapeutic target in the MPTP model of Parkinson’s disease. *J. Neuroinflammation* **18**, 1–21 (2021).
931. World Health Organization. <https://www.who.int/news-room/fact-sheets/detail/the-top-10-causes-of-death>. (2020).
932. Guzman-Martinez, L. *et al.* Neuroinflammation as a common feature of neurodegenerative disorders. *Front. Pharmacol.* **10**, 1–17 (2019).
933. Hou, Y. *et al.* Ageing as a risk factor for neurodegenerative disease. *Nat. Rev. Neurol.* **15**, 565–581 (2019).

VIII. ANNEX

Supplementary Table 1. UPLC-MS/MS assessment of striatal DA and L-DOPA levels (pmol/mg ± SEM) and DA vesicular uptake ratio in AAV-hVMAT2 injected rats at 2 months (m) post-injection

Group	Hemisphere	Animal	DA	L-DOPA	DA vesicular uptake (DA/L-DOPA)
AAV-hVMAT2	Contralateral	1	189.91	0.96	196.94
		2	254.86	2.02	126.21
		3	144.06	3.54	40.72
		4	176.18	1.34	131.06
		5	326.49	5.48	59.56
		6	313.83	6.93	45.28
		7	245.14	4.42	55.48
		8	313.61	8.69	36.08
	Ipsilateral	1	244.76	1.43	171.47
		2	322.61	1.14	282.03
		3	250.39	1.23	204.31
		4	300.48	2.14	140.35
		5	313.82	0.93	337.73
		6	286.01	1.26	226.60
		7	384.66	3.16	121.59
		8	221.20	1.12	197.14

Supplementary Table 2. Immunohistochemical counts in rat SNpc at 1 m post-AAV injection.

	Hemisphere	Animal	Flag expression				TYR expression			
			Flag+	Flag-NM+	TH+	TH-NM+	TYR+	TYR-NM+	TH+	TH-NM+
AAV-hVMAT2	Ipsilateral	1	241	N/A	286	N/A	N/A	N/A	N/A	N/A
		2	460	N/A	560	N/A	N/A	N/A	N/A	N/A
		3	170	N/A	227	N/A	N/A	N/A	N/A	N/A
		4	538	N/A	703	N/A	N/A	N/A	N/A	N/A
		5	395	N/A	398	N/A	N/A	N/A	N/A	N/A
AAV-hTYR	Ipsilateral	1	N/A	N/A	N/A	N/A	1054	9	836	15
		2	N/A	N/A	N/A	N/A	1152	18	861	3
		3	N/A	N/A	N/A	N/A	765	7	783	2
		4	N/A	N/A	N/A	N/A	787	9	809	1
AAV-hTYR + AAV-hVMAT2	Ipsilateral	1	643	14	754	6	706	59	860	1
		2	592	6	822	8	650	27	589	8
		3	656	18	747	1	555	40	747	3
		4	723	2	789	2	580	40	734	1
		5	804	2	675	3	863	13	779	2

N/A not applicable

Supplementary Table 3. Immunohistochemical counts in rat SNpc at 2m post-AAV injections

	Hemisphere	Animal	VMAT2			p62+ Inclusions	
			VMAT2+	VMAT2+	VMAT2-	cytoplasmic	nuclear
			NM-	NM+	NM+		
AAV-VMAT2	Contralateral	1	51	N/A	N/A	N/A	N/A
		2	46	N/A	N/A	N/A	N/A
		3	58	N/A	N/A	N/A	N/A
		4	46	N/A	N/A	N/A	N/A
		5	74	N/A	N/A	N/A	N/A
		6	67	N/A	N/A	N/A	N/A
		7	48	N/A	N/A	N/A	N/A
	Ipsilateral	1	64	N/A	N/A	N/A	N/A
		2	64	N/A	N/A	N/A	N/A
		3	93	N/A	N/A	N/A	N/A
		4	33	N/A	N/A	N/A	N/A
		5	34	N/A	N/A	N/A	N/A
		6	60	N/A	N/A	N/A	N/A
		7	63	N/A	N/A	N/A	N/A
AAV-TYR	Contralateral	1	51	N/A	N/A	0	0
		2	33	N/A	N/A	0	0
		3	45	N/A	N/A	0	0
		4	90	N/A	N/A	0	0
		5	a	N/A	N/A	0	0
		6	a	N/A	N/A	0	0
		7	a	N/A	N/A	0	0
		8	75	N/A	N/A	0	0
	Ipsilateral	1	0	3	42	6	0
		2	12	45	48	0	0
		3	0	3	147	5	0
		4	0	21	90	2	0
		5	a	a	a	5	0
		6	a	a	a	3	0
7		a	a	a	1	0	
8		0	33	54	4	0	
AAV-TYR + AAV-VMAT2	Contralateral	1	39	N/A	N/A	0	0
		2	42	N/A	N/A	0	0
		3	51	N/A	N/A	0	0
		4	78	N/A	N/A	0	0
		5	30	N/A	N/A	0	0
		6	66	N/A	N/A	0	0
		7	69	N/A	N/A	0	0
		8	36	N/A	N/A	0	0
	Ipsilateral	1	6	6	15	1	0
		2	30	21	18	0	0
		3	42	21	39	0	0
		4	15	9	21	0	0
		5	18	33	27	2	0
		6	21	18	9	0	0
7		33	30	33	0	0	
8		6	9	12	0	0	

a sections not available
N/A not applicable

Supplementary Table 4. UPLC-MS/MS assessment of DA metabolites (pmol/mg ± SEM) and their calculated ratios (% ipsilateral vs contralateral) in rat ventral midbrain at 2m post-AAV injections

Group	Hemisphere	Animal	pmol/mg protein								% ipsilateral vs contralateral side					
			DA	L-DOPA	3MT	DOPAC	AC	SSCD	5SCD	5SCDA	DA vesicular uptake (DA/L-DOPA)	DA metabolism (DOPAC:3MT/DA)	3MT production (3MT/DA)	L-DOPA oxidation (SSCD/L-DOPA)	DA oxidation (SSCD+AC/DA)	Catechol Oxidation (L-DOPA ox. + DA ox.)
AAV-VMAT2	Contralateral	1	5.66	2.40	0.93	143.07	0.70	2.79	32.63	2.36	25.4455	0.1649	5.8886	1.1640	1.1640	7.0526
		2	2.87	1.89	0.79	32.71	1.39	2.77	68.17	1.52	11.6557	0.2736	24.2029	1.4645	1.4645	25.6674
		3	4.08	1.78	0.57	323.50	0.20	4.20	58.45	2.29	79.4884	0.1391	14.3865	2.3584	2.3584	16.7448
		4	5.64	3.78	6.09	154.80	1.15	3.74	38.90	1.49	28.5256	1.0790	7.1014	0.9910	0.9910	8.0924
	Ipsilateral	5	4.61	1.85	0.63	74.65	0.76	2.32	30.32	2.49	16.3460	0.1377	6.7482	1.2546	1.2546	8.0028
		6	2.60	2.26	0.84	150.02	0.39	2.05	27.51	1.15	6.1060	0.3232	10.7405	0.9067	0.9067	11.6472
		7	3.69	1.82	1.33	196.43	3.03	3.82	212.03	2.02	53.5819	0.3593	58.2714	2.0981	2.0981	60.3695
		8	8.23	8.96	1.49	221.91	6.55	3.72	154.41	0.92	27.1573	0.1816	19.5654	0.4148	0.4148	19.9803
AAV-TYR	Contralateral	1	48.94	45.12	7.41	35.12	0.88	5.22	117.39	1.08	0.8692	2.4169	2.5326	0.1156	0.1156	2.5326
		2	9.23	10.13	2.52	82.94	1.29	3.53	237.50	0.91	9.2574	0.2779	25.8670	0.3480	0.3480	26.2150
		3	4.80	1.67	0.43	12.15	0.73	1.98	34.27	2.88	2.6227	0.0905	7.2945	1.1854	1.1854	8.4799
		4	5.25	2.03	0.62	6.20	0.58	2.47	27.48	2.59	1.2978	0.1179	5.3429	1.2170	1.2170	6.5599
	Ipsilateral	5	4.69	5.23	1.59	33.49	0.45	3.07	237.02	0.90	7.4839	0.3388	50.6642	0.5861	0.5861	51.2502
		6	3.92	1.52	0.41	28.50	0.58	1.08	31.23	2.57	7.3716	0.1051	8.1104	0.7077	0.7077	8.8181
		7	1.81	3.88	218.69	148.36	0.92	4.65	112.88	0.47	202.8743	120.8742	62.8994	1.1988	1.1988	64.0983
		8	4.66	2.52	1.49	91.61	1.69	9.87	129.37	1.85	19.9920	0.3189	28.1444	3.9173	3.9173	32.0618
AAV-TYR + AAV-VMAT2	Contralateral	1	7.32	5.44	1.96	176.44	1.62	5.34	131.20	1.35	24.3721	0.2672	18.1446	0.9815	0.9815	19.1260
		2	4.79	3.38	1.43	91.61	1.36	5.19	96.35	1.41	19.4358	0.2984	20.4127	1.5337	1.5337	21.9464
		3	3.02	1.84	0.63	22.53	0.61	1.52	31.02	1.64	7.6580	0.2087	10.4612	0.8231	0.8231	11.2842
		4	7.13	3.24	1.64	19.13	1.98	4.57	77.30	2.20	2.9145	0.2304	11.1256	1.4130	1.4130	12.5386
	Ipsilateral	5	4.79	3.38	1.43	91.61	1.36	5.19	96.35	1.41	19.4358	0.2984	20.4127	1.5337	1.5337	21.9464
		6	3.53	4.46	1.76	45.67	1.59	16.96	187.71	0.79	13.4324	0.4972	53.6178	3.8066	3.8066	57.4244
		7	3.19	5.19	1.26	201.58	1.28	6.99	124.52	0.62	63.5395	0.3936	39.4070	1.3481	1.3481	40.7551
		8	1.78	2.85	0.94	121.78	0.60	3.85	31.75	0.63	68.7677	0.5244	18.1304	1.3494	1.3494	19.6797
AAV-TYR + AAV-VMAT2	Contralateral	1	1.47	2.22	0.27	8.04	0.54	1.39	73.03	0.66	5.6743	0.1851	50.2117	0.6235	0.6235	50.8351
		2	2.44	4.37	0.98	329.35	1.29	7.98	182.56	0.56	135.1556	0.4027	75.2201	1.8274	1.8274	77.0475
		3	2.43	3.65	0.96	103.99	1.21	4.54	74.00	0.67	43.1098	0.3948	30.8942	1.2459	1.2459	32.1401
		4	3.41	1.68	0.85	73.53	0.90	2.65	54.82	2.03	21.8218	0.2483	16.3479	1.5797	1.5797	17.9276
	Ipsilateral	5	2.21	2.26	0.92	46.26	0.43	1.71	40.53	0.98	21.3099	0.4175	18.4954	0.7549	0.7549	19.2504
		6	3.41	1.68	0.85	73.53	0.90	2.65	54.82	2.03	21.8218	0.2483	16.3479	1.5797	1.5797	17.9276
		7	5.63	2.26	1.27	47.52	0.59	2.10	49.55	2.49	8.6665	0.2250	8.9062	0.9319	0.9319	9.8381
		8	2.49	1.65	0.65	78.46	1.79	2.78	39.90	1.51	31.8255	0.2598	16.7714	1.6870	1.6870	18.4585
AAV-TYR + AAV-VMAT2	Contralateral	1	2.63	1.24	0.86	101.86	0.64	2.17	45.17	2.13	39.1098	0.3277	17.4429	1.7524	1.7524	19.1953
		2	4.73	1.57	1.26	163.42	1.67	4.75	124.40	3.02	34.7848	0.2668	26.6295	3.0313	3.0313	29.6608
		3	2.76	1.10	0.12	3.69	0.28	2.41	29.40	2.50	1.3787	0.0424	10.7455	2.1816	2.1816	12.9271
		4	5.10	6.31	0.80	77.35	0.98	3.01	72.98	0.81	15.3116	0.1572	15.6642	0.4776	0.4776	16.1418
	Ipsilateral	5	3.97	2.25	0.61	1.04	2.95	52.10	1.77	0.1548	13.3885	0.1548	13.3885	1.3150	1.3150	14.7035
		6	5.78	2.37	1.13	43.28	0.56	2.90	48.25	2.44	8.4518	0.1953	8.4518	0.6749	0.6749	9.1260
		7	3.22	3.30	1.00	121.69	2.17	2.23	44.61	0.97	38.1371	0.3108	14.5404	0.6749	0.6749	15.2153
		8	5.94	4.70	0.40	110.94	1.31	5.54	120.01	1.27	18.7377	0.0678	20.4173	1.1794	1.1794	21.5967
AAV-TYR + AAV-VMAT2	Ipsilateral	1	2.94	1.06	0.50	60.26	0.52	1.46	49.48	2.77	20.6647	0.1694	17.0059	1.3789	1.3789	18.3848
		2	3.51	1.76	0.56	3.48	0.22	5.64	39.76	2.00	1.1513	0.1604	11.3917	3.2133	3.2133	14.6050
		3	5.10	6.31	0.80	77.35	0.98	3.01	72.98	0.81	15.3116	0.1572	15.6642	0.4776	0.4776	16.1418
		4	3.97	2.25	0.61	1.04	2.95	52.10	1.77	0.1548	13.3885	0.1548	13.3885	1.3150	1.3150	14.7035
AAV-TYR + AAV-VMAT2	Ipsilateral	5	5.78	2.37	1.13	43.28	0.56	2.90	48.25	2.44	8.4518	0.1953	8.4518	0.6749	0.6749	9.1260
		6	3.22	3.30	1.00	121.69	2.17	2.23	44.61	0.97	38.1371	0.3108	14.5404	0.6749	0.6749	15.2153
		7	5.94	4.70	0.40	110.94	1.31	5.54	120.01	1.27	18.7377	0.0678	20.4173	1.1794	1.1794	21.5967
		8	2.94	1.06	0.50	60.26	0.52	1.46	49.48	2.77	20.6647	0.1694	17.0059	1.3789	1.3789	18.3848
AAV-TYR + AAV-VMAT2	Ipsilateral	1	3.51	1.76	0.56	3.48	0.22	5.64	39.76	2.00	1.1513	0.1604	11.3917	3.2133	3.2133	14.6050
		2	5.10	6.31	0.80	77.35	0.98	3.01	72.98	0.81	15.3116	0.1572	15.6642	0.4776	0.4776	16.1418
		3	3.97	2.25	0.61	1.04	2.95	52.10	1.77	0.1548	13.3885	0.1548	13.3885	1.3150	1.3150	14.7035
		4	5.78	2.37	1.13	43.28	0.56	2.90	48.25	2.44	8.4518	0.1953	8.4518	0.6749	0.6749	9.1260
AAV-TYR + AAV-VMAT2	Ipsilateral	5	3.22	3.30	1.00	121.69	2.17	2.23	44.61	0.97	38.1371	0.3108	14.5404	0.6749	0.6749	15.2153
		6	5.94	4.70	0.40	110.94	1.31	5.54	120.01	1.27	18.7377	0.0678	20.4173	1.1794	1.1794	21.5967
		7	2.94	1.06	0.50	60.26	0.52	1.46	49.48	2.77	20.6647	0.1694	17.0059	1.3789	1.3789	18.3848
		8	3.51	1.76	0.56	3.48	0.22	5.64	39.76	2.00	1.1513	0.1604	11.3917	3.2133	3.2133	14.6050

a eliminated as a statistically significant outlier
b contralateral sample lost due to technical problems and values calculated as an average of the group. When ipsilateral sample was lost, the animal was eliminated

Supplementary Table 5. UPLC-MS/MS assessment of DA metabolites (pmol/mg ± SEM) and their calculated ratios (% ipsilateral vs contralateral) in rat striatum at 2m post-AAV injections

Group	Hemisphere	Animal	pmol/mg protein								% ipsilateral vs contralateral side							
			DA	L-DOPA	3MT	DOPAC	AC	SSCD	SSCDA	DA vesicular uptake (DA/ L-DOPA)	DA metabolism (DOPAC+3MT/ DA)	L-DOPA oxidation (SSCD/L-DOPA)	DA oxidation (SSCDA+AC/DA)	Catechol Oxidation (L-DOPA ox. + DA ox.)	DA content	DA vesicular uptake	DA metabolism	Catechol oxidation
	Contralateral	1	305.83	4.53	37.39	515.07	1.62	10.31	61.93	67.44	1.8065	2.2726	0.2078	2.4804	115.79	69.42	69.64	107.63
		2	184.14	3.17	28.92	522.93	1.38	17.97	54.20	58.04	2.9968	5.6644	0.3018	5.9662	100.79	51.45	36.61	38.66
		3	302.11	9.07	47.38	572.31	1.30	13.38	70.09	33.29	2.0512	1.4749	0.2363	1.7113	98.46	108.10	47.88	91.57
		4	274.23	8.26	40.95	232.81	0.99	15.85	75.53	33.19	0.9983	1.9178	0.2790	2.1968	114.90	130.12	89.52	158.89
		5	289.97	10.16	29.27	290.63	2.76	9.21	83.09	28.55	1.1032	0.9068	0.2961	1.0322	82.82	79.04	109.04	88.28
		6	179.08	4.70	33.72	319.67	0.97	22.31	68.11	38.14	1.9733	4.7519	0.3857	5.1376	153.55	94.81	76.51	52.39
		7	358.68	9.51	47.53	326.00	2.89	13.09	61.69	37.74	1.0414	1.3770	0.1800	1.5570	82.82	21.37	80.84	30.65
		8	335.04	8.82	46.83	685.21	0.71	15.23	84.59	37.98	2.1849	1.7266	0.2546	1.9812	67.45	53.73	46.15	42.70
AAV-VMAT2	Ipsilateral	1	249.31	5.32	50.04	263.62	1.05	12.85	62.96	46.82	1.2581	2.4128	0.2567	2.6695	115.79	69.42	69.64	107.63
		2	213.21	7.14	31.11	202.78	0.99	14.72	51.25	29.86	1.0970	2.0616	0.2450	2.3066	100.79	51.45	36.61	38.66
		3	304.50	8.46	35.45	263.63	0.35	12.21	37.24	35.99	0.9822	1.4436	0.1234	1.5670	98.46	130.12	89.52	158.89
		4	270.00	6.25	50.16	191.11	1.16	20.38	61.02	43.18	0.8936	1.2447	0.2303	3.4905	114.90	79.04	109.04	88.28
		5	333.18	14.76	38.16	362.66	2.24	11.20	98.77	22.57	1.2030	0.7588	0.3032	1.0619	153.55	94.81	76.51	52.39
		6	274.98	7.61	39.47	375.71	1.34	18.58	67.04	36.16	1.5099	2.4427	0.2487	2.6914	82.82	21.37	80.84	30.65
		7	297.05	36.84	33.86	216.22	4.33	9.80	58.42	8.06	0.8419	0.2659	0.2112	0.8459	67.45	53.73	46.15	42.70
		8	225.98	11.07	24.81	203.06	1.33	4.56	96.69	20.41	1.0084	0.4121	0.4338	0.8459				
AAV-TYR	Contralateral	1	223.28	4.79	26.13	140.39	1.71	17.49	410.40	46.65	0.7458	3.6536	1.8457	5.4993	16.37	22.28	132.56	199.18
		2	370.58	11.28	32.22	259.43	2.58	9.92	96.46	32.85	0.8793	0.2672	0.8793	10.9533	10.86	19.02	193.31	939.32 ^a
		3	363.22	5.97	26.80	258.69	2.20	5.61	223.17	60.88	0.7860	0.9408	0.6205	1.5613	12.13	7.16	475.49	284.01
		4	170.31	4.80	18.23	200.02	0.24	22.32	193.56	35.46	1.2815	4.6469	1.1379	5.7848	24.77	21.26	93.86	297.27
		5	190.06	13.81	22.55	214.02	3.72	16.96	212.61	13.77	1.2447	1.1383	1.2287	1.1383	113.89 ^a	215.48 ^a	78.38	345.89
		6	183.94	6.07	22.06	194.21	2.11	26.18	157.79	30.33	1.1758	4.3158	0.8693	5.1851	26.22	23.92	221.09	138.03
		7	363.57	9.55	42.05	167.76	2.81	20.65	224.67	38.08	0.9052	2.1626	0.6257	2.7883	18.29	16.42	386.34	188.32
		8	316.20	14.41	29.72	256.50	3.98	13.58	262.20	21.94	0.9052	0.9427	0.8418	1.7845	27.71	30.95	132.36	199.76
AAV-TYR	Ipsilateral	1	36.55	3.52	8.26	27.88	0.77	20.39	187.67	10.39	0.9887	5.7974	5.1559	10.9533	16.37	22.28	132.56	199.18
		2	40.26	6.44	14.60	46.65	0.53	45.11	151.12	6.25	1.5214	7.0026	3.7668	10.7694	10.86	19.02	193.31	939.32 ^a
		3	44.06	10.11	6.53	158.16	1.18	15.58	126.29	4.36	3.7373	1.5415	2.8927	4.4342	12.13	7.16	475.49	284.01
		4	42.19	5.60	7.32	43.42	0.56	61.58	260.62	7.54	1.2027	11.0055	6.1907	17.1962	24.77	21.26	93.86	297.27
		5	216.45	7.30	19.93	191.24	2.49	21.22	1140.05	29.66	0.9756	2.9085	5.2785	8.1870	113.89 ^a	215.48 ^a	78.38	345.89
		6	48.23	6.65	7.24	118.12	2.72	20.46	194.05	7.25	2.5994	3.0769	4.0803	7.1571	26.22	23.92	221.09	138.03
		7	66.50	10.64	10.84	137.43	3.88	30.36	155.48	6.25	2.2295	2.8544	2.3963	5.2508	18.29	16.42	386.34	188.32
		8	87.61	12.90	11.33	93.64	2.46	23.10	152.97	6.79	1.1981	1.7906	1.7741	3.5647	27.71	30.95	132.36	199.76
AAV-TYR + AAV-VMAT2	Contralateral	1	360.23	8.25	62.93	500.16	1.60	21.24	146.80	43.65	1.5631	2.5739	0.4120	2.9859	59.41	75.56	115.82	119.95
		2	280.94	8.17	31.82	278.06	1.43	7.14	55.22	34.39	1.1030	0.8741	0.2016	1.0757	48.45	11.50	100.55	110.89
		3	276.02	4.58	45.97	400.51	1.33	29.70	219.27	60.24	1.6176	6.4822	0.7992	7.2814	73.37	51.97	50.32	51.10
		4	162.19	3.87	22.99	203.33	0.41	19.52	61.04	41.94	1.3954	5.0475	0.3789	5.4264	22.04	67.45	108.05	238.64
		5	365.05	10.10	39.52	195.26	1.41	30.70	381.08	36.16	0.6432	3.0404	1.0478	4.0881	220.28	128.82	69.49	99.96
		6	38.72	5.72	8.68	89.57	1.20	7.62	67.64	6.77	2.5375	1.3321	1.7780	3.1101	54.91	114.79	114.80	111.12
		7	295.69	8.37	34.22	152.04	0.67	24.42	547.94	35.31	0.6299	2.9155	1.8554	4.7709	59.41	75.56	115.82	119.95
		8	220.17	11.11	27.72	224.97	1.26	10.98	64.55	19.81	1.1477	0.9885	0.2989	1.2875	48.45	11.50	100.55	110.89
AAV-TYR + AAV-VMAT2	Ipsilateral	1	214.02	6.49	32.44	355.03	0.87	21.45	58.20	32.98	1.8104	3.3054	0.7907	3.5814	73.37	51.97	50.32	51.10
		2	136.11	34.43	20.27	130.68	1.02	13.85	106.60	3.95	1.1090	0.4022	0.7907	1.1929	48.45	11.50	100.55	110.89
		3	202.51	6.47	34.93	129.91	0.95	20.67	105.46	31.31	0.8140	3.1951	0.5255	3.7206	73.37	51.97	50.32	51.10
		4	270.38	8.23	18.69	165.19	1.07	11.77	199.31	32.85	1.4301	1.6670	0.7411	1.6670	22.04	67.45	108.05	238.64
		5	80.44	3.30	16.35	39.55	0.55	25.98	150.70	24.39	0.6949	7.8755	1.8803	9.7558	220.28	128.82	69.49	99.96
		6	85.29	9.78	14.00	136.41	1.37	15.09	132.26	8.72	1.7634	1.5423	1.5666	3.1089	54.91	114.79	114.80	111.12
		7	162.35	10.27	28.52	88.88	0.89	31.53	361.25	15.81	0.7331	3.0710	2.2306	5.2508	54.91	114.79	114.80	111.12
		8	115.35	11.97	18.02	86.24	0.70	21.50	252.73	9.64	0.9039	1.7966	2.1971	3.9937	52.39	48.64	78.76	310.20

^a eliminated as a statistically-significant outlier

Supplementary Table 6. Immunohistochemical counts in rat SNpc at 6m post-AAV injections

	Hemisphere	Animal	TH				Iba1		GFAP	CD68
			TH+ NM-	TH+ NM+	TH- NM+	Extracel NM	Non-activated	Activated	GFAP+	CD68+
AAV-VMAT2	Contralateral	1	9894	N/A	N/A	N/A	1343	0	4774	108
		2	14450	N/A	N/A	N/A	2293	17	7607	70
		3	12036	N/A	N/A	N/A	1617	0	8516	102
		4	14569	N/A	N/A	N/A	1655	34	7175	85
		5	15436	N/A	N/A	N/A	1029	17	5931	114
		6	11118	N/A	N/A	N/A	1922	0	5503	68
		7	10455	N/A	N/A	N/A	1695	0	5889	34
	Ipsilateral	1	8908	N/A	N/A	N/A	1451	0	5587	260
		2	12546	N/A	N/A	N/A	2211	0	7980	276
		3	10336	N/A	N/A	N/A	1805	0	9196	170
		4	14467	N/A	N/A	N/A	1877	17	7714	190
		5	14025	N/A	N/A	N/A	1485	17	6175	158
		6	11067	N/A	N/A	N/A	2047	0	5669	68
		7	11390	N/A	N/A	N/A	1517	17	6411	102
AAV-TYR	Contralateral	1	4063	N/A	N/A	N/A	3413	0	7300	102
		2	9435	N/A	N/A	N/A	3950	85	17500	543
		3	11866	N/A	N/A	N/A	1018	0	9235	183
		4	13770	N/A	N/A	N/A	1611	0	6699	109
		5	12580	N/A	N/A	N/A	1756	34	9391	125
		6	16592	N/A	N/A	N/A	1770	0	8757	156
		7	6783	N/A	N/A	N/A	2060	0	7900	129
		8	9673	N/A	N/A	N/A	2491	0	7384	55
	Ipsilateral	1	17	187	1343	5831	3286	5394	35239	20036
		2	68	357	1513	18173	3835	10107	56225	44922
		3	136	1258	3740	10846	3510	4717	24800	18353
		4	102	1105	1156	8823	3289	6030	29910	18825
		5	34	289	1394	13634	2149	5586	45162	22753
		6	221	2125	3859	13447	2628	7715	28664	20190
		7	102	1904	3060	12920	3179	7201	26537	21508
		8	170	1598	3043	8704	3092	11739	25970	26228
AAV-TYR + AAV-VMAT2	Contralateral	1	13957	N/A	N/A	N/A	1972	57	9232	68
		2	17306	N/A	N/A	N/A	1461	23	4391	68
		3	13787	N/A	N/A	N/A	2255	0	7870	68
		4	11305	N/A	N/A	N/A	703	23	2518	45
		5	14552	N/A	N/A	N/A	1321	0	5392	113
		6	10863	N/A	N/A	N/A	2217	0	5516	68
		7	9741	N/A	N/A	N/A	2033	0	7014	0
	Ipsilateral	1	663	1768	1785	12631	4082	4734	32010	18982
		2	1802	9622	306	3315	3021	2478	13156	5249
		3	748	7531	799	6290	5448	8247	18127	4363
		4	1564	6307	340	2567	1481	1214	5049	3400
		5	3842	10030	289	1173	2617	3065	17212	4072
		6	4607	6953	1054	2788	3421	2668	12429	5432
		7	1785	5746	1190	7650	4131	4061	18998	12115

N/A not applicable

Supplementary Table 7. UPLC-MS/MS assessment of DA metabolites (pmol/mg ± SEM) and their calculated ratios (% ipsilateral vs contralateral) in rat striatum at 6m post-AAV injections

Group	Animal	Hemisphere	pmol/mg protein							% ipsilateral vs contralateral side				
			DA	L-DOPA	3MT	DOPAC	AC	SSCD	SSCDA	DA vesicular uptake (DA/L-DOPA)	DA metabolism (DOPAC+3MT/DA)	L-DOPA oxidation (SSCD/L-DOPA)	DA oxidation (SSCDA+AC/DA)	Catechol Oxidation (L-DOPA ox. + DA ox.)
	1	Contralateral	540.14	3.56	38.03	30.78	0.0790	0.4922	19.4929	151.53	0.1274	0.1381	0.03623	0.1743
	2	Contralateral	460.93	1.61	34.94	20.56	0.0697	0.4056	26.9165	285.62	0.1204	0.2513	0.05855	0.3099
	3	Contralateral	411.41	2.55	26.72	31.34	0.0796	0.3868	16.2507	161.09	0.1411	0.1515	0.03969	0.1912
	4	Contralateral	412.70	2.08	34.76	25.19	0.1479	0.4548	29.4286	198.41	0.1463	0.2186	0.07167	0.2903
AAV-VMAT2	1	Ipsilateral	592.88	7.57	39.22	65.53	0.1489	0.7219	1.3681	78.33	0.1767	0.0954	0.00256	0.0979
	2	Ipsilateral	476.61	2.26	46.05	11.11	0.0778	0.3845	38.9105	210.88	0.1199	0.1701	0.08180	0.2519
	3	Ipsilateral	395.54	1.55	32.62	6.81	0.0704	0.3585	25.1814	255.00	0.0997	0.2311	0.06384	0.2950
	4	Ipsilateral	357.83	2.75	50.28	6.64	0.1168	0.7636	53.1939	130.21	0.1591	0.2779	0.14898	0.4269
	1	Contralateral	422.61	5.26	24.39	21.68	0.1108	0.3701	9.0141	80.39	0.1090	0.0704	0.02159	0.0920
	2	Contralateral	399.26	5.20	21.53	14.34	0.1001	0.3426	7.9362	76.75	0.0898	0.0659	0.02013	0.0860
	3	Contralateral	595.07	3.99	41.37	28.92	0.1529	0.4769	15.3601	149.28	0.1181	0.1196	0.02607	0.1457
	4	Contralateral	472.16	3.89	29.91	17.33	0.1382	0.3780	14.2499	121.42	0.1000	0.0972	0.03047	0.1277
AAV-TYR	1	Ipsilateral	15.38	1.16	3.75	5.62	0.1167		13.24	6.0999	0.6099	0.2633	0.04085	0.3042
	2	Ipsilateral	37.95	2.21	8.75	3.41	0.1558	0.5808	1.3947	17.21	0.3203	0.8219	0.42705	1.2489
	3	Ipsilateral	15.95	5.20	6.32		0.1041	4.2739	6.7088	3.07	0.3564	0.1916	0.04320	0.2348
	4	Ipsilateral	24.97	3.21	6.02	2.67	0.1264	0.6159	0.9524	7.77	0.3481	0.1467	0.03034	0.1771
AAV-TYR + AAV-VMAT2	1	Contralateral	355.24	2.80	27.24	16.22	0.0952	0.4106	10.6817	126.94	0.1223	0.1496	0.03034	0.1771
	2	Contralateral	450.39	2.63	27.54	22.97	0.0930	0.3939	21.4395	171.01	0.1122	0.1467	0.04781	0.1974
	3	Contralateral	404.31	3.99	32.67	12.07	0.0877	0.5349	44.0660	101.34	0.1107	0.1341	0.10921	0.2433
	1	Ipsilateral	377.77	2.20	35.17	7.61	0.1980	0.3861	17.2709	171.81	0.1132	0.1756	0.04624	0.2218
	2	Ipsilateral	257.72	3.88	13.67	14.25	0.1382	0.3061	6.8835	66.36	0.1083	0.0788	0.02725	0.1061
	3	Ipsilateral	243.10	4.00	36.56	11.65	0.0945	0.5307	19.8241	60.83	0.1983	0.1328	0.08193	0.2147
	5	Contralateral	264.38	4.69	65.37	4.62	0.0302	0.0244	0.0743	56.42	0.2647	0.0052	0.00040	0.0056
	6	Contralateral	299.40	3.48	70.37	6.49	0.1116	0.0247	0.0327	86.05	0.2567	0.0071	0.00048	0.0076
	7	Contralateral	304.22	6.23	85.78	2.67	0.0721	0.0402	0.2143	48.82	0.2908	0.0064	0.00094	0.0074
	5	Ipsilateral	257.37	2.80	77.45	4.40	0.0881	0.0298	0.0251	92.05	0.3180	0.0107	0.00044	0.0111
	6	Ipsilateral	338.78	8.62	81.63	13.07	0.0968	0.0250	0.0399	39.30	0.2795	0.0029	0.00040	0.0033
	7	Ipsilateral	181.82	4.11	50.71	0.75	0.0439	0.0207	0.1865	44.19	0.2830	0.0050	0.00127	0.0063
	5	Contralateral	292.17	9.12	25.90	2.81	0.0356	0.0395	1.0797	32.05	0.0983	0.0043	0.00382	0.0081
AAV-TYR	6	Contralateral	402.32	2.06	48.98	9.41	0.0440	0.0700	0.0975	195.24	0.1451	0.0340	0.00035	0.0343
	7	Contralateral	459.21	5.04	51.49	8.68	0.0376	0.0904	0.1280	91.06	0.1310	0.0179	0.00036	0.0183
	8	Contralateral	379.16	6.75	46.98	8.12	0.0800	0.0526	0.0570	56.19	0.1463	0.0078	0.00036	0.0082
	5	Ipsilateral	25.40	6.38	10.59	0.97	0.0737	0.0934	0.0493	3.98	0.4550	0.0146	0.00484	0.0195
	6	Ipsilateral	9.26	2.80	10.37	0.28	0.0613	0.1155	0.0418	3.30	1.1507	0.0412	0.01114	0.0523
	7	Ipsilateral	17.01	2.45	11.98	0.45	0.0953	0.1540	0.2781	3.68	1.3795	0.0628	0.04145	0.1042
	8	Ipsilateral	17.40	5.17	13.98	0.64	0.0719	0.1088	0.0717	3.37	0.8403	0.0210	0.00825	0.0293
	4 ^a	Contralateral	266.58	8.96	63.43	5.01	0.0658	0.2321	0.1619	29.75	0.2567	0.0259	0.00085	0.0267
AAV-TYR + AAV-VMAT2	5	Contralateral	311.59	13.48	74.99	8.53	0.0706	0.0703	0.1110	23.12	0.2680	0.0052	0.00035	0.0058
	6	Contralateral	281.95	6.85	80.76	3.93	0.0942	0.2321 ^e	0.1619 ^e	41.18	0.3003	0.0339	0.00091	0.0348
	7	Contralateral	206.18	6.56	34.54	2.58	0.0264	0.3938	0.2127	31.42	0.1800	0.0600	0.00116	0.0612
	4	Ipsilateral	79.62	5.50	47.15	2.47	0.0929	0.1631	0.0567	14.46	0.6232	0.0296	0.00188	0.0315
	5	Ipsilateral	231.70	7.36	86.88	1.93	0.0797	0.0682	0.0673	31.49	0.3833	0.0063	0.00063	0.0099
	6	Ipsilateral	297.96	14.12	92.87	4.13	0.0642	0.0678	0.0999	21.11	0.3255	0.0048	0.00055	0.0054
	7	Ipsilateral	61.20	2.29	34.23	4.79	0.1064	0.0413	0.0384	26.76	0.6377	0.0181	0.00237	0.0204

a contralateral sample lost due to technical problems and values calculated as an average of the group. When ipsilateral sample was lost, the animal was eliminated

Validation of a Reversed Phase UPLC-MS/MS Method to Determine Dopamine Metabolites and Oxidation Intermediates in Neuronal Differentiated SH-SY5Y Cells and Brain Tissue

Marta Gonzalez-Sepulveda, Ariadna Laguna,^{||} Iria Carballo-Carbajal,^{||} Jordi Galiano-Landeira, Jordi Romero-Gimenez, Thais Cuadros, Annabelle Parent, Nuria Peñuelas, Joan Compte, Alba Nicolau, Camille Guillard-Sirieix, Helena Xicoy, Jumpei Kobayashi, and Miquel Vila*

Cite This: *ACS Chem. Neurosci.* 2020, 11, 2679–2687

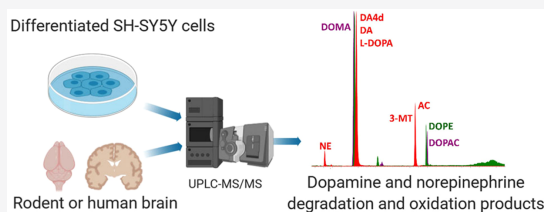
Read Online

ACCESS |

Metrics & More

Article Recommendations

Supporting Information



ABSTRACT: Dopamine is a key neurotransmitter in the pathophysiology of various neurological disorders such as addiction or Parkinson's disease. Disturbances in its metabolism could lead to dopamine accumulation in the cytoplasm and an increased production of *o*-quinones and their derivatives, which have neurotoxic potential and act as precursors in neuromelanin synthesis. Thus, quantification of the dopaminergic metabolism is essential for monitoring changes that may contribute to disease development. Here, we developed and validated an UPLC-MS/MS method to detect and quantify a panel of eight dopaminergic metabolites, including the oxidation product aminochrome. Our method was validated in differentiated SH-SY5Y cells and mouse brain tissue and was then employed in brain samples from humans and rats to ensure method reliability in different matrices. Finally, to prove the biological relevance of our method, we determined metabolic changes in an *in vitro* cellular model of dopamine oxidation/neuromelanin production and in human postmortem samples from Parkinson's disease patients. The current study provides a validated method to simultaneously monitor possible alterations in dopamine degradation and *o*-quinone production pathways that can be applied to *in vitro* and *in vivo* experimental models of neurological disorders and human brain samples.

KEYWORDS: aminochrome, dopamine, brain, SH-SY5Y cells, UPLC-MS/MS, Parkinson

INTRODUCTION

Dopamine (DA) is a key neurotransmitter in the brain that plays an essential role in several functions as the regulation of motivation, reward, spatial memory, and motion, among others.¹ Disturbances of the dopaminergic metabolism or signaling are involved in the pathophysiology of a wide range of diseases from mental disorders, such as addiction,² schizophrenia, or depression,³ to neurodegenerative diseases such as Parkinson's disease.⁴

Metabolism alterations that involve an accumulation of dopamine in the cytoplasm can lead to an enhancement of oxidative stress that could potentially damage several cellular components.⁵ In particular, oxidation of cytosolic DA leads to the production of dopamine *o*-quinone, a transient metabolite that is rapidly transformed in other melanic intermediates.^{4,6} It can react very fast with L-cysteine to produce mainly S-S-

cysteinyldopamine (Cys-DA), which can have neurotoxic effects and lead to the formation of pheomelanin after several steps. On the other hand, the cyclization of dopamine *o*-quinone, which is a slower reaction than the conjugation with L-cysteine, produces aminochrome (AC) as one of the early steps in the process of eumelanin synthesis. Next, 5,6-dihydroxyindole is produced from AC and then 5,6-indolequinone is produced at longer times, establishing AC as the more stable *o*-quinone produced during DA oxidation.⁸

Received: June 3, 2020

Accepted: August 6, 2020

Published: August 6, 2020



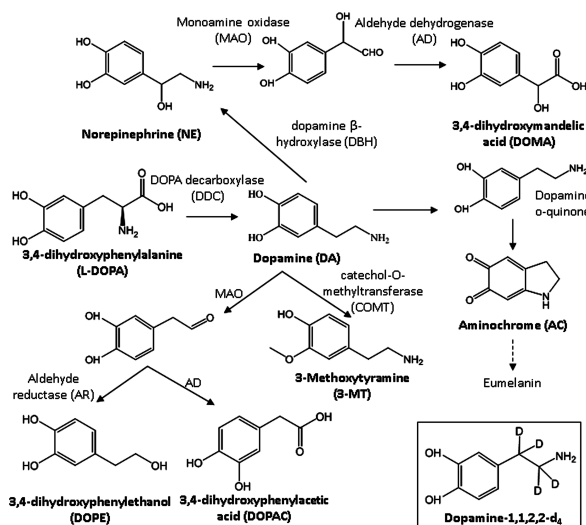


Figure 1. Dopamine and norepinephrine metabolic pathways. Metabolites analyzed in the present study are highlighted with bold characters. The internal standard is also shown (box). Abbreviations for analytes are indicated in parentheses.

and thus allowing its accumulation.⁹ AC accumulation in the cytoplasm can induce several neurotoxic effects⁴ as well as microglia and astrocyte activation.¹⁰ Thus, quantification of Cys-DA and AC levels could be used to monitor DA oxidation linked to neurotoxicity. Several methods can be found in the literature to determine Cys-DA levels in brain tissue.^{11–14} In contrast, AC levels have only been evaluated using HPLC plus electrochemical or photodiode-array detection, either in SH-SY5Y cells,¹⁵ PC-12 cells,¹⁶ or rat plasma samples.^{16,17} Moreover, these studies did not include the concomitant analysis of a wide set of catecholamines. The aim of the present study was to develop and validate a robust and efficient UPLC-MS/MS method to simultaneously detect and quantify AC and other catecholaminergic metabolites, including DA, norepinephrine (NE), 3,4-dihydroxyphenylalanine (L-DOPA), 3,4-dihydroxyphenylacetic acid (DOPAC), 3-methoxytyramine (3MT), 3,4-dihydroxymandelic acid (DOMA), and 3,4-dihydroxyphenylethanol (DOPE) (Figure 1), that could then be used both *in vitro* (i.e., differentiated SH-SY5Y cells) and *in vivo* (i.e., rodent and human brain tissue). Method reliability was also assayed in different brain matrices, including several brain regions of mouse, rat, and human, such as cortex (CTX), striatum (STR), and ventral midbrain (vMB). To our knowledge, this is the first validation report of a simple method to simultaneously measure AC and other catecholaminergic metabolites in differentiated SH-SY5Y cells and rodent or human brains.

Once validated, the method was successfully used to analyze frontal cortex samples from humans and rats. Moreover, we also studied the effects on dopaminergic metabolism of tyrosinase overexpression in differentiated SH-SY5Y cells as an *in vitro* cellular model of dopamine oxidation/neuromelanin production.¹⁸ In view of the biological significance of the

dopaminergic metabolism in many pathological situations and the proven efficacy of our validated method with different matrices, we anticipate this method will be applicable to a wide range of experimental models for neurological disorders.

RESULTS AND DISCUSSION

Method Development. The aim of the present study was to develop and validate a simple and fast method to quantify a panel of closely related catecholaminergic metabolites, including the dopamine oxidation product AC. Some AC features were especially relevant during the development of the sample preparation method. First, it was impossible to efficiently derivatize AC standard with dansyl chloride because it became oxidized producing a black pellet which did not match any of AC published MS/MS transitions.¹⁹ Second, AC has been described to have a poor stability (hours) at 4 or –20 °C.^{16,19} Third, the addition of 1 mM ascorbic acid prevented the AC standard formation and, if added after synthesis, reduced AC signal (*data not shown*); thus, ascorbic acid could not be used to improve sample stability. In fact, ascorbate was described to abolish nitric-oxid-induced dopamine oxidation.²⁰ Fourth, excessive acidification of biological samples can reverse the oxidation process and minimize AC levels.¹⁶ Therefore, sample derivatization was discarded and a simpler approach based on homogenization and both protein and phospholipid precipitation was used. Moreover, homogenization was done with 250 mM formic acid instead of other acids such as perchloric or trichloroacetic acids, commonly used in catecholamine detection, and analyzed in the same day to prevent AC degradation since ascorbic acid was not added. One additional advantage of our extraction procedure is the possibility of using an aliquot of the sample to detect acetylcholine with some

minor adaptations and a different UPLC-MS/MS method²¹ (data not shown).

Chromatographic separation was optimized to obtain an efficient detection of all desired metabolites. Both acetonitrile and methanol were tested as the organic component of the mobile phase in two different chromatographic columns (a Phenomenex Gemini C18 column 3 μm , 150 \times 2 mm and a Waters ACQUITY UPLC HSS T3 1.8 μm 2.1 \times 100 mm) and at two different column temperatures (40 or 65 $^{\circ}\text{C}$). The mobile phase gradient was also adjusted to ensure a proper separation and fast elution of target analytes. Optimal chromatographic performances were obtained with the Waters HSS T3 column at 40 $^{\circ}\text{C}$ and using 100% methanol (solvent A) and 25 mM FA in water (solvent B) as mobile phase at a flow rate of 0.4 mL/min. Under these conditions, the targeted metabolites and the internal standard (IS) were separated within 4 min and the analytical run was completed in 6 min (Figure 2).

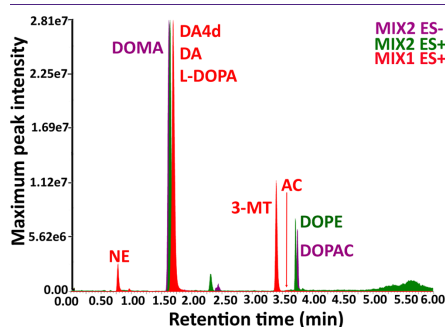


Figure 2. Total-ion chromatograms of 1 μM standards in human brain frontal cortex samples. MIX 1 standards were measured in the positive mode with 0.5 kV of capillary voltage, while MIX 2 standards were measured in both positive and negative modes with 2 kV of capillary voltage. ES mode, retention time, and maximum peak intensity are noted for each MIX.

In order to improve multiple reaction monitoring (MRM) sensitivity, two different capillary voltages (0.5 or 2 kV) were tested. DA, NE, AC, DOPA, and 3MT showed an increased MRM signal with a capillary voltage of 0.5 kV, while DOPAC, DOMA, DOPE, and HVA gave a better result at 2 kV. Target metabolites were then divided into two different MRM methods depending on their capillary voltage, thereby requiring the injection of samples twice in the UPLC-MS/MS system. MRM transitions and cone and collision voltages were individually optimized to ensure a specific and improved signal. AC fragmentation patterns (Figure S-1), and thus the selected transitions, were similar to those of the published MS/MS spectra of aminochromes, particularly that of dopaminochrome.¹⁹

While most compounds were detected in positive electrospray ionization (ES) mode, two of them, DOMA and DOPAC, were only detected in negative mode (Table 1). Operating in both positive and negative modes, with a spliced sample analysis depending on capillary voltage, allowed us to validate DOPAC detection, which could not be done before with a similar method due to sensitivity difficulties.²²

Table 1. MRM Acquisition Settings^a

analyte	transition (m/z)	RT (min)	D (ms)	CV (V)	CE (eV)	CpV (kV)
NE ^b	151.7 > 106.9	0.69	52	15	20	0.5
IS	157.8 > 94.8	1.44	52	10	20	0.5
DA	153.9 > 90.6	1.46	52	10	20	0.5
L-DOPA	198.1 > 152.1	1.48	52	15	15	0.5
3MT ^b	150.7 > 90.9	3.09	52	35	20	0.5
AC	149.6 > 121.9	3.36	52	25	25	0.5
DOMA ^c	182.9 > 136.8	1.62	56	20	14	2
DOPE ^b	137.1 > 91.1	3.69	56	20	20	2
DOPAC ^c	166.9 > 122.8	3.72	56	18	22	2

^aRT, retention time; D, dwell time; CV, cone voltage; CE, collision energy; CpV, capillary voltage. ^bParent mass after loss of water. ^cDetected in negative mode.

Our method was developed to be applied in two different matrices: mouse brain and differentiated SH-SY5Y cells, with some minor adaptations. As the presence of salts in the cell suspension can suppress the MS/MS signal,²³ a final rinse in an appropriate buffer before homogenization with 250 mM FA was mandatory. Both phosphate buffer (PB), PBS, and TBS, were tested (Figure S-2). TBS was selected because it showed an improved AC signal when compared with PB or PBS, facilitating its detection.

Method Validation. Both differentiated SH-SY5Y cells and mouse brain CTX samples were used in order to validate the developed method by analyzing carryover, stability, matrix effect, linearity, sensitivity, accuracy, precision, and recovery. Moreover, method linearity and sensitivity were compared between different mouse brain regions and between mouse, rat, and human CTX samples.

Carryover was absent for all metabolites in both cell and brain samples with most values found under 0.15%. Higher values were found for DOMA or DOPAC (0.3–0.4%, respectively) when analyzing MIX2 in mouse cortex.

Most metabolites showed an adequate stability, except AC. The coefficient of variance (%CV) of AC standard after 7 h in the autosampler was $\geq 20\%$ depending on the studied concentration. Moreover, it could not be efficiently detected after 24 h of storage at 4 $^{\circ}\text{C}$ or -20°C , as stated in the literature.¹⁶ Thus, working mixtures had to be freshly done at the beginning of each experiment, and MIX1 samples had to be injected within a 7 h time period once in the autosampler.

Strong matrix effects were observed in both cell and brain samples for most metabolites with the exception of DOMA in cells and DA and L-DOPA in brain samples (Table 2). Thus, DA cannot be used as a representative of all catecholamine metabolites for matrix effect studies. Suppression was especially important in the case of HVA, which signal was totally abolished making it impossible to be measured in both matrices with this method. As a consequence, HVA validation was abandoned and further validation experiments were conducted with matrix-matched samples spiked with MIX1 or MIX2 standard mixtures.

Six matrix-matched calibration curves were done plotting the corrected response with the spiked concentration for each compound. As shown in Table 3, the linear ranges spanned from 1.72 to 3000 nM and 0.39 to 1000 nM depending on the analyte. Linear weighted (1/x) regression analysis showed mean correlation coefficients (R^2) higher than 0.999 with a variability of residuals smaller than 20%. LOQ values were in

Table 2. Matrix Effects in Differentiated SH-SY5Y Cells and Mouse Brain Cortex^a

differentiated SH-SY5Y cells			mouse brain cortex		
analyte	SC (nM)	ME (%)	analyte	SC (nM)	ME (%)
NE	23.4	26.0	NE	23.4	2.37
	46.9	36.9		46.9	2.2
	93.8	46.3		93.8	2.4
	375	54.0		375	3.7
	1500	57.9		1500	5.4
DA	3000	60.2	DA	3000	6.2
	23.4	61.1		23.4	93.7
	46.9	67.1		46.9	64.2
	93.8	60.8		93.8	100.3
L-DOPA	375	59.5	L-DOPA	375	100.2
	1500	62.8		1500	127.3
	3000	65.4		3000	127.5
	23.44	7.9		7.81	63.0
	46.88	12.6		15.625	84.1
3MT	93.75	18.0	3MT	31.25	68.2
	375	34.9		125	79.3
	1500	45.1		500	88.3
	3000	48.1		1000	100.1
	7.8	2.0		7.8	12.0
AC	15.6	11.2	AC	15.6	4.9
	31.3	24.9		31.3	35.7
	125	48.9		125	65.5
	500	79.3		500	153.7
	1000	93.5		1000	168.5
DOMA	23.4	9.7	DOMA	7.8	33.8
	46.9	7.0		15.6	27.1
	93.8	7.5		31.3	38.0
	375	5.4		125	29.1
	1500	7.7		500	36.7
DOPE	3000	4.8	DOPE	1000	35.2
	23.4	71.3		7.8	40.7
	46.9	100.3		15.6	62.2
	93.8	97.9		31.3	71.6
	375	113.4		125	83.4
DOPAC	1500	119.4	DOPAC	500	85.9
	3000	126.0		1000	87.8
	23.4	37.0		7.8	-1.9
	46.9	52.4		15.6	-1.7
	93.8	56.5		31.3	20.8
DOPA	375	52.7	DOPA	125	29.2
	1500	54.1		500	56.8
	3000	47.4		1000	86.1
	23.4	35.2		7.8	32.0
	46.9	37.0		15.6	31.2
DOPA	93.8	31.9	DOPA	31.3	25.5
	375	32.9		125	28.7
	1500	34.2		500	28.2
	3000	30.6		1000	32.3

^aSC, spiked concentration; ME, matrix effect.

the range of 1.97–10.46 nM in differentiated SH-SY5Y cells and between 1.40 and 8.36 nM in mouse brain cortex. When compared with other UPLC-MS/MS methods in the literature, our DA LOQ values were higher than those with calibrators diluted in FA^{22,24} but similar to LOQs obtained with matrix-matched calibrators.²⁵ In contrast, our method showed an improved sensitivity for DOPAC and NE detection in brain samples.^{22,25} As far as we know, no LOD or LOQ values of

HPLC-MS/MS methods were reported for DOMA, DOPE, or AC using cell or brain samples. Nevertheless, we obtained: lower LOQs for DOMA and other metabolites when compared with rat urine samples;²⁶ a DOPE LOQ value in the same range as that found in derivatized plasma samples,²⁷ and a LOD value for AC similar to a previously reported value for adrenochrome in plasma samples.¹⁷ The method here developed appeared to be sensitive enough to detect and quantify all target metabolites in both matrices. Finally, intraday and interday accuracy, precision, and recovery were analyzed in three independent experiments, each with four different concentration levels, in both differentiated SH-SY5Y cells and mouse brain cortex. As shown in Table 4, the present method displayed a good precision with all analytes showing % CV ≤ 20%, except for the intraday value of the smallest concentration of 3MT in brain samples that had a value of 20.72%.

Moreover, good accuracy (%RE ≤ 20%) and recovery (in the range 80–120%) results were obtained for all interday and intraday metabolite concentrations in both matrices. Taken together, validation results indicate that our method is reliable to analyze DA, NE, and six of their main metabolites in real cell or brain samples. Moreover, while using the appropriate matrix-matched calibrators, the developed method is sensitive enough to be used with cultured cells and both rodent and human brain samples.

Application to Rodent and Human Cortex Samples.

In order to ensure method reliability in different matrices, linearity and sensitivity were compared in rodent and human brain CTX, STR and vMB in a single assay with one matrix-matched calibration replicate. Results are listed in Table S-2. Linear weighted (1/x) regression showed $R^2 \geq 0.999$ in all cases. Similar slopes between matrices could be observed in the equations of most metabolites although L-DOPA and 3MT displayed a greater variability. Moreover, there was also a great variability in the Y-intercept value of all metabolites and matrices, which indicated a differential endogenous metabolite concentration between regions or species, as expected. In spite of variability, LOQ values remained in a quantitative range allowing the application of the present method to different brain samples providing that the specific matrix is used to obtain the calibration curve and to calculate specific LOD and LOQs.

CTX samples from eight rats (6 months of age) were successfully analyzed with our method, which was sensitive enough to detect most metabolites, including low concentrations of AC (Table 5). CTX samples from 6 idiopathic Parkinson's disease patients (PD) and 10 age-matched control (Ctrl) individuals (mean age at death: 78 ± 10.4 years) were also studied to confirm the suitability of our method to evaluate metabolic alterations in brain samples from diseased patients. In PD patients, an enhanced cortical NE degradation was inferred from the decreased NE levels, the increased DOMA levels, and the increasing tendency of the DOMA:NE ratio (Ctrl 100 ± 33.3 $n = 7$ vs PD 342.7 ± 59.6 $n = 2$; % of Ctrl \pm SEM, nonsignificant, $p = 0.11$, Mann-Whitney test). An enhanced DA degradation was also revealed in PD samples by the (3MT + DOPAC + DOPE):DA ratio (Ctrl 100 ± 15.7 $n = 10$ vs PD 200 ± 22.3 $n = 6$; % of Ctrl \pm SEM; $p < 0.005$, Mann-Whitney test) and the increased 3MT and DOPE levels. Although no differences in relative activities of COMT and MAO were observed between Ctrl and PD samples (calculated by the 3MT:(DOPAC + DOPE) ratio), a shift

Table 3. Sensitivity and Linear Range in Differentiated SH-SY5Y Cells and Mouse Brain Cortex^a

analyte	differentiated SH-SY5Y cells				mouse brain cortex			
	LOD (nM)	LOQ (nM)	linear range (nM)	R ²	LOD (nM)	LOQ (nM)	linear range (nM)	R ²
NE	2.04	6.79	1.72–3000	0.9997	1.32	4.39	1.72–3000	0.9998
DA	1.27	4.25	1.72–3000	0.9999	1.43	4.76	1.72–3000	0.9998
L-DOPA	2.06	6.86	1.72–3000	0.9996	0.50	1.67	0.39–1000	0.9998
3MT	0.59	1.97	0.39–1000	0.9996	0.42	1.40	0.39–1000	0.9998
AC	3.14	10.46	0.39–1000	0.9993	0.71	2.36	0.39–1000	0.9996
DOMA	2.58	8.59	1.72–3000	0.9995	2.48	8.27	1.72–3000	0.9996
DOPE	2.53	8.42	1.72–3000	0.9996	1.97	6.55	1.72–3000	0.9997
DOPAC	1.95	6.50	1.72–3001	0.9997	2.24	3.15	1.72–3000	0.9997

^aResults show the mean of six calibration curve replicates.Table 4. Intraday and Interday Precision, Accuracy, and Recovery in Differentiated SH-SY5Y Cells and Mouse Brain Cortex^a

analyte	differentiated SH-SY5Y cells							mouse brain cortex						
	spiked concn (nM)	intraday			interday			spiked concn (nM)	intraday			interday		
		Acc (RE %)	Prec (CV %)	Rec (%)	Acc (RE %)	Prec (CV %)	Rec (%)		Acc (RE %)	Prec (CV %)	Rec (%)	Acc (RE %)	Prec (CV %)	Rec (%)
NE	46.9	-6.6	2.9	86.7	-13.3	16.3	83.8	46.9	0.8	16.4	100.8	-12.6	15.7	87.4
	93.8	-15.1	14.9	82.3	-12.3	11.8	85.0	93.8	2.2	15.0	99.1	-3.2	18.0	93.8
	375	-11.1	11.4	88.9	-9.6	8.8	90.4	375	1.2	7.9	101.2	-0.2	13.3	99.8
	3000	0.7	1.7	100.7	2.5	3.0	102.5	3000	7.4	10.3	107.4	3.0	13.7	102.8
DA	46.9	-4.3	11.2	87.6	1.6	18.9	101.6	46.9	-3.5	5.1	96.5	-3.9	12.0	96.1
	93.8	-16.1	14.2	81.3	-16.0	18.0	89.5	93.8	4.7	3.7	101.4	1.5	12.2	98.4
	375	-12.5	6.8	87.5	-11.8	9.2	88.2	375	1.8	4.0	101.8	3.5	7.2	103.5
	3000	12.5	4.9	112.5	6.6	5.5	106.6	3000	-4.8	4.0	95.3	-3.2	3.9	96.9
L-DOPA	46.9	2.8	6.7	102.8	0.0	19.2	100.0	15.6	-15.8	13.9	93.9	-14.2	17.1	80.8
	93.8	10.3	8.3	106.9	-2.2	15.3	94.8	31.3	-6.4	18.0	93.7	9.3	14.1	109.3
	375	3.5	4.4	103.5	3.3	10.3	103.3	125	13.9	15.4	113.9	13.2	12.2	113.2
	3000	-9.0	2.9	91.0	-17.5	19.6	80.1	1000	-4.4	12.9	95.6	-11.5	13.4	88.5
3MT	15.6	-10.1	5.7	89.9	-13.7	18.4	86.3	15.6	-10.7	20.7	81.4	-14.8	19.2	103.5
	31.3	-13.3	8.5	86.7	-15.0	15.5	85.0	31.3	-2.4	5.8	86.9	-14.8	14.1	90.0
	125	-10.4	9.5	89.6	-15.0	10.5	85.0	125	-9.7	8.3	87.4	-10.4	11.9	91.7
	1000	5.6	5.4	105.6	5.3	6.2	105.3	1000	-0.2	6.9	99.8	-2.5	5.9	96.6
AC	46.9	4.4	18.0	87.0	-0.5	18.7	93.3	15.6	4.8	16.1	104.8	-19.1	19.0	80.9
	93.8	-7.6	6.2	106.3	-5.5	16.8	91.6	31.3	12.6	10.9	112.6	14.5	17.7	114.5
	375	-0.9	10.9	99.1	-3.7	15.0	96.3	125	12.1	14.5	112.1	13.1	15.2	118.9
	3000	-18.7	15.2	81.3	-13.7	18.9	83.0	1000	0.2	13.7	95.0	8.4	15.8	108.4
DOMA	46.9	-5.9	9.9	94.2	5.0	14.2	105.0	46.9	-9.6	4.3	82.5	-8.1	13.4	87.1
	93.8	-0.8	8.5	96.2	-4.2	9.9	92.8	93.8	12.7	17.5	109.2	0.4	14.2	103.2
	375	-1.2	3.4	98.8	-2.7	8.9	91.9	375	2.2	14.5	102.2	-6.4	16.9	90.1
	3000	0.2	2.2	100.2	0.7	4.9	100.7	3000	-7.8	8.3	92.2	-6.4	7.7	93.6
DOPE	46.9	1.1	14.3	101.1	2.2	13.7	111.9	46.9	0.6	8.2	100.6	-9.8	10.2	90.2
	93.8	-1.3	10.5	95.7	-8.4	13.7	88.8	93.8	-5.8	9.0	91.3	-2.0	7.6	94.9
	375	-0.1	8.9	99.9	2.3	11.4	102.3	375	-3.6	7.3	96.4	-4.8	9.3	95.2
	3000	1.6	8.0	101.6	0.6	9.2	100.6	3000	0.3	5.4	100.3	-2.2	10.7	97.8
DOPAC	46.9	10.2	11.8	110.2	3.2	12.2	103.2	46.9	-12.8	9.4	87.2	-15.1	13.8	84.9
	93.8	-1.0	4.8	112.8	-2.8	17.0	94.2	93.8	-7.0	13.8	90.1	-4.9	13.5	92.1
	375	-1.0	8.3	99.0	-1.8	10.3	98.2	375	-5.5	7.4	94.5	-1.2	16.7	86.0
	3000	3.1	5.7	103.1	-4.1	8.6	95.9	3000	-0.8	5.0	99.2	-0.8	6.9	99.2

^aAcc, accuracy; Prec, precision; Rec, recovery.

from AD to AR as the main cytosolic DOPAL detoxification mechanism was suggested in PD by the increased DOPE levels, an increased DOPE production (DOPE:DA ratio, Ctrl 100 ± 16.6 *n* = 10 vs PD 204.9 ± 24.5 *n* = 6; % of Ctrl ± SEM; *p* < 0.005, Mann–Whitney test), a decreasing tendency in DOPAC levels and DOPAC production and a decreasing tendency of the DOPAC: DOPE ratio (Ctrl 100 ± 25.9 *n* = 5 vs PD 13.6 ± 1.4 *n* = 2; % of Ctrl ± SEM, nonsignificant, *p* = 0.09, Mann–

Whitney test). This enhancement of AR activity was previously reported in PD putamen samples.²⁸ Finally, PD samples exhibited increased DA oxidation, as indicated by increased AC levels and an enhanced AC production (AC:DA ratio; Ctrl 100 ± 11.4 *n* = 10 vs PD 152.0 ± 15.6 *n* = 6; % of Ctrl ± SEM; *p* < 0.005, Mann–Whitney test). Overall, these results corroborate that our method can efficiently detect alterations in DA oxidation and metabolism in diseased brain samples.

Table 5. Mean Concentration (pmol/mg Protein \pm SEM) of Catecholaminergic Metabolites Found in Brain Cortex^a

analyte	rat ($N_{x,y,z}$) ^b	human	
		ctrl ($N_{x,y,z}$) ^b	PD ($N_{x,y,z}$) ^b
NE	28.1 \pm 2.6 (8, ^{0,0,0})	0.5 \pm 0.1 (7, ^{3,2,0})	0.2 \pm 0.01 (2, ^{4,2,0}) ^c
DOMA	<LOD	1.0 \pm 0.2 (10, ^{0,2,0})	1.7 \pm 0.3 (6, ^{0,0,0}) ^c
L-DOPA	2.7 \pm 0.3 (7, ^{0,0,1})	2.2 \pm 0.4 (10, ^{0,2,0})	2.7 \pm 0.6 (5, ^{0,1,1})
DA	1.7 \pm 0.3 (8, ^{0,0,0})	0.6 \pm 0.05 (9, ^{0,0,1})	0.6 \pm 0.04 (5, ^{0,3,1}) ^c
3MT	1.0 \pm 0.2 (7, ^{1,1,0})	1.4 \pm 0.1 (10, ^{0,0,0})	2.9 \pm 0.3 (5, ^{0,0,1}) ^c
DOPE	39.3 \pm 1.8 (8, ^{0,0,0})	28.5 \pm 4.7 (10, ^{0,0,0})	62.3 \pm 9.2 (6, ^{0,0,0}) ^c
DOPAC	1.8 \pm 0 (1, ^{7,0,0})	2.5 \pm 0.3 (5, ^{5,0,0})	1.1 \pm 0.3 (2, ^{4,0,0})
AC	0.3 \pm 0 (1, ^{7,0,0})	0.2 \pm 0.01 (10, ^{0,0,0})	0.5 \pm 0.1 (6, ^{0,0,0}) ^c

^a N , number of samples analyzed. ^bSuperscript numbers x,y,z are as follows: x , number of values that are < LOD not included to calculate mean concentration; y , number of values that are between LOD and LOQ; z , number of values that are a statistical outlier, not included to calculate mean concentration. ^c $p \leq 0.05$ vs human control (Mann–Whitney test).

Table 6. Mean Concentration (pmol/mg Protein \pm SEM) of Catecholaminergic Metabolites Found in Differentiated TR5TY6 Cells^a

analyte	OFF ($N_{x,y}$) ^b	ON 1 day ($N_{x,y}$) ^b	ON 3 days ($N_{x,y}$) ^b
NE	9.9 \pm 2.4 (3, ^{0,3})	17.8 \pm 6.4 (3, ^{0,3})	9.3 \pm 0.1 (3, ^{0,3})
DOMA	2.5 \pm 0 (1, ^{2,1})	4.6 \pm 1.7 (3, ^{0,3})	6.5 \pm 2.7 (3, ^{0,2})
L-DOPA	9.4 \pm 1.6 (3, ^{0,1})	134 \pm 20.8 (3, ^{0,0})	270.1 \pm 39.7 (3, ^{0,0}) ^c
DA	99.6 \pm 5.9 (3, ^{0,0})	353 \pm 91.4 (3, ^{0,0})	879 \pm 195.6 (3, ^{0,0}) ^c
3MT	146 \pm 56.2 (3, ^{0,0})	373.5 \pm 205.9 (3, ^{0,0})	5896 \pm 1432 (3, ^{0,0}) ^c
DOPE	43.8 \pm 2.5 (3, ^{0,0})	30.3 \pm 8.9 (3, ^{0,1})	23 \pm 4.4 (3, ^{0,0})
DOPAC	49.6 \pm 22.9 (3, ^{0,0})	104.9 \pm 12.3 (3, ^{0,0})	209.5 \pm 44 (3, ^{0,0}) ^c
AC	<LOD	<LOD	27.1 \pm 8 (3, ^{0,0})

^a N , number of samples analyzed. ^bSuperscript numbers x,y are as follows: x , number of values that are < LOD; not included to calculate mean concentration; y , number of values that are between LOD and LOQ. ^c $p \leq 0.05$ vs OFF (Kruskal–Wallis plus Dunn's test).

Application to a Cellular Model of DA Oxidation/Neuromelanin Production.

To confirm the suitability of our method to detect changes in the levels of catecholaminergic metabolites in *in vitro* disease models, differentiated TR5TY6 cells were induced to express human tyrosinase for 1 or 3 days (i.e., ON) and subsequently analyzed (Table 6). Tyrosinase, which is a key enzyme in melanin biosynthesis via the production of L-DOPA and subsequent molecules,²⁹ can potentially accelerate the induction of catecholamine quinone derivatives by its oxidase activity, resulting in increased intracellular levels of DA and oxidized DA and the formation of melanin pigments in neuronal somata of these cells.^{18,30} In agreement with this, we were able to detect progressive changes in the formation of neuromelanin-precursor AC and an enhanced dopaminergic metabolism, revealed by increased levels of L-DOPA, DA, 3MT, and DOPAC and an increased dopamine degradation 3 days after induction, as indicated by the (3MT + DOPAC + DOPE):DA ratio (OFF 100 \pm 15.1 n = 3; 1 day 55.5 \pm 9.7 n = 3; 3 days 293.3 \pm 7.7* n = 3; % of OFF \pm SEM, * p < 0.05, Kruskal–Wallis plus Dunn's test). In addition, a shift from MAO to COMT as the main DA degradation pathway was indicated at this time-point by an increased 3MT:(DOPAC + DOPE) ratio (OFF 100 \pm 53 n = 3; 1 day 161.4 \pm 102.3 n = 2; 3 days 1341 \pm 71.3 n = 3; % of OFF \pm SEM, p < 0.05 3 days vs OFF, Kruskal–Wallis plus Dunn's test). Taken together, these results confirm that our method can be efficiently used to detect alterations of the dopamine metabolism in both *in vitro* and *in vivo* disease models and samples.

CONCLUSIONS

The present study demonstrates the development of the currently validated method to provide a simple and fast way to simultaneously monitor possible alterations in metabolite levels from cytosolic DA degradation and *o*-quinone production pathways. Thus, we anticipate our method will facilitate the in-depth assessment of the neurochemical changes linked to alterations of the dopaminergic system. Moreover, our method proved to be efficient with different matrices ranging from *in vitro* cellular models to post-mortem rodent and human brain samples, allowing its implementation into a wide range of neurological disorders.

METHODS

Experimental Models and Subject Details. *Animals.* Adult male C57BL/6J mice and adult male Sprague–Dawley rats (Charles River) were housed five or three per cage, respectively, with *ad libitum* access to food and water during a 12 h light/dark cycle. Procedures were conducted in accordance with guidelines established by the Ethical Committee for the use of Laboratory Animals in Spain (53/2013) and the European Ethical Committee (2010/63/EU) and approved by the Vall d'Hebron Research Institute (VHIR) Ethical Experimentation Committee. Animals were euthanized by decapitation, brains were removed, and different brain regions (CTX, STR and vMB) were dissected from each hemisphere. Dissected samples were immediately frozen in dry ice and stored at -80 °C until the day of analysis.

Cell Culture. A stable inducible SH-SY5Y cell line expressing human tyrosinase (TR5TY6) under the transcriptional control of the T-Rex TM Tet-On system (Invitrogen) was provided by Dr. T. Hasegawa (Department of Neurology, Tohoku University, Sendai, Japan). Cells were confirmed negative for mycoplasma contamination by routine PCR analysis. Cells were maintained in low-glucose (1 g/L) Dulbecco's modified Eagle's (Gibco) medium with penicillin/

streptomycin and the appropriate selection of antibiotics (7 $\mu\text{g}/\text{mL}$ blastidicin and 300 $\mu\text{g}/\text{mL}$ Zeocin, both from Life Technologies). At 24 h after seeding, cells were differentiated with 10 μM retinoic acid (Sigma-Aldrich) for 3 days, followed by 80 nM 12-*O*-tetradecanoylphorbol-13-acetate (Sigma-Aldrich) for 3 extra days prior to hTyr induction with 2 $\mu\text{g}/\text{mL}$ doxycycline (Sigma-Aldrich) for up to 6 days. Cells not treated with doxycycline were considered as OFF for comparison with induced cells (i.e., ON) and as differentiated SH-SY5Y cells for the establishment of the method. Cells were harvested with medium using a cell scraper, centrifuged for 5 min at 300g at 4 $^{\circ}\text{C}$, and washed three times with phosphate buffer saline (PBS). Cell pellets were stored at -80°C until the day of analysis.

Human Postmortem Brain Tissue. Fresh-frozen frontal cortex samples from idiopathic PD patients ($n = 6$) and age-matched control individuals ($n = 10$) were provided by the Neurological Tissue BioBank at IDIBAPS-Hospital Clinic (Barcelona). Detailed information about the subjects included in this study is provided in Table S-1. All procedures were conducted in accordance with guidelines established by the BPC (CPMP/ICH/135/95) and the Spanish regulation (223/2004) and approved by the Vall d'Hebron Research Institute (VHIR) Ethical Clinical Investigation Committee [PR(AG)-370/2014].

Chemicals. Ammonium acetate was purchased from Applichem (Germany). LC-MS grade methanol and MS grade formic acid (FA) were purchased from Fisher (UK). Potassium periodate was purchased from Acros Organics (USA). DA hydrochloride, NE HCl, DOPA, 3MT HCl, DOPAC, DOMA and the internal standard DA-*d*₄ HCl were purchased from Sigma-Aldrich. DOPE was obtained from Tokyo Chemical Industry (Japan).

Metabolite standards, except aminochrome, were directly diluted in 25 mM FA. AC solution (0.5 mM) was freshly prepared as described by Lemos-Amado et al.¹⁹ In brief, equal volumes of 1 mM DA dissolved in water and 2 mM KIO₄ dissolved in 100 μM aqueous ammonium acetate buffer (pH 5.8) were mixed at RT with vigorous shaking for 1 min. Successive dilutions were made in 25 mM formic acid.

Calibration Curves and Quality Control (QC) Sample Preparation. A stock solution of the IS was prepared in 25 mM FA and stored at -80°C . Solutions of each metabolite were freshly prepared and used to make two mixtures: MIX1 (DA, L-DOPA, NE, 3MT, AC) and MIX2 (DOMA, DOPE, DOPAC). Mixtures were then serially diluted with 25 mM FA to obtain the concentration series used in calibration curves. Finally, IS was added to both mixtures to achieve a final concentration of 500 nM in working mixtures.

To prepare calibration curves and QC samples, brain tissue samples from six different animals or differentiated TRSTY6 OFF cell pellets from three independent cell culture dishes (150 mm) were pooled and homogenized in 8 mL of 250 mM FA. The sample was then distributed into 120 μL aliquots prior to the addition of 40 μM of the appropriate working mixture (MIX1 or MIX2). Samples were then centrifuged, and 120 μL of the supernatant plus the same amount of 25 mM FA were transferred to an Ostro protein precipitation and phospholipid removal plate (Waters, USA) and filtered. Finally, 7 μL were injected in the UPLC-MS/MS system.

For brain samples, calibration levels cover a range of 1.72–3000 nM for DA, NE, and MIX2 and 0.39–1000 nM for L-DOPA, 3MT, and AC. For cell samples, calibration levels cover a range of 1.72–3000 nM for both MIX1 and MIX2 with the exception of 3MT for which 0.39–1000 nM is used. Four different QC samples were chosen, covering low to high metabolite concentrations.

Sample Preparation. The day of analysis, frozen brain samples were homogenized with an appropriate amount of 250 mM FA (1 mL/hemisphere for CTX; 300 μL /hemisphere for STR and vMB). An aliquot was removed for protein determination by the BCA method prior the addition of IS (500 nM) and then centrifuged at 20 000g for 10 min at 4 $^{\circ}\text{C}$. The supernatant was then filtered with the Ostro plate. Finally, 7 μL was injected in the UPLC-MS/MS system twice to analyze MIX1 and MIX2.

Tyrosinase-induced (ON) and OFF TRSTY6 cell pellets from nine independent cell culture dishes (100 mm) were rinsed with 300 μL of 50 mM PH 7.4 Tris buffered saline (TBS) and centrifuged for 5 min at 400 g at 4 $^{\circ}\text{C}$ before pellet homogenization with 300 μL of 250 mM FA. The following procedures were the same as for brain samples.

UPLC-MS/MS Analysis. A Waters Acquity UPLC system was coupled with a Xevo TQ-S triple quadrupole mass spectrometer with electrospray ionization interface (Waters). Instrument control, data acquisition, and analysis were performed using MassLynx V4.1 (Waters). The chromatographic separation of both brain and cell samples was performed on a Waters Acquity HSS T3 (1.8 μm ; 2.1 \times 100 mm) column coupled to an Acquity HSS T3 VanGuard (100 Å , 1.8 μm , 2.1 mm \times 5 mm). The column temperature was set at 40 $^{\circ}\text{C}$, and samples were maintained at 6 $^{\circ}\text{C}$ in the thermostatic autosampler. The mobile phase consisted of solvent A (methanol 100%) and solvent B (25 mM FA in water) at a flow of 0.4 mL/min with the following gradient profile: 0.5% B maintained for 0.5 min, 8% B at 2.6 min, 55% B at 2.9 min, 60% B at 3.3 min, 80% B at 4.3 min, 90% B at 4.4 min and maintained for 0.5 min, 0.5% B at 5 min followed by 1 min of equilibration.

The mass spectrometer detector operated under the following parameters: source temperature 150 $^{\circ}\text{C}$, desolvation temperature 450 $^{\circ}\text{C}$, cone gas flow 50 L/h, desolvation gas flow 1100 L/h, and collision gas flow 0.15 mL/min. Argon was used as the collision gas. The capillary voltage was set at 0.5 kV for MIX1 and at 2 kV for MIX2 detection. The electrospray ionization source was operated in both positive and negative modes, depending on the analyte. Multiple reaction monitoring acquisition settings for the targeted metabolites are summarized in Table 1.

Validation Study. Method validation includes the analysis of matrix effect, carryover, linearity, sensitivity, accuracy, precision, recovery, and stability both in differentiated SH-SY5Y cells and mouse CTX samples. As endogenous neurotransmitters and metabolites can be found in both samples, the peak-area ratio between the analyte and the IS obtained of a blank sample was subtracted from that of the spiked samples to obtain the corrected response. Carryover was analyzed by preparing standard mixtures with a concentration of each analyte twice the highest concentration used in standard curves and evaluating the chromatograms of two blank samples run consecutively after it. Carryover exists when blank samples have an area bigger than 1% of the area of the corresponding peak in the mixture.

Stability was evaluated with the %CV of two determinations done at different storage conditions: after 7 h in the autosampler (6 $^{\circ}\text{C}$) or after 24 h in the freezer. Standards are considered stable when the % CV is smaller than 20%.

The matrix effect (ME) was evaluated as in Matuszewski et al.³¹ with slight modifications. Briefly, ME was calculated as the ratio of the corrected peak area (result of subtracting the endogenous area of the blank sample from the measured sample) of an analyte spiked after extraction in brain or cell samples to the peak area of the same analyte spiked in FA multiplied by 100. A value higher than 100% indicates ion enhancement, and a value smaller than 100% indicates ion suppression. ME values in the range of 80–120% were considered acceptable. Due to the existence of a strong ME, validation was analyzed in matrix-matched calibration curves.

To analyze linearity and sensitivity, two replicates of three independent calibration curves were injected in the UPLC-MS/MS system. Six weighted (1/ x) linear regression curves excluding the origin were constructed for each analyte by plotting the corrected response with the spiked concentration. Linearity was considered acceptable if $R^2 \geq 0.99$ and more than 75% of the residuals had a variability smaller than 20%. With respect to sensitivity, the limit of detection (LOD) was defined as the concentration level with the signal-to-noise ratio at 3, and the limit of quantification (LOQ) was defined as the concentration level with the signal-to-noise ratio at 10. They were calculated as 3 or 10 times the ratio between the standard deviation of the Y-intercept value and the slope of each calibration curve, respectively. Results are shown as the mean of six calibration curves.

Both intraday and interday accuracy, precision, and recovery were validated. During each of the three independent experiments, six calibration curves and six QC samples at each of the four concentration levels were analyzed. Accuracy was determined as the relative error (RE) between the blank-subtracted concentration and the spiked concentration. Precision was expressed as the coefficient of variance of the determinations. Recovery was calculated as the percentage of the ratio between the blank-subtracted concentration and the spiked concentration. Accuracy, precision, and recovery were considered acceptable if the percent of change is smaller than 20%.

Statistical Analysis. Concentration values (nM) obtained during analysis of cell and tissue samples were corrected by total sample volume and protein content to obtain a final result in picomoles per milligram of protein. Results lower than the LOD were excluded from analysis. Data were analyzed for statistical significance using GraphPad Prism software (ver. 6) (GraphPad Software Inc., USA) using the appropriate statistical tests, as indicated in figure legends. Differences were considered significant if the probability of error was less than 5%.

■ ASSOCIATED CONTENT

Supporting Information

The Supporting Information is available free of charge at <https://pubs.acs.org/doi/10.1021/acscchemneuro.0c00336>.

Human sample information; linearity and sensitivity comparison between mice, rat and human brain regions; ESI-MS/MS fragmentation pattern of AC; signal suppression effects of PB, PBS, and TBS on MIX1 standards (PDF)

■ AUTHOR INFORMATION

Corresponding Author

Miquel Vila – Neurodegenerative Diseases Research Group, Vall d'Hebron Research Institute (VHIR)-Center for Networked Biomedical Research on Neurodegenerative Diseases (CIBERNED), 08035 Barcelona, Spain; Department of Biochemistry and Molecular Biology, Autonomous University of Barcelona, 08193 Barcelona, Spain; Catalan Institution for Research and Advanced Studies (ICREA), 08010 Barcelona, Spain; orcid.org/0000-0002-1352-989X; Email: miquel.vila@vhir.org

Authors

Marta Gonzalez-Sepulveda – Neurodegenerative Diseases Research Group, Vall d'Hebron Research Institute (VHIR)-Center for Networked Biomedical Research on Neurodegenerative Diseases (CIBERNED), 08035 Barcelona, Spain
Ariadna Laguna – Neurodegenerative Diseases Research Group, Vall d'Hebron Research Institute (VHIR)-Center for Networked Biomedical Research on Neurodegenerative Diseases (CIBERNED), 08035 Barcelona, Spain
Iria Carballo-Carbajal – Neurodegenerative Diseases Research Group, Vall d'Hebron Research Institute (VHIR)-Center for Networked Biomedical Research on Neurodegenerative Diseases (CIBERNED), 08035 Barcelona, Spain
Jordi Galiano-Landeira – Neurodegenerative Diseases Research Group, Vall d'Hebron Research Institute (VHIR)-Center for Networked Biomedical Research on Neurodegenerative Diseases (CIBERNED), 08035 Barcelona, Spain
Jordi Romero-Gimenez – Neurodegenerative Diseases Research Group, Vall d'Hebron Research Institute (VHIR)-Center for Networked Biomedical Research on Neurodegenerative Diseases (CIBERNED), 08035 Barcelona, Spain

Thais Cuadros – Neurodegenerative Diseases Research Group, Vall d'Hebron Research Institute (VHIR)-Center for Networked Biomedical Research on Neurodegenerative Diseases (CIBERNED), 08035 Barcelona, Spain

Annabelle Parent – Neurodegenerative Diseases Research Group, Vall d'Hebron Research Institute (VHIR)-Center for Networked Biomedical Research on Neurodegenerative Diseases (CIBERNED), 08035 Barcelona, Spain

Nuria Peñuelas – Neurodegenerative Diseases Research Group, Vall d'Hebron Research Institute (VHIR)-Center for Networked Biomedical Research on Neurodegenerative Diseases (CIBERNED), 08035 Barcelona, Spain

Joan Compte – Neurodegenerative Diseases Research Group, Vall d'Hebron Research Institute (VHIR)-Center for Networked Biomedical Research on Neurodegenerative Diseases (CIBERNED), 08035 Barcelona, Spain

Alba Nicolau – Neurodegenerative Diseases Research Group, Vall d'Hebron Research Institute (VHIR)-Center for Networked Biomedical Research on Neurodegenerative Diseases (CIBERNED), 08035 Barcelona, Spain

Camille Guillard-Sirieix – Neurodegenerative Diseases Research Group, Vall d'Hebron Research Institute (VHIR)-Center for Networked Biomedical Research on Neurodegenerative Diseases (CIBERNED), 08035 Barcelona, Spain

Helena Xicoy – Neurodegenerative Diseases Research Group, Vall d'Hebron Research Institute (VHIR)-Center for Networked Biomedical Research on Neurodegenerative Diseases (CIBERNED), 08035 Barcelona, Spain

Jumpei Kobayashi – Neurodegenerative Diseases Research Group, Vall d'Hebron Research Institute (VHIR)-Center for Networked Biomedical Research on Neurodegenerative Diseases (CIBERNED), 08035 Barcelona, Spain

Complete contact information is available at:

<https://pubs.acs.org/doi/10.1021/acscchemneuro.0c00336>

Author Contributions

[¶]A.L. and I.C.-C. contributed equally. All authors have given approval to the final version of the manuscript.

Notes

The authors declare no competing financial interest.

■ ACKNOWLEDGMENTS

TOC graphic made in BioRender - biorender.com. This work was supported by funds from the Ministry of Economy and Competitiveness (MINECO, Spain) (SAF2016-77541-R and RTC-2014-2812-1, to M.V.), The Michael J. Fox Foundation (USA) (ID15291, to M.V.), La Caixa Banking Foundation (Health Research Project HR17-00513, to M.V.) and CIBERNED (to M.V.). In addition, the authors would like to acknowledge additional support from the Fundación Tatiana Pérez de Guzmán el Bueno (Spain, to A.L.). N.P. is the recipient of a predoctoral fellowship FPI (BES-2017-080191) from MINECO (Spain). A.L. was the recipient of a postdoctoral contract SAF2015-73997-JIN from MINECO (Spain) with cofunding from FEDER (E.U.) and is currently funded by the Junior Leader Program from La Caixa Banking Foundation (Grant LCF/BQ/PR19/11700005). The project that gave rise to these results received the support of a fellowship from "la Caixa" Foundation (ID100010434). The fellowship code of J.C. is (LCF/BQ/DI18/11660063). J.G. holds a PhD grant from the Fundación Tatiana Pérez de Guzmán el Bueno (Becas predoctorales en Neurociencias).

REFERENCES

- (1) Klein, M. O., Battagello, D. S., Cardoso, A. R., Hauser, D. N., Bittencourt, J. C., and Correa, R. G. (2019) Dopamine: Functions, Signaling, and Association with Neurological Diseases. *Cell. Mol. Neurobiol.* 31–59.
- (2) Volkow, N. D., Wise, R. A., and Baler, R. (2017) The Dopamine Motive System: Implications for Drug and Food Addiction. *Nat. Rev. Neurosci.* 741–752.
- (3) Grace, A. A. (2016) Dysregulation of the Dopamine System in the Pathophysiology of Schizophrenia and Depression. *Nat. Rev. Neurosci.* 524–532.
- (4) Segura-Aguilar, J., Paris, I., Muñoz, P., Ferrari, E., Zecca, L., and Zucca, F. A. (2014) Protective and Toxic Roles of Dopamine in Parkinson's Disease. *J. Neurochem.* 129 (6), 898–915.
- (5) Meiser, J., Weindl, D., and Hiller, K. (2013) Complexity of Dopamine Metabolism. *Cell Commun. Signaling* 11 (1), 34.
- (6) Pillaiyar, T., Manickam, M., and Jung, S. H. (2017) Downregulation of Melanogenesis: Drug Discovery and Therapeutic Options. *Drug Discovery Today* 22 (2), 282–298.
- (7) Shen, X., Zhang, F., and Dryhurst, G. (1997) Oxidation of Dopamine in the Presence of Cysteine: Characterization of New Toxic Products. *Chem. Res. Toxicol.* 10, 147–155.
- (8) Bisaglia, M., Mammì, S., and Bubacco, L. (2007) Kinetic and Structural Analysis of the Early Oxidation Products of Dopamine. *J. Biol. Chem.* 282 (21), 15597–15605.
- (9) Bisaglia, M., Soriano, M. E., Arduini, L., Mammì, S., and Bubacco, L. (2010) Molecular Characterization of Dopamine-Derived Quinones Reactivity toward NADH and Glutathione: Implications for Mitochondrial Dysfunction in Parkinson Disease. *Biochim. Biophys. Acta, Mol. Basis Dis.* 1802 (9), 699–706.
- (10) Santos, C. C., Araujo, F. M., Ferreira, R. S., Silva, V. B., Silva, J. H.C., Grangeiro, M. S., Soares, E. N., Pereira, E. P. L., Souza, C. S., Costa, S. L., Segura-Aguilar, J., and Silva, V. D. A. (2017) Toxicology in Vitro Aminochrome Induces Microglia and Astrocyte Activation. *Toxicol. In Vitro* 42 (April), 54–60.
- (11) Murakami, K., Wakamatsu, K., Nakanishi, Y., Takahashi, H., Sugiyama, S., and Ito, S. (2008) Serum Levels of Pigmentation Markers Are Elevated in Patients Undergoing Hemodialysis. *Blood Purif.* 25 (5–6), 483–489.
- (12) Zecca, L., Bellei, C., Costi, P., Albertini, A., Monzani, E., Casella, L., Gallorini, M., Bergamaschi, L., Moscatelli, A., Turro, N. J., Eisner, M., Crippa, P. R., Ito, S., Wakamatsu, K., Bush, W. D., Ward, W. C., Simon, J. D., and Zucca, F. A. (2008) New Melanic Pigments in the Human Brain That Accumulate in Aging and Block Environmental Toxic Metals. *Proc. Natl. Acad. Sci. U. S. A.* 105 (45), 17567–17572.
- (13) Martin, G. B., Chiap, P., Paquet, P., Pierard, G., de Tullio, P., Martin, Y., Rozet, E., Hubert, P., Crommen, J., and Fillet, M. (2007) Development of a Mass Spectrometry Method for the Determination of a Melanoma Biomarker, S-S-Cysteinyl-dopa, in Human Plasma Using Solid Phase Extraction for Sample Clean-Up. *J. Chromatogr. A* 1156 (1–2), 141–148.
- (14) Martin, G., Mansion, F., Houbart, V., Paquet, P., Rorive, A., Chiap, P., Crommen, J., Servais, A. C., and Fillet, M. (2011) Pre-Study and in-Study Validation of a SPE-LC-MS-MS Method for the Determination of S-S-Cysteinyl-dopa, a Melanoma Biomarker, in Human Plasma. *Talanta* 84 (2), 280–286.
- (15) Izumi, Y., Sawada, H., Yamamoto, N., Kume, T., Katsuki, H., Shimohama, S., and Akaïke, A. (2005) Iron Accelerates the Conversion of Dopamine-Oxidized Intermediates into Melanin and Provides Protection in SH-SY5Y Cells. *J. Neurosci. Res.* 82 (1), 126–137.
- (16) Ochs, S. D., Westfall, T. C., and MacArthur, H. (2005) The Separation and Quantification of Aminochromes Using High-Pressure Liquid Chromatography with Electrochemical Detection. *J. Neurosci. Methods* 142 (2), 201–208.
- (17) Remião, F., Milhazes, N., Borges, F., Carvalho, F., Bastos, M. L., Lemos-Amado, F., Domingues, P., and Ferrer-Correia, A. (2003) Synthesis and Analysis of Aminochromes by HPLC-Photodiode Array. Adrenochrome Evaluation in Rat Blood. *Biomed. Chromatogr.* 17 (1), 6–13.
- (18) Carballo-carbajal, I., Laguna, A., Romero-giménez, J., Cuadros, T., Bové, J., Martínez-vicente, M., Parent, A., Gonzalez-sepulveda, M., Peñuelas, N., Torra, A., Rodríguez-Galván, B., Ballabio, A., Hasegawa, T., Bortolozzi, A., Gelpi, E., and Vila, M. (2019) Brain Tyrosinase Overexpression Implicates Age-Dependent Neuromelanin Production in Parkinson's Disease Pathogenesis. *Nat. Commun.* 10 (1), 973.
- (19) Lemos-Amado, F., Domingues, P., Ferrer-Correia, A., Remião, F., Milhazes, N., Borges, F., Carvalho, F. D., and Bastos, M. L. (2001) Electrospray Tandem Mass Spectrometry of Aminochromes. *Rapid Commun. Mass Spectrom.* 15 (24), 2466–2471.
- (20) Nappi, A. J., and Vass, E. (2001) The Effects of Nitric Oxide on the Oxidations of L-Dopa and Dopamine Mediated by Tyrosinase and Peroxidase. *J. Biol. Chem.* 276 (14), 11214–11222.
- (21) Miller, J. V., Lebouf, R. F., Kelly, K. A., Michalovicz, L. T., Ranpara, A., Locker, A. R., Miller, D. B., and O'Callaghan, J. P. (2018) The Neuroinflammatory Phenotype in a Mouse Model of Gulf War Illness Is Unrelated to Brain Regional Levels of Acetylcholine as Measured by Quantitative HILIC-UPLC-MS/MS. *Toxicol. Sci.* 165 (2), 302–313.
- (22) Bergh, M. S. S., Bogen, I. L., Lundanes, E., and Øiestad, Å. M. L. (2016) Validated Methods for Determination of Neurotransmitters and Metabolites in Rodent Brain Tissue and Extracellular Fluid by Reversed Phase UHPLC-MS/MS. *J. Chromatogr. B: Anal. Technol. Biomed. Life Sci.* 1028, 120–129.
- (23) Annesley, T. M. (2003) Ion Suppression in Mass Spectrometry. *Clin. Chem.* 49 (7), 1041–1044.
- (24) González, R. R., Fernández, R. F., Vidal, J. L. M., French, A. G., and Pérez, M. L. G. (2011) Development and Validation of an Ultra-High Performance Liquid Chromatography-Tandem Mass-Spectrometry (UHPLC-MS/MS) Method for the Simultaneous Determination of Neurotransmitters in Rat Brain Samples. *J. Neurosci. Methods* 198 (2), 187–194.
- (25) Zhu, K. Y., Fu, Q., Leung, K. W., Wong, Z. C. F., Choi, R. C. Y., and Tsim, K. W. K. (2011) The Establishment of a Sensitive Method in Determining Different Neurotransmitters Simultaneously in Rat Brains by Using Liquid Chromatography-Electrospray Tandem Mass Spectrometry. *J. Chromatogr. B: Anal. Technol. Biomed. Life Sci.* 789 (11–12), 737–742.
- (26) Lv, C., Li, Q., Liu, X., He, B., Sui, Z., Xu, H., Yin, Y., Liu, R., and Bi, K. (2015) Determination of Catecholamines and Their Metabolites in Rat Urine by Ultra-Performance Liquid Chromatography-Tandem Mass Spectrometry for the Study of Identifying Potential Markers for Alzheimer's Disease. *J. Mass Spectrom.* 50 (2), 354–363.
- (27) Pastor, A., Rodríguez-Morató, J., Olesti, E., Pujadas, M., Pérez-Mañá, C., Khymentis, O., Fitó, M., Covas, M.-I. I., Solá, R., Motilva, M.-J. J., Farré, M., and de la Torre, R. (2016) Analysis of Free Hydroxytyrosol in Human Plasma Following the Administration of Olive Oil. *J. Chromatogr. A* 1437, 183–190.
- (28) Goldstein, D. S., Sullivan, P., Holmes, C., Miller, G. W., Alter, S., Strong, R., Mash, D. C., Kopin, I. J., and Sharabi, Y. (2013) Determinants of Buildup of the Toxic Dopamine Metabolite DOPAL in Parkinson's Disease. *J. Neurochem.* 126 (5), 591–603.
- (29) Sánchez-Ferrer, A., Neptuno Rodríguez-López, J., García-Cánovas, F., and García-Carmona, F. (1995) Tyrosinase: A Comprehensive Review of Its Mechanism. *Biochim. Biophys. Acta, Protein Struct. Mol. Enzymol.* 1247 (1), 1–11.
- (30) Hasegawa, T., Matsuzaki, M., Takeda, A., Kikuchi, A., Furukawa, K., Shibahara, S., and Itoyama, Y. (2003) Increased Dopamine and Its Metabolites in SH-SY5Y Neuroblastoma Cells That Express Tyrosinase. *J. Neurochem.* 87 (2), 470–475.
- (31) Matuszewski, B. K., Constanzer, M. L., and Chavez-Eng, C. M. (2003) Strategies for the Assessment of Matrix Effect in Quantitative Bioanalytical Methods Based on HPLC – MS/MS. *Anal. Chem.* 75, 3019–3030; (2003) *Anal. Chem.* 75 (13), 3019–3030.